IMPERIAL

Geospatial Modelling Framework for Assessing Chemical Processes and Energy Systems

Applications in Direct Air Capture and Electrolytic Hydrogen Production

Marwan Saeed A Sendi

The Sargent Centre for Process Systems Engineering
Department of Chemical Engineering
Imperial College London

Submitted in part fulfilment of the requirements
for the degree of Doctor of Philosophy at
Imperial College London, December 2024

DECLARATION

I hereby declare that the work presented in this thesis is my own, except where otherwise stated. Information derived from the published and unpublished work of others has been appropriately referenced in the text, with sources listed in the references section. Portions of the work presented in this thesis have appeared in, or been submitted to, the following journal publications and conferences.

1) Sendi, M., Bui, M., Mac Dowell, N., and Fennell, P. (2022). Geospatial analysis of regional climate impacts to accelerate cost-efficient direct air capture deployment. One Earth, 5(10):1153–1164. 10.1016/j.oneear.2022.09.003. This work is part of Chapter 2. Contributions: Marwan Sendi developed the methodology, conducted the investigation and wrote the original draft. Mai Bui supervised the project and reviewed and edited the manuscript. Niall Mac Dowell and Paul Fennell conceptualised and supervised the project and reviewed and edited the manuscript.

2) Sendi, M., Bui, M., Mac Dowell, N., and Fennell, P. Regional techno-economic analysis of different solid sorbent-based direct air capture configurations. The 16th Greenhouse Gas Control Technologies Conference (GHGT-16). Lyon, France, 23–27 October 2022.This work is part of Chapter 2. Contributions: Marwan Sendi developed the methodology, conducted the investigation and wrote the original draft. Mai Bui supervised the project and reviewed and edited the manuscript. Niall Mac Dowell and Paul Fennell conceptualised and supervised the project and reviewed and edited the manuscript.

3) Sendi, M., Bui, M., Mac Dowell, N., and Fennell, P. Exploring energy supply options and opportunities for cost-effective direct air capture deployment. The 12th Trondheim Conference on CO_2 Capture, Transport and Storage (TCCS-12). Trondheim, Norway, 20–21 June 2023.This work is part of Chapter 3. Contributions: Marwan Sendi conceptualised the project, developed the methodology, conducted the investigation

and wrote the original draft. Mai Bui, Niall Mac Dowell and Paul Fennell conceptualised and supervised the project and reviewed and edited the manuscript.

4) Sendi, M., Bui, M., Mac Dowell, N., and Fennell, P. Geospatial modelling and optimisation of direct air capture and its energy supply options for cost-effective deployment. The 34th European Symposium on Computer Aided Process Engineering and the 24th International Symposium on Process Systems Engineering (ESCAPE34-PSE24). Florence, Italy, 2–6 June 2024. This work is part of Chapters 2 and 3. Contributions: Marwan Sendi conceptualised the project, developed the methodology, conducted the investigation and wrote the original draft. Mai Bui, Niall Mac Dowell and Paul Fennell conceptualised and supervised the project and reviewed and edited the manuscript.

5) Sendi, M., Bui, M., Mac Dowell, N., and Fennell, P. Identifying the most cost-effective and environmentally suitable energy supply options for direct air capture in different regions around the world. The 3rd International Conference on Negative CO_2 Emissions. Oxford, UK, 18–21 June 2024. This work is part of Chapter 3. Contributions: Marwan Sendi conceptualised the project, developed the methodology, conducted the investigation and wrote the original draft. Mai Bui, Niall Mac Dowell and Paul Fennell conceptualised and supervised the project and reviewed and edited the manuscript.

6) Sendi, M., Bui, M., Mac Dowell, N., and Fennell, P. (2024). Geospatial techno-economic and environmental assessment of different energy options for solid sorbent direct air capture. Cell Reports Sustainability, 1:100151. 10.1016/j.crsus.2024.100151. This work is part of Chapter 3. Contributions: Marwan Sendi conceptualised the project, developed the methodology, conducted the investigation and wrote the original draft. Mai Bui, Niall Mac Dowell and Paul Fennell conceptualised and supervised the project and reviewed and edited the manuscript.

7) Sendi, M., Mersch, M., and Mac Dowell, N. (2024). Electrolytic hydrogen production; how green must green be? Submitted to Joule.This work is part of Chapter 4. Contributions: Marwan Sendi developed the methodology, conducted the investigation and wrote the original draft. Matthias Mersch conducted the ESO modelling (not presented in this thesis) and reviewed and edited the manuscript. Niall Mac Dowell conceptualised and supervised the project and reviewed and edited the manuscript.

Marwan Saeed A Sendi
December, 2024

COPYRIGHT

The copyright of this thesis rests with the author. Unless otherwise indicated, its contents are licensed under a Creative Commons Attribution-Non Commercial 4.0 International Licence (CC BY-NC).

Under this licence, you may copy and redistribute the material in any medium or format. You may also create and distribute modified versions of the work. This is on the condition that: you credit the author and do not use it, or any derivative works, for a commercial purpose.

When reusing or sharing this work, ensure you make the licence terms clear to others by naming the licence and linking to the licence text. Where a work has been adapted, you should indicate that the work has been changed and describe those changes.

Please seek permission from the copyright holder for uses of this work that are not included in this licence or permitted under UK Copyright Law.

ABSTRACT

The global transition towards net-zero emissions will require increased adoption of technologies with location-dependent performance. Geospatial analysis can be a rapid and cost-effective tool in screening the performance of technologies and systems with location-dependent performance. It can aid decision-makers in the crucial task of identifying optimal deployment locations.

This thesis presents a geospatial modelling framework that integrates detailed process- and system-level modelling with regional data. The framework can account for variations in regional climate, intermittent renewable energy availability and economic factors, providing a holistic understanding of the factors influencing the performance of low-carbon technologies. The utility of the framework is illustrated in three case studies. First, it is used for technology assessment, specifically direct air capture. The study assesses how ambient temperature and relative humidity affect direct air capture process performance and costs. It then analyses multiple years of high-resolution climatic data to identify optimal locations for direct air capture deployment. Building on this, the framework is extended to system-level assessments using a process systems engineering approach. This enables the geospatial assessment of direct air capture systems coupled with different low-carbon energy sources, including intermittent renewables, nuclear power and natural gas. Finally, the framework is used in policy assessment by examining the policy implications of enforcing an hourly time-matching requirement for grid-connected electrolytic hydrogen production from intermittent renewable energy. By analysing two decades of wind and solar data, the study highlights the challenges and economic impacts of hourly aligning hydrogen production with variable renewable energy availability. The findings offer insights into designing policies that balance economic and environmental objectives.

Overall, this thesis offers a valuable tool for screening and identifying the optimal deployment of low-carbon technologies by incorporating regional variations and

system-level interactions. This can support policymakers and stakeholders in ensuring a cost-effective and sustainable transition to a low-carbon economy.

ACKNOWLEDGEMENTS

Completing this PhD has been a significant milestone in my professional and personal development, and it would not have been possible without the support of many people to whom I am deeply grateful.

First and foremost, I would like to express my sincere gratitude to my supervisors, Paul Fennell, Niall Mac Dowell, and Mai Bui. Their invaluable guidance, insightful discussions, and continuous support have been instrumental in shaping my research. Their mentorship inspired me to strive for impactful work and uphold a strong work ethic. I am also thankful to Nilay Shah for his valuable feedback on my PhD research and our collaborative projects.

My appreciation extends to my colleagues and friends—Ahmad Khan, Matthias Mersch, David Danaci, and Nixon Sunny—for the engaging discussions and for sharing their expertise. I would also like to thank different past and current research group members: Nadin, Maria, Solene, Roghayeh, Ahmed, Diego, Augustin, Piera, Yoga, Julian, Antigoni, Caroline, Quinn, Huan, and Davis, for their friendship and making my time at Imperial enjoyable.

I have been fortunate to have the support of many great friends during my PhD journey, including Ali, Abdulrahman, Ghassan, Bader, Nasser, Kita, Andrea, Marta, Neil, Ibrahim, Alex, Nikita, Maliq, Yannik, Saphina, Jessica, Abel, Jorge and Nick. Thank you for creating and sharing wonderful memories.

Most importantly, I wish to express my deepest gratitude to my parents and family for their unconditional love, support and encouragement throughout this journey.

To everyone who has been part of this journey, your support has been invaluable, and I am sincerely grateful.

CONTENTS

Nomenclature **xxi**

1 Introduction **1**
1.1 Background and motivation 1
1.2 Thesis aim and contribution 4

2 Technology assessment: Geospatial modelling of direct air capture performance—the effect of ambient conditions **7**
2.1 Abstract 7
2.2 Introduction 8
2.3 Background 9
2.3.1 Why direct air capture? 9
2.3.2 Direct air capture processes 10
2.3.3 The effect of ambient conditions on direct air capture performance 16
2.3.4 Geospatial modelling of direct air capture performance 18
2.4 Methodology 21
2.4.1 Process modelling 22
2.4.2 Geospatial modelling 45
2.5 Results and discussion 49
2.5.1 Effect of ambient conditions on direct air capture process performance 49
2.5.2 Geospatial techno-economic performance of direct air capture 53
2.6 Conclusions and future work 62
2.6.1 Conclusions 62
2.6.2 Limitations and future work 62

3 System assessment: Geospatial modelling of direct air capture and its

energy supply options **65**
3.1 Abstract . . . 65
3.2 Introduction . . . 66
3.3 Background . . . 67
3.3.1 Direct air capture and its energy supply . . . 67
3.3.2 Geospatial modelling of direct air capture and its energy supply options . . . 68
3.4 Methodology . . . 70
3.4.1 Geospatial and temporal representation . . . 71
3.4.2 System representation . . . 74
3.4.3 System Scenarios Considered . . . 77
3.4.4 Mathematical formulation and technologies description . . . 79
3.4.5 System performance indicators . . . 89
3.4.6 Representative locations . . . 91
3.5 Results and discussion . . . 93
3.5.1 Direct air capture powered by today's regional electricity grids 93
3.5.2 Overview of the techno-economic performance of coupling DAC to different energy sources . . . 95
3.5.3 Benefits of co-production of electricity from direct air capture systems . . . 101
3.5.4 Direct air capture cost sensitivity analysis . . . 118
3.5.5 Environmental performance . . . 122
3.6 Conclusions and future work . . . 130
3.6.1 Overall performance of different energy supply options for direct air capture . . . 132
3.6.2 Direct air capture cost reduction potential . . . 136
3.6.3 Limitations and future work . . . 137

4 Policy assessment: Implication of hourly time-matching requirement in hydrogen production **139**
4.1 Abstract . . . 139
4.2 Introduction . . . 140
4.3 Background . . . 141
4.3.1 Why low-carbon hydrogen? . . . 141
4.3.2 Hydrogen production . . . 142
4.3.3 Low-carbon hydrogen in net-zero strategies . . . 145

4.3.4 Policies and considerations around electrolytic low-carbon hydrogen production . . . 147
4.3.5 Current understanding of the hourly time-matching requirement and its implication in reducing CO_2 emissions . . . 149
4.4 Methodology . . . 150
4.4.1 Grid-connected electrolytic hydrogen production modelling . . . 150
4.4.2 Mathematical formulation . . . 151
4.4.3 Performance indicators . . . 154
4.5 Results and discussion . . . 156
4.5.1 The techno-economics of hourly time-matching . . . 156
4.5.2 CO_2 avoidance cost of hourly time-matching . . . 162
4.5.3 The levelised lifecycle emissions of grid-connected hydrogen . . . 166
4.5.4 The environmental value of electrolytic hydrogen in prospective applications . . . 169
4.6 Conclusions and future work . . . 173
4.6.1 Conclusions . . . 173
4.6.2 Limitations and future work . . . 174

5 Conclusions and future work **177**
5.1 Key findings and contributions . . . 178
5.1.1 Chapter 2: Technology assessment of direct air capture . . . 178
5.1.2 Chapter 3: System assessment of direct air capture and its energy supply options . . . 180
5.1.3 Chapter 4: Policy assessment of hourly time-matching requirement in electrolytic hydrogen production . . . 183
5.2 Future Work . . . 185

References **189**

Appendix A Direct air capture process model **227**
A.1 Process performance maps . . . 227
A.2 Process sensitivity analysis . . . 230

Appendix B Techno-economic assumptions **237**
B.1 Energy generation, storage and conversion technologies . . . 237
B.2 Direct air capture and point-of-source carbon capture and storage . . . 240
B.3 Regional weighted average capital cost . . . 242

Appendix C Environmental assumptions **243**
C.1 Lifecycle greenhouse gas emissions 243
C.2 Land requirement 244
C.3 Water requirement 244

Appendix D Solar and wind resources validation **245**
D.1 Solar resources 245
D.1.1 Global horizontal irradiation and solar photovoltaic potential . . 245
D.1.2 Direct normal irradiation and concentrated solar power potential 248
D.2 Wind speed 250

LIST OF TABLES

2.1 Overview of direct air capture (DAC) technologies 11
2.2 Adsorption process cycle model selection 26
2.3 Adsorption model parameters 31
2.4 Mechanistic adsorption model fitting parameters 33
2.5 GAB model fitting parameters 33
2.6 Adsorption model boundary conditions 34
2.7 Algorithm used for compression section modelling 38
2.8 Summary of sensitivity analysis for DAC process operating parameters 42
2.9 DAC collector operating parameters. 45
2.10 Regional DAC performance and LCOD at different climate conditions . 56

3.1 Performance of energy storage technologies 87
3.2 Selected representative locations to illustrate DAC system performance 92
3.3 Performance indicators for DAC+NuP and DAC+CCGT scenarios . . . 102
3.4 Break-even points for selected cases when DAC is coupled to a nuclear power plant 104
3.5 Summary of energy requirements and second-law (exergy) efficiency for different DAC technologies and configurations 108
3.6 Break-even points for selected cases when DAC is coupled to a CCGT power plant 113
3.7 Summary of the environmental performance 123

4.1 Long-haul heavy goods vehicles (HGVs) assumptions 155

B.1 Cost assumptions for energy generation, storage and conversion . . . 237
B.2 DAC process economic assumptions 240

C.1 Lifecycle greenhouse gas emissions from infrastructure and supply chain assumptions 243
C.2 Land requirement assumptions 244
C.3 Water requirement assumptions 244

LIST OF FIGURES

2.1 Methodology overview 21
2.2 DAC process flow diagram 23
2.3 DAC process cycle configuration 24
2.4 DAC CO_2 collector modelling 25
2.5 Flow diagram of the CO_2 compression section design and modelling . 37
2.6 Simplifed 3D model of the SA-VTSA DAC process productivity 46
2.7 Performance of DAC process based on SA-VTSA under different ambient conditions 49
2.8 Breakdown of electricity requirements for SA-VTSA cycle configuration 50
2.9 Performance of DAC process based on VTSA under different ambient conditions 52
2.10 The change ($\triangle$) in process performance between the SA-VTSA cycle and VSTA at different ambient conditions 53
2.11 Global performance of DAC 54
2.12 Aggregated climate regions based on DAC performance 55
2.13 Regional LCOD and global supply DAC supply curves for SA-VTSA at different electricity prices 58
2.14 Regional LCOD and global supply DAC supply curves for SA-VTSA at different electricity prices and fixed WACC 59
2.15 Regional water consumption for DAC based on SA-VTSA cycle configuration 60

3.1 Geospatial framework methodology overview 71
3.2 Aggregated regions for DAC with its energy supply options assessment 72
3.3 Simplified process flow diagram for the adsorption-based DAC process 73
3.4 System representation using RTN framework 76
3.5 System scenarios when electricity is co-produced 79

3.6 Performance of coupling DAC to today's regional electricity grid 93
3.7 Performance of regional electricity grids 94
3.8 Summary of DAC cost for the different considered scenarios 95
3.9 Normalised energy flows for the AllTech scenario 96
3.10 Effect of natural gas prices and regional WACC levels on DAC system scenarios 98
3.11 Performance of coupling DAC to iRE system with energy storage . . . 99
3.12 Effect intermittency on DAC systems 100
3.13 Performance of coupling direct air capture to nuclear power plants . . 105
3.14 Performance of coupling DAC to CCGT power plants 111
3.15 Performance of co-producing electricity from DAC coupled with iRE systems 115
3.16 Hourly profile for a REw/S system located in Riyadh, SA that is co-producing electricity 117
3.17 Levelised cost of DAC sensitivity analysis 119
3.18 Methane leakage and CCS capture rate effect on CO_2 removal efficiency and DAC cost 126
3.19 Mapping of potential CO_2 storage sites with current and under-construction nuclear power plants 128
3.20 Land requirement for coupling DAC to renewable energy and storage system 129
3.21 Comparison of the different DAC energy supply options 133

4.1 Hydrogen production system representation using RTN framework . . 151
4.2 Regional levelised cost of hydrogen ($LCOH_2$) for electrolytic hydrogen production 158
4.3 The performance hourly time-matched hydrogen production system . 160
4.4 Overview of the different solutions for hourly time-matched hydrogen production systems 161
4.5 Levelised cost of hydrogen ($LCOH_2$) when the hourly time-matching requirement is relaxed 162
4.6 Hydrogen carbon intensity when the hourly time-matching requirement is relaxed as a function of consumed grid electricity and its carbon intensity 163
4.7 CO_2 avoidance cost of imposing 100% hourly time-matching requirement 164

4.8 CO_2 avoidance cost, for a system that is placed in Texas, US, of imposing a 100% hourly time-matching requirement for grid-connected hydrogen production as a function of grid carbon intensity and avoided CO_2 165
4.9 Projected hydrogen CI for selected regions for 100% grid-powered hydrogen production 167
4.10 Projected 100% grid-powered hydrogen CI as a function of grid carbon intensity when the project starts producing hydrogen and years remaining for the net-zero electrical grid 168
4.11 Avoided CO_2 as a function of lifetime grid hydrogen CI relative to counterfactual 169
4.12 CO_2 avoidance cost when 100% grid-powered hydrogen displaces grey hydrogen as a function of its lifetime carbon intensity 170
4.13 CO_2 avoidance cost when 100% grid-powered hydrogen displaces natural gas as a function of its lifetime carbon intensity 171
4.14 CO_2 avoidance cost when 100% grid-powered hydrogen displaces diesel—in long-haul heavy goods vehicles (HGVs)—as a function of its lifetime carbon intensity 172

A.1 SA-VTSA DAC process low-temperature heat requirements simplified 3D model 227
A.2 SA-VTSA DAC process total electricity requirements simplified 3D model 228
A.3 SA-VTSA DAC process compressors and vacuum pumps electricity requirements simplified 3D model 228
A.4 SA-VTSA DAC process required air volume simplified 3D model . . . 229
A.5 SA-VTSA DAC process water production simplified 3D model 229
A.6 SA-VTSA adsorption step sensitivity analysis 231
A.7 SA-VTSA bed heating step sensitivity analysis 232
A.8 VTSA bed heating step sensitivity analysis 233
A.9 SA-VTSA bed desorption (bed heating and steam purging steps) sensitivity analysis 234
A.10 SA-VTSA steam purging step sensitivity analysis 235

B.1 Regional WACC assumptions 242

D.1 Yearly global horizontal irradiance data for 2020 246

D.2 Yearly global horizontal irradiance obtained from the Global Solar Atlas 2.0 246
D.3 Yearly solar photovoltaic potential for 2020 247
D.4 Yearly solar photovoltaic potential obtained from the Global Solar Atlas 2.0 247
D.5 Yearly direct normal irradiance for 2020 248
D.6 Yearly direct normal irradiance obtained from the Global Solar Atlas 2.0 249
D.7 Normalised concentrated solar power potential for 2020 249
D.8 Average wind speed calculated at 100m for 2020 250
D.9 Average wind speed calculated at 100m obtained from Global Wind Atlas 3.0 251

NOMENCLATURE

BECCS	bioenergy with carbon capture and storage
BPMED	bipolar membrane electrodialysis
CapEx	capital expenditure
CCGT	natural gas-fired combined cycle gas turbines
CCGTw/CCS	natural gas-fired combined cycle gas turbines with carbon capture and storage
CCS	point-of-source carbon capture and storage
CDR	carbon dioxide removal
CF	capacity factor
CI	carbon intensity
COP	coefficient of performance
CSP	concentrated solar power
CST	condensing steam turbine
DAC	direct air capture
DNI	direct normal irradiance
EB	electric boiler
efuels	electrofuels
EV	electric vehicles
FB	gas-fired boiler
GCC	Gulf Cooperation Council
GHG	greenhouse gas
GHI	global horizontal irradiance
GT	gas turbine
Gtpa	Giga (billion) tonnes per annum
HGV	heavy goods vehicle
HHV	high heating value
HP	Heat pump

HPS	high-pressure steam
HRSG	heat recovery steam generator
HT	high-temperature
IEA	International Energy Agency
instCap	installed capacity
iRE	intermittent renewable energy
iRE+ES	intermittent renewable energy with energy storage
ktpa	kilo (thousand) tonnes per annum
LCOD	levelised cost of direct air capture
$LCOD_{gross}$	Gross levelised cost of direct air capture
$LCOD_{net}$	Net levelised cost of direct air capture
LCODriving	levelised cost of driving
LCOE	levelised cost of electricity
LCOH	levelised cost of heating
$LCOH_2$	levelised cost of hydrogen
LDF	linear driving force
LHV	lower heating value
LPS	Low-pressure steam
LT	low-temperature
MEA	monoethanolamine
MILP	mixed-integer linear programming
MRV	monitoring, reporting and verification
Mtpa	Mega (million) tonnes per annum
NG	natural gas
ODE	ordinary differential equation
OpEx	operating expenses
PDE	partial differential equation
PEM	proton exchange membrane
PST	steam turbine that partially expands HPS to LPS
PTC	production tax credit
PV	photovoltaic
RGGI	Regional Greenhouse Gas Initiative
RH	relative humidity
RTN	Resource-Task Network
SA-VTSA	steam-assisted vacuum-pressure temperature swing adsorption
SMR	steam methane reforming

SOEC	solid oxide electrolysis cell
ST	steam turbine
STN	State-Task Network
THS	thermal heat storage
tpa	tonnes per annum
TRL	Technology Readiness Level
VTSA	vacuum-pressure temperature swing adsorption
WACC	weighted average capital cost

CHAPTER 1

INTRODUCTION

1.1 Background and motivation

According to the Intergovernmental Panel on Climate Change (IPCC), human-induced greenhouse gas (GHG) emissions, which include carbon dioxide (CO_2) and methane (CH_4), have led to an increase in global surface temperature—commonly referred to as global warming [1, 2]. This warming is resulting in significant impacts, such as ocean acidification, sea-level rise, prolonged droughts, and increasingly severe wildfires [1, 2]. As human-induced GHG emissions continue and escalate, the impacts of global warming are projected to become even more severe, threatening water availability, food production, biodiversity, and human health [1, 2].

Recognising the critical urgency of addressing human-induced global warming, most nations pledged through the 2015 Paris Agreement to limit the rise in global surface temperature to well below 2℃ above pre-industrial levels (1850–1900), while aiming to keep the increase below 1.5℃ by 2100 [3]. As of 2020, the global average surface temperature had already risen by approximately 1.1℃ above pre-industrial levels [1]. This translates to a remaining carbon budget—the estimated amount of additional CO_2 emissions permissible before reaching the targeted temperature increase—of around 500 $GtCO_{2,eq}$ to limit warming to 1.5℃ and around 1,150 $GtCO_{2,eq}$ to limit warming to 2℃ [1]. If GHG emissions continue at the current rate of around 59 $GtCO_{2,eq}$ annually, the 1.5℃ budget will be exhausted before 2030, and the 2℃ budget before 2040. Thus, achieving the goals of the Paris Agreement will require a rapid and global transition from the current high-emissions economy to a net-zero—or even net-negative—emissions economy, while simultaneously ensuring

sustained economic growth and prosperity [4, 5].

Energy use accounts for approximately three-quarters of current total GHG emissions, with primary world energy consumption historically dominated by unabated fossil fuels, including coal, oil and natural gas [6–8]. Transitioning to net-zero energy systems will require the widespread availability of affordable and low-carbon electricity, as sectors such as heating, cooling, and road transport can be electrified. Low-carbon electricity can be generated through a combination of intermittent renewable energy (iRE) sources, such as solar and wind, and dispatchable (i.e., on-demand) energy sources, such as nuclear power and fossil fuels with carbon capture and storage (CCS) [9]. Additionally, low-carbon fuels or energy vectors, such as hydrogen and biofuels, will be essential for decarbonising sectors that are challenging to electrify (i.e., hard-to-abate sectors), including aviation and marine transport [9]. Possibly, electrofuels (e-fuels) will also play a small role.

In addition to emission reduction by transitioning to low-carbon energy sources, carbon dioxide removal (CDR) will also be critical to achieving the Paris Agreement's temperature goals [5]. These CDR methods contribute to climate change mitigation by offsetting emissions from hard-to-abate sectors and enabling net-negative emissions, which are necessary to compensate for emissions overshoot and potentially reverse global temperature rise [10, 11]. Currently, around 2 $GtCO_2$ per year of CDR contributes to emission reduction, mainly achieved through nature-based methods, which primarily include land management practices such as afforestation, reforestation and soil carbon sequestration [12].

However, to meet the Paris Agreement targets, large-scale engineered CDR—up to 2 $GtCO_2$ per year by 2050 and 10 $GtCO_2$ per year by 2100—will be needed [12]. There have been several proposed engineered CDR methods that could offer potential solutions, such as bioenergy with carbon capture and storage (BECCS) and direct air capture (DAC) [13]. Each of these methods presents unique advantages and challenges [14]. For example, DAC can capture CO_2 directly from the atmosphere regardless of location, offering high flexibility, but it is an energy-intensive process that may compete with future demand for low-carbon energy [15]. Conversely, BECCS can co-produce low-carbon energy while providing CDR, but it requires sustainable biomass sourcing, which may compete with other uses such as biofuels and biochemicals [16].

Overall, the transition from current fossil-based energy systems to future energy

systems incorporating a high proportion of iRE sources marks a key transformation in our approach to energy production and management. Compared to technologies currently used in energy systems, the technologies required for this transition are heavily dependent on regional factors, including the availability of renewable energy resources, climate conditions, financing costs and local policies [17]. For example, the performance of iRE technologies like wind turbines and solar photovoltaic (PV) systems highly depends on geographic and environmental conditions. Wind turbines yield higher power outputs in regions with strong and consistent winds, while solar PV systems are most effective in areas with high solar irradiation. Similarly, DAC performance is affected by weather conditions, including temperature and relative humidity [18].

This geographical influence will extend to chemical processes and systems powered by iRE, such as in 'green' hydrogen production, or that utilise CO_2 supplied by DAC, such as in the production of e-fuels. In these cases, the variability in the performance of iRE and DAC can significantly impact the techno-economic and environmental aspects of these processes and systems [19]. Additionally, these technologies are capital-intensive, making them sensitive to regional variations in financing costs and economic factors [20].

Capturing regional variations when assessing these technologies is crucial for identifying optimal deployment locations where costs and resources can be optimised to maximise economic and environmental benefits. Thus, geospatial mapping becomes essential in pinpointing optimal locations for various future system components, aiding in cost reduction and resource allocation optimisation.

Geospatial modelling can be pivotal in identifying regions where technologies with region-dependent performance can operate optimally. It can capture different regional aspects, such as resource availability and temporal variations, such as seasonal and daily climate fluctuations. This approach can quickly and cost-effectively identify regions that offer the best conditions for certain technologies, enhancing resource allocation and maximising environmental benefits.

This dissertation builds on the importance of understanding regional variations in deploying future technologies required for climate mitigation. It presents a geospatial modelling framework designed to assess chemical processes, energy technologies and systems with region-dependent performance. The developed framework provides a method to quickly and cost-effectively identify regions offering optimal conditions

for specific technologies (e.g., DAC) or systems of different technologies (e.g., DAC coupled with iRE). While this dissertation presents case studies involving DAC and electrolytic hydrogen production, the framework can generally be used to evaluate the performance of various technologies and systems with region-dependent performance.

1.2 Thesis aim and contribution

The primary aim of this thesis is to develop a modelling framework that can assess chemical processes and energy systems from a geospatial perspective, taking regional variations into account. By providing a method to map out optimal deployment locations for different technologies and systems, the thesis seeks to guide project developers and inform policymakers, thereby supporting the transition to a low-carbon economy in a cost-effective and efficient manner.

To achieve this aim, the thesis presents a comprehensive geospatial modelling framework that integrates detailed process-level and system-level modelling with regional data, capturing ambient conditions, renewable energy availability and economic factors.

This thesis is structured to progressively develop and apply the developed geospatial modelling framework. Each chapter builds upon the previous one, with each chapter reporting on the relevant literature and the enhancement of the methodological modelling framework.

Chapter 2 provides an efficient framework for evaluating the regional performance of technologies with region-dependent performance. The framework is applied to the technology assessment of DAC. A detailed process-level modelling of the adsorption-based DAC process is developed. The influence of ambient temperature and relative humidity on the performance of a DAC process is explored. By utilising multiple years of high-resolution hourly spatial data from NASA's MERRA-2 dataset, the framework captures inter- and intra-annual variations in ambient conditions across different regions. This application demonstrates how the framework can assist in identifying optimal deployment locations for DAC by rapidly assessing technology performance across various regions.

Building upon this, Chapter 3 extends the geospatial modelling framework to include system-level assessments. By employing a Resource-Task Network (RTN)

representation, the complex interactions between resources (e.g., energy, materials) and tasks (technologies) are modelled. This approach facilitates the design and optimisation of systems integrating multiple technologies with region-dependent performance. The framework is applied to assess the techno-economic and environmental performance of coupling DAC with various low-carbon energy supply options, including iRE sources, nuclear power and natural gas with CCS. This extension enables a holistic evaluation of DAC systems, capturing the synergies between different system elements and considering regional variations and constraints.

In Chapter 4, the geospatial modelling framework is utilised to explore the implications of policy implementation on electrolytic hydrogen production. Specifically, the study analyses the policy implications of hourly time-matching requirement for grid-connected electrolytic hydrogen production using iRE sources. By employing 20 years of wind and solar availability, this analysis presents the challenges associated with hourly synchronising hydrogen production with fluctuating renewable energy availability, as well as the impact on system design and costs when supplying a highly reliable baseload hydrogen demand. The chapter provides insights into the techno-economic and environmental impacts of such policy mandates, offering guidance on designing balanced policy frameworks to maximise economic and environmental return on investment.

In summary, this thesis contributes to the field by:

- Developing a geospatial modelling framework that integrates process-level and system-level assessments with regional data to be applied to chemical processes and energy systems.
- Providing detailed analyses of DAC technology, highlighting the influence of ambient conditions on performance and costs, and mapping DAC geospatial performance.
- Evaluating the integration of DAC with various low-carbon energy supply options, offering a holistic system perspective on the performance of coupling DAC with the different energy supply options in different regions.
- Assessing the techno-economic and environmental implications of an hourly time-matching requirement on electrolytic hydrogen production, guiding balanced policy design.

CHAPTER 2

TECHNOLOGY ASSESSMENT: GEOSPATIAL MODELLING OF DIRECT AIR CAPTURE PERFORMANCE—THE EFFECT OF AMBIENT CONDITIONS

2.1 Abstract

This chapter presents a computationally efficient geospatial modelling framework for evaluating technologies with location-dependent performance, such as direct air capture and intermittent renewable energy technologies across various regions, thereby assisting decision-makers in pinpointing ideal operational sites. The framework's effectiveness in analysing technologies based on multiple performance-influencing variables is demonstrated through a regional techno-economic and environmental assessment of direct air capture based on solid sorbent technology. This assessment utilises multi-year, high-resolution hourly spatial data from NASA MERRA-2 to account for the impact of varying ambient temperature and relative humidity. Beyond ambient conditions, the framework can also incorporate other regional economic factors, such as capital costs, into the analysis.

For the analysed sorbent, the analysis shows that cold and drier regions generally offer favourable conditions for direct air capture operations. However, approximately 25% of the global land area is potentially unsuitable due to substantial periods of extremely cold temperatures. The analysis also estimates the levelised cost of

direct air capture ($320–$540 per tCO_2), along with the process's water and land requirements, based on regional performance metrics.

These insights significantly enhance our understanding of regional variations in direct air capture performance, providing valuable information for policymakers, investors and system planners. This knowledge is crucial for making informed decisions that optimise the deployment and effectiveness of direct air capture technologies. Furthermore, as new data on direct air capture sorbents and technologies emerge, the framework can serve as a practical tool for matching specific direct air capture solutions with locations where their performance can be maximised, ensuring more strategic and effective technological deployments in pursuit of global sustainable energy goals.

2.2 Introduction

The impact of geospatial characteristics on technology performance is not limited to intermittent renewable energy (iRE) generation technologies. It extends to emerging technologies like direct air capture (DAC), where ambient conditions—temperature and relative humidity—can have a significant influence on the CO_2 removal rate, productivity and energy demands of the process. While established iRE technologies like wind turbines and solar photovoltaic (PV) have well-documented correlations between their performance and geospatial location [21, 22], there is still limited understanding and modelling work on newer technologies such as DAC and their geospatial performance.

This chapter introduces a comprehensive framework, illustrated through a case study on the solid sorbent adsorption-based DAC process, aimed at modelling and mapping the geospatial performance of the technology. The chapter is organised as follows. Section 2.3 provides a review of the current state of DAC technologies, the existing understanding of how ambient conditions affect DAC performance, and published work on DAC geospatial analysis. Section 2.4 details the geospatial modelling framework, including a comprehensive description of the DAC process model. Section 2.5 presents and discusses the results of the DAC case study. The chapter concludes in Section 2.6 with a summary of the work and its limitations.

2.3 Background

2.3.1 Why direct air capture?

To meet the Paris Agreement's objective of limiting the global temperature increase below 2℃ and to achieve net-zero emissions cost-effectively, carbon dioxide removal (CDR) will be needed on a billion-tonne per-year scale [1, 2]. CDR will be crucial for offsetting overshoots and compensating for hard-to-abate emission sources [5, 10, 11]. These might include scattered or remote emission sources where the cost of connecting them to CO_2 infrastructure is uneconomical or sectors that are difficult to decarbonise, such as aviation and agriculture. Several CDR technologies are under development that differ in their advantages and drawbacks regarding efficiency; CO_2 storage permanence; timing; monitoring, reporting and verification (MRV) protocols; and biophysical limits [13, 14, 23].

Currently, the total global CDR is around 2 $GtCO_2$ per year, which is mostly achieved by utilising land management methods, such as afforestation/reforestation, while engineered CDR methods, including bioenergy with carbon capture and storage (BECCS) and DAC when combined with storage, only contribute around 1.3 million tonnes per annum of CO_2 ($MtpaCO_2$), which is less than 0.01% of the total [24]. However, achieving the Paris Agreement goal will require an estimated Engineered CDR of 2.4–4.5 $GtCO_2$ per year by 2050 and 6.4–13.2 $GtCO_2$ per year by 2100 [25]. This implies that the current engineered CDR capacity will need to scale up by more than 1,800 folds in the next 30 years, indicating the need for large, rapid deployment in engineered CDR. However, this deployment must be both sustainable and cost-effective to ensure prosperity for humans and the planet.

Among the various engineered CDR methods, DAC allows for immediate CO_2 removal from the atmosphere once DAC facilities become operational since captured CO_2 can be stored underground in geological formations such as reactive mineral deposits, depleted oil and gas fields and saline aquifers [26–28]. This can provide permanent and durable CO_2 storage with straightforward MRV protocols with high CO_2 removal efficiency if low-carbon emissions energy is used [13, 14]. Additionally, DAC has no theoretical biophysical limits due to the relatively low land and water requirements [23]. This, combined with the location flexibility and modularity of the technology, offers the potential for rapid large-scale deployment and makes DAC an appealing option for CDR [15, 29].

2.3.2 Direct air capture processes

DAC is a gas separation process where CO_2 is separated from other atmospheric gases [30–32]. Established gas separation technologies can be used for DAC applications, including physical separation technologies such as membrane and cryogenic air separation [33]. However, the low concentration of CO_2 in the atmosphere generally requires using materials with a high affinity for CO_2 [34]. Since CO_2 exhibits acidic properties in certain reactions, such as when it dissolves in water, these materials typically have basic properties [35–37]. Moreover, they are typically utilised in cyclic processes, where they bind to CO_2 during the loading phase and release it during the regeneration (or unloading) phase, facilitating CO_2 capture and removal [34]. Using materials with a high affinity for CO_2 translates to higher binding energy for CO_2, which in turn requires higher energy input to release the CO_2 when the material is regenerated [38]. This is the primary reason why DAC is an energy-intensive process. This, in addition to the requirement to process large volumes of air due to the diluted CO_2 concentration, adds to the energy requirements and necessitates the use of larger process equipment, which drives up the cost of the process.

Table 2.1 shows some DAC technologies grouped based on the employed separation technology: absorption and adsorption. The technologies shown vary in their development stage, with Technology Readiness Levels (TRL) from 3–9 [18, 39]. To date, the two most developed technologies are the adsorption process being developed by Climeworks, utilising solid sorbents—in vacuum-pressure temperature swing adsorption (VTSA) cycle, which has a TRL of 8–9, and the absorption process being developed by Carbon Engineering, utilising an aqueous solution of potassium hydroxide (KOH)—where the calciner is oxy-fired with natural gas. This process configuration has a TRL of 6–7 [18, 40, 41].

One critical difference between the DAC technologies is the energy type needed for sorbent regeneration. These energy types need to be available at low-cost and low-carbon footprint for DAC to be effective and ensure the process does not result in more CO_2 emissions than it captures [42–44]. Although the two most developed DAC technologies (Climeworks and Carbon Engineering) processes rely on heat input—in the form of low-temperature (LT) or high-temperature (HT) heat—to drive the CO_2 capture, there is increasing interest in developing DAC processes—current TRL 3–5—driven by electric power, either using electrochemical reaction or joule heating, due to the potential availability of low-carbon electricity in the future. The

following sections briefly describe the different DAC processes, with electrochemical processes grouped separately.

Table 2.1: Overview of direct air capture (DAC) technologies. Summary of energy requirements and second-law (exergy) efficiency for different DAC technologies and configurations based on literature data and this work is presented later in Chapter 3 in Table 3.5.

Separation technology	Active material	Regeneration method
Absorption	Hydroxide (KOH)	HT thermal heat/calciner
		Electric power/BPMED
	Amines	LT thermal heat/stripper
		Electric power/BPMED
	Amino acid	LT thermal heat/stripper
Adsorption	Amine functionalised solid sorbent	LT thermal heat/(SA-)VTSA
	Carbonate minerals (e.g., MgCO3)	HT thermal heat/calciner
	Ion-exchange resins	Water/moisture swing
	Redox-active molecule (e.g., quinone)	Electric power/electro-swing

Abbreviation: high-temperature (HT), low-temperature (LT), bipolar membrane electrodialysis (BPMED), steam-assisted vacuum-pressure temperature swing adsorption (SA-VTSA).

2.3.2.1 Absorption

The Carbon Engineering process is the most developed absorption-based DAC technology, which utilises aqueous hydroxide (KOH) solution [41]. This process primarily consists of two process loops: (1) the CO_2 capture and alkali solution regeneration loop and (2) the calcium loop. In the first loop, the aqueous KOH solution scrubs CO_2 from the air in absorption columns (i.e., air contactors), where potassium carbonate (K_2CO_3) is formed, following the reaction in Equation 2.1. The KOH solution is then regenerated in a pellet reactor by reacting it with lime ($Ca(OH)_2$), where limestone ($CaCO_3$) is formed and precipitates at the bottom of the reactor following the reaction in Equation 2.2. The aqueous KOH solution is selected here instead of NaOH because it offers higher CO_2 absorption kinetics [45, 46]. In the

calcium loop, the solid limestone is dried and then heated to temperatures above 900 ℃ in the calciner, where it decomposes into quicklime (CaO), releasing the CO_2, which is captured following Equation 2.3. Lastly, the quicklime is rehydrated to lime in the slaker and returned to the pellet reactor following Equation 2.4.

CO_2 capture and alkali solution regeneration loop

$$\textbf{Adsorption column: } CO_{2(g)} + 2\,KOH_{(aq)} \rightarrow H_2O_{(l)} + K_2CO_{3(aq)} \tag{2.1}$$

$$\textbf{Pellet reactor: } K_2CO_{3(aq)} + Ca(OH)_{2(s)} \rightarrow 2\,KOH_{(aq)} + CaCO_{3(s)} \tag{2.2}$$

Calcium loop

$$\textbf{Calciner: } CaCO_{3(s)} \rightarrow CaO_{(s)} + CO_{2(g)} \tag{2.3}$$

$$\textbf{Slaker: } CaO_{(s)} + H_2O_{(l)} \rightarrow Ca(OH)_{2(s)} \tag{2.4}$$

The calcination step for the absorption-based process is the most energy-intensive, with heat desorption of CO_2 equal to 1.13 MWh per tCO_2. The most developed Carbon Engineering process (TRL 6–7) uses oxy-combustion of natural gas (NG) to provide the reaction heat at a temperature above 900 ℃. Carbon Engineering estimates 1.46 $MWh_{th\text{-}HT}$ per tCO_2[†] for the heat requirement for this configuration—around a thermal efficiency of 77% [41]. Moreover, Carbon Engineering is exploring alternative approaches to electrifying this process and avoiding using fossil fuels. These approaches include electrified calciners—joule heating—and firing with hydrogen—produced through electrolysis (TRL 4–5). Preliminary results show that firing with hydrogen is more cost-effective than an electrified calciner [47].

Another absorption-based process being considered for DAC uses amine-based solutions [46, 48]. Amine-based CO_2 capture is the benchmark technology used for point-source CCS, using various amines [49]. Amine solutions such as monoethanolamine (MEA) are highly effective in capturing CO_2 because of their strong CO_2 affinity. The process typically consists of one process loop involving two columns: an absorber and a stripper. In the absorber, the lean amine solution scrubs CO_2 from the air, while in the stripper, the rich amine solution is thermally regenerated using LT heat, where CO_2 is released and captured [50]. This process's estimated LT thermal energy requirement is 2.97 $MWh_{th\text{-}LT}$ per tCO_2[†] [51]. Compared to the KOH-based

[†]Summary of energy requirements and second-law efficiency for different DAC technologies is presented in Table 3.5.

process, the sorbent is regenerated using LT heat (∼100–120 °C), allowing for cheaper energy sources. Nonetheless, amines with high CO_2 capture efficiency, e.g., MEA, have relatively high vapour pressure, causing significant amine evaporation–due to the requirement of processing large air volume for DAC application—which can increase the process costs and potentially emit toxic chemicals [50]. To reduce evaporation losses, amino acid salt solutions have been suggested, offering less toxic, lower vapour pressure solutions [52, 53]. However, this approach is still under development (TRL 4-5) by the Commonwealth Scientific and Industrial Research Organisation (CSIRO), Australia [51, 54].

2.3.2.2 Adsorption

Adsorption-based DAC technologies use solid sorbents that bind to CO_2 at low concentrations found in ambient air [55, 56]. These solid sorbents are used in a cyclic adsorption (i.e., loading) and desorption (i.e., unloading) process [57]. The most used solid sorbents are amine-functionalised solid sorbents, where amines are immobilised on solid sorbents, such as cellulose, resins, metal oxides and metal-organic frameworks [38, 58, 59]. Thus, the process capitalises on the amines' strong affinities for CO_2 while reducing their evaporation and losses compared to amine-based solution processes. Moreover, solid supports with lower heat capacity than water could be used, which can help reduce energy requirements during sorbent regeneration [38]. Besides amine-functionalised solid sorbents, other solid sorbents without amine-functionalised are also being investigated for DAC applications [60–64].

Climeworks has commercialised the amine-functionalised solid sorbent using a fixed bed and VTSA cycle (TRL 8–9) [40]. In this process's adsorption cycle, air passes through the sorbent bed, where CO_2 binds to the sorbent. When the sorbent is saturated with CO_2, the desorption cycle starts, where the sorbent bed is sealed, and the remaining air in the bed void is removed using vacuum pressure. The bed is then heated using LT heat to around 100 °C, where CO_2 is desorbed from the sorbent and captured. Steam purging can also be used to lower the CO_2 partial pressure, where more CO_2 can be recovered from the sorbent [65–68]. This is known as steam-assisted VTSA (SA-VTSA). The process's primary energy requirements are in the form of LT heat, where Climeworks reports current requirements of 3.31 $MWh_{th\text{-}LT}$ per tCO_2 with a future target of 1.5 $MWh_{th\text{-}LT}$ per tCO_2[†] [42]. When em-

[†]Summary of energy requirements and second-law efficiency for different DAC technologies is presented in Table 3.5.

ploying amine-functionalised sorbents, removing air from the bed before heating the sorbent becomes important since oxygen in the air can oxidise the amines at elevated temperatures, lowering the sorbents' effectiveness in binding to CO_2 [69]. In addition to the fixed bed design employed by Climeworks, different bed designs have been proposed, including fixed beds with joule heating, fluidised beds and rotating beds [70–73].

Carbonate minerals, such as magnesite ($MgCO_3$) and limestone ($CaCO_3$), can also be used as solid sorbents for DAC [74–78]. When these carbonate minerals are calcined at temperatures exceeding 600 ℃, CO_2 is released and can be captured, similar to the KOH absorption-based DAC process. The resultant metal oxides, CaO and MgO, can subsequently react with CO_2 in the air, converting back into carbonate minerals. Nonetheless, this reaction is slow—typically weeks to months for high levels ($\geq$75%) of carbonation by ambient air [75]. As a result, this DAC process generally requires large land areas to disperse and store the metal oxides, providing sufficient time for the reaction with CO_2 in the air to occur. However, solutions to overcome the large land area requirement have been proposed, such as using developed warehouse technologies, including vertical racking with automated stackers, cranes, vertical lifts and shuttles [79]. Heirloom is working to commercialise this technology utilising natural gas in an oxy-fired calciner (TRL 6–7) with plans to use electrified calciners in the future [79, 80]. The estimated HT heat requirement for the calcination step—for the MgO-based process—is 1.64–2.21 $MWh_{th\text{-}HT}$ per tCO_2[†], equivalent to a calciner thermal efficiency of 34%–46% [76].

Moisture-swing adsorption using functionalised ion-exchange resins offers an alternative to the thermally generated DAC processes using solid sorbents [81]. In this process, the moisture content (i.e., water partial pressure) controls the adsorption and desorption cycle. CO_2 is adsorbed to the sorbent at dry conditions (i.e., low water partial pressure). Then, CO_2 can be released from the sorbent by increasing humidity in the sorbent bed (i.e., high water partial pressure). This has the potential to lower energy requirements compared to thermally driven DAC approaches since the adsorption cycle is driven by changes in humidity. However, this limits the feasibility of the process to only dry regions. The estimated water requirement is 4.9–15.1 tH_2O per tCO_2 [82]. Carbon Collect is developing this process, which is still at an early stage with a TRL of 4–5.

[†]Summary of energy requirements and second-law efficiency for different DAC technologies is presented in Table 3.5.

2.3.2.3 Electrochemical

Using electrochemical approaches for DAC application can selectively target desired CO_2 molecules, avoiding heating all the solution or the bed containing the sorbent compared to thermal-based DAC, which potentially can reduce energy requirements for sorbent regeneration [83]. Electrochemical DAC approaches can be categorised based on their chemistry to indirect and direct methods [84, 85].

Indirect methods involve high CO_2 affinity compounds not directly affected by electrochemical activity in a protic solution. Thus, when the solution is reduced, the pH of the solution increases, leading to the absorption of CO_2 as a (bi)carbonate. On the other hand, when the solution is oxidised, the pH of the solution decreases, reversing the absorption process and releasing CO_2.

An example of this method is replacing the calcium loop—including the calciner—in the hydroxide solution-based DAC process with bipolar membrane electrodialysis (BPMED) [86, 87]. The processed carbonate (CO_3^{2-}) from the absorber column (Equation 2.1) can be regenerated using a BPMED following Equation 2.5–2.9. However, this process has relatively high minimum energy requirements of 1.03 MWh_{el} per tCO_2[†], corresponding to water splitting of 2 mol per 1 mol CO_2 captured at a minimum voltage drop of 0.829 V. Nonetheless, experimental and modelling results show energy demand in the range of 2.36–6.67 MWh_{el} per tCO_2 [87, 88].

To decrease the energy requirements of this process, the use of potassium bicarbonate ($KHCO_3$) solution was suggested recently as an alternative [89]. The application of a lower voltage across the BPMED can maintain the concentration of bicarbonate and prevent its full conversion to carbonate. However, this results in a lower pH for the capture solution than a KOH solution, affecting process productivity and CO_2 capture kinetics—thus, the process's techno-economic performance. Modelling shows minimum energy requirements of around 0.63 MWh_{el} per tCO_2 [89]. Other solutions, including amines, neutral red and phenazine derivatives, have been processed using the same approach [90–93]. For example, Mission Zero Technology is developing a BPMED-based process utilising polyethyleneimine (PEI) solution as the CO_2 capture material based on their patent [94]. However, this technology is at an early stage of development (TRL 4–5).

[†]Summary of energy requirements and second-law efficiency for different DAC technologies is presented in Table 3.5.

Andoe (acidic side)

$$CO_3^{2-} + H^+ \leftrightarrow HCO_3^- \tag{2.5}$$

$$HCO_3^- + H^+ \leftrightarrow H_2CO_3 \tag{2.6}$$

$$H_2CO_3 \leftrightarrow CO_2 + H_2O \tag{2.7}$$

Cathode (base side)

$$2\ H_2O \leftrightarrow 2\ OH^- + H_2 \tag{2.8}$$

$$2\ K^+ + 2\ OH^- \leftrightarrow 2\ KOH \tag{2.9}$$

Direct methods use redox-active compounds in cyclic electrochemical processes. Electrochemical reduction of these compounds makes them active for binding to CO_2 (Equations 2.10–2.11). Once the compounds are saturated with CO_2, electrochemical oxidation releases the CO_2, which can be captured (Equation 2.12). An example of these compounds is redox-active quinone compounds.

Quinone compounds were studied for CO_2 capture in liquid absorption and solid sorbent cycles [95–98]. However, these approaches are at a very early stage of development (TRL 3–4) and still need to be proven suitable for DAC applications since quinones are prone to oxygen oxidation [99].

$$Q + e^- \leftrightarrow Q^- \tag{2.10}$$

$$CO_2 + Q^- \leftrightarrow QCO_2^- \tag{2.11}$$

$$QCO_2^- - e^- \leftrightarrow Q + CO_2 \tag{2.12}$$

2.3.3 The effect of ambient conditions on direct air capture performance

As illustrated in the previous section, DAC processes use sorbents to drive the CO_2 removal from the air. On a molecular level, these sorbents' thermal and kinetic properties—including CO_2 loading equilibrium, mass transfer and reaction rate—are affected by the treated air's conditions, especially temperature and water concentration (i.e., relative humidity) [57, 100–102]. This, in return, can affect the DAC process performance in terms of process productivity (amount of CO_2 removed per amount of

sorbent per time) and energy and water requirements [100, 103, 104].

Different sorbents have different molecular properties that can result in DAC processes that operate favourably under different air conditions. This is also the case for DAC process design and configuration, where one DAC process design can be optimal under specific climate conditions but perform poorly under other conditions. On the other hand, climate and weather conditions vary between regions. Thus, certain sorbents and process designs might provide better process performance in certain regions with specific climate and weather conditions. This highlights the importance of screening DAC sorbents and process configuration for different regions.

There is still limited published research on the effect of ambient conditions on different DAC sorbents and processes, and it mainly focuses on the (KOH) absorption-based and (amine-functionalised solid sorbent) adsorption-based processes.

2.3.3.1 Adsorption processes

An et al. [100] studied the effect of varying the ambient temperature and relative humidity on the KOH solution-based process developed by Carbon Engineering [41]. They found that the CO_2 capture rate is more sensitive to temperature than relative humidity, where higher temperatures and relative humidity result in higher CO_2 capture rates. This, in return, results in higher process productivity and lower process energy requirements, making these conditions favourable for this process. Nonetheless, higher temperatures (and lower relative humidity) can increase the process water requirements.

2.3.3.2 Absorption processes

Leonzio et al. [105] assessed the techno-economic and environmental performance of various solid sorbents for DAC based on temperature swing adsorption (TSA) across several regions. Their study demonstrated that increasing ambient temperature negatively impacts DAC performance. However, their modelling approach did not account for temporal variations in ambient temperature throughout the year, relying instead on yearly average temperatures. Furthermore, their modelling did not consider the impact of water co-adsorption, and therefore, the influence of relative humidity was not included in their analysis.

Schellevis et al. [106] modelled the effect of temperature and relative humidity on

amine-functionalised sorbent (Lewatit VP OC 1065) adsorption rate. They showed that although CO_2 equilibrium capacity is higher at low temperatures, corresponding to higher adsorption CO_2 driving force, the adsorption rate is lowest due to low reaction kinetics. In contrast, higher relative humidity enhances the adsorption rate due to the enhancement of CO_2 loading caused by humidity. Using the same model, they studied the effect of temperature and relative humidity on SA-VTSA DAC process performance, showing relatively high ambient temperatures (25–35℃) and low relative humidity (<70%) provide the cheapest DAC cost [107]. On the other hand, Wiegner et al. [104] modelled a similar DAC process (VTSA) and found that low temperature and high relative humidity provide the cheapest DAC cost. This is mainly due to modelling an exemplary sorbent with high CO_2 capacity at low temperatures and high relative humidity.

Although Schellevis et al. [106] model account for the temperature dependency of CO_2 adsorption kinetics, the CO_2 adsorption enhancement due to water co-adsorption was modelled using empirical correlation based on a limited CO_2/H_2O co-adsorption dataset at the lower relative humidity range and extrapolated to the high the relative humidity range. Young et al. [102] developed a mechanistic model for the CO_2/H_2O co-adsorption (used in this work). However, they did not evaluate the effect of ambient conditions on process performance using this model.

Recent studies also show that not only can temperature have an effect on the CO_2 reaction kinetics for amine-functionalised sorbents, but also relative humidity can also influence reaction kinetics [108–110]. Therefore, there is still much-needed work to be done to improve understanding of the modelling of these sorbents for different ambient conditions.

2.3.4 Geospatial modelling of direct air capture performance

Ambient conditions not only vary between regions but also fluctuate throughout the day and seasons. Consequently, the performance of regional DAC processes is influenced by these climatic and weather changes over time. It is crucial to account for both temporal and spatial variations in ambient conditions when modelling regional variations in DAC performance. This involves utilising high-resolution temporal profiles of temperature and relative humidity for various locations.

However, detailed DAC process modelling—such as VTSA cycle configuration requiring solving partial differential equations (PDEs)—might require significant com-

putational resources. Thus, modelling such intricate processes on an hourly basis across different locations may not be the most efficient method for evaluating various sorbents and process configurations. Therefore, more computationally efficient tools are being developed to rapidly screen DAC processes at various locations, while still capturing the essential temporal variations in ambient conditions. These tools, along with published studies on the geospatial modelling of DAC performance, mainly focus on absorption and adsorption DAC processes.

2.3.4.1 Adsorption processes

Brooks et al. [111] used the model for the absorption-based DAC process from An et al. [100] to develop a correlation using multivariate regression between the process capture rate and ambient conditions (temperature and relative humidity). They used the correlation, along with hourly data, to estimate the absorption-based DAC process performance in the US. They found that the CO_2 capture rate can vary by up to threefold across different locations in the US.

2.3.4.2 Absorption processes

Wiegner et al. [104] developed an optimisation framework for the annual operation of a solid adsorption-based VTSA process, taking into account variations in temperature and relative humidity over time. This framework establishes a Pareto front for different combinations of temperature and relative humidity to optimise process productivity and energy requirements. The Pareto front is then linearised using piecewise linearisation techniques. These linearised Pareto fronts are integrated into a mixed-integer linear programming (MILP) model, which uses hourly regional temperature and relative humidity profiles to select operational parameters that minimise annual CO_2 capture costs. However, incorporating multiple Pareto fronts in the MILP model introduces a large number of decision variables, which can lead to high computational costs. To address this, the framework suggests clustering hourly temporal profiles and reducing breakpoints in the piecewise linearisation of the Pareto front to expedite solution times. Additionally, simplifying the combinations of temperature and relative humidity—such as rounding temperatures to the nearest 5℃ and relative humidity to the nearest 10%—helps generate faster solutions across multiple locations [112].

While Wiegner et al. [104] framework allows for more precise control over the DAC process by offering flexibility in deciding whether to increase energy requirements for higher productivity, the resulting increase in computational demand may render

it unsuitable for early-stage screening of various DAC sorbents and process configurations. Furthermore, a recent study [113] noted that while cost-optimal design in adsorption-based processes offers some benefits, it may lack the necessary process flexibility required for DAC, given the variability in ambient conditions. Using their performance map developed based on an exemplary sorbent, Wiegner et al. [104] have only used this framework to analyse DAC performance in three locations.

Schellevis et al. [107] developed another framework to optimise DAC cost based on yearly ambient conditions. The framework first finds cost-optimal operation points at different temperatures and relative humidity to develop a correlation between the three variables. This correlation is then used to estimate the hourly CO_2 capture cost at different time intervals, where the yearly average cost can be obtained. They used their sorbent model based on Lewatit VP OC 1065 to estimate the optimal CO_2 capture cost in different cities based on the Koppen climate classification [106]. The disadvantage of this method is that correlation maps need to be updated based on capital and energy costs for different locations. However, their study focused on understanding the variation in ambient conditions on DAC costs for different regions, and they did not account for different regional costs.

2.3.4.3 Current state of research and contributions of current work

Although understanding the effects of region-specific variables on DAC performance is important to ensure that DAC is deployed in regions where it can perform optimally, the current published research on the geospatial modelling of DAC is still limited. These limitations include 1) considering limited numbers of regions and locations, 2) computationally efficient screening frameworks to be able to screen different sorbents and process configurations rapidly and 3) not accounting for other regional variations such as cost of capital.

This chapter presents a computationally efficient geospatial modelling framework for evaluating technologies based on regional variation. The framework is applied to evaluate DAC performance globally using high-resolution temporal and spatial weather data. In addition, the framework can capture other regional variations, such as weighted average capital cost (WACC).

The modelling framework can help screen the regional techno-economic and environmental performance of different technologies. In the DAC technology context, this can help identify regions where different DAC processes can operate optimally.

Additionally, by understanding how WACC influences DAC costs across various regions, more cost-effective and sustainable DAC deployment strategies can be developed, ensuring the achievement of sustainable CDR targets.

2.4 Methodology

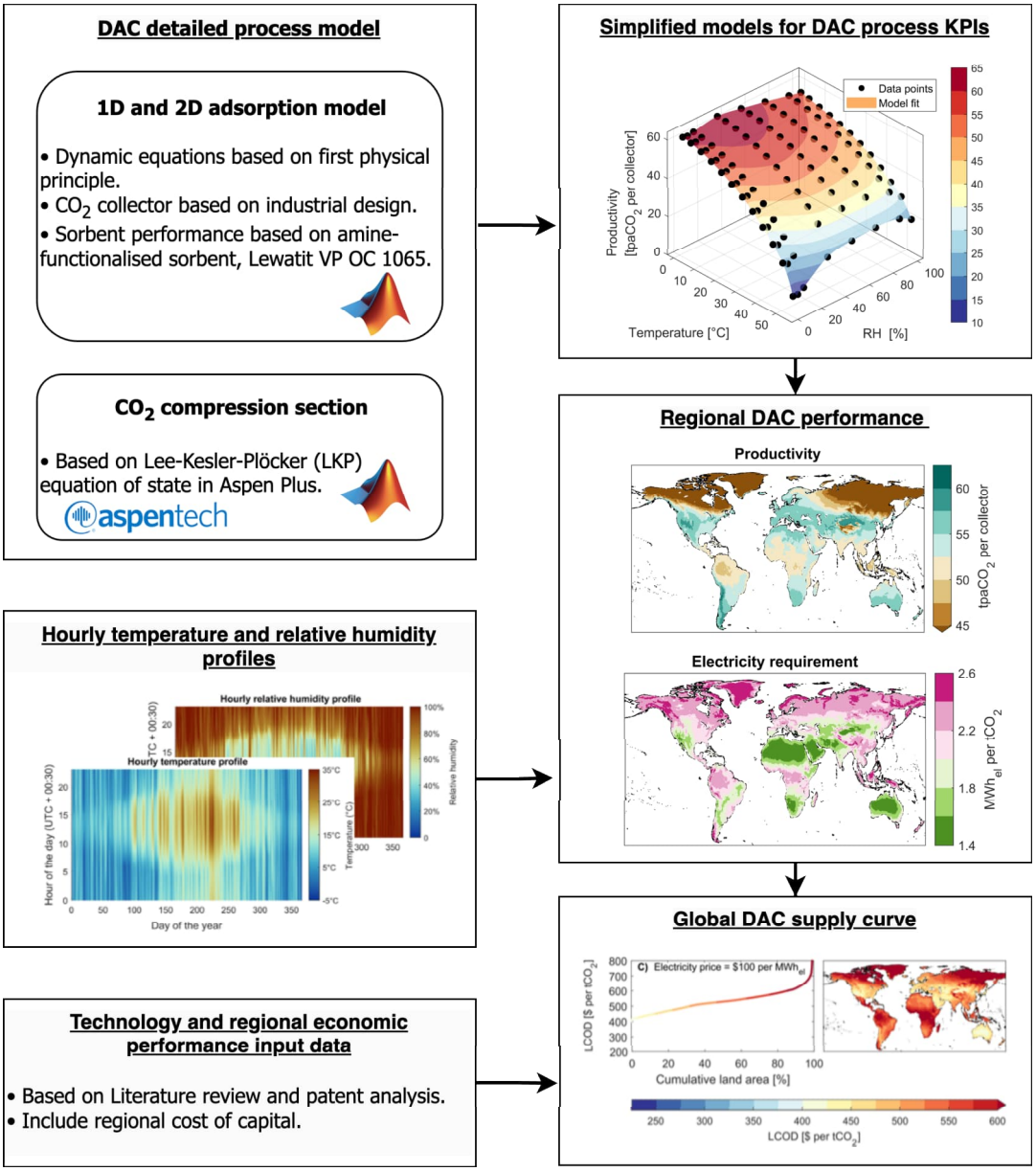


Figure 2.1: Methodology overview.

An overview of the methodology is shown in Figure 2.1. The methodology primarily comprises two levels of modelling: 1) detailed DAC process-level modelling and 2) geospatial modelling using a simplified DAC model derived from the developed process-level model.

In this case study, adsorption-based DAC technology utilising amine-functionalised solid sorbents is selected. This choice is due to the process's advantage of utilising LT heat, thereby requiring less exergy compared to DAC processes that use KOH solution absorption-based DAC [46]. Additionally, data are more readily available for modelling and assessing the adsorption-based DAC processes relative to other LT thermal heat-based DAC technologies, like amine scrubbing with amino acid salts.

The solid sorbent adsorption-based DAC process is modelled based on an industrial DAC process utilising 1D and 2D adsorption models alongside a binary CO_2-H_2O isotherm specifically developed for DAC applications. The developed model is used to compare the regional performance for two process configurations: VSTA and SA-VTSA.

2.4.1 Process modelling

2.4.1.1 Process description

Figure 2.2 illustrates the DAC process configuration selected for this analysis. The DAC section includes CO_2 collectors designed to process ambient air and capture CO_2. These collectors employ amine-functionalised solid adsorbents, specifically Lewatit VP OC 1065, capable of co-adsorbing water along with CO_2. Consequently, the output from the DAC section is a mixture of CO_2 and water. This mixture is then directed to a subsequent section—the CO_2 compression section—where the CO_2 is progressively compressed using a series of compressors equipped with intercoolers. Flash drums are used between the compressor stages to condense and separate the water. Air-source heat pumps supply the necessary process heat, including steam production. Thus, the only external energy requirement beyond the process boundaries is electricity.

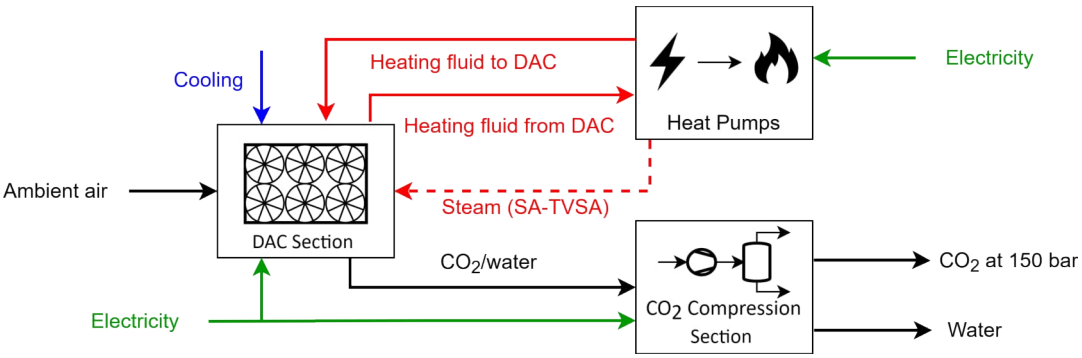


Figure 2.2: DAC process flow diagram. Adapted from [114, 115].

Figure 2.3 displays the VTSA and SA-VTSA cycle configurations examined in this study. Each box in the diagram corresponds to the same CO_2 collector, with different boxes illustrating the various stages of the cyclic process. During the adsorption step, fans drive air towards the CO_2 collector and through the sorbent bed, where the sorbent captures CO_2 and water. This continues until the sorbent is fully saturated with CO_2. At this point, the CO_2 collector is sealed, and vacuum pumps are utilised to reduce the pressure within the collector to the targeted vacuum level—known as the blowdown step. This quick step primarily vents the gases in the void space—mostly nitrogen and oxygen—back into the atmosphere. Subsequently, while maintaining vacuum conditions, the sorbent bed is heated. During this heating step, CO_2 and water are simultaneously desorbed and removed due to the vacuum pressure. In the SA-VTSA cycle, once the sorbent reaches the required temperature, steam is introduced into the collector—the steam purging step—reducing the partial pressure of CO_2 and enhancing its desorption from the sorbent. Once the CO_2 has been fully desorbed and before the cycle restarts, the bed is cooled down—the cooling step. This cooling is critical to prevent the oxidation of the amine-functionalised solid adsorbents when exposed to oxygen at elevated temperatures.

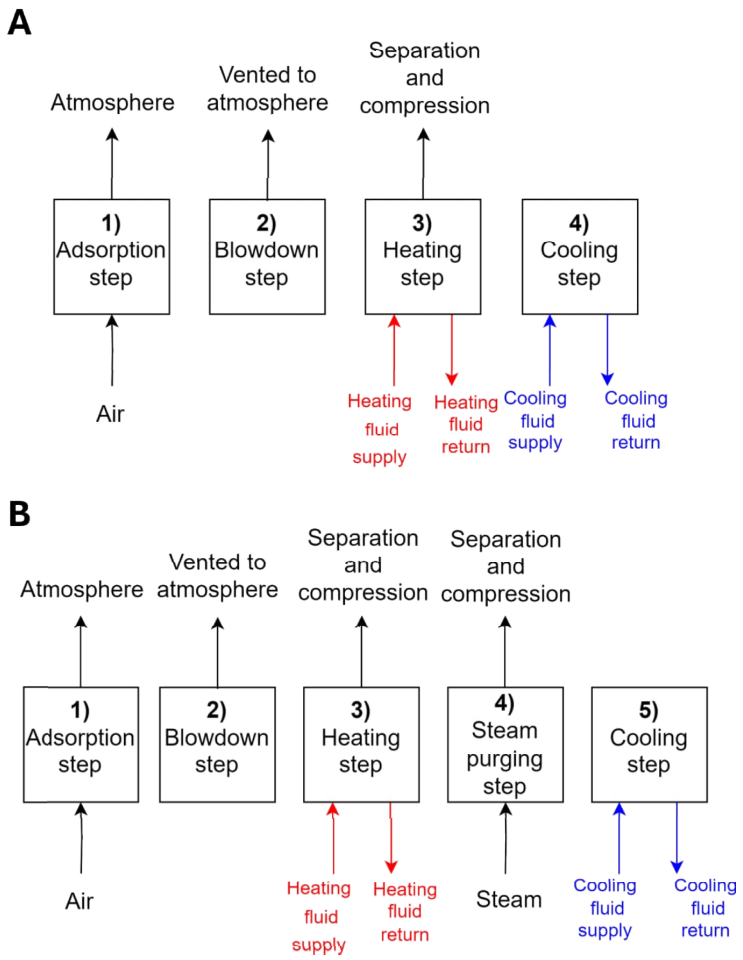


Figure 2.3: DAC process cycle configuration. A) Vacuum-pressure temperature swing adsorption (VTSA). **B)** steam-assisted vacuum-pressure temperature swing adsorption (SA-VTSA). Each box in the diagram corresponds to the same CO_2 collector, with different boxes illustrating the various stages of the cyclic process. Adapted from [114, 115].

2.4.1.2 Direct air capture section modelling

The CO_2 collector is modelled using dynamic 1D and 2D adsorption models based on an industrial design (patents [65, 66]) and a mechanistic binary CO_2-H_2O isotherm, specifically developed for DAC applications with the amine-functionalised sorbent, Lewatit VP OC 1065 [102]. Figure 2.4 presents a visual representation of the modelled CO_2 collector. Externally, the collectors are cuboid with dimensions of 1.44, 1.45 and 1.47 m (width, depth and height, respectively). Within each collector, 88 slim frames, each 0.01 m thick, are arranged in a zig-zag pattern to maximise the sorbent density

within the collector's volume, thereby reducing the cost. This design allows air to enter through one side, pass through the sorbent frames, and exit on the opposite side. Each frame is segmented by heat transfer tubes into 13 compact cells filled with sorbent material. These tubes facilitate the heating and cooling of the sorbent cells from three sides. Additionally, the sorbent cells are outfitted with a thin aluminium mesh to enhance heat transfer within the bed.

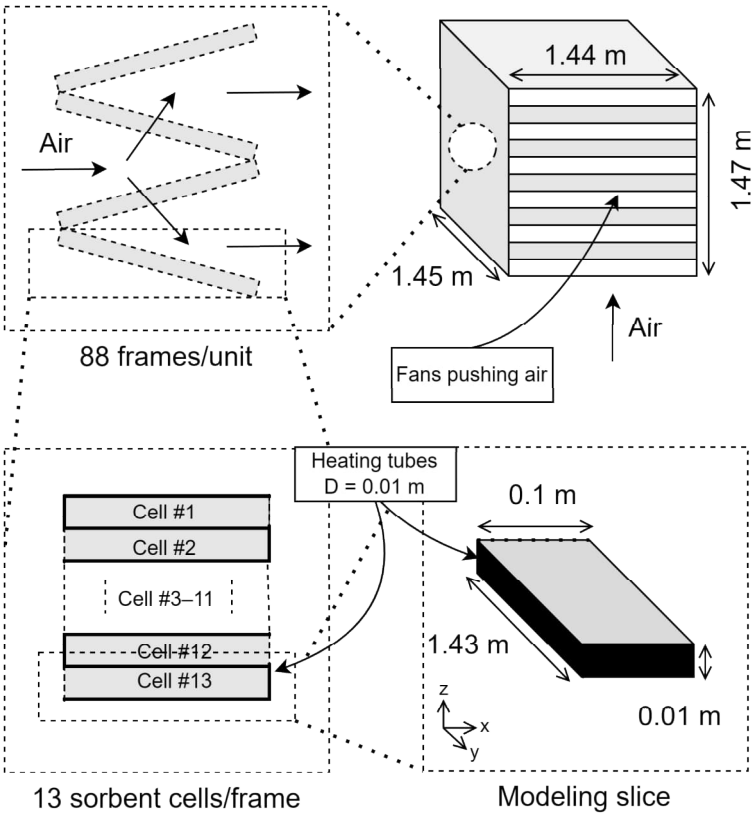


Figure 2.4: DAC CO_2 collector modelling. The collector design is based on industrial design (patents [65, 66]). Adapted from [114].

A rectangular modelling slice that represents a sorbent cell, as illustrated in Figure 2.4, is modelled using dynamic 1D and 2D adsorption models to characterise the various stages of the cycle. Given that each sorbent cell within a collector is identical, overall collector performance can be extrapolated by scaling up from this modelled slice (i.e., multiplying by the total number of sorbent cells in the collector)—this assumes a uniform airflow. Compared to only using a 1D model to simulate the DAC process, as in previous studies [104, 106, 116–119], the integration of both 1D and 2D models enhances accuracy in describing the collector's performance, without

significantly compromising computational efficiency. The 2D model provides detailed concentration and temperature distributions across the sorbent bed (the x-y plane in Figure 2.4), whereas the 1D model, which resolves more quickly, delivers profiles along the flow direction (i.e., the z-axis), including pressure drop data critical for calculating fan energy requirements. Accordingly, process cycles involving heating and cooling by the tubes are modelled with the 2D model, while other stages of the process cycles utilise the 1D model as shown in Table 2.2.

Table 2.2: Adsorption process cycle model selection.

Step	Model
Adsorption	1D model
Blowdown	1D model
Bed heating	2D model
Steam purging	1D model
Bed cooling	2D model

The dynamic 1D adsorption model employed in this study aligns with the models detailed in numerous prior publications [68, 120–124]. This model is comprised of a series of PDEs. The principal assumptions and characteristics of the 1D adsorption model include:

- Concentration, pressure and temperature gradients are only considered in the flow direction (z-axis);
- The gas phase is described by the ideal gas law;
- Dispersion and thermal conductivity in the flow direction are neglected;
- Thermal equilibrium is established instantaneously between gas and solid phases, including heating elements;
- A linear driving force (LDF) model is used to describe the mass transfer rate;
- The Ergun equation is used to describe the pressure drop;
- Bed voidage and particle diameter are uniform throughout the sorbent bed;
- Heat capacities are independent of temperature;
- Sorbent and the bed (i.e., heat transfer tubes and aluminium mesh) heat capacities are lumped into one term for simplicity as the heat capacity of the sorbent bed (Cp_s).

Equations 2.13 and 2.14 show the mathematical formulation for the overall and

component mass balance, respectively.

$$\varepsilon_t \frac{\partial c}{\partial t} + \frac{\partial (uc\,)}{\partial z} + \rho_b \sum_i^I \frac{\partial q_i}{\partial t} = 0, \quad i = \mathrm{CO_2},\ \mathrm{H_2O},\ \mathrm{Air} \tag{2.13}$$

$$\varepsilon_t \frac{\partial c_i}{\partial t} + \frac{\partial (uc_i)}{\partial z} + \rho_b \frac{\partial q_i}{\partial t} = 0, \quad i = \mathrm{CO_2},\ \mathrm{H_2O},\ \mathrm{Air} \tag{2.14}$$

where t and z are variables for time and space in the flow direction, respectively; c and q are concentration in the gas phase and adsorbed phase, respectively; ε_t and ρ_b are total porosity and bulk density, respectively; and u is superficial velocity. Here, air is defined as dry air, which is mostly nitrogen and oxygen.

Equation 2.15 shows the mathematical formulation for the energy balance.

$$\begin{aligned} &\left(\varepsilon_t \sum_i^I MW_i c_i Cp_{i,g} + \rho_b Cp_s + \rho_b \sum_i^I MW_i q_i Cp_{i,ads}\right) \frac{\partial T}{\partial t} \\ &- \varepsilon_t \frac{\partial P}{\partial t} + u \sum_i^I MW_i c_i Cp_{i,g} \frac{\partial T}{\partial z} - \rho_b \sum_i^I \Delta h_{ads,i} \frac{\partial q_i}{\partial t} = 0, \\ &i = \mathrm{CO_2},\ \mathrm{H_2O},\ \mathrm{Air} \end{aligned} \tag{2.15}$$

where MW, Cp, T, P and Δh_{ads} are molecular weight, heat capacity, temperature, pressure and heat of adsorption, respectively; and the subscripts g and ads correspond to the gas phase and adsorption phase, respectively.

The dynamic 2D adsorption model employed in this study was formulated and empirically validated by Wurzbacher et al. [125, 126]. This model shares similar assumptions with the 1D adsorption model, and its principal features and assumptions are outlined as follows:

- Concentration and temperature gradients are only considered in the x-y plane;
- The gas phase is described by ideal gas law;
- Constant and uniform pressure throughout the sorbent bed;
- Uniform heating from the wall, and heating tube surface temperature is the same as the fluid temperature;
- Thermal equilibrium is established instantaneously between gas and solid phases;
- Uniform and constant bed thermal conductivity throughout the sorbent bed;
- LDF model is used to describe the mass transfer rate;

- Bed void and particle diameter are uniform throughout the sorbent bed;
- Heat capacities are independent of temperature;
- Sorbent and the bed (i.e., heat transfer tubes and aluminium mesh) heat capacities are lumped in one term for simplicity.

Equations 2.16 and 2.17 show the mathematical formulation for the transient mass balance for the 2D adsorption model.

$$\begin{aligned} & MW_i \frac{\partial c_i}{\partial t} + \rho_b \, MW_i \frac{\partial q_i}{\partial t} + \nabla \cdot \overrightarrow{j_i} + \frac{1}{v_{i,g}} \cdot \\ & \left(\rho_b \, MW_{\mathsf{CO_2}} \frac{\partial q_{\mathsf{CO_2}}}{\partial t} \left(v_{\mathsf{CO_2},ads} - v^P_{\mathsf{CO_2}} \right) + \right. \\ & \rho_b \, MW_{\mathsf{H_2O}} \frac{\partial q_{\mathsf{H_2O}}}{\partial t} \left(v_{\mathsf{H_2O},ads} - v^P_{\mathsf{H_2O}} \right) + \\ & \left. \frac{\partial T}{\partial t} \cdot \frac{\varepsilon_t}{T} - \sum_i^I v_i^P \cdot \nabla \cdot \overrightarrow{j_i} \right) = 0, \\ & i = \mathsf{CO_2}, \mathsf{H_2O}, \mathsf{Air} \end{aligned} \tag{2.16}$$

$$\overrightarrow{j_i} = -D \cdot \nabla \left(MW_i \, c_i \right), \quad i = \mathsf{CO_2}, \mathsf{H_2O}, \mathsf{Air} \tag{2.17}$$

where $\overrightarrow{j}$, $v_{i,g}$, v_i^P, ∇ and D are diffusion flux, specific volume of species i at its partial pressure in the gas phase, specific volume of species i at total pressure, del operator and averaged diffusion coefficient, respectively.

Equation 2.18 shows the mathematical formulation for the energy balance for the 2D adsorption model.

$$\begin{aligned} & \left(\varepsilon_t \sum_i^I MW_i \, c_i \, Cp_{i,g} + \rho_b \, Cp_s + \rho_b \sum_i^I MW_i \, q_i \, Cp_{i,ads} \right) \frac{\partial T}{\partial t} = \\ & k_{eff} \, \nabla^2 T + \rho_b \, \Delta h_{ads,\mathsf{CO_2}} \frac{\partial q_{\mathsf{CO_2}}}{\partial t} + \rho_b \, \Delta h_{ads,\mathsf{H_2O}} \frac{\partial q_{\mathsf{H_2O}}}{\partial t} + \\ & \varepsilon_t \sum_r MW_i \, Cp_{i,g} \, D \left(\nabla c_i \cdot \nabla T \right), \quad i = \mathsf{CO_2}, \mathsf{H_2O}, \mathsf{Air} \end{aligned} \tag{2.18}$$

where k_{eff} is the effective thermal conductivity.

Equation 2.19 shows the mathematical formulation for the LDF model.

$$\frac{\partial q_i}{\partial t} = k_i \left(q_i^* - q_i \right), \quad i = \mathsf{CO_2}, \mathsf{H_2O}, \mathsf{Air} \tag{2.19}$$

where k is the mass transfer coefficient, and q^* is adsorbed phase concentration at equilibrium. Equation 2.20 shows the Ergun equation that describes the pressure drop across the sorbent bed.

$$\frac{\partial P}{\partial z} = -\frac{150\mu(1-\varepsilon_p)^2}{\varepsilon_p^3 d_P^2}u - \frac{1.75\ (1-\varepsilon_p)\,\rho_g}{\varepsilon_p^3 d_P}u^2 \tag{2.20}$$

where μ, ε_p, and d_P are dynamic viscosity, internal porosity and particle diameter, respectively.

In this work, the CO_2 and H_2O adsorption models are adapted from Young et al. [102] along with their fitting parameters based on Lewatit VP OC 1065. For CO_2 adsorption model, their mechanistic isotherm model is used to describe the adsorption of CO_2 in the presence of H_2O, which is shown in Equations 2.21–2.28. For H_2O adsorption model, the Guggenheim-Anderson-de Boer (GAB) isotherm model is used as shown in Equations 2.29–2.34.

$$q^*_{\mathsf{CO_2}} = \frac{\phi}{\phi_{dry}} \frac{q_\infty(T)\, b(T)\, p_{\mathsf{CO_2}}}{\left(1 + \left(b(T)\, p_{\mathsf{CO_2}}\right)^{\tau(T)}\right)^{\frac{1}{\tau(T)}}} \tag{2.21}$$

$$q_\infty(T) = q_{\infty,0} e^{\chi\left(1-\frac{T}{T_0}\right)} \tag{2.22}$$

$$b(T) = b_0 e^{\frac{-\Delta H_{ave}}{RT}} \tag{2.23}$$

$$\tau(T) = \tau_0 + \alpha\left(1 - \frac{T_0}{T}\right) \tag{2.24}$$

$$\phi = \phi_{dry} + (\phi_{available} - \phi_{dry})\, e^{\frac{-A}{q_{\mathsf{H_2O}}}} \tag{2.25}$$

$$\phi_{available} = \phi_{max} - f_{blocked} \tag{2.26}$$

$$f_{blocked} = f_{blocked,max}\left(1 - e^{-\left(k q_{\mathsf{H_2O}}\right)^n}\right) \tag{2.27}$$

$$\Delta H_{ave} = \left(1 - e^{\frac{-A}{q_{\mathsf{H_2O}}}}\right)\Delta H_{dry} + \left(e^{\frac{-A}{q_{\mathsf{H_2O}}}}\right)\Delta H_{wet} \tag{2.28}$$

$$q^*_{\mathsf{H_2O}} = \frac{q_m\, k_{GAB}\, c_{GAB}\, x_{RH}}{(1 - k_{GAB}\, x_{RH})\,(1 + (c_{GAB} - 1)\, k_{GAB}\, x_{RH})} \tag{2.29}$$

$$c_{GAB} = e^{\frac{E_1 - E_{10+}}{RT}} \tag{2.30}$$

$$k_{GAB} = e^{\frac{E_{2-9} - E_{10+}}{RT}} \tag{2.31}$$

$$E_{10+} = -44.38T + 57220 \tag{2.32}$$

$$E_1 = C - e^{DT} \tag{2.33}$$

$$E_{2-9} = F + G\,T \tag{2.34}$$

where x_{RH} is relative humidity.

During model implementation, the finite volume method was used to discretise the PDEs for the 1D adsorption model into equally spaced cells along the z-axis and the PDEs for the 2D adsorption model into equally spaced cells along the x-y plane, similar to previous works [68, 122, 123, 125, 126]. Additionally, The 1D adsorption model was converted to its dimensionless form and the van Leer flux limiter [127] was applied to the model to minimise non-physical oscillations in the solution, similar to previous work [124]. For the 2D adsorption model, given the symmetrical nature of the modelling slice, only half of the modelling cell is simulated, and the results are then expanded to describe the entire modelling slice. The derived time-dependent ordinary differential equations (ODEs) from the discretisation of the 1D and 2D adsorption models were executed in MATLAB R2021a using the ode15s solver, which is suitable for stiff problems, such as those solved here. All model parameters, along with the ODEs boundary conditions, are shown below.

Process model parameters

Table 2.3: Adsorption model parameters. Adapted from [114].

	Symbol	Value	Unit	Source
Bed				
Width of the sorbent bed	b	1.43	m	
Height of the sorbent bed	h	0.1	m	
Length of the sorbent bed	l	1.72 × 10 $^{-2}$	m	
Solid density	ρ_s	812.2	kg m $^{-3}$	[128]
Envelope density	ρ_e	635.2	kg m $^{-3}$	[102]
Bulk density	ρ_b	356.4	kg m $^{-3}$	Calculated
Internal porosity	ε_P	0.22		Calculated
Total porosity	ε_t	0.56		Calculated
Particle size	d_P	7.5 × 10 $^{-4}$	m	[102]
Thermal conductivity of sorbent and bed	k_{eff}	0.16 × 3.6	W m $^{-1}$ K $^{-1}$	[66, 125]
Heat capacity of sorbent and bed	Cp_s	1.5 + 0.38	kJ kg $^{-1}$ K $^{-1}$	[66, 128]
Feed				
Feed gas velocity	u_{feed}	0.028	m s $^{-1}$	
CO_2				
Heat capacity of adsorbed CO_2	$Cp_{CO_2,ads}$	2.0	kJ kg $^{-1}$ K $^{-1}$	[125]
Heat capacity of CO_2(g)	$Cp_{CO_2,g}$	0.86	kJ kg $^{-1}$ K $^{-1}$	[125]
Heat of adsorption of CO_2	$\Delta h_{ads,CO_2}$	70	kJ mol $^{-1}$	[102]
Mass transfer coefficient of CO_2	k_{CO_2}	3 × 10 $^{-3}$	s $^{-1}$	[102]
Specific volume of adsorbed CO_2	$v_{CO_2,ads}$	1 × 10 $^{-3}$	m^3 kg $^{-1}$	[125]

Molecular weight of CO_2	MW_{CO_2}	44 × 10 $^{-3}$	kg mol $^{-1}$	
Concentration of CO_2	y_{CO_2}	400	ppm	
H_2O				
Heat capacity of adsorbed H_2O	$Cp_{H_2O,ads}$	4.19	kJ kg $^{-1}$ K $^{-1}$	[125]
Heat capacity of H_2O (g)	$Cp_{H_2O,g}$	1.9	kJ kg $^{-1}$ K $^{-1}$	[125]
Heat of adsorption of H_2O	$\Delta h_{ads,H_2O}$	46	kJ mol $^{-1}$	[102]
Mass transfer coefficient of H_2O	k_{H_2O}	8.6 × 10 $^{-3}$	s $^{-1}$	[102]
Specific volume of adsorbed H_2O	$v_{H_2O,ads}$	1 × 10 $^{-3}$	m^3 kg $^{-1}$	[125]
Molecular weight of H_2O	MW_{H_2O}	18 × 10 $^{-3}$	kg mol $^{-1}$	
Concentration of H_2O	y_{H_2O}	[a]	mol H_2O mol $^{-1}$	
Air (mostly N_2 and O_2)				
Heat capacity of air(g)	$Cp_{air,g}$	1.01	kJ kg $^{-1}$ K $^{-1}$	[125]
Molecular weight of air	MW_{air}	28.97 × 10 $^{-3}$	kg mol $^{-1}$	
Concentration of air	y_{air}	[b]	mol air mol $^{-1}$	
Diffusion				
Average diffusion coefficient	D_0	2.2 × 10 $^{-5}$	m^2 s $^{-1}$	[125]

[a] The concentration of H_2O varies based on the relative humidity.

[b] The concentration of air varies based on the concentration of H_2O which calculated as $1 - y_{CO_2} - y_{H_2O}$.

Isotherm model parameters

Table 2.4: Mechanistic adsorption model fitting parameters. Adapted from Young et al. [102].

Parameter	Value	Unit
T_0	298.15	K
$q_{\infty,0}$	4.86	mol kg^{-1}
χ	0	(–)
b_0	2.85 × 10^{-21}	Pa^{-1}
$-\Delta H_0$	117,798	J mol^{-1}
τ_0	0.209	(–)
α	0.523	(–)
ϕ_{max}	1.000	(–)
$f_{blocked,max}$	0.433	(–)
k	0.795	kg mol^{-1}
ϕ_{dry}	1.000	(–)
A	1.535	mol kg^{-1}
$-\Delta H_{wet}$	130,155	J mol^{-1}
n	1.425	(–)

Table 2.5: GAB model fitting parameters. Adapted from Young et al. [102].

Parameter	Value	Unit
q_m	3.63	mol kg^{-1}
C	47,110	J mol^{-1}
D	0.023744	K^{-1}
F	57.706	J mol^{-1}
G	-47.814	J mol^{-1} K^{-1}

CO_2 collector model boundary conditions

The boundary conditions for all simulated cyclic steps are shown in the table below where N is the number of finite-volume cells. $\dot{F}$, A, y_i, P and p are volumetric flow rate, cross-sectional area in the flow direction, gas concentration of component i, total pressure and partial pressure, respectively. x, y and z are spital variables. In the 1D adsorption model, ${}^1/_2$ represents the boundary wall of the first finite-volume cell, which is equivalent to $z = 0$, and $N + {}^1/_2$ represents the boundary wall of the last finite-volume cell, which is equivalent to $z = l$.

For each cyclic step, the initial conditions for the variables are the final values of the variables from the previous step. When there is a transition from the 1D to the 2D adsorption model, the variable average over the z-axis or x-y plane in the case of the 1D or 2D adsorption model, respectively, from the previous step, is used as an initial condition for the current step. k_{BL} corresponds to the valve equation controlling the pressure where a value of 0.25 s^{-1} is used.

Table 2.6: Adsorption model boundary conditions. Adapted from [114].

Adsorption (1D)	
At $z_{1/2}$**:**	**At** $z_{N+1/2}$**:**
· Pressure	· Pressure
$P_{1/2} = P_1 - \frac{1}{2}\frac{\partial P}{\partial z}_{1/2}$	$P_{N+1/2} = P_{ads}$
· Gas velocity	· Gas velocity
$u_{1/2} = \frac{\dot{F}_{feed}}{A}$	$\frac{\partial u}{\partial z}_{N+1/2} = 0$
· Temperature	· Temperature
$T_{1/2} = T_{\text{Air}}$	$\frac{\partial T}{\partial z}_{N+1/2} = 0$
· Concentration	· Concentration
$y_{i1/2} = y_{i,\text{Air}1/2}, \quad i = \text{CO}_2, \text{H}_2\text{O}, \text{Air}$	$\frac{\partial y_i}{\partial z}_{N+1/2} = 0, \quad i = \text{CO}_2, \text{H}_2\text{O}, \text{Air}$

Blowdown (1D)

At $z_{1/2}$:

· Pressure

$\frac{\partial P}{\partial z}_{1/2} = 0$

· Gas velocity

$u_{1/2} = 0$

· Temperature

$\frac{\partial T}{\partial z}_{1/2} = 0$

· Concentration

$\frac{\partial y_i}{\partial z}_{1/2} = 0, \quad i = \mathrm{CO_2}, \mathrm{H_2O}, \mathrm{Air}$

At $z_{N+1/2}$:

· Pressure

$\frac{\partial P}{\partial z}_{N+1/2} = k_{BL}\left(P_{Des} - P_{N+1/2}\right)$

· Gas velocity

$\frac{\partial u}{\partial z}_{N+1/2} = 0$

· Temperature

$\frac{\partial T}{\partial z}_{N+1/2} = 0$

· Concentration

$\frac{\partial y_i}{\partial z}_{N+1/2} = 0, \quad i = \mathrm{CO_2}, \mathrm{H_2O}, \mathrm{Air}$

Bed heating (2D)

At $x = 0$ or $y = 0$

· Temperature

$T\left(x = 0, y, t\right) = T_{wall}\left(t\right)$

$T\left(x, y = 0, t\right) = T_{wall}\left(t\right)$

· Concentration

$\frac{\partial p_i}{\partial x}\Big|_{x=0} = 0, \quad i = \mathrm{CO_2}, \mathrm{H_2O}, \mathrm{Air}$

$\frac{\partial p_i}{\partial y}\Big|_{y=0} = 0, \quad i = \mathrm{CO_2}, \mathrm{H_2O}, \mathrm{Air}$

At $x = \frac{b}{2}$ or $y = h$

· Temperature

$\frac{\partial T}{\partial x}\Big|_{x=\frac{b}{2}} = 0$

$\frac{\partial T}{\partial y}\Big|_{y=h} = 0$

· Concentration

$\frac{\partial p_i}{\partial x}\Big|_{x=\frac{b}{2}} = 0, \quad i = \mathrm{CO_2}, \mathrm{H_2O}, \mathrm{Air}$

$\frac{\partial p_i}{\partial y}\Big|_{y=h} = 0, \quad i = \mathrm{CO_2}, \mathrm{H_2O}, \mathrm{Air}$

Steam purging (1D)

At $z_{1/2}$:

· Pressure

$P_{1/2} = P_1 - \frac{1}{2}\frac{\partial P}{\partial z}_{1/2}$

· Gas velocity

$u_{1/2} = u_{inlet\ steam}$

· Temperature

$\frac{\partial T}{\partial z}_{1/2} = 0$

· Concentration

$\frac{\partial c_i}{\partial z}_{1/2} = 0, \quad i = \mathrm{CO_2}, \mathrm{Air}$

$\frac{\partial c_{\mathrm{H_2O}}}{\partial z}_{1/2} = 1$

At $z_{N+1/2}$:

· Pressure

$\frac{\partial P}{\partial z}_{N+1/2} = 0$

· Gas velocity

$\frac{\partial u}{\partial z}_{N+1/2} = 0$

· Temperature

$\frac{\partial T}{\partial z}_{N+1/2} = 0$

· Concentration

$\frac{\partial c_i}{\partial z}_{N+1/2} = 0, \quad i = \mathrm{CO_2}, \mathrm{H_2O}, \mathrm{Air}$

Cooling (2D)	
At $x = 0$ **or** $y = 0$	**At** $x = \frac{b}{2}$ **or** $y = h$
· Temperature	· Temperature
$T\left(x = 0, y, t\right) = T_{wall}\left(t\right)$	$\frac{\partial T}{\partial x} \mid_{x=\frac{b}{2}} = 0$
$T\left(x, y = 0, t\right) = T_{wall}\left(t\right)$	$\frac{\partial T}{\partial y} \mid_{y=h} = 0$
· Concentration	· Concentration
$\frac{\partial p_i}{\partial x} \mid_{x=0} = 0, \quad i = \mathrm{CO_2}, \mathrm{H_2O}, \mathrm{Air}$	$\frac{\partial p_i}{\partial x} \mid_{x=\frac{b}{2}} = 0, \quad i = \mathrm{CO_2}, \mathrm{H_2O}, \mathrm{Air}$
$\frac{\partial p_i}{\partial y} \mid_{y=0} = 0, \quad i = \mathrm{CO_2}, \mathrm{H_2O}, \mathrm{Air}$	$\frac{\partial p_i}{\partial y} \mid_{y=h} = 0, \quad i = \mathrm{CO_2}, \mathrm{H_2O}, \mathrm{Air}.$

2.4.1.3 CO_2 compression section modelling

In this section, the output from the DAC section, primarily comprising CO_2 and water, undergoes stages of cooling, flash separation and compression. During these stages, H_2O is removed from the stream, and CO_2 is compressed to the dense phase at 150 bar. This compression level of 150 bar is selected based on previous DAC techno-economic assessments [41] and the criteria outlined in the US Department of Energy guidelines [69] for CO_2 transportation and sequestration.

Figure 2.5 shows a flow diagram of how the CO_2 compression section is designed and modelled. The CO_2 compression section was modelled using a combination of Aspen Plus V11 and MATLAB R2021a. The maximum allowable temperatures for vacuum pumps and compressors are capped at 135℃ to preserve their mechanical integrity and prevent thermal degradation of internal components [129]. Aspen Plus is used to provide fluid properties calculation where LKP EOS was selected as it was found to be suitable for the CO_2 and H_2O mixture [130]. MATLAB is used to automate the process synthesis as the section feed and operating parameters change due to changes in ambient conditions and feed conditions.

In the automated process synthesis, HX-1 (Figure 2.5) only recovers heat if the feed inlet temperature for HX-1 ($T_{inlet,\text{HX-1}}$) is above the heating fluid temperature ($T_{heating}$) by the minimum approach temperature (ΔT_{min}), which is 10℃ in this work. HX-2 (Figure 2.5) recovers the remaining heat and cools down the stream to ΔT_{min} above the ambient temperature (T_{amb}) so that CO_2 does not change from the liquid phase to the liquid phase. When the feed stream contains mostly water, HX-2 recovers a substantial amount of low-temperature heat that is caused by condensing water,

which cannot be recovered for preheating the steam water supply. Therefore, when accounting for the amount of heat that can be recovered from HX-2, if the inlet stream has a water mole fraction of more than 0.5, the heat is neglected and not recovered. The remaining amount of heat from HX-2 is recovered at 80% efficiency to account for any remaining water phase change.

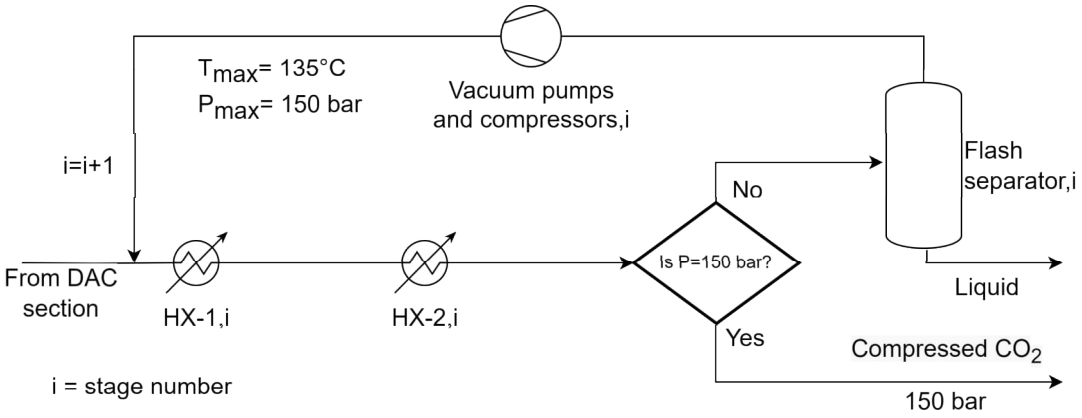


Figure 2.5: Flow diagram of the CO_2 compression section design and modelling. Adapted from [114].

Table 2.7 shows the algorithm used to set the parameters of the two heat exchangers where P_{sat,CO_2} and T_{sat,CO_2} are saturation vapour pressure and its temperature (i.e., boiling temperature), respectively. A higher temperature than CO_2 critical temperature and T_{sat,CO_2} are used as a design margin.

Table 2.7: Algorithm used for compression section modelling. Adapted from [114].

Equipment	Algorithm
HX-1	**if** $\boldsymbol{T_{inlet,\text{HX-1},i} > T_{heating} + \Delta T_{min}}$ $T_{outlet,\text{HX-1},i} = T_{heating} + \Delta T_{min}$ **else** $T_{outlet,\text{HX-1},i} = T_{inlet,\text{HX-1}}$
HX-2	**If** $\boldsymbol{P_{inlet,\text{HX-2},i} = 150}$ **bar** $T_{outlet,\text{HX-2},i} = T_{amb} + \Delta T_{min}$ **elseif** $\boldsymbol{P_{inlet,\text{HX-2},i} > 74}$ **bar** $T_{outlet,\text{HX-2},i} = \max\left(T_{amb} + \Delta T_{min}, 35\right)$ **else** **if** $\boldsymbol{P_{inlet,\text{HX-2},i} < P_{sat,\text{CO}_2}\left(T = T_{amb} + 5\right)}$ $T_{outlet,\text{HX-2},i} = T_{amb} + \Delta T_{min}$ **else** $T_{outlet,\text{HX-2},i} = T_{sat,\text{CO}_2}\left(P_{in,\text{HX-2}}\right) + 5$

2.4.1.4 Process performance indicators

Equation 2.35 define the process productivity for one DAC collector where $m_{DACoutlet,\text{CO}_2}$ is the total CO_2 mass recovered from one collector during the cycle with total time of t_{cycle}.

$$process\ productivity\ =\ \frac{m_{DACoutlet,\text{CO}_2}}{t_{cycle}} \tag{2.35}$$

Equation 2.36 defines the total thermal heat requirement (Q_{tot}) in MWh per tCO_2, which includes the thermal heat consumed for heating the bed (Q_{bed})—Equation 2.37, heating the steam water supply ($Q_{steam,sens.}$)—Equation 2.38—and generating the steam ($Q_{steam,gen.}$)—Equation 2.39.

$$Q_{tot} = Q_{bed} + Q_{steam,sens.} + Q_{steam,gen.} \tag{2.36}$$

$$
\begin{aligned}
Q_{bed} =& \frac{1}{m_{DACoutlet,CO_2}} \\
& \int_0^{t_{des}} \Bigg(\Bigg(\varepsilon_t \sum_i^I MW_i \; c_i \; Cp_{i,g} \\
& + \rho_b \; Cp_s + \rho_b \sum_i^I MW_i \; q_i \; Cp_{i,ads} \Bigg) \frac{\partial T}{\partial t} \\
& - \rho_b \; \Delta h_{ads,CO_2} \frac{\partial q_{CO_2}}{\partial t} - \rho_b \; \Delta h_{ads,H_2O} \frac{\partial q_{H_2O}}{\partial t} \Bigg) \, dt, \\
& i = CO_2, H_2O, Air
\end{aligned}
\tag{2.37}
$$

$$
Q_{steam,sens.} = \frac{m_{steam} \; \left(h_{\mathsf{H_2O}} \left(P_{atm}, sat.\; liq \right) - h_{\mathsf{H_2O}} \left(P_{atm}, T_{amb} \right) \right)}{m_{DACoutlet,\mathsf{CO_2}}} \tag{2.38}
$$

$$
Q_{steam,gen.} = \frac{m_{steam} \; \Delta H_{\mathsf{H_2O},v} \; \left(P_{atm} \right)}{m_{DACoutlet,\mathsf{CO_2}}} \tag{2.39}
$$

where m_{steam}, $h_{\mathsf{H_2O}}$, P_{atm}, $sat.\; liq$ and $\Delta H_{v,\mathsf{H_2O}}$ refer to the mass of steam used, the enthalpy of water, atmospheric pressure, saturated liquid and water enthalpy of vaporisation. When heat is provided by heat pumps, the heat requirement is converted to electrical requirement (E) in MWh per tCO_2 using the coefficient of performance (COP) shown in Equations 2.40–2.43.

$$
E_i = \frac{Q_i}{COP} \tag{2.40}
$$

$$
COP = \frac{T_H}{T_H - T_C} \eta_{2^{nd}} \tag{2.41}
$$

$$
T_H = T_{heating} + \Delta T_{min} \tag{2.42}
$$

$$
T_C = T_{ambient} - \Delta T_{min} \tag{2.43}
$$

where $\eta_{2^{nd}}$, T_H, T_C and $T_{heating}$ are second law efficiency, which is assumed to be 50% (typical values for heat pumps 50%–70% [131, 132]), heat pump heat sink temperature, heat pump heat source temperature and heating temperature, which is assumed to be 110 °C, respectively.

Equation 2.36 defines the total electricity requirement (E_{tot}) in MWh per tCO_2, which includes electricity consumed by heat pumps for heating the bed ($E_{heating}$), heating the steam water supply ($E_{steam,sens.}$) and generating steam ($E_{steam,gen.}$);

vacuum pumps and compressors ($E_{comp.}$) and fans (E_{fan}).

$$E_{tot} = E_{bed} + E_{steam,sens.} + E_{steam,gen.} + E_{comp.} + E_{fan} \tag{2.44}$$

$E_{comp.}$ includes electricity consumed during the blowdown step by the vacuum pumps, which is calculated using Equation 2.45, and by compressors in the CO_2 compression and separation section ($E_{comp.,comp.\ sec.}$), which is calculated from Aspen Plus. Vacuum pump and compressor efficiencies (η_{comp}) of 70% were used.

$$E_{comp.,BL} = \frac{1}{\eta_{comp}} \frac{\sum_i^I n_i RT \ln\left(P_{atm}/P_{des}\right)}{m_{DACoutlet,CO_2}}, \quad i = CO_2, H_2O, Air \tag{2.45}$$

where P_{atm} and P_{des} are atmospheric pressure and pressure during the desorption step, respectively.

Equation 2.46 shows how E_{fan} is calculated.

$$E_{fan} = \frac{1}{\eta_{fan}} \frac{V_{inlet} \Delta P_{bed}}{m_{DACoutlet,CO_2}} \tag{2.46}$$

where η_{fan}, V_{inlet} and ΔP_{bed} are fan efficiency, which is assumed to be 70%, volume of procced air and pressure drop across the sorbent bed, respectively.

2.4.1.5 Selection of process operating parameters

The DAC process operating parameters were selected through a multi-objective (process productivity and energy requirements) sensitivity analysis of the different cyclic steps at 9 different ambient conditions (3 different temperatures and relative humidity) to maximise process productivity while minimising energy requirements—except for air feed velocity which was selected to maintain the pressure drop across the sorbent bed to 1 mbar, which is based on patents [65, 66]. Table 2.8 summarises sensitivity analysis (with further details provided in Appendix A.2). The following discusses the examined variables for the different adsorption steps.

- **Adsorption Step (Figure A.6):** Varied parameters are feed velocity (u_{feed}), which is directly related to feed flow rate, and average bed loading at adsorption completion, expressed as a percentage of equilibrium CO_2 loading (CO_2 loading %), which is a proxy for adsorption time.
- **Bed Heating Step (Figure A.7 and A.8):** This was analysed separately for

VTSA and SA-VTSA configurations. The parameters varied were vacuum pressure during desorption (P_L) and the minimum bed temperature at the end of heating ($\min(T_{bed,des\,step}(t = end))$), which directly influences heating step duration.

- **Steam purging step (Figure A.9 and A.10):** $\min(T_{bed,des\,step}(t = end))$and steam velocity ($u_{steam}$), which is proportional to the steam flow rate, are varied to explore the interplay between bed heating and steam purging in SA-VTSA. Finally, $u_{steam}$was varied with average bed CO_2 loading at the end of steam purging ($q_{CO_2,steam}(t = end)$), which is directly related to steam purging time.

Table 2.8: Summary of sensitivity analysis for DAC process operating parameters. Adapted from [114].

Variable	Observation	Remarks
Adsorption (Figure A.6)		
Feed velocity (u_{feed}) volumetric flow rate	Increasing the feed flow rate increases productivity as well as energy requirement.	There is a trade-off between the sorbent bed pressure drop (fan energy requirement) and the time required to saturate the sorbent bed.
Average bed CO_2 loading at the end of the adsorption step (CO_2 loading %)	When increasing the target bed CO_2 saturation at the end of the adsorption bed, process performance improves in terms of productivity and energy requirement to a certain level, then decreases. In other words, an optimal range for target bed saturation increases productivity and decreases energy requirements.	There is a trade-off between achieving higher CO_2 working capacities and operating at less favourable CO_2 kinetics (as well as higher H_2O working capacity)
Bed heating step for SA-VTSA (Figure A.7))		
Desorption operating vacuum pressure—P_L	Lower vacuum pressure (in the analysed range, below 200 mbar) increases process productivity and lowers total energy requirement.	Lower vacuum pressure enhances the desorption kinetics and steam requirement (to achieve the same CO_2 working capacity).

The lowest temperature in the sorbent bed at the end of the bed heating step—$min(T_{bed,des\ ,step}(t = end))$	Operating at a lower temperature at the end of the bed heating step increases process productivity and total energy requirement.	There is a trade-off between desorbing CO_2 by heating the sorbent bed (slower) and steam purging (faster and requires more steam).
Bed heating step for VTSA (Figure A.8)		
Desorption operating vacuum pressure—P_L	Same as for SA-VTSA	Same as for SA-VTSA
The lowest temperature in the sorbent bed at the end of the bed heating step—$min(T_{bed,des\ ,step}(t = end))$	Operating at a higher temperature at the end of the bed heating step decreases energy requirement. However, it can increase or decrease productivity depending on the ambient conditions.	There is a trade-off between achieving higher CO_2 working capacities and operating at less favourable CO_2 kinetics.
Desorption step—bed heating and steam purging (Figure A.9)		
The lowest temperature in the sorbent bed at the end of the bed heating step—$min(T_{bed,des\ ,step}(t = end))$	Operating at a lower temperature at the end of the bed heating step increases process productivity at a higher steam flow rate but decreases productivity at a lower steam flow rate. For all scenarios, the total energy requirement increases when operating at a lower temperature at the end of the bed heating step.	At a lower steam flow rate, the CO_2 desorption rate is higher during the bed heating step. It is the other way around at a higher steam flow rate. Total energy increases correspond to higher steam consumption.

Steam velocity (u_{steam})—Steam flow rate	Increasing the steam flow rate increases process productivity and energy requirements.	There is a trade-off between faster kinetics at higher steam flow rates (until the mass transfer limit is reached) and higher energy requirements.
Steam purging step (Figure A.10)		
Average bed CO_2 loading at the end of the steam purging step ($q_{CO_2,steam}(t = end)$)	Achieving low CO_2 loading at the end of the steam purging step can improve process productivity and energy requirements; however, achieving very low CO_2 loading decreases process performance and energy requirements.	There is a trade-off between achieving higher CO_2 working capacities and operating at less favourable CO_2 kinetics.
Steam velocity (u_{steam})—Steam flow rate	Same as above for u_{steam}.	Same as above for u_{steam}.

Table 2.9 shows the selected process operating parameters.

Table 2.9: DAC collector operating parameters.

Step	Variable	Value	unit
Adsorption	Air feed velocity	0.028	m/s
	Average bed CO_2 loading at the end of the adsorption step	97	%
Bed heating	Desorption operating vacuum pressure	50	mbar
	The lowest temperature in the sorbent bed at the end of the bed heating step	95	°C
Steam purging	Average bed CO_2 loading at the end of the steam purging step	0.1	mol CO_2/kg sorbent
	Steam velocity	0.01	m/s

2.4.2 Geospatial modelling

2.4.2.1 Process geospatial performance

NASA's MERRA-2 hourly temperature and relative humidity data spanning 2016 to 2020 were employed to assess DAC performance across various locations. This dataset has a spatial resolution of 0.5° × 0.625° (latitude, longitude), resulting in a spatial grid comprising of 361 × 576 nodes (n) [133]. Thus, hourly temperature and relative humidity profiles can be described as a multi-dimensional array or matrix with a size of [361, 576, 8760 or 8784] (i.e., [# of latitude nodes, # of longitude nodes, # of hours in a year]) for each year.

Leveraging the developed DAC process model, performance metrics were computed at 96 data points encompassing an ambient temperature range of 1-55℃ (12 points) and relative humidity (RH) of 1%–100% (8 points). This number of sample points was shown to be adequate to capture the process behaviour—as illustrated in Figure 2.6 and Appendix A.1. This generated dataset can be visualised as 3D grids for each performance indicator, with ambient temperature and relative humidity constituting the other two axes. Figure 2.6 shows an example of the simplified 3D model for process productivity based on the SA-VTSA cycle. Appendix A.1 shows

the simplified 3D models for the other process performance parameters.

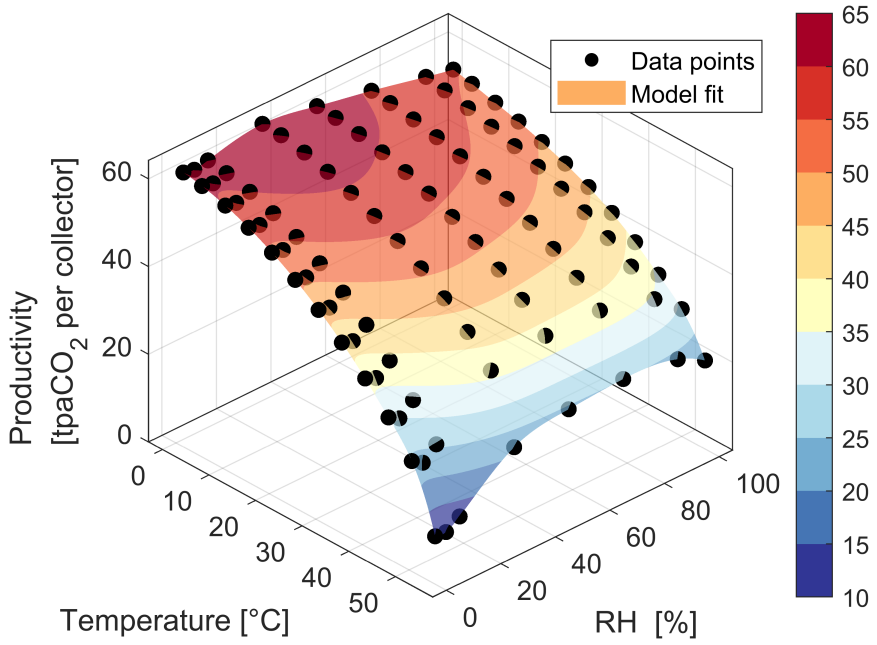


Figure 2.6: Simplifed 3D model of the SA-VTSA DAC process productivity. Adapted from [134].

To determine hourly DAC performance at each node, MATLAB R2021a's 3D spline interpolation was utilised to interpolate the node's hourly temperature and relative humidity data against the developed 3D grid DAC performance dataset. This computational method is time-efficient—it takes a few minutes to compute each performance indicator for each year on a personal laptop (Intel Core i7-10750H Processor)—since MATLAB is optimised for matrix-focused computations, including parallelization.

Subsequently, the node's productivity ($productivity_n$) was determined as the hourly average across all years (Equation 2.47), and the node's electricity requirement ($el\ requirement_n$) was calculated as the average electricity consumed per mass of CO_2 produced (Equation 2.48). Other performance indicators, such as water requirements or production, can be calculated in a similar fashion. Overall, this approach significantly reduces the computational burden associated with simulating an entire year at each spatial node using the cyclic adsorption model.

$$productivity_n = \frac{\sum_{h=1}^{hours} hourly\ productivity_{n,h}}{hours} \tag{2.47}$$

$$el\ requirement_n = \frac{\sum_{h=1}^{hours} hourly\ productivity_{n,h} \times hourly\ el\ requirement_{n,h}}{\sum_{h=1}^{hours} hourly\ productivity_{n,h}} \tag{2.48}$$

While sorbents capable of operating at very low ambient temperatures (e.g., -20 ℃) are under development [135, 136], a minimum DAC process operating temperature of -15 ℃ was adopted in this study. This serves as a safety margin, as significant water production and circulation within the process, which can elevate the risk of freezing within pipes and equipment at extremely low ambient temperatures, even with effective insulation. This -15 ℃ limit also aligns with the specifications for the 1st generation Climeworks unit [137]. Furthermore, given the lack of data on Lewatit VP OC 1065 performance at low temperatures, including adsorption capacity, mass transfer and kinetics, it was assumed that operation between -15 ℃ and -1 ℃ yields performance equivalent to 1 °C.

2.4.2.2 Process economic performance

Equation 2.49 shows how the levelised cost of DAC at each node (n) ($LCOD_n$) is calculated.

$$LCOD_n = \frac{\sum_p (CapEx_{\ n,p} \times AF_{n,p}\ + OpEx_{n,p}) + OpEx_{sorbent}}{productivity_n} + (price_{el} \times el\ requirement_n) \tag{2.49}$$

where AF, $CapEx$, $OpEx$ and $price_{el}$ are the annualised factor, capital expenditures, operating expenses for process equipment (p) and electricity price, respectively, calculated using Equations 2.50–2.58.

$$AF_p\ = \frac{WACC\ \times (1+WACC)^{LT_p}}{(1+WACC)^{LT_p}-1} \tag{2.50}$$

$$CapEx = \text{installed cost + offsite cost + contingency} \tag{2.51}$$

$$OpEx = \text{maintenance + overhead} \tag{2.52}$$

$$OpEx_{sorbent} = \text{sorbent weight}\ \times\ \text{sorbent cost}\ \times AF \tag{2.53}$$

$$\text{installed Cost}\ =\ \text{Lang Factor}\ \times\ \text{purchased cost} \tag{2.54}$$

$$\text{offsite Cost}\ = 0.4 \times\ \text{installed cost} \tag{2.55}$$

$$\text{contingency } = 0.1 \times (\text{installed cost + offsite cost}) \tag{2.56}$$

$$\text{maintenance } = 0.03 \times \text{ (installed cost + offsite cost)} \tag{2.57}$$

$$\text{overhead } = 0.65 \times \text{ maintenance} \tag{2.58}$$

where $WACC$ and LT represent the weighted average capital cost and equipment (or sorbent) lifetime, respectively. Lang Factor is employed to estimate the overall cost of the DAC plant, establishing a relationship between the purchase cost of major process equipment and the total capital or fixed capital investments. Regional WACC, specific to low-carbon investments, are adopted from Ameli et al. [20], which divides the world into 16 regions. The regional WACC is illustrated in world maps in Appendix B.3 as the low WACC assumption.

In this work, a large-scale DAC plant is considered. Assumptions regarding equipment and sorbent costs are detailed in Appendix B.2. The cost of heat exchangers, being relatively minor, is disregarded. For example, the cost of heat pumps is estimated based on the cost of compressors, and the estimated heat pump cost aligns with values reported in the literature [138]. The purchased cost for fans and compressors is based on the maximum equipment size specified in the source, as the scale of the DAC plant is not the focus of this study. However, in large-scale DAC deployment scenarios (the assumption for process cost calculations), plant construction would be optimised to leverage economies of scale.

Furthermore, a Lang factor of 3 is assumed [139], representing the lower range for chemical plants. This value was chosen because the DAC technology considered here is modular, allowing units to be assembled quickly on-site to achieve large capacities while reducing complexity, time, and labour costs. This approach differs from conventional stick-built facilities, which are constructed entirely on-site and, therefore, require extensive engineering, foundation work, and sequential installation of equipment—factors that lead to longer construction timelines, higher labour costs, and increased complexity in project execution.

2.5 Results and discussion

2.5.1 Effect of ambient conditions on direct air capture process performance

2.5.1.1 Steam-assisted vacuum-pressure temperature swing adsorption (SA-VTSA) cycle configuration

Figure 2.7 illustrates the influence of ambient temperature and relative humidity on the performance of a DAC system utilising the SA-VTSA cycle, which shows a major impact on DAC plant performance. This highlights that assuming constant conditions, as done in previous DAC assessments [46, 68, 116–118], fails to capture the variability in DAC performance across different seasons and geographic locations. This variability impacts both productivity and energy requirements, both of which directly affect the cost of DAC.

Comparing the yearly average DAC performance across the four sampled locations in Figure 2.7 to a fixed performance at 20 °C and 50% relative humidity shows an overestimation of yearly average plant productivity for all four locations. Furthermore, the yearly average electricity requirement is underestimated for three of the four locations (Albuquerque, London and Jakarta).

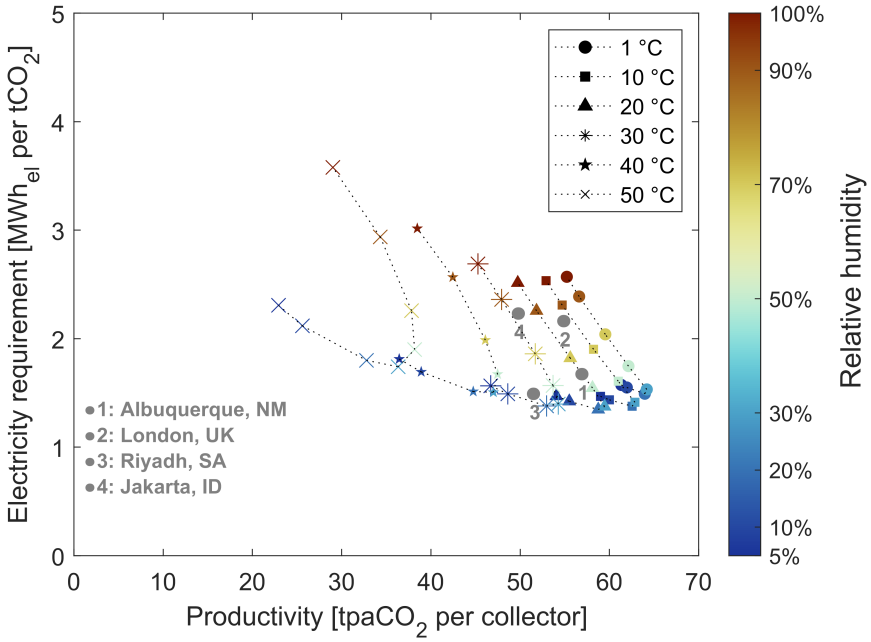


Figure 2.7: Performance of DAC process based on SA-VTSA under different ambient conditions. Adapted from [114].

Within the examined temperature range (1–30 ℃) and relative humidity range (5%–100%), each CO_2 collector can capture between 45.3–64.2 tonnes per annum of CO_2 ($tpaCO_2$), with electricity requirements ranging from 1.35–2.69 MWh_{el} per tCO_2. As shown in Figure 2.7, within this temperature and relative humidity range, changes in relative humidity have a noticeable impact on both electricity requirements and productivity. In contrast, temperature changes only notably affect productivity. Therefore, within this temperature range, relative humidity can be considered a more influential factor on DAC performance than temperature. However, as the temperature rises to 40 and 50 ℃, the effect of temperature on electricity requirements becomes more pronounced.

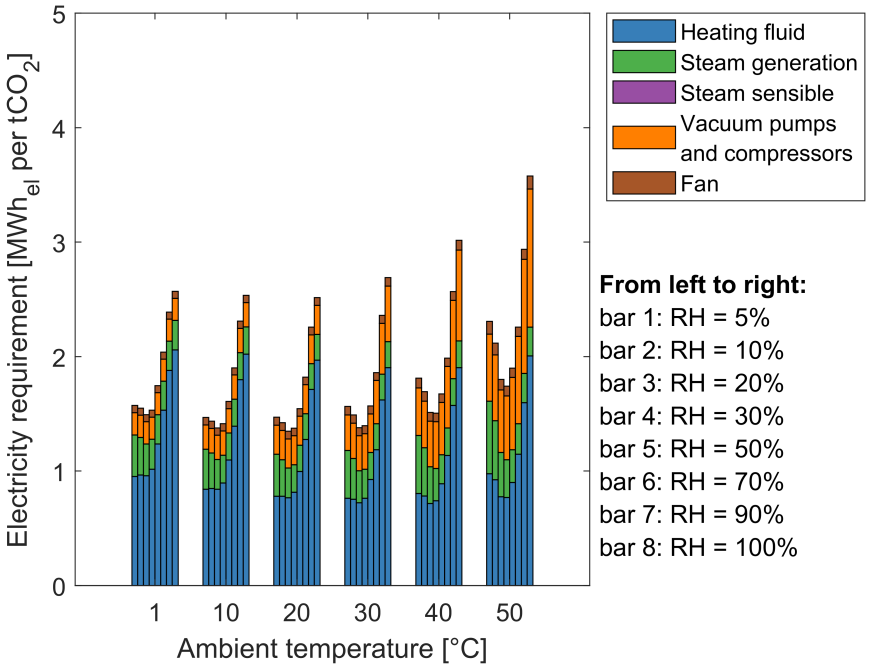


Figure 2.8: Breakdown of electricity requirements for SA-VTSA cycle configuration. Adapted from [114].

Figure 2.8 presents a breakdown of electricity requirements for the SA-VTSA cycle configuration. Generally, within a mild relative humidity range of 20%–60%, collector productivity rises while electricity requirements fall (Figures 2.7 and 2.8). This is primarily attributed to enhanced CO_2 adsorption on the amine-functionalised sorbent in the presence of water [102, 125]. This enhancement boosts CO_2 working capacity, leading to improved process productivity and energy efficiency. However, this effect diminishes at higher relative humidity levels due to increased sorbent water loading,

requiring greater heat input for sorbent regeneration. This results in a longer heating step and reduced productivity. This is aligned with previous lab experiments involving bed heating after sorbent saturation with dry and wet CO_2 [125].

A similar phenomenon occurs at high ambient temperatures, where CO_2 working capacity decreases while sorbent water capacity increases. This leads to higher heat input demands for sorbent regeneration and lower process productivity, as shown in Figure 2.7. However, this is not reflected in the electricity requirements of the heat pump, which supplies thermal energy for bed heating and steam generation. This is due to the heat pump's increased COP at elevated ambient temperatures.

Furthermore, as ambient temperature decreases, the bed heating requirement increases slightly due to the greater sensible heat needed to raise the bed temperature to the desorption point. This, combined with the reduced heat pump COP at lower ambient temperatures, leads to higher electricity requirements for both bed heating and steam generation, as shown in Figure 2.8. Finally, at higher ambient temperatures, less heat can be recovered from the intercoolers between the vacuum pump and compressor stages. Consequently, the inlet gas temperature for both the vacuum pump and compressor rises, increasing their electricity consumption.

2.5.1.2 Vacuum-pressure temperature swing adsorption (VTSA) cycle configuration

Figure 2.9 illustrates the impact of varying ambient temperature and relative humidity on the performance of a DAC system based on the VTSA cycle. The general observation is similar to the previous case of the SA-VTSA cycle. The lowest achievable energy requirement is 1.32 MWh_{el} per tCO_2, observed at a low relative humidity of 20% and a mild temperature of 20 ℃, which is slightly lower than what is observed in the SA-VTSA cycle. Conversely, the highest productivity of 59.3 $tpaCO_2$ per collector is achieved at the lowest analysed temperature of 1 ℃ and low humidity of 30%, which is notably lower than what is observed in the SA-VTSA cycle. Generally, relatively low relative humidity (approximately 20%–60%) enhances both electricity requirements and productivity due to the improved CO_2 adsorption capacity of the sorbent in the presence of water. However, this improvement in CO_2 working capacity diminishes at higher relative humidity levels—typically above 30%–60% relative humidity at lower temperatures—due to the reasons discussed previously in the SA-VTSA cycle. This, coupled with the increased water working capacity at higher relative humidity, leads

to increased electricity requirements and decreased process productivity.

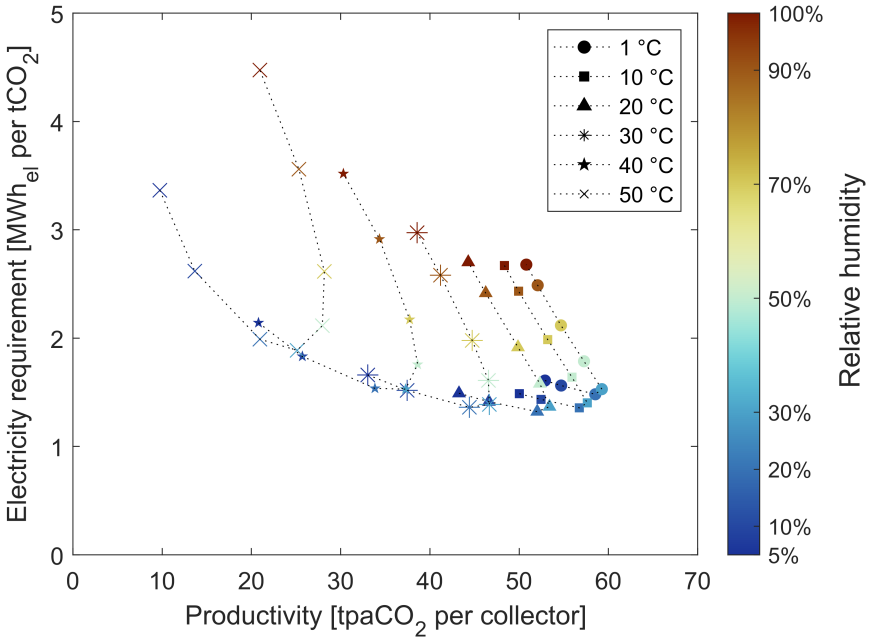


Figure 2.9: Performance of DAC process based on VTSA under different ambient conditions. Adapted from [115].

2.5.1.3 Comparison between the two cycle configurations

Figure 2.10 demonstrates the impact of incorporating a steam purging step into the process cycle. In all scenarios, the addition of a steam purging step led to increased process productivity. This is attributed to the enhanced CO_2 working capacity resulting from the lower CO_2 partial pressure after the desorption step and the relatively rapid CO_2 desorption rate during this step. The productivity improvement from steam purging is more pronounced at lower relative humidity, as the CO_2 working capacity for VTSA tends to be reduced under these conditions. Consequently, the relative enhancement in CO_2 working capacity and process productivity is greater in such conditions.

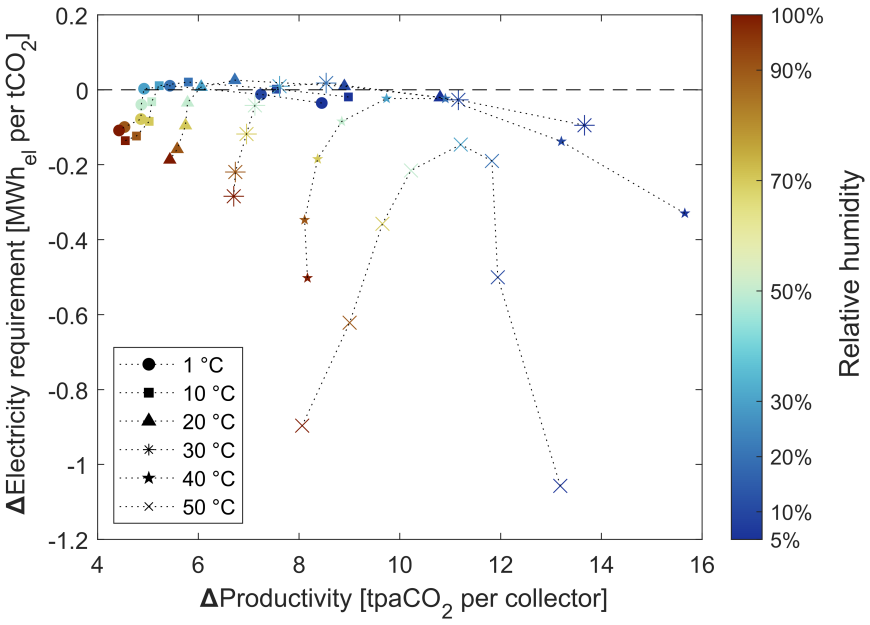


Figure 2.10: The change (△) in process performance between the SA-VTSA cycle and VSTA at different ambient conditions. The change (△) is calculated as the performance of the SA-VTSA cycle subtracted from the performance of the VTSA cycle. Adapted from [115].

Furthermore, the addition of a steam purging step generally decreases electricity requirements due to the improved energy efficiency of desorbing CO_2 during this step and the overall increase in CO_2 working capacity. However, at temperatures below 30 ℃ and low relative humidity (around 10%–30%), the VTSA cycle slightly outperforms the SA-VTSA cycle in terms of electricity requirements.

Overall, adding a steam purging step can enhance process performance across all ambient conditions. Consequently, the SA-VTSA cycle is selected for the geospatial DAC performance analysis due to its enhanced process productivity and generally lower electricity requirements.

2.5.2 Geospatial techno-economic performance of direct air capture

2.5.2.1 Regional direct air capture process performance

Figure 2.11 shows the regional correlation between CO_2 collector productivity and electricity requirement with yearly average temperature and relative humidity. Productivity shows a noticeable correlation with both average temperature and relative humidity, while electricity requirement exhibits a stronger correlation with average

relative humidity compared to average temperature. Generally, productivity is higher in regions with low relative humidity and low temperature. However, a sharp decline in productivity to below 45 tpaCO_2 per collector is observed in areas where the temperature remains below −15 °C (the assumed minimum operating temperature) for a significant part of the year, such as high-latitude regions. This decrease is attributed to the lower plant capacity factor in these regions. Additionally, regions with lower average relative humidity—drier regions—tend to have lower electricity requirements.

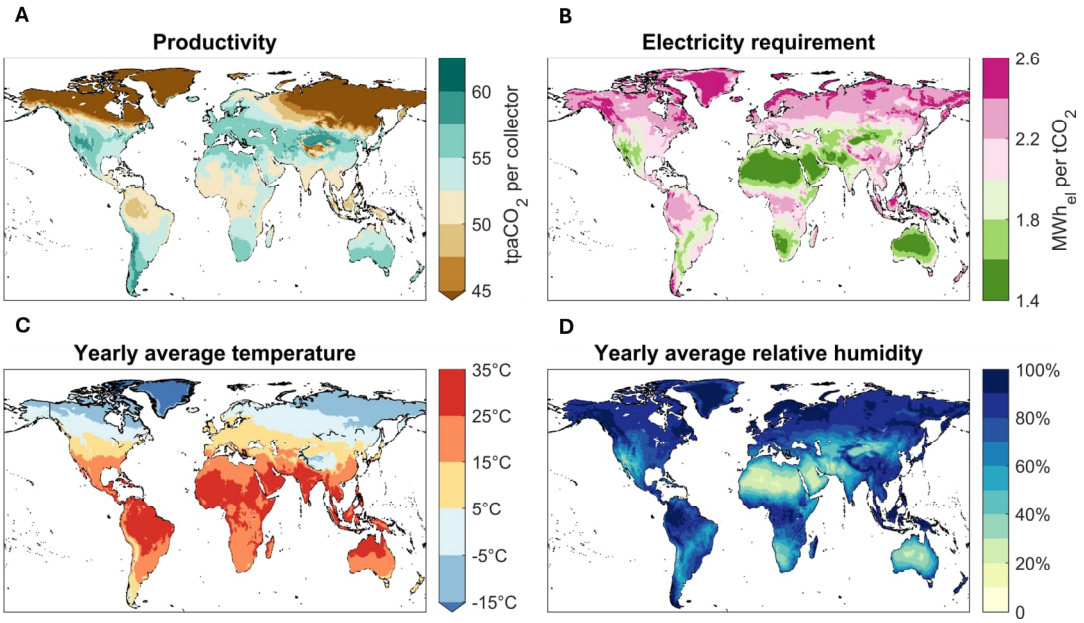


Figure 2.11: Global performance of DAC. A) Process productivity. **B)** Total electricity requirements. **C)** Yearly average temperature. D) yearly average relative humidity. Adapted from [114].

To examine regional performance based on climate, global regions were categorised into four groups using two temperature intervals: cold—yearly average temperature below 18 °C—or hot—yearly average temperature above 18 °C, and two relative humidity intervals: dry—yearly relative humidity below 65%—or humid—yearly relative humidity above 65%. Extremely cold regions with temperatures below −15 °C for more than 30 days per year are excluded due to the resulting low DAC plant productivity. The four aggregated regions are cold dry, cold humid, hot dry and hot humid. These broadly correspond to cold arid/semi-arid, continental/cooler temperate, hot arid/semi-arid, and tropical/warmer temperate climates, respectively. Figure 2.12 provides a visual representation of these four aggregated regions.

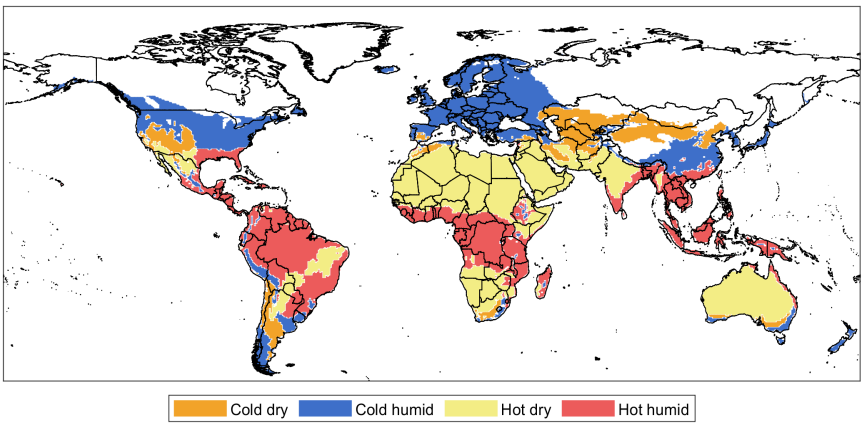


Figure 2.12: Aggregated climate regions based on DAC performance. Region's aggregation is performed based on yearly average temperature and relative humidity, categorised as above or below 18 ℃ and 65%, respectively. Regions experiencing temperatures below −15 ℃ for more than 30 days annually are excluded. Adapted from [114].

Table 2.10 summarizes the DAC performance metrics. Comparing the four regions, cold dry regions exhibit the highest DAC plant productivity, reaching up to 60.6 tpaCO_2, with a mean of 56.8 tpaCO_2. A relatively low electricity requirement accompanies this high productivity, with a mean of 1.76 MWh_{el} per tCO_2. Following this, cold humid regions demonstrate better productivity—a mean of 54.8 tpaCO_2, compared to hot dry regions—a mean of 53.5 tpaCO_2. However, hot dry regions have lower electricity requirements—a mean of 1.64 MWh_{el} per tCO_2, compared to cold humid regions—a mean of 2.15 MWh_{el} per tCO_2. Finally, hot humid regions show the lowest process productivity—a mean of 51.6 tpaCO_2 and have relatively high electricity requirements—a mean of 2.11 MWh_{el} per tCO_2.

Table 2.10: Regional DAC performance and LCOD at different climate conditions. Region's aggregation–hot/cold and humid/dry–is performed based on yearly average temperature and relative humidity, categorised as above or below 18 °C and 65%, respectively. Regions experiencing temperatures below −15 °C for more than 30 days annually are excluded. Adapted from [92].

Climate	**Regions include**		**Productivity [tpaCO_2]**	**Energy req. [MWh_{el} per tCO_2]**	**LCOD [$ per tCO_2] Electricity price [$ per MWh_{el}]**		
					0	**50**	**100**
Cold dry	Cold arid and semi-arid regions in the US, e.g., New Mexico and Wyoming, Southern Spain and Central Asia.	range mean	52.6–60.6 56.8	1.50–1.97 1.76	240–374 277	324–469 365	403–565 453
Cold humid	US states with a continental climate, UK, Europe, East Asia, part of Southern Australia and New Zealand.	range mean	50.4–58.8 54.8	1.81–2.56 2.15	220–405 281	320–525 388	421–645 496
Hot dry	Hot arid and semi-arid regions in the US, e.g., West of Texas, Sahara Desert, Middle East and Australia.	range mean	50.0–57.7 53.6	1.45–1.94 1.64	243–402 338	327–499 420	405–596 501
Hot humid	Tropical regions in Central and South America, Africa, South India and Southeast Asia.	range mean	48.5–55.8 51.6	1.79–2.47 2.11	243–421 357	337–540 462	432–659 568

2.5.2.2 Regional levelized cost of direct air capture

The regional DAC plant performance data in Figure 2.11 has been used to estimate the levelised cost of direct air capture (LCOD), assuming that the modelled CO_2 collectors can be manufactured and purchased at a cost of $20,000 per collector. This is a preliminary cost assumption made due to the limited information available on large-scale commercial DAC technology. It is based on the assumption that these CO_2 collectors are comparable to a mid-sized car in terms of materials and construction, where similar raw materials and assembly/construction processes used in car manufacturing could be employed to manufacture DAC collectors. Furthermore, current solid sorbent-based technology utilises modular collectors that are more readily scaled out—adding more collectors—than scaled up—increasing collector size. Consequently, as demand for CO_2 collectors grows, it can be anticipated that mass production will employ automated manufacturing and, more broadly, leverage existing automotive industry expertise, thereby driving their cost closer to that of cars. Nonetheless, a sensitivity analysis on the collector cost is presented in Chapter 3 to further evaluate this assumption.

Figure 2.13 illustrates the global LCOD estimates at different electricity price values, presented as supply curves and global maps. When considering all global land areas, the estimated LCOD ranges from $320–$1,518 per tCO_2 at an electricity price of $50 per MWh_{el} and from $403–$1,646 per tCO_2 at an electricity price of $100 per MWh_{el}. However, when excluding cold regions experiencing temperatures below -15℃ for more than 30 days annually, these ranges narrow down to $320–$540 and $403–$659 per tCO_2, respectively. These remaining regions account for 76% of the total global land area—this does not mean that all this land area is available for DAC deployment. These LCOD estimates align with the cost range of $100–$600 per tCO_2 suggested in the existing literature [10, 140]—though suggest some unrealistic optimism at the lower end.

The range in LCOD results from variations in regional WACC and DAC plant performance, including both process productivity and electricity requirements. Figure 2.14 presents DAC supply curves with a fixed WACC of 5%, allowing for differentiation between the influence of regional climate and WACC variation on LCOD.

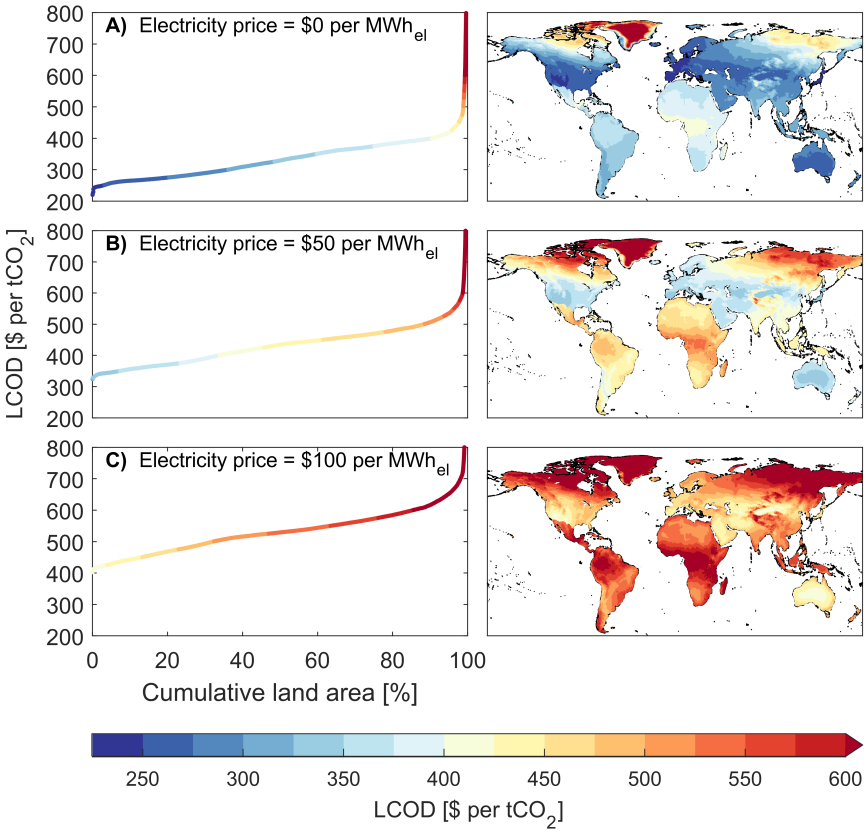


Figure 2.13: Regional LCOD and global supply DAC supply curves for SA-VTSA at different electricity prices. The figures on the left show global DAC supply curves at different electricity prices plotted against the total land area capable of delivering DAC at the respective LCOD. The colour of the data points on the supply curves corresponds to their location on the accompanying map on the right. Darker blue signifies a lower LCOD, while darker red indicates a higher LCOD. Adapted from [114].

Lower regional WACC generally corresponds to the lower end of the LCOD range for each climate group, as shown in Table 2.10. On average, assuming a fixed electricity price, cold dry regions exhibit the lowest LCOD due to their relatively high process productivity and low energy requirements. The lower range of LCOD for this climate group is observed in some US states with cold dry climates, like New Mexico and Wyoming, as well as colder regions in Southern Spain, Southern Australia and Northwest China. In certain instances, at lower electricity prices, cold humid regions can achieve a lower LCOD than cold dry regions. This is because they include regions with lower WACC, such as Japan, Western Europe and the UK. However, this trend does not hold at higher electricity prices, as cold humid regions generally have higher

energy requirements compared to cold dry regions.

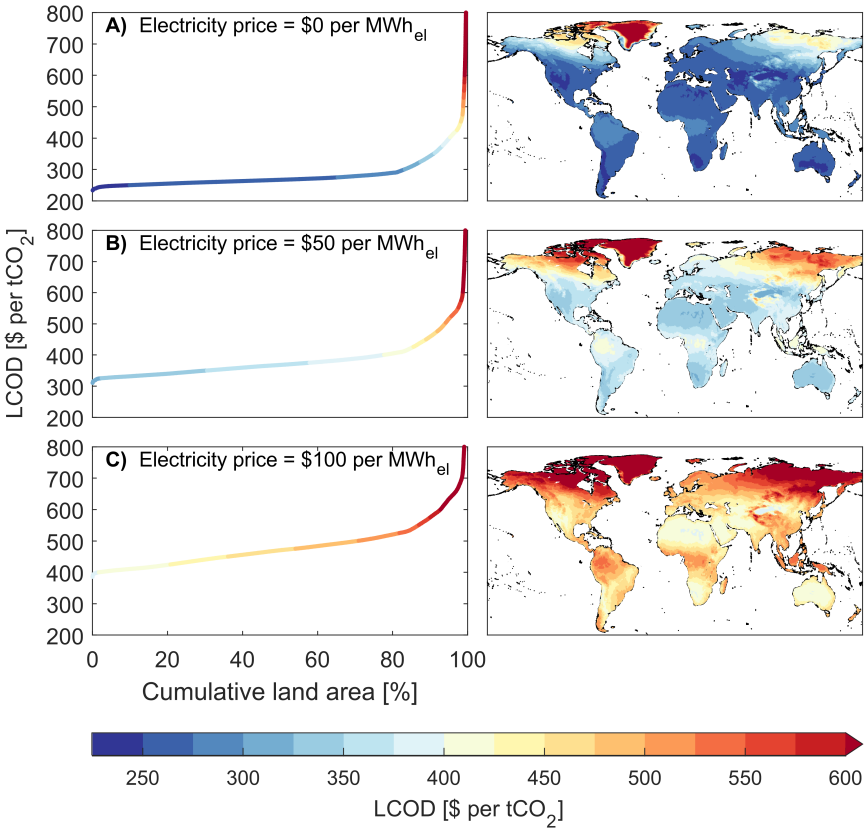


Figure 2.14: Regional LCOD and global supply DAC supply curves for SA-VTSA at different electricity prices and fixed WACC. The figures on the left show global DAC supply curves at different electricity prices plotted against the total land area capable of delivering DAC at the respective LCOD. The colour of the data points on the supply curves corresponds to their location on the accompanying map on the right. Darker blue signifies a lower LCOD, while darker red indicates a higher LCOD. Adapted from [114].

A similar trend emerges when comparing cold humid regions—higher productivity—with hot dry regions—lower energy requirements. At low electricity prices, cold humid regions can achieve a lower LCOD, while hot dry regions become more cost-competitive at higher electricity prices. However, this is not reflected in the average LCOD values for these two climate groups in Table 2.10. This discrepancy is due to the inclusion of lower WACC regions—such as Japan and Western Europe—within the cold humid group, and the presence of a large portion of Africa—relatively high WACC —within the hot dry group.

This phenomenon can be better illustrated in Figure 2.13 by comparing hot humid regions with moderate WACC—such as Australia and the Middle East—to cold humid regions—such as Europe and the Northern US. At low electricity prices (Figure 2.13A), Europe and the Northern US exhibit lower LCODs among these four regions. As electricity price increases to \$50 per MWh_{el} (Figure 2.13B), the LCODs become comparable across the four regions. At even higher electricity prices, reaching \$100 MWh_{el} (Figure 2.13C), the LCOD in Australia and the Middle East starts to become relatively cheaper among these four regions.

Lastly, hot humid regions consistently display the highest average LCOD. This is attributed to a combination of low process performance—lower productivity and higher energy requirements—and the fact that a significant portion of these regions comprises Africa and Latin America, which have relatively high WACC values.

2.5.2.3 Regional environmental consideration

Figure 2.15 illustrates the water consumption of the DAC process based on the SA-VTSA cycle configuration. Importantly, the process can co-produce water alongside CO_2 removal in all global regions, with water production ranging from 0.4–3.5 tH_2O per tCO_2. Notably, humid regions exhibit higher water production potential.

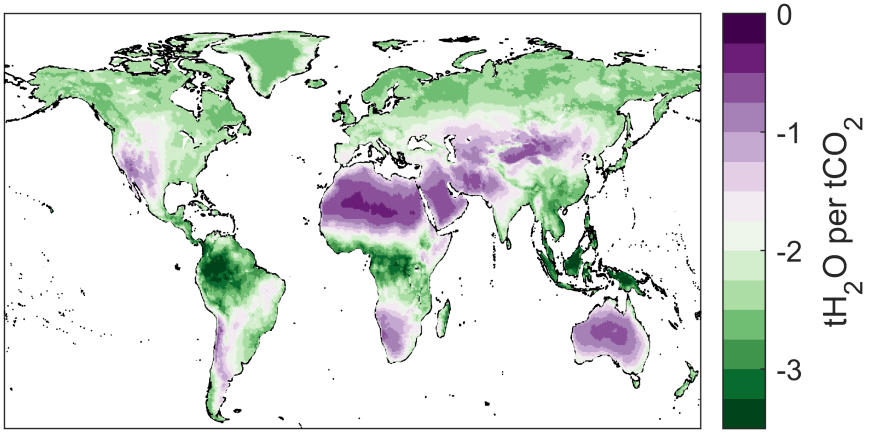


Figure 2.15: . Regional water consumption for DAC based on SA-VTSA cycle configuration.

The land requirements for DAC can be estimated based on the Climeworks plant in Hinwil, Switzerland, where 18 DAC collectors with an average productivity of 50 $tpaCO_2$ (tonnes of CO_2 per annum) per collector and a size similar to the one modelled in this study occupy an area of 90 m^2 [141]. Using this land area requirement and

the collector productivities from Table 2.10, capturing 10 $GtCO_2$ per year using DAC would require between 825 km^2—for the maximum productivity of 60.6 $tpaCO_2$ per collector—and 1,031 km^2—for the minimum productivity of 48.5 $tpaCO_2$ per collector. This range represents less than 0.001% of the total global land area. Such a level of DAC could be achieved at the lowest supply cost of $320 per tCO_2, assuming an electricity price of $50 per MWh_{el}.

However, this scenario assumes all DAC plants would be concentrated in a small area, which may not be feasible due to limitations in land availability, energy supply, or access to secure CO_2 storage sites. For instance, the electricity required to capture 10 $GtCO_2$ per year is estimated to be between 14,500 and 25,600 TWh per year (Table 2.10). If this energy were supplied by nuclear power, an additional land area of 3,500–6,200 km^2 would be needed, based on a land requirement of 2 km^2 per 1 GWel nuclear power plant and a capacity factor of 95%—assuming nuclear requires 0.24 m^2/MWh per year [142]. If solar PV were used, the land requirement would increase to 200,000–350,000 km^2, based on a land requirement of 13.8 m^2 to produce 1 MWh of solar PV electricity per year [143]. The land requirement for solar-powered DAC is 60 times greater than that for nuclear-powered DAC, equivalent to 40%–70% of Spain's land area.

It is important to acknowledge that different energy sources have varying land footprints and requirements. While nuclear power facilities necessitate specific licensed land and access to water, solar PV offers greater flexibility in installation, including the potential for deployment on remote arid lands.

In a more pragmatic view, sustainable DAC deployment hinges on several factors: achieving a low LCOD based on regional climate and WACC; access to affordable, low-carbon energy sources; and proximity to secure CO_2 storage sites [36, 42]. Additionally, the availability of suitable land for DAC plant construction and its associated energy supply infrastructure is important since it may be limited due to competition—such as with agricultural land and urbanisation—or other geological and geographical restrictions—such as nature reserves, mountains, forests and bodies of water.

2.6 Conclusions and future work

2.6.1 Conclusions

This chapter presents a computationally efficient geospatial modelling framework for evaluating technologies based on regional variations. This framework is applied to comprehensively analyse and screen the global performance of direct air capture (DAC) technology—specifically solid sorbent adsorption-based—utilising high-resolution temporal and spatial weather data. The framework encompasses detailed modelling and analysis of the influence of ambient conditions on DAC performance on a process level. Building upon this process-level understanding, geospatial modelling and analysis of the techno-economic and environmental performance of DAC are performed and presented. This framework and analysis can aid in identifying the most suitable climates and regions for maximising DAC performance.

Colder and drier regions where the temperature generally remains above the DAC operating temperature of -15℃ are found to be most favourable for DAC performance. However, these regions may not necessarily offer the lowest LCOD, as regional weighted average capital cost (WACC) and the cost of energy can significantly affect the levelised cost of DAC (LCOD). For example, at an electricity price of \$50 per MWh_{el}, the estimated LCOD for 76% of the global land area, representing regions where temperatures do not drop below -15℃ for more than 30 days per year, falls within the range of \$320–\$540 per tCO_2. This range is influenced by both regional climates and WACC.

2.6.2 Limitations and future work

A primary limitation of this study is the scarcity of accurate isotherm models for various potential DAC sorbents, particularly those describing the co-adsorption of CO_2 and H_2O at high relative humidity. Additionally, there is a lack of mass transfer and kinetic models and data detailing the rate of CO_2 and H_2O adsorption at different ambient temperatures, especially at very low temperatures. This information is crucial for assessing DAC performance globally and identifying suitable sorbents tailored to specific regional climates.

Another limitation is that this work did not address the regional variation in energy costs and carbon intensity, which can influence LCOD and carbon removal efficiency. The next chapter addresses these gaps by expanding the current framework to

include a system analysis where different energy sources—such as renewables or regional electricity grids—can be incorporated and assessed on a techno-economic and environmental basis. This will enable a more comprehensive regional DAC assessment that considers regional energy costs and carbon intensity, helping to identify regions where DAC can be deployed most efficiently in terms of both cost and environmental benefits.

Overall, as more information becomes available for existing and new DAC technologies, this framework can be used for rapid geospatial screening and mapping of suitable technologies to different regions. Depending on the specific DAC technology, other parameters influencing process performance can also be incorporated, such as wind speed and intensity in passive DAC technologies that do not utilise fans to drive air over the sorbent.

CHAPTER 3

SYSTEM ASSESSMENT: GEOSPATIAL MODELLING OF DIRECT AIR CAPTURE AND ITS ENERGY SUPPLY OPTIONS

3.1 Abstract

This chapter extends the geospatial modelling framework introduced in the previous chapter to include system-level assessments, enabling a more comprehensive analysis that captures the synergies between different system elements. The enhanced framework models the system's structure and components using a process systems engineering approach, mapping out resources—such as raw materials and energy streams—and tasks—-technologies—to understand their interactions. This approach is applied to geospatial applications to determine optimal system design configurations and operations based on regional variations and constraints. The framework is demonstrated in a case study assessing the regional techno-economic and environmental performance coupling direct air capture to different energy supply options, aiming to identify the most energy-efficient and cost-effective direct air capture systems. This also considers the CO_2 removal efficiency, land requirement and water footprint for each option. The assessments cover a broad spectrum of technologies, including energy generation, conversion, storage technologies and the direct air capture process, with different energy types and materials flows expressed in hourly resolution and reflecting regional variation.

Findings from the case study indicate that many regions currently have carbon-

intensive energy systems and are unable to achieve net CO_2 removal with direct air capture, resulting in a net emission of CO_2 over the lifetime of the projects. Therefore, direct air capture requires the deployment of a dedicated energy supply, making it crucial to determine the optimal energy sources for coupling with direct air capture. The most cost- and energy-efficient option is to couple direct air capture with thermal power plants, such as nuclear or natural gas-fired combined cycle gas turbines with carbon capture and storage, where low-temperature heat can be extracted alongside electricity generation. The gross levelised cost of direct air capture is lowest for direct air capture coupled with nuclear power plants, at \$246–\$503 per tCO_2, whereas direct air capture coupled with combined cycle gas turbines with carbon capture and storage shows a gross levelised cost of \$314–\$557 per tCO_2—assuming a gas price of \$50 per MWh. For the renewable energy with energy storage option, regions with high solar irradiation can achieve the lowest gross levelised cost starting at \$319 per tCO_2 when utilising concentrated solar power. Conversely, regions with poor solar irradiation seem to be unsuitable for renewable-powered direct air capture due to high costs and large land requirements. Cost sensitivity analysis indicates that achieving a gross levelised cost of direct air capture of $\leq$\$200 per tCO_2 would require significant reductions in direct air capture collector costs and improvements in current direct air capture technology.

The results provide a foundation of evidence essential for developing business models, strategies and policies for the sustainable and cost-effective large-scale deployment of direct air capture systems. Furthermore, the current framework can be expanded to include additional technologies such as electrolytic hydrogen production to assess a wide range of applications and chemical productions such as green methanol and electrofuels.

3.2 Introduction

This chapter expands upon the geospatial modelling framework introduced in Chapter 2, extending its capabilities to incorporate system-level assessments. This extension is crucial as it enables a holistic analysis of systems integrating multiple technologies and chemical processes with region-dependent performance. Such comprehensive analysis is crucial for understanding the interplay between various technologies within a system, considering regional variability, which can provide critical insights for decision-makers and optimise regional deployment strategies.

The extended framework is illustrated through a case study that evaluates the coupling of direct air capture (DAC) to different low-carbon energy sources, including intermittent renewable energy (iRE)—solar and wind—and conventional sources—nuclear and natural gas with carbon capture and storage (CCS). This analysis assesses the techno-economic and environmental impacts, highlighting how regional differences in DAC performance and energy production can influence DAC system design, dynamics and sustainability.

The chapter is structured as follows. Section 3.3 reviews existing work on assessing the coupling of DAC with different energy sources, including geospatial assessments. Section 3.4 details the extended geospatial modelling framework, including a comprehensive description of the modelling of energy generation technologies. Section 3.5 discusses the results from the case study, focusing on the interaction between DAC performance and various energy sources across different regions. Finally, Section 3.6 concludes with a summary of the chapter's key findings, discusses the limitations of the current study and outlines potential avenues for future research and policy implications.

3.3 Background

3.3.1 Direct air capture and its energy supply

As discussed in Chapter 2, DAC is an energy-intensive process due primarily to the low concentration of CO_2 in the atmosphere. The modelled fully electrified process requires 1.45–2.56 MWh_{el} per tCO_2 [114]. This corresponds to an energy demand of 1,450–2,560 TWh to capture 1 $GtCO_2$, representing 5.7–10.1% of global electricity consumption in 2021 [144]. Moreover, the carbon intensity (CI) of the electricity used for DAC significantly affects its CO_2 removal efficiency [14, 42, 44]. For example, if a DAC project utilises electricity with a CI of 0.5 $kgCO_2$ per KWh_{el}—which approximates the 2019 global average CI for generated electricity—the project will result in net CO_2 emissions over its lifecycle [42, 145].

Given DAC's substantial energy requirements, it is crucial to couple it with low-carbon energy sources to ensure its effectiveness as a carbon dioxide removal (CDR) technology. Utilising the current global electricity mix would undermine its environmental benefits. Therefore, large-scale DAC deployment will necessitate the development of dedicated, clean energy infrastructure. Thus, it is imperative to

assess DAC projects from a holistic systems perspective, which includes their energy sources.

Published work exploring DAC from a system-level perspective includes techno-economic assessments of coupling DAC with various energy sources [77, 78, 146–153] and lifecycle assessments [14, 42–44, 154–159]. Lifecycle assessment studies have primarily focused on the two most developed DAC processes—KOH solution aboption-based DAC using a calciner [14, 42–44, 156, 157] and solid sorbent adsorption-based DAC using (steam-assisted) vacuum-pressure temperature swing adsorption (SA-)VTSA technology [14, 43, 155, 157]. These studies consistently highlight that the energy requirements of DAC are the main contributors to lifecycle emissions.

Techno-economic assessments that investigated different DAC energy supply options also mainly considered the two developed DAC technologies—KOH solution aboption-based DAC using calciner [148, 151, 153] and solid sorbent absorption-based DAC using (SA-)VTSA [146–153]. However, a few studies have considered other DAC approaches, including electric-driven KOH adoption-based DAC using bipolar membrane electrodialysis (BPMED) [153] and absorption-based DAC using carbonate minerals [77, 78, 153]. These studies examined various energy sources, including regional electricity grids [153], iRE [148, 151, 153], hydropower [153], geothermal [148, 150, 153], nuclear [146, 148, 150, 152, 153], biomass [148, 149] and natural gas with carbon capture and storage (CCS) [77, 78, 147, 153]. However, all these referenced studies did not consider regional variation in DAC process performance—assuming that DAC performance is independent of ambient conditions.

3.3.2 Geospatial modelling of direct air capture and its energy supply options

3.3.2.1 Current state of research

While large-scale deployment of sustainable and effective DAC requires a substantial amount of low-carbon energy, limited research has explored the interplay between DAC and its energy supply across different regions, particularly considering the variable performance of different technologies due to spatial and temporal factors. Previous studies that took a system-level perspective and regionally assessed the coupling of DAC to different energy sources either assumed that DAC performance is independent of ambient conditions or were limited in scope concerning the regional

context and the range of energy sources considered.

Breyer et al. [160, 161] developed a geospatial modelling tool and used it to assess the performance of coupling DAC based on solid sorbents to an iRE system in Morocco [160] and globally [160]. However, they assumed a fixed DAC performance corresponding to one ambient condition based on their previous work [30] and a fixed weighted average capital cost (WACC).

Brooks et al. [111] conducted a geospatial assessment of the performance of KOH solution adsorption-based DAC in the US using hourly data. They utilised DAC performance maps developed by An et al. [100] under different ambient conditions. Their assessment included supplying the process energy requirements from the electric grid, natural gas, or a combination of both.

Similarly, focusing only on the US, Pett-Ridge et al. [162] conducted a geospatial assessment of the performance of coupling both KOH solution adsorption-based DAC and solid sorbent adsorption-based DAC to the current and future US grid, iRE and natural gas. Their geospatial assessments were based on daily average ambient conditions and utilised DAC performance maps developed by An et al. [100] for the absorption-based DAC and those developed in Chapter 2 for the adsorption-based DAC. Notably, their iRE coupling scenario only considered iRE generation potential and its land requirements—without accounting for the temporal interaction between iRE generation and DAC performance, as they assessed these separately.

Wiegner et al. [104] employed their DAC optimisation framework—discussed in Section 2.3.4.2—to evaluate the coupling of adsorption-based DAC based on hourly resolution DAC and iRE performance data. Thus, their modelling framework can account for the temporal synergy between iRE generation and DAC performance. However, they only applied the framework to evaluate three locations.

Terlouw et al. [112] utilised the framework developed by Wiegner et al. [104] to assess the geospatial performance of DAC in Europe. However, they only used the framework to calculate average DAC process productivity and energy requirements, and the evaluated energy sources were assumed to be independent of temporal variation. The evaluated energy sources included the national power grid, waste heat and curtailed iRE electricity.

3.3.2.2 Contribution of the current work

This chapter expands the scope of the previously developed geospatial modelling framework to assess the integration of DAC with diverse energy sources across numerous global regions. This expansion is not merely geographical, but also methodological, as it adopts a holistic perspective on DAC system performance, including costs—accounting for regional WACC, CO_2 removal efficiency, land requirements and water footprint.

In essence, this chapter presents a geospatial framework for analysing DAC systems on a global scale, considering multiple performance metrics beyond just costs. This multidimensional analysis offers actionable insights for policymakers, researchers and industry stakeholders to optimise DAC deployment strategies in alignment with regional resources and environmental considerations.

3.4 Methodology

An overview of the methodology is presented in Figure 3.1. Regional variation is captured using geospatial data, including hourly meteorological and DAC process performance and regional WACC. These data—along with techno-economic and environmental data for the different considered technologies—is utilised to develop a mixed-integer linear programming (MILP) model (discussed in Section 3.4.4). The model is solved at each spatial node based on hourly resolution and using regional data to optimise a DAC system—including its energy supply—design and operation, aiming for minimum total annual system cost. The results from different spatial and different considered scenarios (discussed in Section 3.4.3) are collected and combined for plotting and analysis based on performance metrics (discussed in Section 3.4.5).

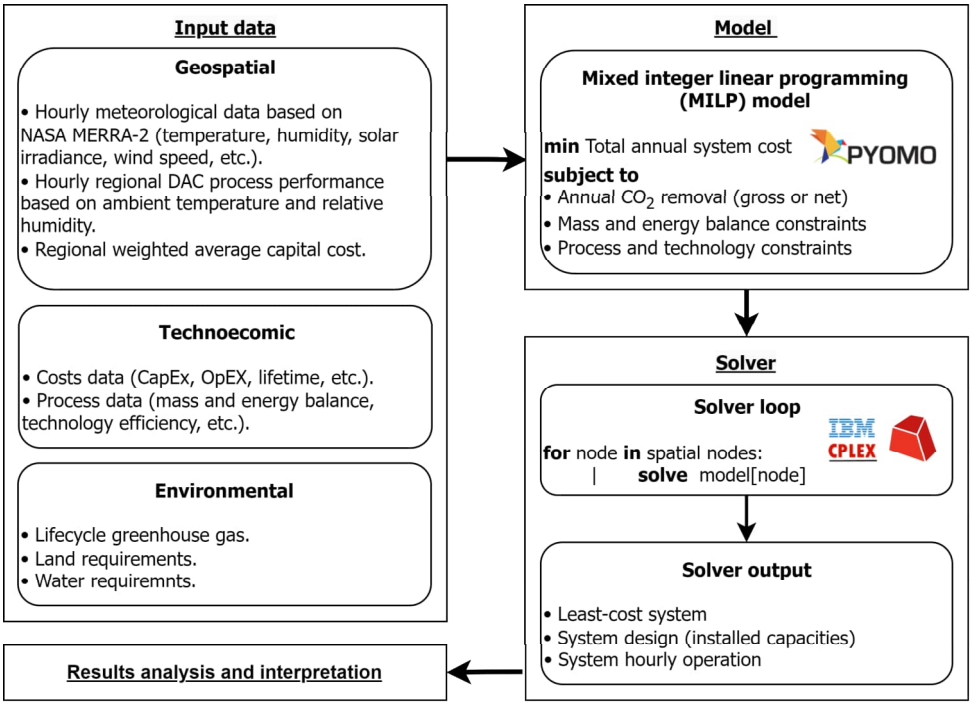


Figure 3.1: Geospatial framework methodology overview. Adapted from [114, 134].

3.4.1 Geospatial and temporal representation

3.4.1.1 Spatial representation

The spatial resolution of 0.5° × 0.625° (latitude, longitude) provided by NASA's MERRA-2 data is utilised to capture regional variations in the performance of different technologies, considering factors such as solar irradiation, wind and ambient conditions [133]. Using this MERRA-2 spatial resolution, the globe is divided into a grid comprising 361 × 576 nodes in the latitudinal and longitudinal directions, respectively. However, as the DAC process developed in Chapter 2 is employed in this analysis, cold regions where the ambient temperature drops below −15℃ for a substantial part of the year are excluded due to the resulting low process performance. Furthermore, to simplify the presentation of results, the world is divided into 9 regions, as shown in Figure 3.2.

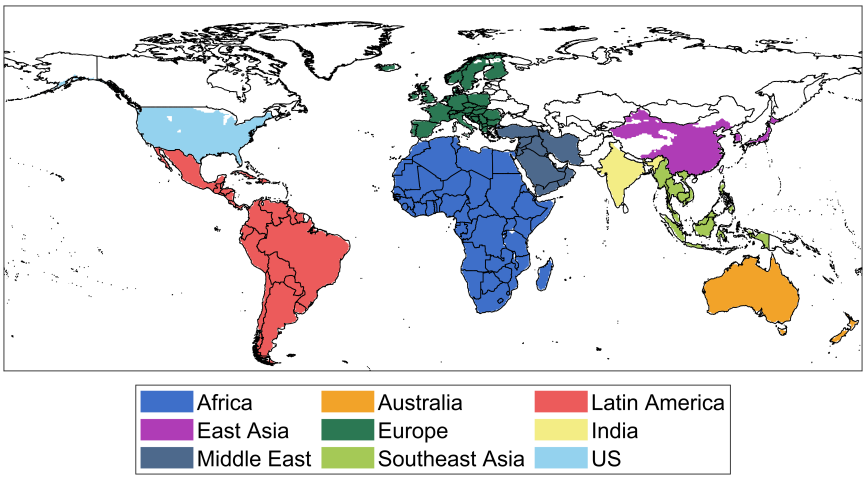


Figure 3.2: Aggregated regions for DAC with its energy supply options assessment. Adapted from [114, 134].

3.4.1.2 Temporal representation

Hourly resolution data for the entire year 2020 is used to capture both daily and seasonal variations in the performance of each technology at every spatial node. This hourly data—sourced from NASA's MERRA-2 dataset—includes ambient temperature (T2M), surface temperature (TS), specific humidity (QV2M), global horizontal irradiance (SWGDN), wind speed (U10M and V10M) and surface roughness (Z0M).

Hourly DAC performance data

DAC hourly performance data is obtained using the adsorption-based DAC process based on the SA-VTSA cycle configuration developed in Chapter 2. Figure 3.3 illustrates a simplified process flow diagram of the process. The process primarily involves adsorption and desorption cycles, where CO_2 is adsorbed from the air using the solid sorbent and subsequently desorbed using a combination of LT heat and vacuum pressure.

The simplified 3D models for DAC process indicators, including process productivity, low-temperature heat requirements—for bed heating and steam purging, electrical energy requirements—for fans, vacuum pumps and compressors and required air volume, which are based on temperature and relative humidity, were utilised to derive hourly DAC process performance data using hourly temperature and relative humidity values from the NASA MRRA-2 dataset. The fittings of these simplified models are visually represented in Appendix A.1.

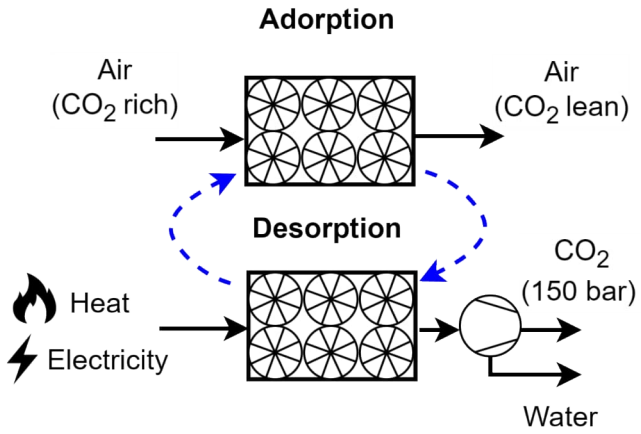


Figure 3.3: Simplified process flow diagram for the adsorption-based DAC process. Adapted from [134].

For temperatures below 1 °C, DAC performance is assumed to remain constant—equivalent to its operation at 1 °C. This assumption is used due to the limited data on the sorbent's behaviour at low temperatures. Additionally, a minimum operating temperature of −15 °C has been established for the DAC process as a safety precaution. This is because a considerable amount of water is generated and circulated within the process, and operating at very low temperatures could lead to water freezing and expanding within the process equipment, potentially compromising its reliability. Consequently, regions experiencing temperatures below −15 °C for over 30 days annually have been excluded from this analysis, which corresponds to approximately 25% of the global land area.

It is important to acknowledge that this temporal representation of DAC process performance assumes a cyclical steady state at each hour. In reality, the DAC process may operate in a transient state due to hourly fluctuations in temperature and relative humidity. This simplification could lead to either an overestimation or underestimation of DAC process performance during these fluctuations, representing a limitation of this modelling approach. However, this approach significantly reduces computational demands compared to solving more complex adsorption models based on partial differential equations (PDEs) using full-year hourly temperature and relative humidity profiles. Crucially, since this temporal representation does not systematically bias the DAC plant performance—i.e., it does not consistently overestimate or underestimate, the modelling accuracy should remain reasonable over longer time scales, such as on a yearly basis, as any inaccuracies from overestimation and underestimation would

balance out.

3.4.2 System representation

Resource-Task Network (RTN) framework is used to formulate the MILP model in this work, which was presented by Pantelides [163] based on the State-Task Network (STN) framework developed by Professor Roger Sargent's group at Imperial College London in the early 1990s [164, 165]. The RTN is a powerful modelling framework primarily used in process systems engineering that can facilitate the design and optimisation of complex production processes. It provides a systematic way to describe the process structure by defining how resources, such as raw materials and energy, are transformed into products through a series of tasks, i.e., technologies.

Figure 3.4 illustrates the key technologies and resources incorporated into the model. The model includes technologies and process equipment—tasks—for energy generation: solar photovoltaic (PV), concentrated solar power (CSP), wind, nuclear, gas turbine (GT) with CCS and gas-fired boiler (FB) with CCS; energy storage: battery, high-temperature (HT) thermal heat storage (THS) and low-temperature (LT) THS; and energy conversion: electric boiler (EB), heat pump (HP), steam turbine (ST) and battery inverter; and DAC process including fans, CO_2 collectors, vacuum pumps and compressors.

The model resources include 3 energy types: electricity, HT heat and LT heat, and different materials, including CO_2, water and natural gas (NG). HT heat is defined as high-pressure steam (HPS) at 560℃ and 100 bar, whereas LT heat is defined as saturated low-pressure steam (LPS) at 120℃. This distinction in heat grades enables the differentiation between HT heat produced by thermal power generation technologies, such as nuclear and CSP, and the LT heat consumed by various technologies, such as DAC and CCS.

Additionally, technologies that generate HT heat in the form of HPS–typically used in ST for electricity production, such as in nuclear and combined cycle gas turbine (CCGT) power plants—are decoupled into HPS generators and two ST configurations capable of consuming HPS. This allows the model the flexibility to choose the most cost-optimal use of generated HPS, whether it be in one of the ST configurations, storing it in HT THS or directly converting it to LT heat in the form of LPS. Further details about the ST configurations are provided in the model formulation section.

It is important to note that CO_2 captured via CCS when utilising natural gas technologies—e.g., GT and FB—is not considered part of the gross CO_2 removal from the atmosphere by the DAC system. On the other hand, any CO_2 emissions resulting from natural gas utilisation that are not captured by the CCS system are subtracted from the gross CO_2 removed by the DAC process, thereby influencing the gross CO_2 removed from the atmosphere. The precise definition of gross CO_2 removed from the atmosphere is discussed in Section 3.4.5.

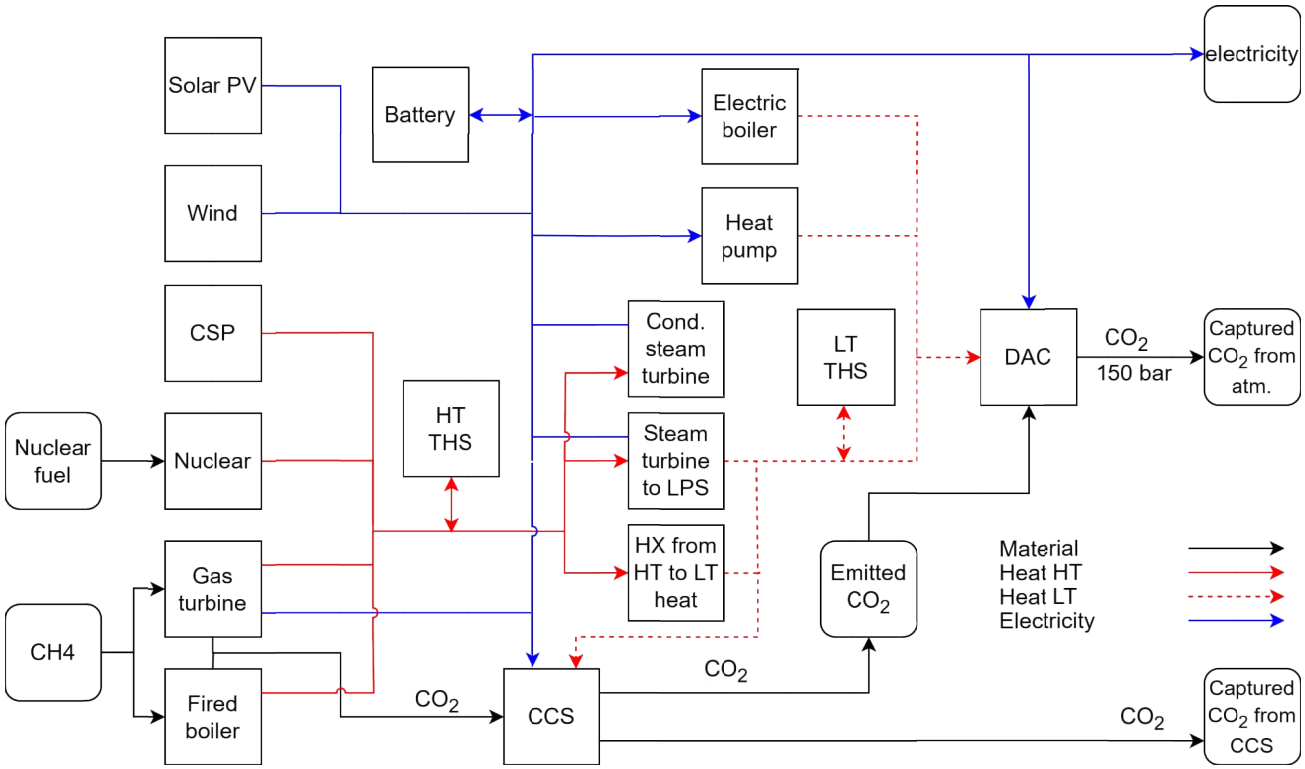


Figure 3.4: System representation using RTN framework. The model components include tasks—technologies—shown as boxes with sharp corners and resources shown as boxes with rounded corners. The coloured lines and arrows correspond to different material and energy type and their flow direction. Abbreviations: atmosphere (atm.), carbon capture and storage (CCS), condensing (cond.), concentrated solar power (CSP), direct air capture (DAC), electric boiler (EB), fired boiler (FB), gas turbine (GT), heat exchanger (HX), heat pump (HP), high-pressure steam (HPS), high-temperature (HT), low-temperature (LT), low-pressure steam (LPS), methane—natural gas (CH_4), steam turbine (ST), thermal heat storage (THS). Adapted from [134].

3.4.3 System Scenarios Considered

Initially, an analysis is conducted to assess the feasibility of meeting DAC energy demands through regional electrical grids. Subsequently, the developed system model is employed to investigate regional DAC performance under the following six system scenarios, each involving the integration of DAC with different energy technologies.

1. **All Technologies (AllTech):** In this scenario, the model has the freedom to select any of the considered technologies depicted in Figure 3.4 for DAC operation without any further restrictions. The system's production of excess electricity does not yield any additional benefits.
2. **Nuclear Power Plant (DAC+NuP):** This scenario couples DAC with a nuclear power plant. The LT heat required for DAC operation is exclusively supplied by an ST that partially expands HPS produced by the nuclear reactors into LPS, as illustrated in Figure 3.5A. Both the DAC and the nuclear power plant are assumed to operate at a 100% capacity factor (CF). Any excess electricity generated by the DAC+NuP system is assumed to be sold at the levelised cost of electricity (LCOE) corresponding to a standalone nuclear power plant without DAC, operating solely for electricity production at 100% CF and under the same economic assumptions.
3. **Natural Gas with Carbon Capture and Storage (NGTech):** This scenario exclusively considers energy generation technologies utilising NG coupled with CCS, namely GT with CCS (GTw/CCS) and FB with CCS (FBw/CCS). Energy storage technologies are excluded from this scenario, and the generation of excess electricity does not provide any additional benefits.
4. **Combined Cycle Gas Turbine with Carbon Capture and Storage Power Plant (DAC+CCGT):** In this scenario, DAC is integrated with a CCGT power plant equipped with CCS (CCGTw/CCS). The LT heat required for DAC operation is solely provided by the ST, which partially expands the HPS generated by the flue gas heat recovery steam generator unit (HRSG) into LPS, as depicted in Figure 3.6B. While DAC operates at a 100% CF, the CCGT power plant operates at the minimum load necessary to fulfil the DAC's energy requirements (both electricity and LT heat). Any excess electricity generated by the system is assumed to be sold at the LCOE of a standalone CCGTw/CCS plant operating exclusively for electricity production at 100% CF, under the same economic assumptions.

5. **Intermittent Renewable Energy with Energy Storage (REw/S):** This scenario exclusively considers wind, solar PV and CSP as energy generation technologies. Energy storage technologies are permitted. The generation of excess electricity by the system does not yield any additional benefits. However, The sale of excess electricity is assessed separately in this scenario due to its intermittent temporal profile, making analysis more complex compared to DAC+NuP and DAC+CCGT scenarios where excess electricity exhibits a near-baseload characteristic.
6. **Intermittent Renewable Energy with Energy Storage and Free Heating (REw/S+FH):** scenario restricts energy generation to wind, solar PV and CSP, and incorporates energy storage technologies. The DAC's LT heat requirements are supplied externally at no cost, simulating a scenario where waste heat is readily available. As in previous scenarios, the generation of excess electricity offers no additional benefits. It is crucial to acknowledge that this represents a niche application, and the availability of free waste heat is likely to be quite limited.

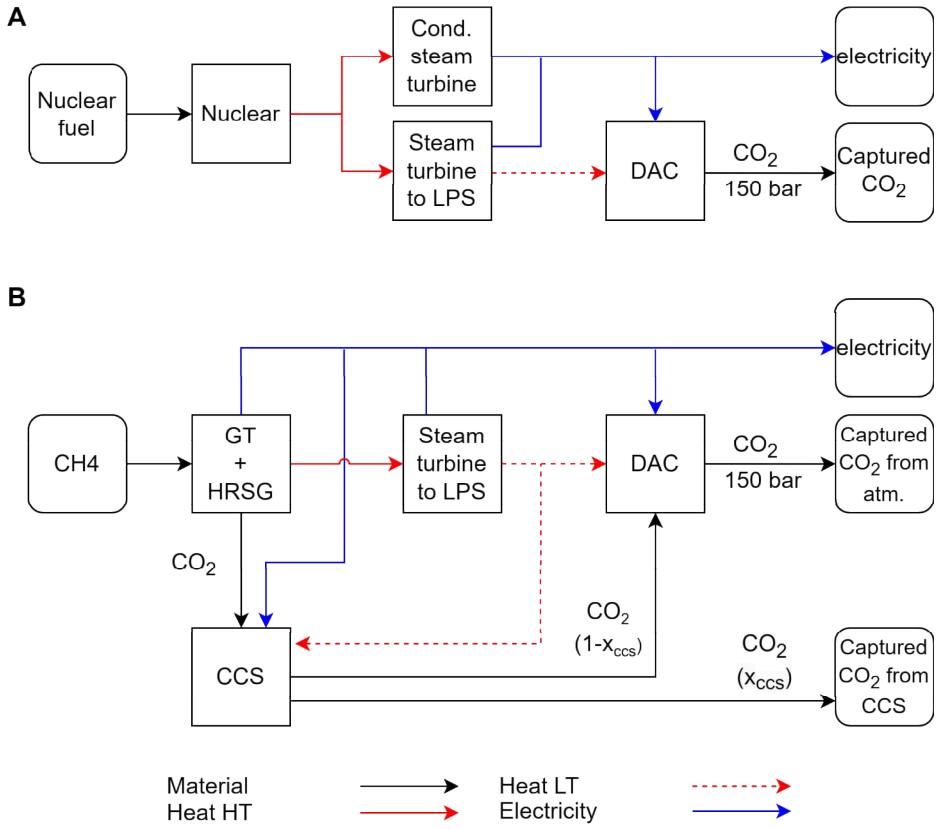


Figure 3.5: System scenarios when electricity is co-produced. A) DAC coupled with nuclear power plant (DAC+NuP). **B)** DAC coupled with natural gas-fired combined cycle gas turbines (CCGT) with CCS power plant (DAC+CCGT). Abbreviations: atmosphere (atm.), carbon capture and storage (CCS), condensing (cond.), CO_2 capture rate by CCS (x_{CCS}), flue gas heat recovery steam generator unit (HRSG), gas turbine (GT), high-temperature (HT), low-temperature (LT), low-pressure steam (LPS), methane—natural gas (CH_4). Adapted from [134].

3.4.4 Mathematical formulation and technologies description

Presented below is the formulation of the MILP model, accompanied by detailed descriptions of the technologies incorporated within the model.

3.4.4.1 Model constraints

Energy balance

The hourly energy balance for the three types of energy (et) considered in the model is defined by Equation 3.1. The equation establishes a relationship between the energy generated (gen) and consumed ($cons$) by non-energy storage technologies (Tns),

and the energy discharged ($dish$) and charged ($char$) from/to different energy storage technologies (Ts). For each energy type, an energy curtailment ($curt$) variable has been introduced to serve as a slack variable, ensuring the balance of any excess energy produced by intermittent renewable technologies.

$$\begin{aligned} &\sum_{t \in Tns} (gen_{t,et,h} - cons_{t,et,h}) \\ &+ \sum_{t \in Ts} (dish_{t,et,h} - char_{t,et,h}) \\ &- curt_{et,h} = 0, \quad \forall et, h \end{aligned} \tag{3.1}$$

where Indices t and h refer to technology and hourly time period.

Technology installed capacity

The installed capacity of different technologies can be expressed as the upper bound of its generation or consumption. Equation 3.2 shows an example of the installed capacity ($instCap$) constraints for conventional energy technologies (Tc)—e.g., nuclear reactor. In this equation, the specific energy generation type associated with the installed capacity is determined based on the technology cost assumptions shown in Appendix B. Constraints pertaining to the installed capacity of intermittent renewable energy technologies are presented below. Similar equations are employed for DAC process equipment and energy storage technologies, with their specific forms depending on the relevant technology cost assumptions. For example, the installed capacity of an energy storage system is determined based on its state of charge, while the installed capacity of a compressor is determined based on its electricity consumption.

$$gen_{t,et,h} \leq instCap_t, \quad \forall h, t \in Tc \tag{3.2}$$

Solar photovoltaic

The hourly generation of electricity by solar PV ($gen_{\text{solarPV,El},h}$) is determined using Equation 3.3, which incorporates the solar PV installed capacity ($instCap_{\text{solarPV}}$), global horizontal irradiance (GHI) and solar PV efficiency (η_{solarPV}). The solar PV efficiency is computed employing a simplified model developed by Huld et al. [166], which accounts for the local optimum angle. The model is a function of ambient

surface temperature ($Temp^{\text{S}}$) at the surface and GHI. The GHI data utilised in the model, along with the resulting solar PV electricity generation potential obtained based on Huld et al. [166] model, were validated against the Global Solar Atlas 2.0 [22]—which provides data calculated over a period exceeding 10 years for most global locations—demonstrating a good agreement. Further details regarding this validation are presented in Appendix D.1.

$$gen_{\text{solarPV,El},h} = instCap_{\text{solarPV}} \times GHI_h \times \eta_{\text{solarPV},h}(GHI_h, Temp_h^{\text{S}}), \quad \forall h \tag{3.3}$$

Wind turbine

The hourly electricity generated by a wind turbine ($gen_{\text{wind,El},h}$) is determined by the installed capacity of the wind turbine ($instCap_{\text{wind}}$) and its corresponding capacity factor (CF_{wind}), which is a function of wind speed (WS), as shown in Equation 3.4. The CF_{wind} curve utilised in this work is obtained from Staffell and Green [167], based on a 50 MW farm consisting of Vestas V80 2 MW turbines. The logarithmic profile model [168] shown in Equation 3.5 is used to calculate wind speed at a height of 150m (z)—which is used in this work—using NASA MERRA-2 wind speed data at a height of 10m (z_r) along with surface roughness data (z_0).

$$gen_{\text{wind,El},h} = instCap_{\text{wind}} \times CF_{\text{wind},h}(WS_h), \quad \forall h \tag{3.4}$$

$$WS(z) = WS(z_r) \times \frac{\ln(z/z_0)}{\ln(z_r/z_0)} \tag{3.5}$$

For data validation, the wind speed at a height of 100m was validated against the Global Wind Atlas 3.0 [21]— which is based on sample data from 1998 to 2017—using the same methodological approach. A good agreement was observed between the two datasets. Further details regarding this validation are presented in Appendix D.2

Concentrated solar power

CSP is modelled as a solar power tower system utilising molten salt as the heat transfer fluid. CSP with solar power towers uses an array of controlled mirrors—called heliostats—to concentrate sunlight to a central receiver on the top of a tower. This concentration of solar energy generates HT heat, which heats the fluid transfer fluid. Melton salt is commonly used due to its low cost, ability to operate at high

temperatures and capacity for thermal heat storage. The heated fluid from either the receiver or storage tanks can then be used to produce HPS, driving STs to generate electricity. The heated fluid is then cycled back to the receiver.

The CSP is modelled using Equations 3.6–3.9, which are adapted from previous works [169, 170]. The hourly HT heat generated by CSP ($gen_{\text{CSP,HeatHT},h}$) is a function of the installed capacity of CSP plant ($instCap_{\text{CSP}}$)—which is based on the heliostat field area—heliostat field efficiency ($\eta^{\text{field}}_{\text{CSP}}$), direct normal irradiance (DNI) and radiative ($Loss^{\text{red}}_{\text{CSP}}$) and convective ($Loss^{\text{conv}}_{\text{CSP}}$) losses, as shown in Equation 3.6.

$$\begin{aligned} gen_{\text{CSP,HeatHT},h} = \; & instCap_{\text{CSP}} \times \eta^{\text{field}}_{\text{CSP},h}(\theta_h) \\ & \times DNI_h(GHI_h, \theta_h, DOY_h) \\ & \times \Big(1 - Loss^{\text{red}}_{\text{CSP},h}(Temp_h) \\ & \quad - Loss^{\text{conv}}_{\text{CSP},h}(Temp_h, WS_h)\Big), \quad \forall h \end{aligned} \tag{3.6}$$

$$\begin{aligned} Loss^{\text{red}}_{\text{CSP},h}(Temp_h) = \; & \frac{1}{\varphi^{\text{rec}}_{\text{CSP}}} \times \sigma \times \varepsilon^{\text{rec}}_{\text{CSP}} \\ & \times \Big(\left(Temp^{\text{eff}}_{\text{CSP}}\right)^4 - (Temp_h)^4\Big), \quad \forall h \end{aligned} \tag{3.7}$$

$$\begin{aligned} Loss^{\text{conv}}_{\text{CSP},h}(Temp_h, WS_h) = \; & Loss^{\text{red}}_{\text{CSP},h}(Temp_h) \\ & \times (-5.645 \times 10^{-4}\, {WS_h}^3 + 0.01561\, {WS_h}^2 \\ & - 0.00911\, WS_h + 0.48124), \quad \forall h \end{aligned} \tag{3.8}$$

$$Temp^{\text{eff}}_{\text{CSP}} = 0.55\,(Temp^{\text{out}}_{\text{CSP}} + Temp^{\text{in}}_{\text{CSP}}) \tag{3.9}$$

$\eta^{\text{field}}_{\text{CSP}}$ is calculated using the performance curve presented by Ghirardi et al. [169], which is a function of the solar zenith angle (θ) as input. DNI is calculated using the Direct Insolation Simulation Code (DISC) model available in MATLAB and Python via the PVLIB package [171], with GHI, θ and day of the year (DOY) as model inputs. $Loss^{\text{red}}_{\text{CSP}}$ and $Loss^{\text{conv}}_{\text{CSP}}$ are calculated using Equations 3.7 and 3.8, respectively, where a CSP receiver heat flux ($\varphi^{\text{rec}}_{\text{CSP}}$) of 600 kW per m^2 is used to estimate the receiver area, and the CSP receiver emissivity ($\varepsilon^{\text{rec}}_{\text{CSP}}$) is assumed to be 0.88 [172]. Molten salt outlet temperature ($Temp^{\text{out}}_{\text{CSP}}$) and inlet temperature ($Temp^{\text{in}}_{\text{CSP}}$) of 574 ℃ and 290 ℃, respectively, were used to calculate an area-weighted average molten salt temperature at the receiver ($Temp^{\text{eff}}_{\text{CSP}}$) as shown in Equation 3.9 [170, 172].

CSP deployment was restricted to regions with annual direct normal irradiance

(DNI) exceeding 1,800 kWh per m^2 to ensure stable operation. Data validation for the obtained DNI from the DISC model against DNI data from the Global Solar Atlas 2.0 [22], and a comparison of the DNI-to-electricity conversion efficiency with literature data, shows good agreement between the datasets. Further details regarding this validation are presented in Appendix D.1.

Nuclear power

Nuclear power plants generate electricity through nuclear fission, where the nuclei of a nuclear fuel—such as uranium—are split in a reactor core, releasing heat. This heat is used to produce HPS, which is then used to drive STs, which produce electricity. In this work, the nuclear reactor and the ST section are modelled as separate tasks—technologies, where the hourly HT heat generated ($gen_{\text{Nuclear,HeatHT},h}$) is a function of the hourly nuclear fuel consumption ($cons^{\text{fuel}}_{\text{Nuclear},h}$), as shown in Equation 3.10.

$$gen_{\text{Nuclear,HeatHT},h} = cons^{\text{fuel}}_{\text{Nuclear},h}, \quad \forall h \tag{3.10}$$

Currently, light water-cooled reactors (LWRs) constitute the majority—over 80%—of commercial nuclear reactors, utilising water as a coolant [173, 174]. These reactors typically generate HPS with a pressure of up to 155 bar and a maximum temperature of around 330 ℃, achieving an efficiency of up to 38% [173]. In contrast, advanced gas-cooled reactors, the most common type in the UK, employ CO_2 as a coolant and can supply steam at elevated temperatures reaching up to 640 ℃ [175, 176]. Recently, China has commercialised the High-Temperature Reactor - Pebble-bed Module (HTR-PM), which utilises helium as a coolant and is capable of providing heat at even higher temperatures, up to 750 ℃ [173]. These high-temperature reactors can achieve a high thermal-to-electrical efficiency of 42% and can supply HPS at the specifications employed in this study [173].

Natural gas technologies

CCGT power plants are among the most energy-efficient methods for electricity generation when utilising natural gas. They enhance energy efficiency by integrating a GT cycle with an ST cycle where natural gas-to-electricity efficiency of more than 60% can be achieved [177]. In a CCGT power plant, air is compressed and mixed with fuel, typically natural gas, in the GT and combusts to generate electricity. The exhaust heat from this process is then captured by an HRSG, which produces steam to drive a second turbine, thereby generating additional electricity.

CCGT power plants can be fitted with a post-combustion CCS unit to lower the CO_2 emissions from burning natural gas. The most widely deployed CCS technology is based on absorption using an amine-based solution, such as monoethanolamine (MEA) [178]. The exhaust gas containing CO_2 from the GT is scrubbed by the amine solution in an adsorption column. The CO_2-rich solution can then be regenerated using LT heat in a stripper column, where CO_2 is released and captured. The regenerated solution is then recycled back to the adsorption column.

In this work, the GT and ST cycles in the CCGT power plant are modelled as different tasks. The hourly ST—including HRSG—electricity ($gen_{\text{GT,El},h}$) and HT heat ($gen_{\text{GT,HeatHT},h}$) generation are defined in Equations 3.11 and 3.12), respectively, which are a function of the hourly fuel consumption ($cons^{\text{fuel}}_{\text{GT},h}$) and GT fuel-to-electricity efficiency ($\eta^{\text{GT}}_{\text{El}}$)—assumed to be 0.4 based on the fuel's lower heating value (LHV) [177]. Additionally, generating steam using natural gas-fired heaters is also considered here, where the hourly HT heat generated by the boiler ($gen_{\text{FB,HeatHT},h}$) is shown in Equation 3.13, which is a function of the boiler's hourly fuel consumption ($cons^{\text{fuel}}_{\text{FB},h}$) and its fuel-to-thermal heat efficiency ($\eta^{\text{FB}}_{\text{HeatHT}}$)—assumed to be 95% [179]. A ratio of high heating value (HHV) to LHV of 1.108 is used when calculating the fuel cost (based on methane heating value), and a fuel cost of \$50 per MWh_{NG} is assumed for base case scenarios.

$$gen_{\text{GT,El},h} = \eta^{\text{GT}}_{\text{El}} \times cons^{\text{fuel}}_{\text{GT},h}, \quad \forall h \tag{3.11}$$

$$gen_{\text{GT,HeatHT},h} = (1 - \eta^{\text{GT}}_{\text{El}}) \times cons^{\text{fuel}}_{\text{GT},h}, \quad \forall h \tag{3.12}$$

$$gen_{\text{FB,HeatHT},h} = \eta^{\text{FB}}_{\text{HeatHT}} \times cons^{\text{fuel}}_{\text{FB},h}, \quad \forall h \tag{3.13}$$

Point-source CCS is used to lower CO_2 emission when natural gas is used and modelled based on amine-based technology using Equations 3.14—3.17. Equations 3.14 and 3.15 define hourly captured ($CCScaptured^{\text{CO}_2}_{t,h}$) and emitted ($emitted^{\text{CO}_2}_{t,h}$) CO_2 for natural gas (NG) technologies (Tng), respectively, which is a function of the capture rate (CR^{CCS})—assumed to be 97% [180, 181], fuel CO_2 emission factor ($emission^{\text{NG}}$)—assumed to be 0.203 $kgCO_2$ per kWh [182] and hourly fuel consumption ($cons^{\text{fuel}}_{t,h}$).

$$CCScaptured^{\text{CO}_2}_{t,h} = CR^{\text{CCS}} \times emission^{\text{NG}} \times cons^{\text{fuel}}_{t,h}, \quad \forall t \in Tng, h \tag{3.14}$$

$$emitted_{t,h}^{\mathsf{CO_2}} = (1 - CR^{\mathsf{CCS}}) \times emission^{\mathsf{NG}} \times cons_{t,h}^{\mathsf{fuel}}, \quad \forall t \in Tng, h \tag{3.15}$$

$$cons_{t,\mathsf{El},h} = cons_{\mathsf{El}}^{\mathsf{CCS}} \times CCScaptured_{t,h}^{\mathsf{CO_2}}, \quad \forall t \in Tng, h \tag{3.16}$$

$$cons_{t,\mathsf{HeatLT},h} = cons_{\mathsf{HeatLT}}^{\mathsf{CCS}} \times CCScaptured_{t,h}^{\mathsf{CO_2}}, \quad \forall t \in Tng, h \tag{3.17}$$

The hourly electricity ($cons_{t,\mathsf{El},h}$) and LT heat ($cons_{t,\mathsf{HeatLT},h}$) requirements for the CCS unit are supplied by the system and calculated using Equations 3.16 and 3.17, respectively, which are a function of the hourly amount of captured CO_2 ($CCScaptured_{t,h}^{\mathsf{CO_2}}$). These calculations assume a CCS electricity requirement ($cons_{\mathsf{El}}^{\mathsf{CCS}}$) of 0.203 MWh_{el} per tCO_2 and an LT heat requirement ($cons_{\mathsf{HeatLT}}^{\mathsf{CCS}}$) of 1.143 MWh_{LTheat} per tCO_2 [183, 184].

While NG leakage (methane leakage) is not considered in the main scenarios, a sensitivity analysis is conducted to examine the impact of NG leakage when utilising NG technologies for DAC. In this analysis, a global warming potential over 100 years (GWP-100) of 29.8 is used, along with a conversion factor of 12.51 MWh_{NG} per tCH_4 based on LHV [185, 186].

Steam turbines

STs convert thermal energy from steam into mechanical energy, and then into electrical energy. Two ST configurations (Tst) are considered in this work and modelled using Equations 3.18 and 3.19. Equation 3.18 shows a correlation between the ST hourly electricity generation ($gen_{t,\mathsf{El},h}$) to the hourly HPS steam consumption ($cons_{t,\mathsf{HeatHT,h}}$) using the ST thermal-to-electricity efficiency (η_t^{ST}). The first considered ST (CST) is condensing ST with $\eta_{\mathsf{CST}}^{\mathsf{ST}}$ of 0.38. The second considered ST partially expands HPS to LPS (PST) with $\eta_{\mathsf{PST}}^{\mathsf{ST}}$ of 0.27, where its hourly generated LT heat ($gen_{t,\mathsf{HeatLT},h}$) is calculated using Equation 3.19.

$$gen_{t,\mathsf{El},h} = \eta_t^{\mathsf{ST}} \times cons_{t,\mathsf{HeatHT,h}}, \quad \forall t \in Tst, h \tag{3.18}$$

$$gen_{\mathsf{PST,HeatLT},h} = (1 - \eta_{\mathsf{PST}}^{\mathsf{ST}}) \times cons_{\mathsf{PST,HeatHT,h}}, \quad \forall h \tag{3.19}$$

Heat pumps and low-temperature heat generation approaches

HPs operate by transferring heat from one location—heat source—to another—heat sink—using the refrigeration cycle. In this work, HPs are modelled as air source HPs—ambient air is used as a heat source—to generate LT heat using

Equations 3.20—3.23. The HP hourly LT heat generation ($gen_{\text{HP,HeatLT},h}$) is a function of the hourly HP coefficient of performance (COP_h^{HP})—which is a function of ambient temperature ($Temp_h$)—and the HP hourly electricity consumption ($cons_{\text{HP,El},h}$) as shown in Equation 3.20. COP_h^{HP} is defined in Equations 3.21—3.23, where η_{2nd}, $Temp_{\text{cold}}^{\text{HP}}$, $Temp_{\text{hot}}^{\text{HP}}$ and ΔT_{min} are second law efficiency—assumed to be 50% (typical values for heat pumps 50%–70% [131, 132]), heat source temperature, heat sink temperature and minimum approach temperature—assumed to be 10 °C.

$$gen_{\text{HP,HeatLT},h} = COP_h^{\text{HP}}(Temp_h) \times cons_{\text{HP,El},h}, \quad \forall h \tag{3.20}$$

$$COP_h^{\text{HP}}(Temp_h) = \frac{Temp_{\text{hot}}^{\text{HP}}}{Temp_{\text{hot}}^{\text{HP}} - Temp_{\text{cold}}^{\text{HP}}(Temp_h)} \eta_{2nd}, \quad \forall h \tag{3.21}$$

$$Temp_{\text{hot}}^{\text{HP}} = Temp_{\text{HeatLT}} + \Delta T_{\text{min}} \tag{3.22}$$

$$Temp_{\text{cold}}^{\text{HP}}(Temp_h) = Temp_h + \Delta T_{\text{min}}, \quad \forall h \tag{3.23}$$

Two other methods are considered to generate LT heat: EBs and HT heat via heat exchangers. The hourly LT generation for the two approaches ($gen_{\text{EB,HeatLT},h}$) and ($gen_{\text{HTtoLTHeat,HeatLT},h}$) are shown in Equations 3.24 and 3.25, which are functions of the hourly energy consumptions ($cons_{\text{EB,El},h}$) and ($cons_{\text{HTtoLTHeat,HeatHT},h}$), respectively.

$$gen_{\text{EB,HeatLT},h} = cons_{\text{EB,El},h}, \quad \forall h \tag{3.24}$$

$$gen_{\text{HTtoLTHeat,HeatLT},h} = cons_{\text{HTtoLTHeat,HeatHT},h}, \quad \forall h \tag{3.25}$$

Energy storage

Energy storage helps smooth out the variability of iRE by storing excess energy when demand is low and releasing it when demand is high. In this work, three energy storage technologies—battery, HT THS and LT THS—are considered, corresponding to the different energy types considered. All considered energy storage technologies are modelled similarly using Equations 3.26—3.30. Equations 3.26 and 3.27 update the hourly state of charge ($SOC_{t,h}$) for the first and remaining periods, respectively, where $char_{t,h}$ and $disch_{t,h}$ are hourly charge and discharge, respectively; η_t^{char} and η_t^{disch} are charging and discharging efficiency, respectively; and SD_t is self-discharge.

Assumed values are shown in Table 3.1.

$$SOC_{t,1} = SOC_{t,H_{end}} \times (1 - SD_t) - \frac{disch_{t,1}}{\eta_t^{disch}} + char_{t,1} \times \eta_t^{char}, \quad \forall t \in Ts \tag{3.26}$$

$$SOC_{t,h} = SOC_{t,h} \times (1 - SD_t) - \frac{disch_{t,h}}{\eta_t^{disch}} + char_{t,h} \times \eta_t^{char}, \quad \forall t \in Ts, h \in (2, H_{end}) \tag{3.27}$$

$$disch_{t,h} \leq M \times y_{t,h}^{\text{disch}}, \quad \forall t \in Ts, h \tag{3.28}$$

$$char_{t,h} \leq M \times y_{t,h}^{\text{char}}, \quad \forall t \in Ts, h \tag{3.29}$$

$$y_{t,h}^{\text{disch}} + y_{t,h}^{\text{char}} = 1, \quad \forall t \in Ts, h \tag{3.30}$$

Equations 3.28—3.30 are used to ensure that energy storage technologies cannot operate in charging and discharging states at the same time, where $y_{t,h}^{\text{char}}$ and $y_{t,h}^{\text{disch}}$are binary decision variables that are activated—with the value of 1—if energy storage technology is in charging and discharging state, respectively, and M is a large value.

Table 3.1: Performance of energy storage technologies. adapted from [134].

		Unit	Value	Source
Battery	Discharging efficiency	%	92	[187]
	Charging efficiency	%	92	[187]
	Self-discharge	% per day	0.05	[187]
Thermal heat storage	Discharging efficiency	%	98.5	[188]
	Charging efficiency	%	100	[188]
	Self-discharge	% per day	0.72	[188]

3.4.4.2 Objective function

The objective function is to minimise the total annualised cost of the system (TAC). This includes the sum of all annualised capital expenditures ($CapEx$), fixed and variable operating expenses ($OpEx$), fuel costs and costs associated with point-source CCS for all technologies, as expressed in Equation 3.31. The annualised $CapEx$ is derived using the region-specific annualised factor (AF), which is based

on technology lifetime (LT) and regional weighted average cost of capital ($WACC$).

$$\begin{aligned}\textbf{min} \quad TAC = & \sum_{t} (CapEx_t \times AF_t + OpEx_t^{\text{fix}}) \times instCap_t \\ & + \sum_{t \in Tns, et, h} OpEx_{t,et}^{\text{var}} \times gen_{t,et,h} \\ & + \sum_{t \in Ts, et, h} OpEx_{t,et}^{\text{var}} \times disch_{t,et,h} \\ & + \sum_{t,h} cost_t^{\text{fuel}} \times cons_{t,h}^{\text{fuel}} \\ & + \sum_{t,h} cost^{\text{CCS}} \times CCScaptured_{t,h}^{\text{CO}_2}\end{aligned} \tag{3.31}$$

$$AF_t = \frac{WACC \times (1 - WACC)^{LT_t}}{(1 + WACC)^{LT_t} - 1} \tag{3.32}$$

Three levels of regional WACC are considered: low, mid and high. Low WACC represents low-interest loans, such as those backed by governments or designated for green projects, and is adapted from Ameli et al. [20] based on low-carbon investments. Mid WACC represents medium-interest loans, typically provided by traditional banks, and is assumed to be twice the low WACC value. High WACC represents high-risk investments, such as those made by venture capitalists, and is assumed to be three times the low WACC value. The WACC values are shown in Appendix B.3.

3.4.4.3 Solution strategy and solver

The combined MILP model was implemented in Pyomo V6.4.2, with solutions obtained using CPLEX V22.1.0 or, in cases where CPLEX failed to converge in a timely manner, Gurobi V9.0.1. The model is solved at various spatial land nodes with a full hourly resolution to estimate regional performance variations.

Depending on the specific scenario considered, a typical optimisation problem for each node involves approximately 0.4–0.5 million variables and 0.4–0.5 million constraints. Solver times remain below 1 minute when utilising 12 CPU threads on Imperial's research computing cluster for scenarios with fewer allowed technologies and more constraints, such as DAC+NuP, and extend up to a few minutes (i.e., 5–20) for more complex scenarios like REw/S. Python multiprocessing module was used to parallelise solving several spatial nodes simultaneously.

Given the substantial number of spatial nodes and evaluated scenarios, only overland nodes with odd numbers are assessed to maintain reasonable computational costs while preserving adequate spatial resolution. This results in around 7900 spatial nodes to be evaluated per scenario.

3.4.5 System performance indicators

3.4.5.1 Carbon balance

Equation 3.33 defines the total annual CO_2 captured from the atmosphere by the system ($TACO_2Prod$). This is calculated as the sum of the CO_2 captured by DAC ($DACcaptured^{CO_2}$) over the year minus the sum of emitted CO_2 ($emitted^{CO_2}$) when natural gas is utilised for energy production—representing scope 1 emissions.

$$TACO_2Prod = \sum_{h} DACcaptured_{h}^{CO_2} - \sum_{t \in Tng, h} emitted_{t,h}^{CO_2} \tag{3.33}$$

3.4.5.2 Environmental metrics

Equation 3.34 defines CO_2 removal efficiency (η^{CDR}). In this study, η^{CDR} exclusively accounts for the normalised total system lifecycle greenhouse gas (GHG) emissions, as represented by the second term of Equation 3.34. This is calculated based on the sum of all annualised technology lifecycle GHG emissions ($ALCA^{GHG}$) divided by $TACO_2Prod$.

$$\eta^{CDR} = 1 - \frac{\sum_{t} ALCA_{t}^{GHG}}{TACO_2Prod} \tag{3.34}$$

It is important to note that this work only considers lifecycle GHG emissions associated with the energy production and storage infrastructure, including the supply chain of feedstock/utilities. Lifecycle GHG emissions for DAC units and sorbents are not incorporated. This exclusion is due to the limited availability of information regarding these emissions from large-scale industrial projects. However, published studies suggest that the DAC plant construction and sorbent consumption have a relatively minor impact on lifecycle GHG emissions, with the primary contributor being emissions associated with energy supply [42, 44, 154].

The values for $ALCA^{GHG}$ are obtained either using the technology's installed capacity or the technology's energy generation/discharge, depending on the specific lifecycle GHG emissions assumptions for that technology. To calculate lifecycle emissions based on the technology's installed capacity—such as for wind turbines and solar PV, the lifetime of the technology is used to determine the annualised lifecycle emissions. For technologies where lifecycle emissions are based on energy generation/discharge—such as for nuclear power plants and batteries, the annualised lifecycle emissions are obtained by summing the hourly lifecycle emissions over the year.

A similar approach is adopted to determine the total system land requirement and water footprint. lifecycle GHG emissions, land requirement and water footprint values and assumptions are provided in Appendix C.

3.4.5.3 Economic metrics

The gross levelised cost of DAC ($\text{LCOD}_{\text{gross}}$) is calculated using Equation 3.35. This considers any emitted CO_2 during natural gas utilisation—categorised as scope 1 emissions, as defined in Equation 3.33. This levelised cost of DAC (LCOD) formulation aligns with those reported by Keith et al. [41] and other prior DAC studies [46, 114].

$$\text{LCOD}_{\text{gross}} = \frac{TAC}{TACO_2Prod} \tag{3.35}$$

Subsequently, by incorporating η^{CDR}, the net levelised cost of DAC (LCOD_{net}) is calculated using Equation 3.36, which considers the lifecycle GHG emissions associated with technology infrastructure and supply chains. This LCOD formulation is consistent with previous studies [18, 37, 153] that accounted for emissions from energy supply; however, it is important to note that CO_2 storage costs are not included here.

$$\text{LCOD}_{\text{net}} = \frac{LCOD_{gross}}{\eta^{CDR}} \tag{3.36}$$

Similarly, for a system co-generating an annual output of electricity ($\sum_h output_h^{\text{El}}$), the levelised cost of electricity (LCOE) is calculated using Equation 3.37.

$$\text{LCOE} = \frac{TAC}{\sum_h output_h^{\text{El}}} \tag{3.37}$$

In scenarios where the system provides both electricity output and CO_2 removal, the $\text{LCOD}_{\text{gross}}$ is modified to reflect the total revenue generated from selling the surplus electricity over the year, as illustrated in Equation 3.38.

$$\text{LCOD}_{\text{gross}} = \frac{TAC - \sum_h LCOE \times output_h^{\text{El}}}{TACO_2Prod} \tag{3.38}$$

3.4.6 Representative locations

Four representative locations—shown in Table 2—have been chosen to illustrate the details of the optimised system configuration for different scenarios. These locations are based on the climate groups presented in Chapter 2—cold dry, cold humid, hot dry and hot humid—representing different DAC regional performances. Furthermore, these four locations also represent diverse renewable energy resource potentials. Albuquerque, New Mexico (NM) and Riyadh, Saudi Arabia (SA) are characterised by favourable solar resources, while London, UK, possesses good wind resources. Jakarta, Indonesia (ID), on the other hand, exemplifies a region with limited solar and wind resources.

Table 3.2: Selected Representative locations to illustrate DAC system performance. The locations are chosen due to their different regional DAC performance and renewable energy resources. adapted from [134].

Location	DAC[a]				iRE[a]		
	Climate	Productivity	LT heat	Electricity	GHI	DNI	Wind turbine
		$tpaCO_2$ per collector	MWh per tCO_2	MWh per tCO_2	kWh/m^2 per year	kWh/m^2 per year	CF
Albuquerque, NM	Cold dry	57.6	2.45	0.30	2,156	2,818	16.2%
London, UK	Cold humid	55.5	3.32	0.28	1,305	1,482	40.2%
Riyadh, SA	Hot dry	52.4	2.28	0.36	2,351	2,708	17.3%
Jakarta, ID	Hot humid	50.1	3.75	0.43	1,744	973	4.4%

Regions include Albuquerque in New Mexico (NM), Riyadh in Saudi Arabia (SA), London in the United Kingdom (UK) and Jakarta, Indonesia (ID). Abbreviations: global horizontal irradiance (GHI), direct normal irradiance (DNI) and capacity factor (CF).

[a] Annual mean values.

3.5 Results and discussion

3.5.1 Direct air capture powered by today's regional electricity grids

Figure 3.6 shows the CO_2 removal efficiency of DAC when utilising grid electricity—using mean 2019 regional CI values. It is evident that only a limited number of regions—approximately 21% globally—can achieve a CO_2 removal efficiency of $\geq$50%. This capability is attributed to their lower CI electricity grids, often characterised by a high share of hydropower and/or nuclear power, as exemplified by Norway, Iceland, France, Ethiopia and Washington State in the US (Figure 3.7).

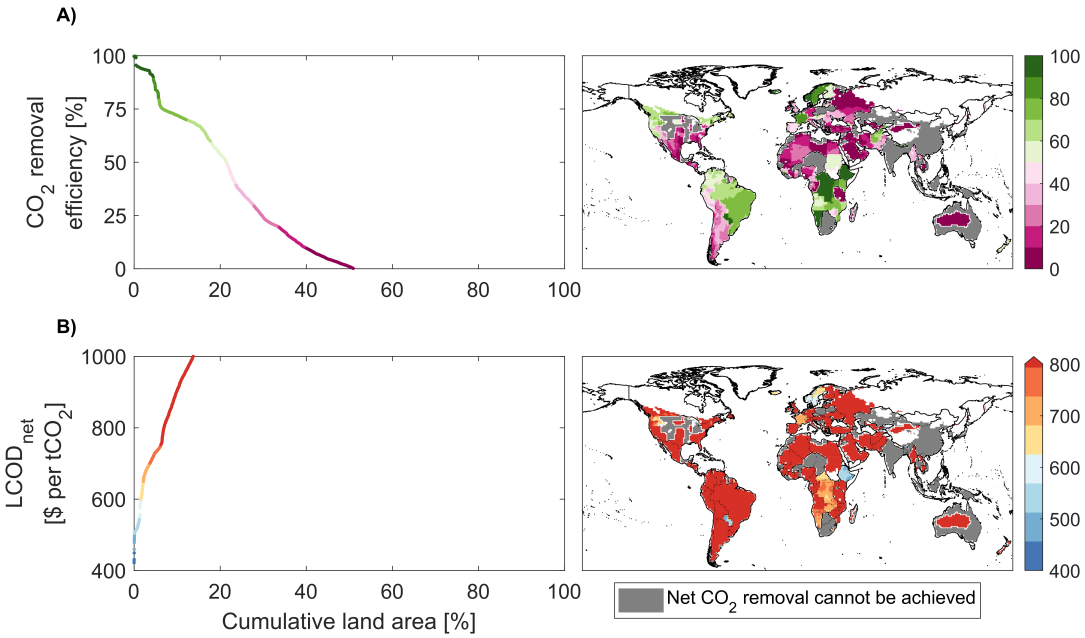


Figure 3.6: Performance of coupling DAC to today's regional electricity grid. **A)** CO_2 removal efficiency. **B)** $LCOD_{net}$ using regional grid electricity prices. The 2019 CI data was used and obtained from [189, 190]. Regional electricity prices were obtained from [190, 191]. Adapted from [134].

Regions with low CO_2 removal efficiency generally experience higher DAC costs, reflected in the increase in $LCOD_{net}$ observed in Figure 3.6. For example, at a CO_2 removal efficiency of 50%, DAC plants must capture 2 tCO_2 to achieve a net removal of 1 tCO_2 from the atmosphere. This implies that the $LCOD_{net}$ is double the $LCOD_{gross}$. Moreover, in regions with high CI electricity grids, DAC not only fails to achieve net CO_2 removal but results in CO_2 emissions, as indicated by the grey regions in Figure 3.6 .

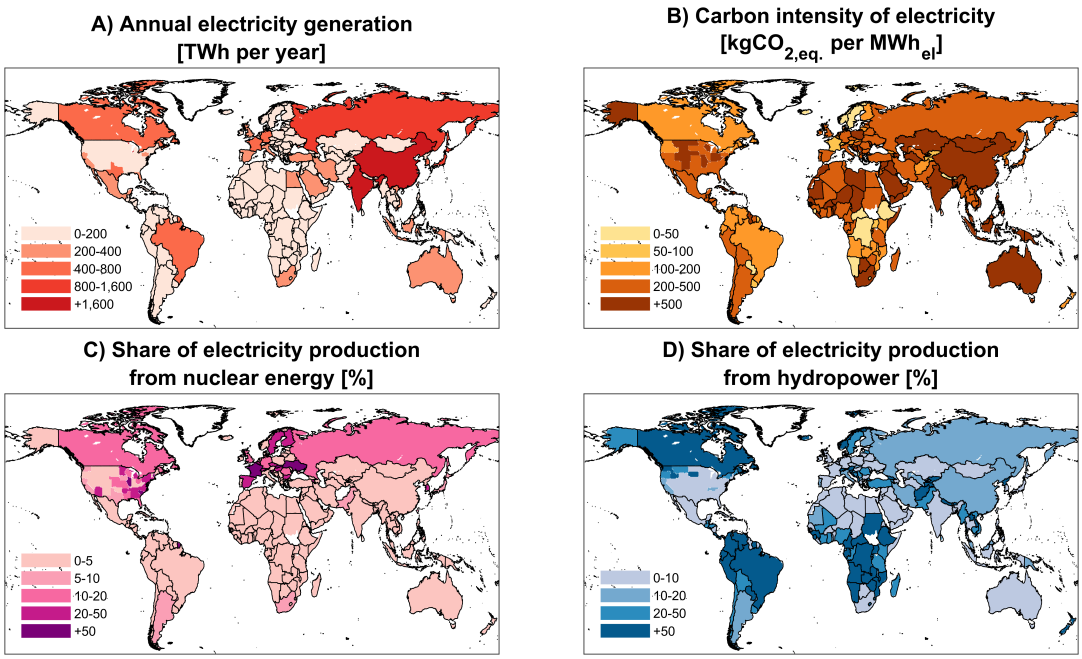


Figure 3.7: Performance of regional electricity grids. A) Annual electricity generation. **B)** carbon intensity (CI) of generated electricity. **C)** Share of electricity production from nuclear energy. D) Share of electricity production from hydropower. Data from [189, 190], adapted from [134].

While certain regions exhibit the potential for high CO_2 removal efficiency, the feasibility of large-scale DAC deployment is limited by both the extensive energy requirements of DAC and the capacity constraints of existing electricity grids—shown in Figure 3.6A. To illustrate, it is estimated that the UK will require up to 100 million tonnes per annum of CO_2 MtpaCO_2 removal by 2050 through engineered CDR methods [192, 193]. Achieving this target exclusively through a fully electrified DAC process—where LT heat is generated using HPs—would require around 200 TWh_{el} per year from the grid. This amount corresponds to around 60% of the current annual electricity generation in the UK, emphasising the need for a significant expansion of low-carbon electricity capacity to accommodate the additional demand required for DAC.

The presented results are based on the CI of regional electrical grids in 2019. However, it is acknowledged that global decarbonisation efforts are ongoing, targeting net-zero electrical grids as early as 2035 for the US and UK and 2050 for a handful of countries and regions such as the EU. This transition could potentially enhance the viability of supplying DAC energy requirements from regional grids in the coming

decades, matching with the anticipated deployment of large-scale DAC facilities. Nevertheless, subsequent sections will explore the potential benefits of supplying DAC with newly developed, dedicated low-carbon energy infrastructure. Such infrastructure, specifically designed for DAC integration, could enable more efficient energy utilisation compared to relying only on future decarbonised electricity grids.

3.5.2 Overview of the techno-economic performance of coupling DAC to different energy sources

Figure 3.8 presents a summary of the $LCOD_{gross}$ results for the six system scenarios—detailed in Section 3.4.3—at the three assumed regional WACC levels and regions shown in Figure 2.3.

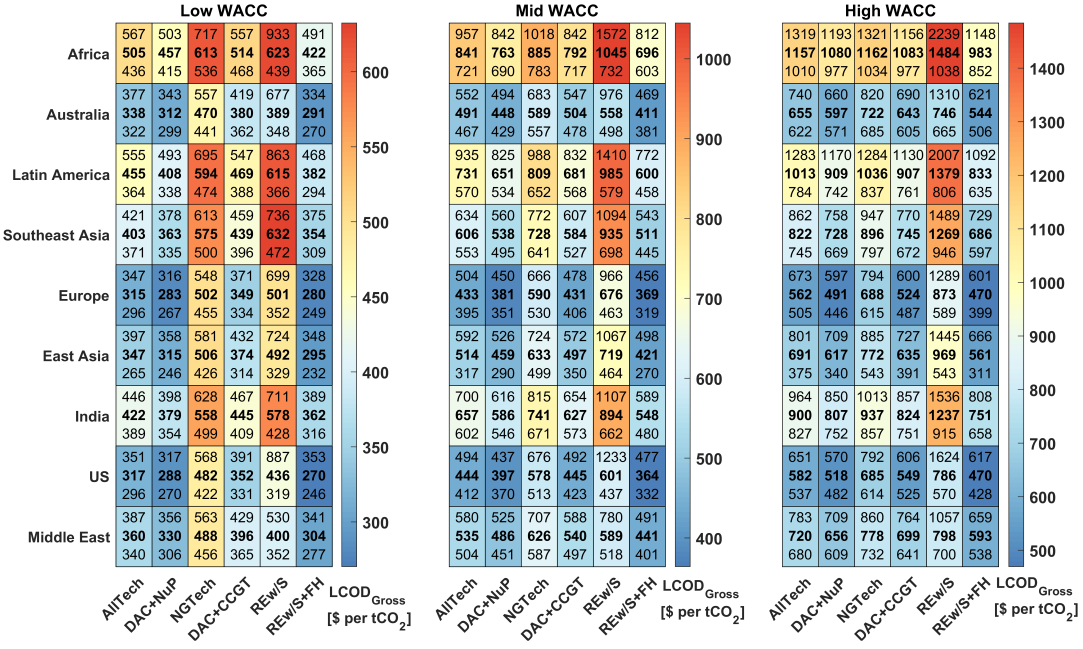


Figure 3.8: Summary of DAC cost for the different considered scenarios. Presented values correspond to $LCOD_{gross}$ for the different regions and WACC assumptions, where the bold middle value is the weighted mean for the region, which also corresponds to the cell's colour. The top and bottom values in each cell represent the maximum and minimum values in each region, respectively. Adapted from [134].

3.5.2.1 All technologies (AllTech) and natural gas with carbon capture and storage (NGTech) scenarios

For the AllTech scenario, the selected system that achieves the lowest $LCOD_{gross}$ in most regions is a system that uses nuclear technology to produce HT heat. Since

electricity co-production by the system is not rewarded in this scenario, the DAC process utilises the HT heat produced by the nuclear reactors to meet its LT heat requirements. This is illustrated by Figure 3.9 for the low WACC scenario. This approach is thermodynamically inefficient, leading to a higher $LCOD_{gross}$ when compared to the DAC+NuP scenario (Figure 3.8).

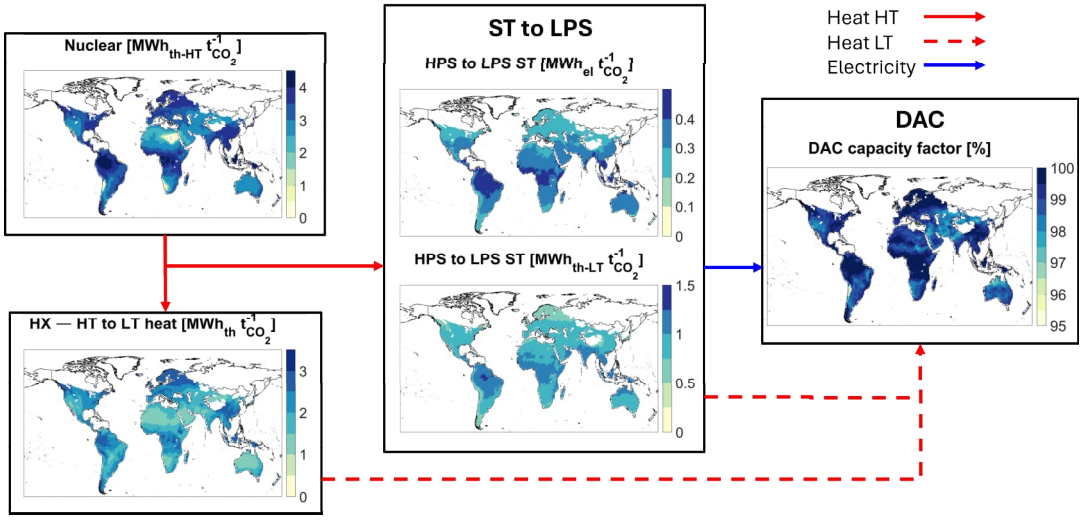


Figure 3.9: Normalised energy flows for the AllTech scenario. The results are based on the regional low WACC assumption. Only technologies of interest are shown. Abbreviation: electricity (el); thermal heat (th); heat exchanger (HX); high-temperature (HT); low-temperature (LT); high-pressure steam (HPS); low-pressure steam (LPS); steam turbine (ST).

Similar inefficiency in using HT heat for LT heat requirements by DAC is also observed in the NGTech scenario since electricity co-production by the system is not rewarded in this scenario. As a result, the $LCOD_{gross}$ for NGTech scenario is notably higher compared to the DAC+CCGT scenario, where the co-production of electricity is rewarded (Figure 3.8).

Additionally, for the NGTech scenario, FB is not found to be a cost-effective solution for the solid sorbent DAC system across all regions and WACC assumptions. Instead, GT is selected, where excess produced electricity—that is not utilised by DAC—is converted to LT heat utilising HPs and EBs to be utilised for DAC LT heat requirements.

3.5.2.2 Nuclear power plant (DAC+NuP) and combined cycle gas turbine with carbon capture and storage power plant (DAC+CCGT) scenarios

Excluding the REw/S+FH scenario, the DAC+NuP scenario emerges as the most cost-effective energy option for DAC across all regions, particularly at low and mid WACC levels. For instance, a relatively low $LCOD_{gross}$ of \$300 per tCO_2 can be achieved at low WACC in Australia, Europe, East Asia and the US. Moreover, at mid and high WACC levels, $LCOD_{gross}$ values of \$400 and \$500 per tCO_2, respectively, are achievable in Europe, East Asia and the US (Figure 3.8).

The DAC+CCGT scenario shows a lower sensitivity to increases in WACC compared to the DAC+NuP scenario. Consequently, as WACC rises, the difference in $LCOD_{gross}$ between the two scenarios diminishes, eventually leading to the DAC+CCGT scenario exhibiting a lower $LCOD_{gross}$. Thus, at the base case NG price of \$50 per MWh_{NG}, in regions with high WACC, such as Africa and Latin America, the DAC+CCGT scenario tends to yield a lower $LCOD_{gross}$ compared to the DAC+NuP scenario, as illustrated in Figure 3.10A.

The sensitivity of the DAC+CCGT scenario to NG prices is illustrated in Figure 3.10A. It is evident that DAC+CCGT presents a more favourable $LCOD_{gross}$ compared to the DAC+NuP scenario below certain NG price thresholds in most regions—e.g., $\leq$\$25 per MWh_{NG} at mid and high WACC. Conversely, when NG prices are high and/or WACC is low (e.g., NG price of $\geq$\$25 per MWh_{NG} and low WACC, or NG price of $\geq$\$50 per MWh_{NG} and mid WACC), the DAC+NuP scenarios demonstrate a lower $LCOD_{gross}$. This is attributed to the higher CapEx ratio associated with the DAC+NuP scenario.

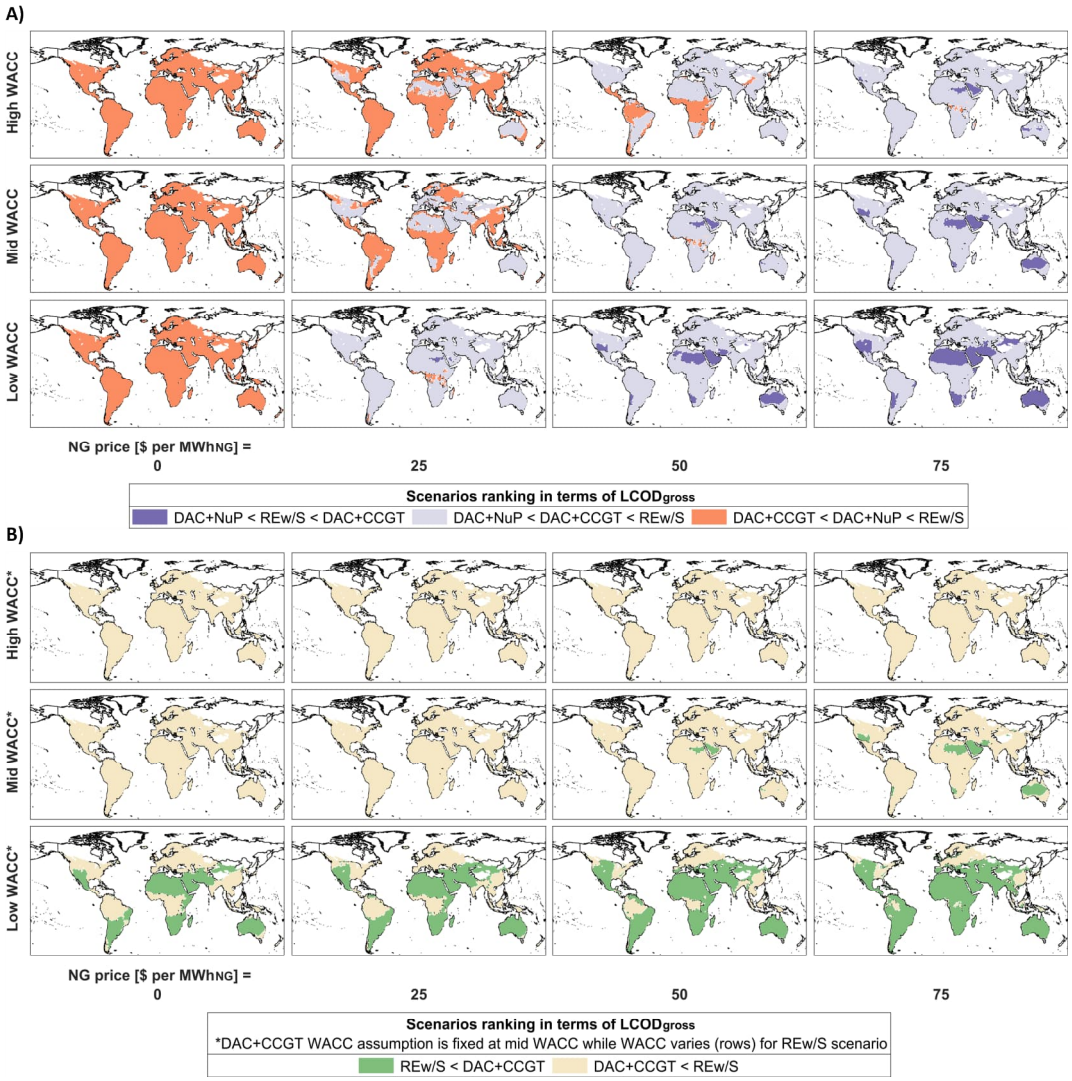


Figure 3.10: Effect of natural gas prices and regional WACC levels on DAC system scenarios. A) Scenarios ranking in terms of $LCOD_{gross}$ at different natural gas (NG) prices. **B)** Scenarios ranking in terms of $LCOD_{gross}$ at different regional WACC levels, where the WACC used for the DAC+CCGT scenario is fixed at mid WACC assumption while WACC varies for the REw/S scenario. NG price of \$50 per MWh_{NG} is assumed for the base case scenario. Adapted from [134].

3.5.2.3 Intermittent Renewable Energy with Energy Storage (REw/S) scenario

The REw/S systems demonstrate superior performance in regions with good solar resources, such as Australia, parts of Europe, the USA and the Middle East, as illustrated in Figure 3.11 at the low regional WACC assumption. Within these regions, REw/S systems can achieve an $LCOD_{gross}$ starting around \$320 per tCO_2. Conversely, the lowest achievable $LCOD_{gross}$ at mid and high WACC is around \$440 and \$540 per tCO_2, respectively, as illustrated in Figure 3.8.

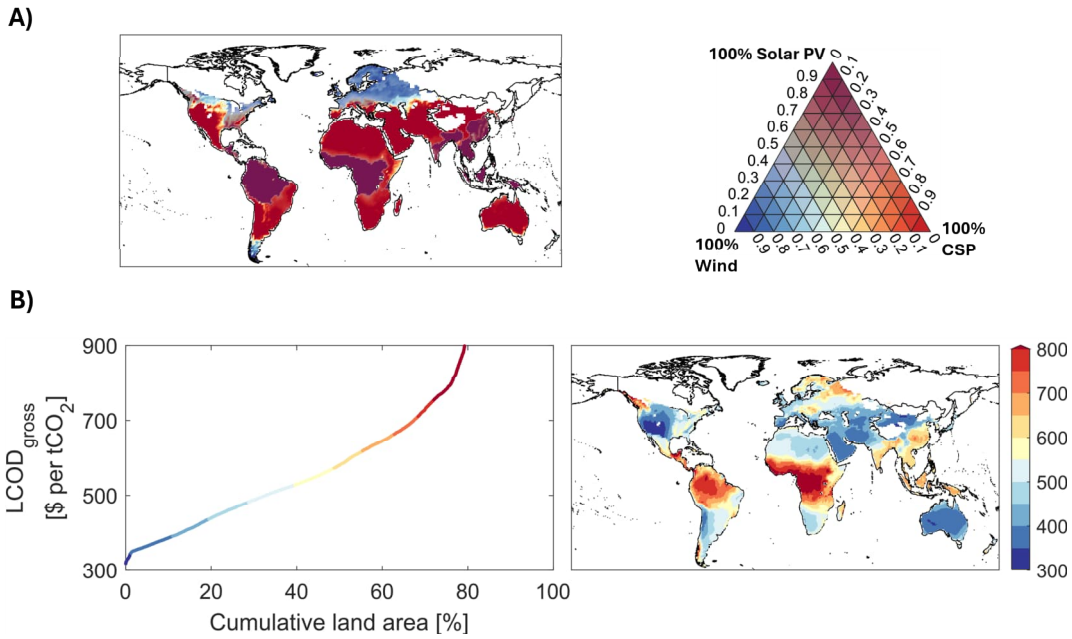


Figure 3.11: Performance of coupling DAC to iRE system with energy storage. **A)** Shows how iRE energy is generated for the REw/S scenario, where different colour corresponds to different ratios as indicated by the ternary plot. **B)** shows the supply curve. Results are based on the low WACC assumption. System configuration is not sensitive to changes in WACC for this scenario. Adapted from [134].

The REw/S system configurations yielding the lowest $LCOD_{gross}$ are predominantly CSP-dominant, hybrid CSP with wind, or hybrid solar PV with wind systems, as shown in Figure 3.11. Across all regions, the integration of energy storage with renewable energy sources is crucial to enabling DAC plants to operate at high CFs—a range of 82–98% for 90% of considered regions—and thus reduce $LCOD_{gross}$. Regions capable of deploying CSP can leverage HT THS, which is significantly more cost-effective than batteries, resulting in lower $LCOD_{gross}$ values.

It is important to note that operating DAC at lower CFs can lead to an exponential increase in LCOD, even though the LCOE from the iRE system with energy storage may decrease at lower DAC CFs, which is demonstrated in Figure 3.12 for the representative locations. This is primarily attributed to the high CapEx associated with DAC systems. Consequently, operating DAC flexibly at low CFs to utilise excess intermittent electricity, as suggested in previous studies [151, 194], proves to be economically unviable.

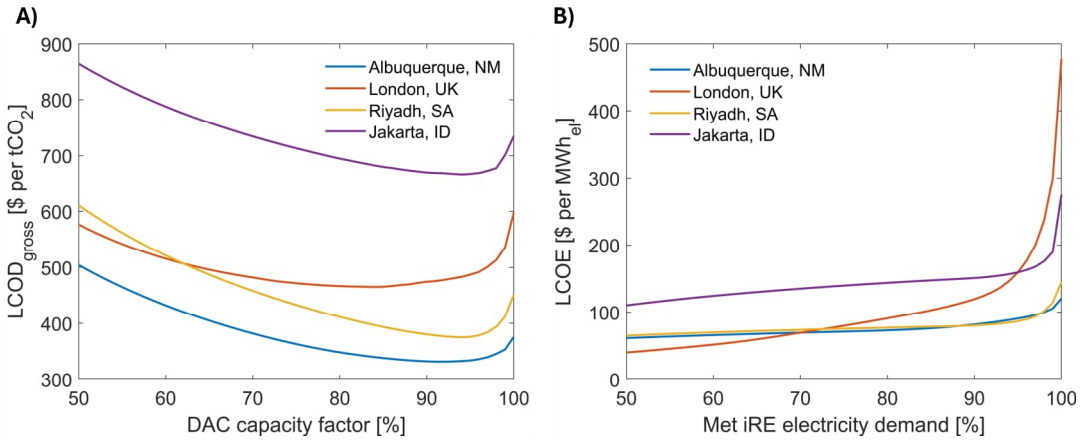


Figure 3.12: Effect intermittency on DAC systems. A) DAC cost ($LCOD_{gross}$) as a function of DAC CF. **B)** LCOE from iRE system with energy storage as a function of met yearly electricity demand. Results are based on system optimisation to minimise cost with CF or meet electricity demand as a constraint. Results are based on the low WACC assumption. Adapted from [134].

In regions with favourable solar resources and low WACC, the REw/S systems demonstrate $LCOD_{gross}$ values comparable to those of DAC+CCGT systems, as shown in Figure 3.8. However, within these regions, areas with a drier climate exhibit even lower $LCOD_{gross}$ for REw/S systems, considering the base case NG price, as shown in Figure 3.10A. As WACC increases, REw/S systems become less economically attractive than DAC+CCGT systems due to the higher CapEx associated with REw/S. However, it is important to note that this cost comparison is also dependent on the assumed NG price. As illustrated in Figure 3.10B, the REw/S system can outperform the DAC+CCGT system in regions with good solar resources when NG prices are high, and WACC levels are low. Furthermore, Figure 3.10B shows that providing lower WACC—i.e., facilitating access to cheaper capital—can enhance the cost-effectiveness of REw/S systems, particularly in comparison to DAC+CCGT systems in this specific scenario.

3.5.2.4 Intermittent renewable energy with energy storage and free heating (REw/S+FH) scenario

The REw/S+FH scenario corresponds to a situation where LT heat is freely accessible or at low cost, such as—in some cases—near geothermal sites or industrial clusters. Additionally, the electricity required to power the DAC fans, vacuum pumps and compressors is provided by the iRE and energy storage system. Among the six energy system scenarios considered, the REw/S+FH scenario yields the lowest $LCOD_{gross}$ for the majority of regions. Under the low WACC assumption, an $LCOD_{gross}$ of $\leq$\$250 per tCO_2 can be achieved in Europe, East Asia and the US, while an $LCOD_{gross}$ of $\leq$\$300 per tCO_2 is achievable in Australia, Latin America and the Middle East (Figure 3.8). However, it is crucial to acknowledge that instances of free or low-cost LT heat would be uncommon and represent a niche application with highly limited availability.

3.5.3 Benefits of co-production of electricity from direct air capture systems

For the DAC+NuP and DAC+CCGT scenarios, the co-production of electricity is allowed. However, the viability of these scenarios depends on the presence of a demand for the generated electricity. Nevertheless, the co-production of electricity allows the system to efficiently utilise the higher quality heat for electricity generation, while the lower grade heat is supplied to the DAC process. This has the potential to enhance the system's overall energy efficiency and reduce CO_2 removal costs compared to scenarios that do not incorporate electricity production.

Table 3.3 presents the performance indicators associated with achieving the lowest $LCOD_{gross}$ in the DAC+NuP and DAC+CCGT scenarios. These indicators represent the minimum required installed nuclear or CCGT capacity necessary to satisfy the DAC process LT heat requirements. The variation in these values is due to regional variation.

Table 3.3: Performance indicators for DAC+NuP and DAC+CCGT scenarios. Ranges are due to regional technologies' performance variation. Adapted from [134].

	Value		**Unit**
DAC+NuP[a]			
instCap ratio	4.0 –5.3		[ktpaCO_2 per MW_{el} rated capacity]
Captured CO_2 to electricity output ratio	0.71–1.05		[tCO_2 captured per MWh_{el} output]
Compared to a stand-alone power plant:			
electricity output	0.50–0.67		[MWh_{el} output per MWh_{el} output from stand-alone power plant]
reduction in electricity production	0.61–1.04		[MWh_{el} from stand-alone power plant per tCO_2 captured]
DAC+CCGT[b]	**Base case**[c]	**Case II**[c]	
instCap ratio	0.80–1.06	0.80–1.06	[ktpaCO_2 per MW_{el} rated capacity]
Captured CO_2 to electricity output ratio	0.09–0.19	0.09–0.12	[tCO_2 captured per MWh_{el} output]
Compared to a stand-alone power plant:			
reduction in fuel-to-electricity efficiency	8.5 –12.5	6.5 –10.0	[%]
reduction in electricity production	0.64–1.17	0.67–1.18	[MWh_{el} output from stand-alone power plant per tCO_2 captured]
NG equivalent	1.16–2.11	1.21–2.13	[MWh_{NG} (LHV) per tCO_2 captured]

[a] For maximum install capacity ratio.

[b] Assumes no methane leakage.

[c] Base case: electricity co-production is minimised. Case II: electricity co-production is maximised.

3.5.3.1 Direct air capture coupled with nuclear power plants

Using the values from Table 3.3, a nuclear power plant with a capacity of 1 GW_{el} can be coupled DAC plant capable of removing 4–5.3 MtpaCO_2, depending on the region (i.e., 4–5.3 ktpaCO_2 per MW_{el} rated capacity). The integrated system would yield an electricity output of 1 MWh_{el} for every 0.71–1.05 tCO_2 captured. Specifically, the electricity output of this configuration represents approximately 50–67.5% of the total power output achievable by a standalone nuclear power plant without DAC integration. This translates to a reduction of 0.61–1.04 MWh_{el} in output from the standalone nuclear power plant when compared to the DAC+NuP configuration for the capture of 1 tCO_2. This reduction can be compared with the electricity requirement of a fully electrified DAC system—where heat pumps provide the DAC process LT heat requirements, which range from 1.45–2.56 MWh_{el} per tCO_2.

The direct coupling of DAC to nuclear plants results in enhanced energy efficiency compared to scenarios without electricity co-generation. This is evident in regions utilising nuclear technology within the AllTech scenario or those relying on an electrical grid with a substantial share of nuclear power. In the latter case, the DAC process LT heat requirements can be met with approximately 60% less energy—i.e., 0.61–1.04 MWh_{el} per tCO_2 compared to 1.45–2.56 MWh_{el}. This is also supported by the higher second-law (exergy) efficiency of 12.1%—20.7% for this scenario configuration compared to other DAC technologies and configurations presented in Table 3.5.

In the design of a system based on the DAC+NuP configuration, the ratio between the capacities of the DAC plant and the nuclear plant can be adjusted to prioritise either increased electricity output or enhanced CO_2 capture. This is illustrated in Figure 3.13 which shows possible ratios of nuclear power plant installed capacity (instCap) to DAC plant instCap as a function of the reduction in electricity output—when DAC+NuP configuration is compared to a standalone nuclear power plant—and the system's captured CO_2 from the atmosphere to electricity output for systems based in Albuquerque, NM and London, UK. The minimum feasible ratio of nuclear power plant to DAC plant instCap, which was presented above, corresponds to the highest instCap ratio observed in Figure 3.13 for Albuquerque and London. Table 3.4 summarises the value for four representative locations.

Table 3.4: Break-even points for selected cases when DAC is coupled to a nuclear power plant (DAC+NuP). Albuquerque, NM and London, UK data can be mostly extracted from Figure 3.13.

	Albuquerque, NM		**London, UK**		**Riyadh, SA**		**Jakarta,ID**	
System design and operation								
instCap ratio [ktpaCO_2 per MW_{el}]	1		1		1		1	
System output [tCO_2 per MWh_{el}]	0.12		0.12		0.12		0.13	
Break-even	**$\triangle$LCOE**[a]	**LCOD**[b]	**$\triangle$LCOE**[a]	**LCOD**[b]	**$\triangle$LCOE**[a]	**LCOD**[b]	**$\triangle$LCOE**[a]	**LCOD**[b]
	0	292	0	294	0	352	0	385
	11	200	12	200	19	200	24	200
	24	100	24	100	31	100	37	100
	36	0	37	0	44	0	50	0
System design and operation								
instCap ratio [ktpaCO_2 per MW_{el}]	4.6		4.4		4.2		4	
System output [tCO_2 per MWh_{el}]	0.81		0.82		0.72		0.83	
Break-even	**$\triangle$LCOE**[a]	**LCOD**[b]	**$\triangle$LCOE**[a]	**LCOD**[b]	**$\triangle$LCOE**[a]	**LCOD**[b]	**$\triangle$LCOE**[a]	**LCOD**[b]
	0	275	0	277	0	335	0	368
	61	200	64	200	97	200	140	200
	142	100	146	100	170	100	224	100
	223	0	229	0	242	0	307	0

[a]Marginal electricity price compared to a LCOE of a power plant that only produces electricity at 100% CF using the same techno-economic assumption in [\$ per MWh_{el}].
[b]$LCOD_{gross}$, i.e., CDR credit price, in [\$ per tCO_2].

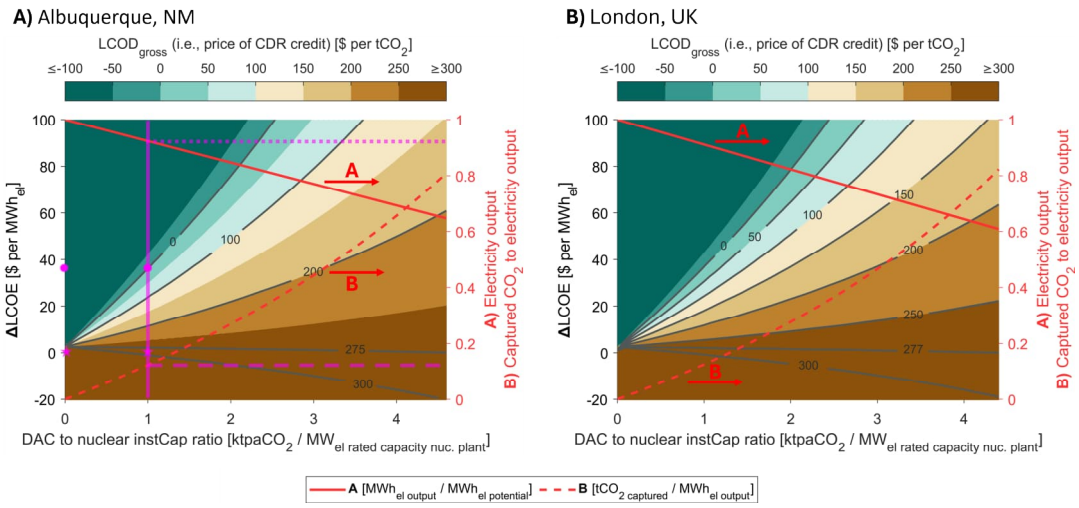


Figure 3.13: Performance of coupling direct air capture to nuclear power plants. **A)** shows the performance for a system that is placed in Albuquerque, NM, while **B)** shows it for London, UK, assuming low WACC assumption. The price of CDR credit is defined as the $LCOD_{gross}$ needed to achieve the system break-even point when co-produced electricity is sold at ΔLCOE, which is the marginal electricity price compared to an LCOE of a nuclear plant that only produces electricity at 100% capacity factor. In these figures, The x-axis corresponds to the feasible installed capacity ratios between a DAC unit and a nuclear power plant. The heat map corresponds to the CDR credit price needed to achieve the system's break-even point for any given installed capacity ratio and ΔLCOE. For example, as ΔLCOE increases for a fixed installed capacity ratio, the CDR credit price needed to achieve the system's break-even point decreases. The right y-axis shows two system's performance indicators that correlate with the installed capacity ratio (x-axis): electricity output, which is the amount of electricity produced from DAC+NuP system compared to a stand-alone nuclear power plant with the same rated capacity in $MWh_{el\ output}$ per $MWh_{el\ potential}$; and captured CO_2 to electricity output ratio, which is ratio between the amount of CO_2 captured by the system and the amount of the system's electricity output in tCO_2 per $MWh_{el\ output}$. The purple marking in subplot A is used to illustrate the example provided in the text below. Adapted from [134].

Analogous to BECCS power plants, the DAC+NuP configuration offers two distinct services: electricity generation and CO_2 removal. Consequently, the total revenue generated by the DAC+NuP system would comprise the combined revenue from the sale of electricity and carbon dioxide removal (CDR) credits.

To evaluate the economic viability of different DAC to nuclear power plant capacity ratios, a costing methodology has been introduced that considers both revenue streams: electricity and CDR credit sales. By utilising Equation 3.38, the $LCOD_{gross}$

and LCOE can be calculated for the system break-even point, considering annualised system cost, the annual system production of captured CO_2 from the atmosphere—CDR credits—and electricity output. The resulting $LCOD_{gross}$ and LCOE values serve as proxies for the CDR credit price and electricity price, respectively, needed for the system to achieve the break-even point.

For a given system's annual output of electricity and CDR credits, it is evident that if the generated electricity is sold at a higher electricity price (a higher $\triangle$LCOE), it would lead to a reduction in the CDR credit price required to achieve the systems's break-even point. In this context, $\triangle$LCOE is defined as the marginal electricity price compared to the LCOE of a nuclear plant operating solely for electricity production at 100% CF, under the same techno-economic assumptions.

Figure 3.13 illustrate examples of the system's break-even point—as CDR credit price and $\triangle$LCOE combinations—as a function of the feasible ratios between DAC to nuclear power plant capacity and the other performance indicators for systems based in Albuquerque, NM and London, UK.

As illustrated in 3.13 (and with the purple marking in Figure 3.13A), considering a 1 $MtpaCO_2$ DAC plant coupled with a 1 GW_{el} nuclear power plant (i.e., 1 $ktpaCO_2$ per 1 $GW_{el\ rated\ capacity}$—the solid purple line in Figure 3.13A) that is based in Albuquerque, NM and London, UK, the system's electricity output is reduced to 92% and 91% (the red line A on the right y-axis and the dotted purple line in Figure 3.13A), respectively, compared to a standalone nuclear power plant operating at 100% CF. This 8%–9% reduction in output electricity is sufficient to meet the energy demands of the 1 $MtpaCO_2$ DAC plant, allowing it to operate at 100% CF and achieve a CO_2 capture rate of 0.12 tonnes of CO_2 per MWh_{el} of electricity output (the red line B on the right y-axis and the dashed purple line in Figure 3.13A). At this specific instCap ratio, if the electricity generated by the DAC+NuP system is sold at LCOE of a standalone nuclear power plant (i.e., $\triangle$LCOE = 0), CDR credit prices of \$292 and \$294 per tCO_2, respectively, are required to reach the break-even point (the purple star markers in Figure 3.13A).

Additionally, achieving a system break-even at a zero CDR credit price is possible if the generated electricity is sold at a premium ($\triangle$LCOE) of \$36 and \$37 per MWh_{el}, respectively (the purple circle markers in Figure 3.13A). In these scenarios, the revenue generated from electricity sales would be sufficient to cover the system's costs. Consequently, any additional revenue derived from CO_2 removal through the

sale of CDR credits could contribute to profit generation. The co-production and sale of electricity thus emerges as a potentially promising business model for DAC, offering a mechanism to finance and facilitate the scaling up of DAC deployment. Table 3.4 summarises the data for similar cases considering the other repressive locations.

Table 3.5: Summary of energy requirements and second-law (exergy) efficiency for different DAC technologies and configurations.

Separation technology	Process/ configuration (reference)	Energy requirements		Work equivalent[a]	Second-law efficiency[b]
		Thermal MWh per tCO_2 (GJ per tCO_2)	Electricity MWh per tCO_2	MWh per tCO_2	%
Absorption	KOH/oxy-fired calciner (theoretical minimum[c])	1.13 (4.05)	0.37[d]	1	12.6
	KOH/oxy-fired calciner (Keith et al. [41])	2.45 (8.81)[e]		1.36	9.2
		1.46 (5.25)	0.37	1.18	10.7
	Amines/stripper with LT heat (Kiani et al. [51])	2.97 (10.7)	0.42	1.91	6.6
	KOH process/BPMED (theoretical minimum[f])		1.03+0.13[g]	1.16	10.9
Adsorption	Solid sorbent/LT heat (Deutz et al. [42], Climeworks—current)	3.31 (11.9)	0.7	2.36	5.4
	Solid sorbent/LT heat (Deutz et al. [42], Climeworks—future target)	1.5 (5.4)	0.5	1.25	10.1
	Solid sorbent/LT heat supplied by heat pumps (Chapter 3)		1.45–2.56	1.45–2.56	4.9–8.7

Solid sorbent/coupled with nuclear power plant (this work)			0.61–1.04	12.1–20.7
Solid sorbent/coupled with CCGT with CCS power plant (this work)			0.64–1.18	10.7–19.7
MgO/oxy-fired calciner (theoretical minimum[c])	0.75 (2.68)	0.37[d]	0.79	16
MgO/oxy-fired calciner (McQueen et al.[76])	1.64 (5.89)[h]	0.37[d]	1.28	9.8

[a]Assuming a 55.6% efficiency of converting natural gas to work and a heat pump coefficient of performance (COP) of 2.

[b]Based on minimum work for separation of 20 kJ per mol CO_2 (0.13 MWh per tCO_2) [195].

[c]Based on the heat of desorption.

[d]To account for an air separation unit and compressing CO_2 to 150 bar.

[e]Calciner thermal efficiency of 77%.

[f]Based on water splitting of 2 mol per 1 mol CO_2 captured at a minimum voltage drop of 0.829 V.

[g]To account for compressing CO_2 to 150 bar.

[h]Calciner thermal efficiency of 46%.

Abbreviation: high-temperature (HT), low-temperature (LT), bipolar membrane electrodialysis (BPMED), natural gas-fired combined cycle gas turbines (CCGT), point-of-source carbon capture and storage (CCS).

3.5.3.2 Direct air capture coupled with combined cycle gas turbine power plants

Table 3.3 presents selected performance indicators for DAC+CCGT systems. In general, the DAC+CCGT system can remove 0.09–0.19 tCO_2 from the atmosphere for every 1 MWh of electricity output. When compared to a standalone CCGTw/CCS power plant, the integration of DAC results in a decrease in power plant efficiency—measured as fuel-to-electricity output from the system—ranging from 8.5%—12.5%. This translates to a reduction of 0.64–1.17 MWh_{el} per tCO_2 captured, or, when converted to the natural gas (NG) equivalent, a reduction of 1.16–2.11 MWh of NG per tCO_2 captured. This case—referred to here as the **base case**—considers the minimum GT CF needed to operate the DAC plant at 100% CF.

In contrast to the base case, case II allows the GT to function at 100% CF to maximise electricity generation. This configuration differs from that shown in Figure 3.5B, as an additional condensing steam turbine (ST) is incorporated, similar to the DAC+NuP scenario shown in Figure 3.5A.

A DAC+CCGT system operating under **case II** generates more electricity compared to the base case. Consequently, it exhibits a lower ratio of CO_2 captured from the atmosphere to electricity output (0.09–0.12 tCO_2 captured per MWh_{el} output) and a smaller decrease in power plant efficiency (6.5–10.0%) when compared to a standalone CCGTw/CCS power plant. The NG equivalent for this reduction in electricity output is 1.21–2.13 MWh_{NG} per tCO_2 captured.

The above NG equivalent values for both cases can be compared with the KOH absorption-based DAC process, which solely utilises NG and has energy requirements of 2.45 MWh of NG per tCO_2 captured [41]. Additionally, it can be seen from Table 3.5 that the coupling of solid sorbent-based DAC to CCGT with CCS power plants–such as in the DAC+CCGT scenario configuration—can achieve higher second-law efficiency of 10.7%–19.7% compared to the KOH absorption-based DAC process, which has an efficiency of 9.2%–10.7%. This highlights the energy efficiency improvement of coupling solid sorbent-based DAC to thermal power plants.

Comparable to the DAC+NuP configuration, the DAC+CCGT scenario provides CO_2 removal and electricity generation. Figure 3.14 illustrates the system's break-even point as a function of ΔLCOE and CDR credit price under varying NG prices for the base case and case II and systems based in Albuquerque, NM and London, UK.

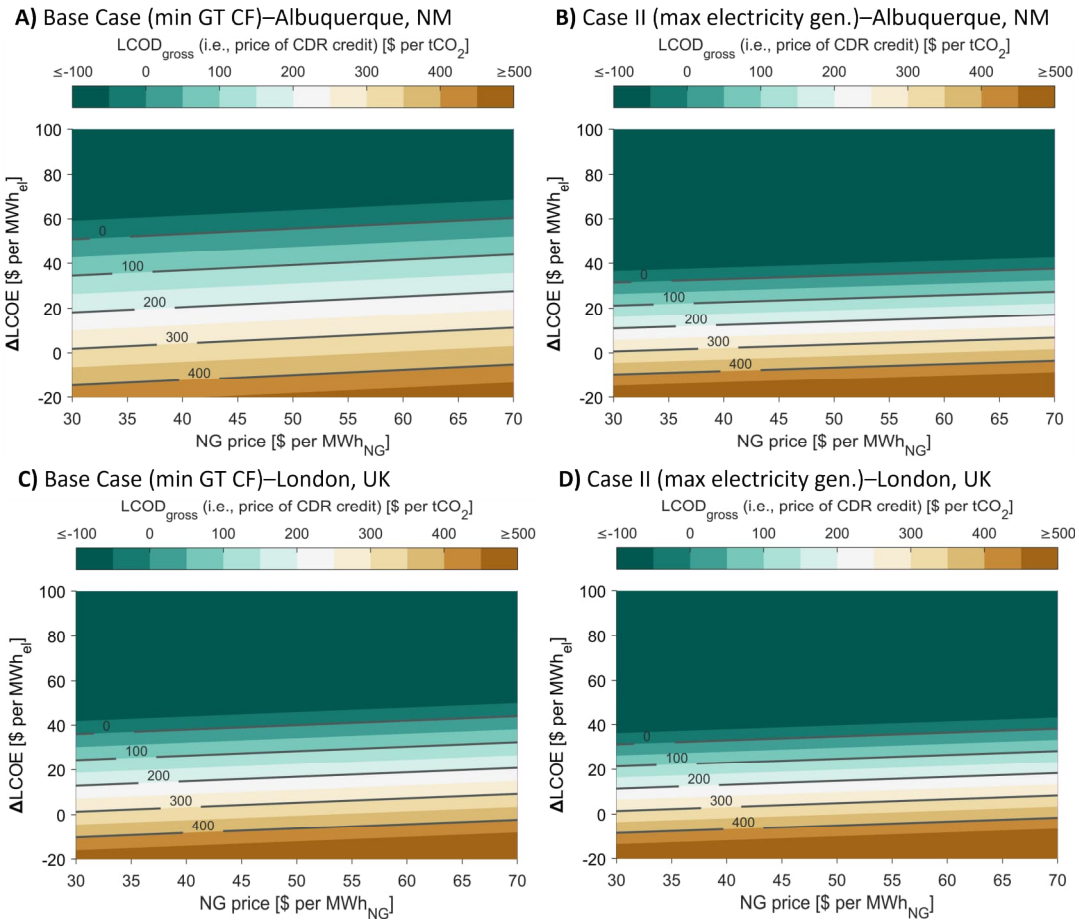


Figure 3.14: Performance of coupling DAC to CCGT power plants. A) and **B)** show the performance for a system operating under base case and case II, respectively, and placed in Albuquerque, NM, while **C)** and **D)** show them for London, UK, assuming low WACC assumption. The price of CDR credit is defined as the $LCOD_{gross}$ needed to achieve the system break-even point when co-produced electricity is sold at ΔLCOE, which is the marginal electricity price compared to an LCOE of a CCGTw/CCS power plant that only produces electricity at 100% CF. The heat map corresponds to the CDR credit price needed to achieve the system's break-even point for any given natural gas (NG) price and ΔLCOE. For example, as ΔLCOE increases for a fixed NG price, the CDR credit price needed to achieve the system's break-even point decreases. Adapted from [134].

Lower NG prices lead to a decrease in the required CDR credit prices to attain the break-even point, assuming the electricity is sold at ΔLCOE of 0. Additionally, a lower ΔLCOE can be achieved for the same CDR credit price to achieve the break-even point for case II compared to the base case. This is caused by the higher electricity-to-CDR credit production ratio for case II. However, this observation holds

true only above the $\triangle$LCOE = 0 line. Operating below this line would require an increase in the CDR credit price to compensate for the electricity being sold negative $\triangle$LCOE. Table 3.6 provides illustrative data points for the two presented DAC+CCGT cases, showcasing different break-even CDR credit and electricity prices for the four representative locations.

The presented scenarios represent the two extremes possible with the DAC+CCGT system configuration, where the CCGT plant operates at the lowest and highest possible CFs that can support the DAC energy requirements operating at 100% CF. However, other potential scenarios exist with varying GT CFs between these two extremes.

There appears to be noteworthy potential for coupling DAC with CCGTw/CCS power plants. In regions with abundant and affordable NG resources, the co-produced electricity could serve as baseload power, partially financing the removal of CO_2 from the atmosphere. Additionally, similar to the DAC+NuP scenario, this system configuration could give rise to new business models and policies. For instance, a policy analogous to the USA's Renewable Fuels Standard—which mandates a minimum volume of renewable fuels in transportation fuel—could be implemented. This policy could demand a minimum supply of CDR credits when generating carbon-neutral electricity from fossil fuels like NG. Such a measure could ensure higher energy utilisation and maximise the co-benefits of fossil fuel usage.

Table 3.6: Break-even points for selected cases when DAC is coupled to a CCGTw/CSS power plant (DAC+CCGT). Albuquerque, NM and London, UK data can be mostly extracted from Figure 3.13.

	Albuquerque, NM		**London, UK**		**Riyadh, SA**		**Jakarta,ID**	
System design and operation: base case[c,d]								
instCap ratio [ktpaCO_2 per MW_{el}]	0.93		0.90		0.85		0.81	
System output [tCO_2 per MWh_{el}]	0.16		0.12		0.18		0.10	
Break-even	**△LCOE**[a]	**LCOD**[b]	**△LCOE**[a]	**LCOD**[b]	**△LCOE**[a]	**LCOD**[b]	**△LCOE**[a]	**LCOD**[b]
	0	340	0	346	0	408	0	447
	23	200	17	200	37	200	25	200
	39	100	28	100	55	100	35	100
	56	0	40	0	73	0	46	0
System design and operation: case II[c,d]								
instCap ratio [ktpaCO_2 per MW_{el}]	0.93		0.90		0.85		0.81	
System output [tCO_2 per MWh_{el}]	0.10		0.10		0.09		0.09	
Break-even	**△LCOE**[a]	**LCOD**[b]	**△LCOE**[a]	**LCOD**[b]	**△LCOE**[a]	**LCOD**[b]	**△LCOE**[a]	**LCOD**[b]
	0	336	0	349	0	399	0	451
	14	200	15	200	18	200	23	200
	24	100	25	100	28	100	32	100
	35	0	35	0	37	0	41	0

[a] Marginal electricity price compared to a LCOE of a power plant that only produces electricity at 100% CF using the same techno-economic assumption in [$ per MWh_{el}].
[b] $LCOD_{gross}$, i.e., CDR credit price, in [$ per tCO_2].
[c] Assumes NG price of $50 per MWh.
[d] Assumes no methane leakage.

3.5.3.3 Direct air capture coupled with intermittent renewable energy with energy storage system

As discussed in Section 3.5.2.3 and illustrated in Figure 3.12, the least $LCOD_{gross}$ solution for the REw/S system configuration is subject to DAC achieving high CFs of >80%. This is accomplished through the use of energy storage technologies and the deliberate oversizing of the system's energy generation components. While this system oversizing can prove more cost-effective at certain hours throughout the year, it also leads to increased energy curtailment within the system, resulting in inefficiencies.

Another instance of inefficient energy utilisation is observed in regions where systems rely on CSP for energy generation. In these regions, a significant portion of the generated HT heat from CSP is directly utilised to meet the DAC's LT heat requirements. This direct conversion results in inefficient energy utilisation, mirroring the situation observed in the AllTech scenario shown in Figure 3.9, which happens due to the absence of any incentives for electricity generation.

This raises the question of whether it is possible to identify improved REw/S system configurations that exhibit more effective energy utilisation and higher technology capacity utilisation while maintaining the same $LCOD_{gross}$. An attempt is made to address this question by comparing the LCOE from two distinct systems: 1) a REw/S system and 2) a stand-alone iRE with an energy storage system dedicated solely to electricity production.

For the REw/S system, the LCOE is calculated based on the marginal annualised cost required to co-produce and provide electricity at specific baseload demand—expressed as a function of the system's CO_2 removal output—and the proportion of electricity demand met by iRE throughout the year, as shown on the y and x-axes, respectively, Figure 3.15. This electricity demand profile can be representative of a continuous chemical process, such as hydrogen electrolysis, where a lower met electricity demand could signify a lower electrolyser CF or situations where unmet demand can be fulfilled through a grid connection.

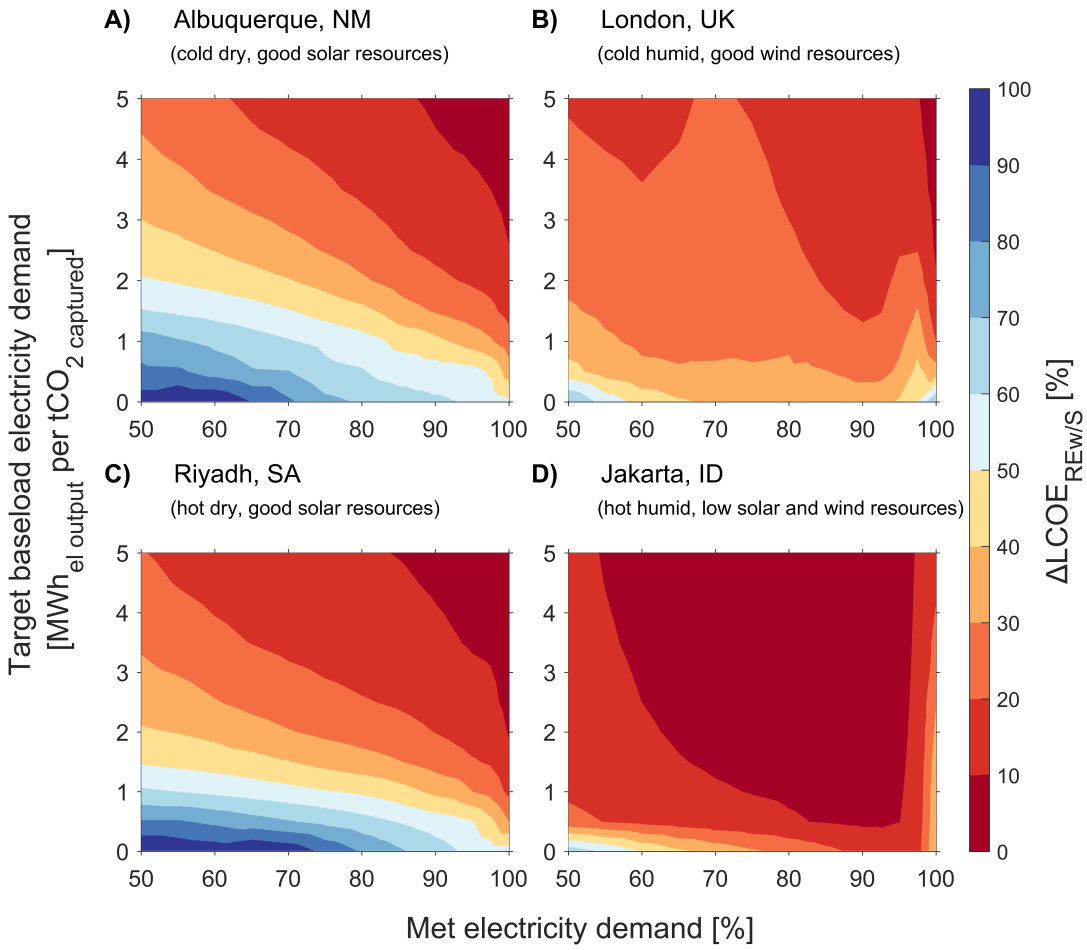


Figure 3.15: Performance of co-producing electricity from DAC coupled with iRE systems. Albuquerque, NM and Riyadh, SA have good solar resources where high electricity reliability—i.e., met electricity demand—is achieved mainly using CSP and THS. London, UK has good wind resources and relatively lower solar resources; thus, high electricity reliability is achieved mainly using a combination of wind, solar PV and batteries. Jakarta, ID has low solar and wind resources and achieves high electricity reliability using solar PV and batteries. Adapted from [134].

For the same data points under examination, the LCOE of the stand-alone iRE with an energy storage system is also calculated. Subsequently, the ratio between the—marginal—LCOE from the REw/S system and the LCOE from a standalone iRE system is calculated. This ratio, denoted as $\Delta LCOE_{REw/S}$, is presented as heatmaps in Figure 3.15 for the four representative locations. A $\Delta LCOE_{REw/S}$ value of 100% signifies a scenario where the electricity produced from an REw/S system has zero marginal cost. Conversely, a $\Delta LCOE_{REw/S}$ value of 0% indicates that the LCOE from a stand-alone iRE system is equivalent to that of the co-produced electricity from the

REw/S system, suggesting no synergistic effect in co-producing electricity from the coupled system with DAC.

The results indicate that comparatively cheaper renewable electricity can be supplied at a moderate target baseload electricity demand and met demand from REw/S systems when compared to iRE systems that solely provide electricity with regions with good solar resources having better performance. This is primarily attributed to the coupled system's capability to store energy as LT heat, which can subsequently be utilised for DAC, and to share the iRE generation capacity, thereby achieving higher technology utilisation.

To contextualise these results, an REw/S system located in Albuquerque, NM, or Riyadh, SA, can supply renewable electricity at a baseload rate of 1 MWh_{el} per tCO_2 captured, with 90% of demand met, at an LCOE approximately 40% lower than a standalone system. In London, UK, the cost savings are roughly 20%, while in Jakarta, ID, the savings are around 10%. For a DAC capacity of 100 $MtpaCO_2$, 90 TWh of electricity can be supplied annually. If this electricity is utilised for hydrogen production via electrolysis, assuming an energy requirement of 60 MWh_{el} per tH_2, 1.5 Mt of hydrogen can be produced annually. This represents approximately 2% of current global hydrogen production [196]. Furthermore, this amount of hydrogen is sufficient to utilise up to 11% of the captured CO_2 in the production of sustainable fuels, assuming a molar ratio of H_2 to CO_2 of 3.

In a more region-specific example, a REw/S system located in Riyadh, SA, can produce electricity at a rate of 0.05 MWh_{el} per tCO_2 captured, with approximately 56% of the electricity demand met and at zero marginal cost. Although identifying a suitable demand for such intermittent electricity might prove challenging, an examination of the met electricity demand profile for this case (Figure 3.16A) reveals a correlation between the times when electricity can be supplied from the system and ambient temperature (Figure 3.16B).

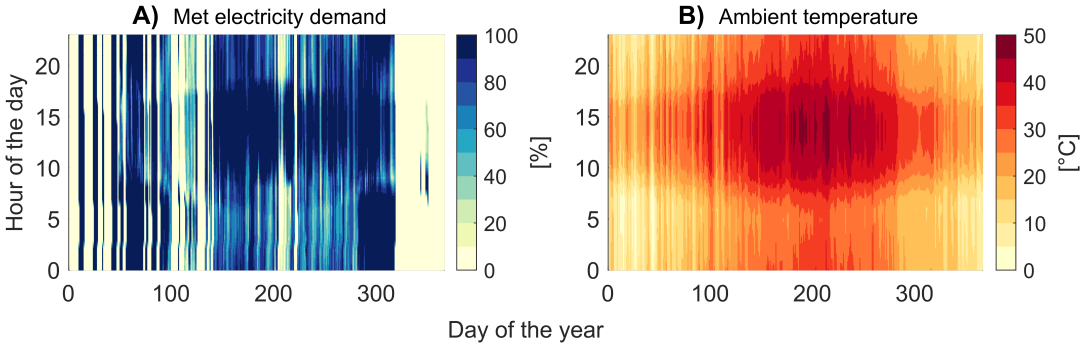


Figure 3.16: Hourly profile for a REw/S system located in Riyadh, SA that is co-producing electricity. Electricity co-production is at a rate of 0.05 MWh_{el} per tCO_2 captured, with approximately 56% of the electricity demand met. Adapted from [134].

The majority of the met electricity demand occurs during high-temperature hours. This correlation is attributed to the fact that days with elevated temperatures are associated with higher DNI, leading to increased HT heat output from the CSP plant. Additionally, this coincides with relatively lower DAC plant energy requirements due to the reduced relative humidity and plant productivity resulting from the higher ambient temperatures. Therefore, the combination of increased CSP HT heat generation and relatively lower DAC plant energy demands creates the possibility of greater electricity generation during periods of higher ambient temperature, which can then be supplied to meet the electricity demand.

In hot regions such as Saudi Arabia, air conditioning and cooling demands can constitute more than 70% of the total electricity consumption. This electricity demand profile correlates strongly with increases in ambient temperature [197, 198]. Therefore, the electricity co-produced by the REw/S system could potentially be supplied to the grid to meet some of the seasonal cooling demands. This would not only enhance the system's energy utilisation efficiency but also reduce the reliance on electricity generated from fossil fuels, thereby mitigating CO_2 emissions.

Based on the considered example, 2.8 TWh_{el} per year could be supplied at a DAC capacity of 100 $MtpaCO_2$. If this electricity were to displace electricity generated from fossil fuels, it could potentially avoid additional CO_2 emissions. For instance, considering the current electricity CI in Saudi Arabia of 571 $kgCO_{2,eq}$ per MWh_{el} [189], this could potentially avoid an additional 1.6 $MtpaCO_2$.

While these figures might appear marginal in this specific case, the subsequent

analysis aims to demonstrate the potential benefits of co-supplying electricity from DAC systems that rely on renewable energy. Identifying and exploiting system synergies in this manner can enhance regional system performance, leading to both economic and environmental co-benefits. Other potential applications for the co-produced electricity include sustainable fuel production, desalination by reverse osmosis, irrigation or powering data centres [199–202].

3.5.4 Direct air capture cost sensitivity analysis

In the previous six considered scenarios achieving an $LCOD_{gross}$ $\leq$\$200 per tCO_2 was not feasible, as shown in Figure 3.8. Here, it is investigated how solid sorbent DAC might achieve a cost target $\leq$\$200 per tCO_2, a goal set by some DAC companies, or even if it would be possible to achieve a cost below \$100 per tCO_2, a target established by the US Department of Energy (DOE) for CDR in general [203–205].

Figure 3.17 presents $LCOD_{gross}$ supply curves at varying DAC collector purchase costs, LCOE and levelised cost of heat (LCOH), based on a DAC plant operating at 100% CF and under the low WACC assumption. In this work, the cost estimate for the DAC collector purchase cost is derived from a material assessment of an industrial design for a solid sorbent DAC collector and a manufacturing method suitable for large-scale production of modular technology, as preliminary presented in Chapter 2. The baseline collector purchase cost was estimated to be \$20k per 1000 kg of sorbent material. Additionally, when the three variables—collector purchase cost, LCOE and LCOH—are held constant, the variation in $LCOD_{gross}$ is attributed to regional differences in DAC performance, which are associated with varying regional climates and WACC.

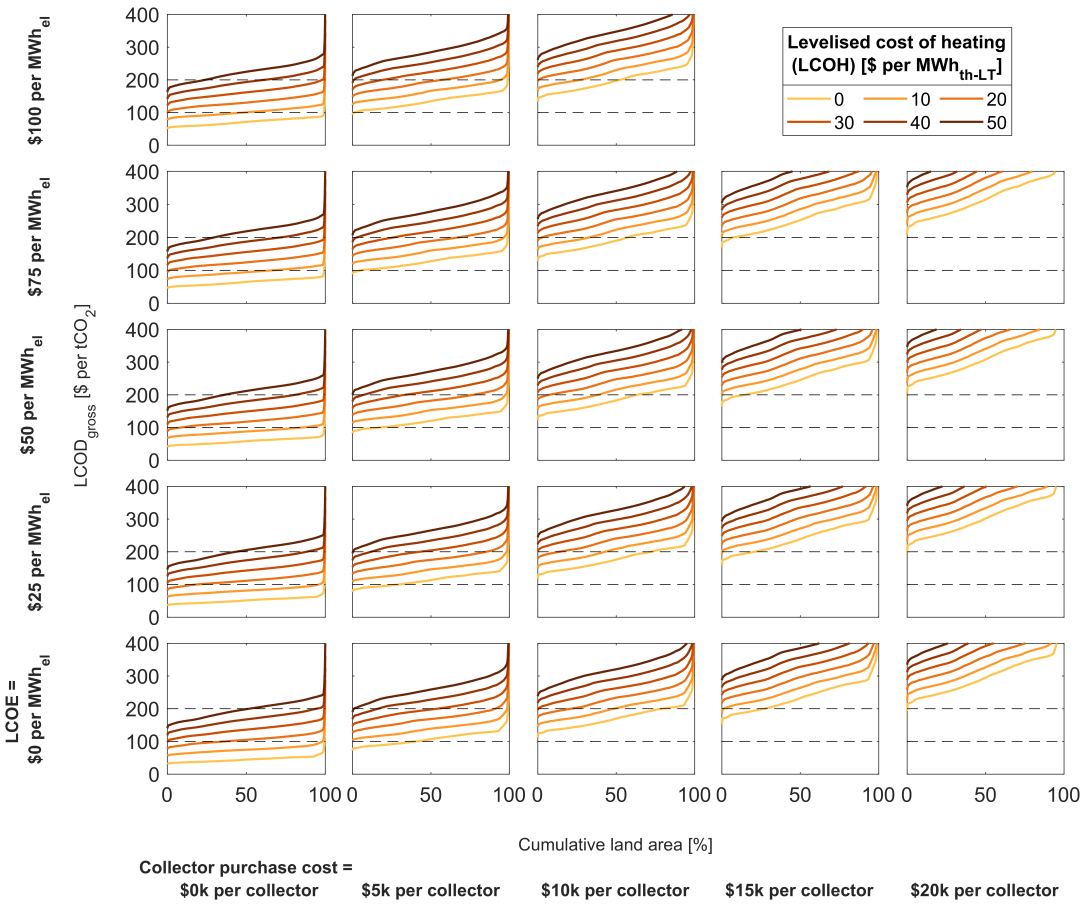


Figure 3.17: Levelised cost of DAC sensitivity analysis. Adapted from [134].

3.5.4.1 Electricity cost

$LCOD_{gross}$ shows less sensitivity to changes in the LCOE compared to the LCOH. This is anticipated, as the LT heat requirements for DAC are 6–14 times greater than its electricity requirements, in terms of absolute values, as shown in Appendix A. To illustrate, if the LCOE increases from \$50 per MWh_{el} to \$100 per MWh_{el} or decreases to \$0 per MWh_{el}, the variation in $LCOD_{gross}$ would be less than ±5% in most locations, assuming a collector purchase cost of \$20k per collector. This variation increases to less than ±10% for a collector purchase cost of \$10k per collector. Consequently, while cheaper electricity would lead to a slight reduction in $LCOD_{gross}$, it is not the primary factor enabling an $LCOD_{gross}$ $\leq$\$200 per tCO_2 for the analysed DAC technology.

3.5.4.2 Heat cost

Due to the high LT heat requirements of DAC, LCOH shows a significant influence on the $LCOD_{gross}$. If LCOH increases from \$25 per MWh_{th} to \$50 per MWh_{th}, $LCOD_{gross}$ can increase by up to 25% and 35% for collector purchase costs of \$20k and \$10k per collector, respectively. Conversely, if LCOH decreases from \$25 per MWh_{th} to \$0 per MWh_{th}, $LCOD_{gross}$ can decrease by 30% and 40% for collector purchase costs of \$20k and \$10k per collector, respectively.

It is worth noting that LCOH is dependent on the quality of the heat. For the quality of LT heat required by DAC, it is anticipated that an LCOH in the range of \$10–\$20 per MWh_{th}—or even lower if inexpensive natural gas is available—can be achieved through thermal power plants, such as nuclear, CCGT and CSP, based on the assumptions employed in this work. For instance, if a nuclear power plant with an LCOE of \$80 per MWh_{el} were modified to partially expand all its HPS to LPS—in steam turbines co-genrating electricity—to meet the specifications for DAC LT heat requirements, the break-even LCOH would be \$12 per $MWh_{th\text{-}LT}$. This calculation does not incorporate the capital costs associated with revamping the power plant and results in an approximate 30% decrease in the nuclear power plant's thermal-to-electrical efficiency. Lower LCOH values might also be attainable if waste heat is available, although such availability would be limited.

A low LCOH will be a crucial factor in achieving an $LCOD_{gross} \leq$\$200 per tCO_2. However, as illustrated in Figure 3.17, even with the availability of free electricity and heat, an $LCOD_{gross} \leq$\$200 per tonne of CO_2 is not feasible in most regions globally at the base case collector purchase cost of \$20k.

3.5.4.3 Collector cost

Reducing the collector purchase cost is identified as a key enabler for achieving an $LCOD_{gross} \leq$\$200 per tCO_2. This cost reduction may be realised through various means, including improvements in the collector's CO_2 productivity, process intensification, the use of cheaper construction materials, sorbent enhancement and improved adsorption bed thermal conductivity through collector or sorbent design modifications.

Estimating a lower bound on the collector cost is inherently uncertain, primarily due to the limited public information available regarding the performance and costs of industrial collectors, such as their physical properties and associated costs. Nev-

ertheless, an attempt is made here to hypothesise on a potentially achievable lower range for the collector purchase cost based on current information. Based on the collector material assessment, using information from patents [65, 66], it is estimated that each collector would require approximately 1 tonne of steel and 0.5 tonnes of aluminium. Assuming steel and aluminium prices of $1k and $2k per tonne, respectively [206, 207], this would result in a total raw material cost of $2k per collector. If the raw material cost is assumed to constitute 20% of the total manufacturing cost—accounting for fabrication, manufacturing facility and labour costs—this translates to a purchase cost of $10k per collector.

To put these numbers into context, the cost of pressure vessels can also be estimated based on the amount of materials required to manufacture them (i.e., vessel weight) [139]. In this context, the pressure vessel material cost can reach as low as 15%–20% of its purchase cost as the vessel approaches the upper range of size (economies of scale) [139]. This is also observed in mass-produced items, where the final cost tends to approach the material cost when manufacturing capacity (or volume) increases.

Furthermore, from a process perspective, a higher collector CO_2 productivity would contribute to lowering the collector cost. While higher productivity can be achieved operationally for the studied DAC system, this approach is not considered here due to the associated increase in energy requirements. Alternative approaches to enhance productivity involve improvements in sorbent or collector design. Several studies have explored how optimising sorbent and collector design parameters—such as mass transfer, thermal conductivity and sorbent density—can lead to increased productivity. However, a definitive upper limit for productivity has not been identified due to the complex interplay between these variables [38, 46, 208]. For example, increasing sorbent density might enhance thermal conductivity but could negatively affect mass transfer—and pressure drop through the bed. Due to these complexities, estimating the future potential collector productivity remains highly uncertain.

Nevertheless, a previous global DAC process sensitivity analysis demonstrated that bed thermal conductivity—expressed as the heat transfer coefficient—has the most significant impact on process productivity [208]. The analysis shows that a 50% improvement in the heat transfer coefficient could result in an average increase of around 20% in process productivity, accompanied by an average reduction of around 10% in thermal energy requirements [208]. Assuming these improvements

are attainable—whether through enhancements in bed thermal conductivity alone or more broadly through sorbent and collector design optimisation—the estimated minimum purchase cost for a collector could potentially be reduced to $8k.

3.5.4.4 Target direct air capture cost

Figure 17 shows that achieving an $LCOD_{gross}$ $\leq$\$200 per tCO_2 is feasible with a collector purchase cost of $10k per collector and low energy costs. For instance, at an LCOE of $50 per MWh_{el} and an LCOH of $20 per $MWh_{th\text{-}LT}$, approximately 8% of the global land area possesses conditions that could potentially yield an $LCOD_{gross}$ $\leq$\$200 per tCO_2. These areas, distributed across Asia, Europe, the USA and Australia, correspond to regions characterised by dry and cool climates and low regional WACC. At this collector purchase cost and LCOE, it can be predicted that even if the process's LT heat requirements were to be improved (represented by a lower LCOH), the lower limit for the $LCOD_{gross}$ supply curve would be $123 per tonne of CO_2 at zero LCOH. It is important to acknowledge that a significant reduction in LT heat requirements might not be feasible due to inherent thermodynamic limitations.

As previously discussed, it is estimated that design improvements in solid sorbent or collector technology could potentially lead to a minimum collector purchase cost of $8k per collector. However, achieving an $LCOD_{gross}$ $\leq$\$100 per tonne of CO_2 requires a further reduction in the collector purchase cost to $5k per collector, coupled with a very cheap LCOH and/or a substantial decrease in the DAC's LT heat requirements. This is illustrated by the $LCOD_{gross}$ supply curve for zero LCOH at a collector purchase cost of $5k and an LCOE of $50 per tCO_2. This curve indicates that some regions with high process productivity and low WACC could potentially achieve an $LCOD_{gross}$ $\leq$\$100 per tCO_2. Nevertheless, attaining such ambitious process improvements might be unrealistic for the current technology without a significant technological breakthrough.

3.5.5 Environmental performance

Table 5 provides a summary of the key environmental metrics for the various DAC system scenarios, including CO_2 removal efficiency, land requirement and water consumption.

Table 3.7: Summary of the environmental performance. Baseline, min and max assumptions are detailed in Appendix C. Adapted from [134].

Scenario	CO_2 removal efficiency[a] [%]			Land requirement [km^2 per MtpaCO_2]	Water consumption[b] [tH_2O per tCO_2]		
	Baseline	Min	Max	Baseline	Baseline	Min	Max
AllTech	≥95	≥95	80–90	0.4– 21.6	(3.5)–(0.4)	(3.5)–(0.4)	(3.5)–(0.3)
DAC+NuP	≥95	≥95	75–85	0.7– 0.9	(3.3)– 1.6	(3.4)–(0.1)	(3.3)– 2.7
NGTech[c]	≥95	≥95	≥95	0.3– 0.5	(2.3)– 0.3	(2.3)– 0.3	0.7 – 2.1
DAC+CCGT[c]	85–95	75–95	≥90	1.6– 2.3	2.2 – 2.7	2.2 – 2.7	9.6 – 17.0
REw/S:							
CSP dominant[d]	80–95	50–85	≥95	20.1– 74.1	(2.9)–(0.4)	(2.9)–(0.4)	(2.9)–(0.4)
Wind dominant[d]	80–≥95	25–95	90–≥95	38.3–158.2	(2.7)–(1.6)	(2.7)–(1.7)	(2.7)–(1.6)
SolarPV dominant[d]	40–75	≤0–15	80–95	54.8–179.5	(3.3)–(1.6)	(3.4)–(1.7)	(2.9)–(1.3)
REw/S_FH:							
CSP dominant[e]	90–≥95	80–≥95	≥95	5.2– 19.8	(3.1)– 0.1	(3.1)– 0.4	(3.1)–(0.3)
Wind dominant[e]	90–≥95	75–≥95	≥95	9.9– 28.8	(3.1)–(0.7)	(3.1)–(0.9)	(3.0)–(0.5)
SolarPV dominant[e]	85–95	55-80	≥95	8.8– 32.1	(3.4)–(1.1)	(3.5)–(1.2)	(3.4)–(1.1)

[a] Due to uncertainties associated with life cycle emissions, values are reported as ranges with 5-unit intervals.
[b] Red values in parentheses are negative values representing that the DAC system is producing water.
[c] Assumes 97% CCS capture rate and no methane leakage.
[d] Technology dominant is defined as the technology normalised energy generation >3 MWh per tCO_2.
[e] Technology dominant is defined as the technology normalised energy generation >0.5 MWh per tCO_2.

3.5.5.1 CO_2 removal efficiency and life cycle greenhouse gas emissions

Scenarios that achieve higher CO_2 removal efficiency emit significantly lower amounts of CO_2 compared to the amount of CO_2 captured from the atmosphere throughout their lifecycle. This effectively reduces the lifecycle GHG emissions that need to be offset to achieve net CO_2 removal. Consequently, such scenarios result in more efficient CDR projects and a smaller increase in $LCOD_{net}$ compared to $LCOD_{gross}$. Scenarios utilising nuclear energy—DAC+NuP and a large portion of the AllTech scenario—achieve very high CO_2 removal efficiencies of $\geq$95%, leading to an increase in $LCOD_{net}$ of less than 5% compared to $LCOD_{gross}$.

The NGTech scenario can also achieve a CO_2 removal efficiency of $\geq$95%, despite its inefficient energy utilisation approach. In contrast, the DAC+CCGT scenario, while benefiting economically from the sale of co-produced electricity, exhibits a lower CO_2 removal efficiency in the range of 85%–95% due to the allocation of generation capacity for additional electricity production.

For REw/S scenarios, regions with good solar resources that utilise CSP can achieve high CO_2 removal efficiencies between 80%–95%. However, this can increase to $\geq$95% at the minimum emissions factors, or drop to 50%–85% at the maximum emissions factors. Regions with low solar resources but good wind resources employ a combination of solar PV and wind turbines and can achieve CO_2 removal efficiencies of $\geq$80%. This efficiency drops below 50% in some regions when considering the maximum emissions factors, rendering these systems economically unviable.

In regions utilising a combination of solar PV and wind turbines, such as in London, UK, systems optimised for minimum $LCOD_{net}$ tend to select less solar PV capacity compared to systems optimised for minimum $LCOD_{gross}$. This is due to solar PV having higher estimated lifecycle emissions than wind turbines.

Consequently, regions with low solar and wind resources that rely heavily on solar PV exhibit low CO_2 removal efficiencies of 65%–75%. This is attributed to the high lifecycle emissions associated with solar PV and the substantial solar PV installed capacity required to compensate for the limited availability of solar irradiation. When considering the maximum emissions factors, some regions employing high levels of solar PV systems would fail to achieve net CO_2 removal over their lifecycle (i.e., the CO_2 removal efficiency falls below zero).

Finally, the REw/S+FH scenario, benefiting from the utilisation of waste heat, demonstrates a superior CO_2 removal efficiency compared to REw/S due to lower energy requirements and technologies installed capacities.

3.5.5.2 Impact of methane leakage

Methane leakage, which can occur during NG production, transportation, processing and distribution, has the potential to undermine the benefits of coupling DAC with CCGTw/CCS.

A sensitivity analysis was conducted for the two regional DAC+CCGT scenarios, shown in Figure 3.18, to illustrate the impact of methane leakage and the CCS capture rate on the overall system's CO_2 removal efficiency and LCOD. This was done assuming a global warming potential over 100 years (GWP-100) of 29.8 [186]. It's important to note that this analysis did not consider infrastructure and construction GHG emissions. The reference base case LCOD assumed a CCS capture rate of 97% and no methane leakage.

As illustrated, methane leakage led to a decrease in the net equivalent CO_2 removal efficiency and an exponential increase in LCOD. With higher methane emissions, the DAC system needs to compensate by removing more CO_2. Consequently, scenarios that consume more NG experience a greater decline in CO_2 removal efficiency due to methane leakage, thus diminishing the value proposition of co-producing electricity. Additionally, the results show the importance of employing high CO_2 capture rates for CCS to minimise residual CO_2 emissions, which would otherwise require additional CO_2 removal by DAC.

In summary, low CCS CO_2 capture rates and high methane leakage rates contribute to increased fugitive emissions. This, in turn, results in higher energy requirements due to the additional CO_2 removal needed, ultimately leading to lower CO_2 removal efficiencies and a higher LCOD. Therefore, for DAC+CCGT systems to be economically viable, it is imperative to ensure high CCS CO_2 capture rates and maintain low methane leakage rates.

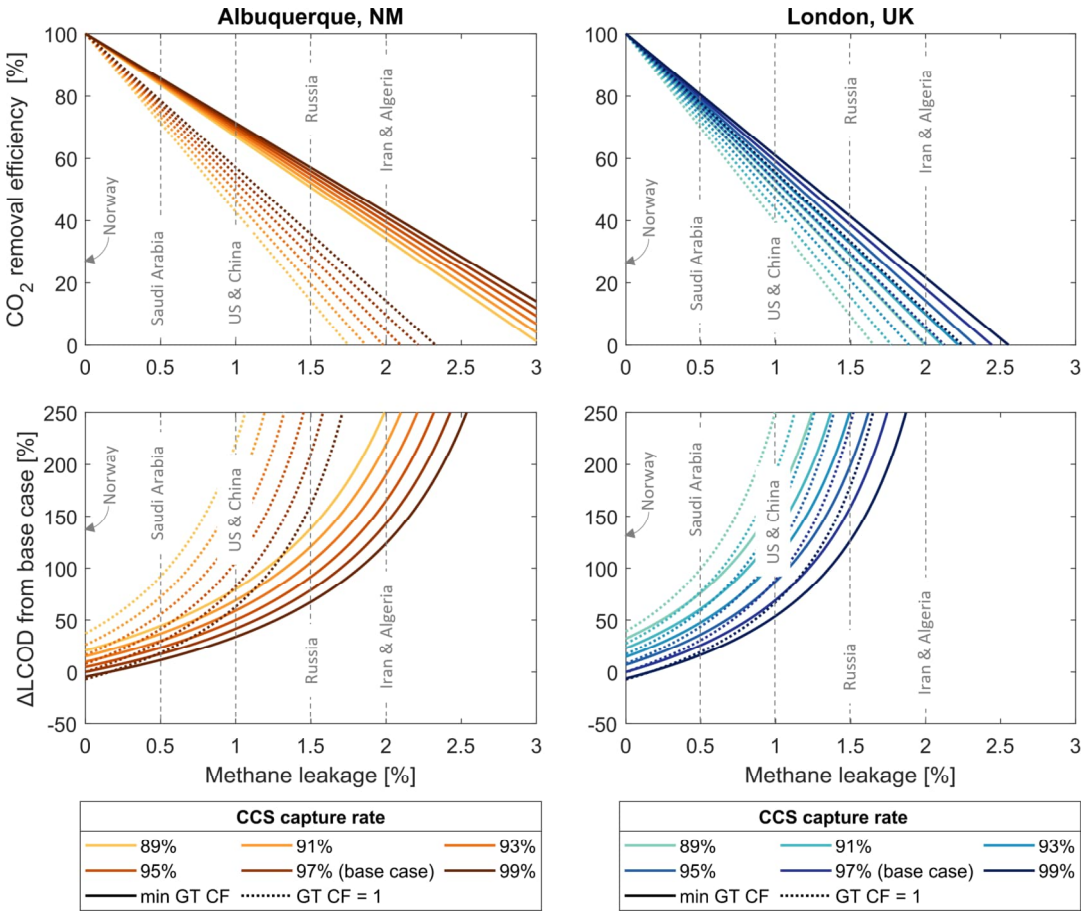


Figure 3.18: Methane leakage and CCS capture rate effect on CO_2 removal efficiency and DAC cost. Results are based on the DAC+CCGT system configuration that is placed in Albuquerque, NM and London, UK. DAC+CCGT base case scenario—shown as min GT CF—assumes minimum electricity co-generation, while case II—shown as GT CF = 1—assumes maximum electricity co-generation. Regional methane leakage is estimated based IEA methane intensity of oil and gas production [209]. Adapted from [134].

3.5.5.3 Land requirement

The land requirements for the different system scenarios are summarised in Table 3.7. It is important to highlight that this land requirement only accounts for the energy supply for DAC and does not include the land footprint of the DAC collectors, as their land requirements are comparatively marginal [114]. For example, current pilot-scale DAC plants require approximately 0.1 km^2 of land per MtpaCO_2 plant capacity [141]. However, innovative DAC collector designs, especially those incorporating vertical orientations, could potentially lead to further reductions in land requirements. Such de-

signs could enable the integration of DAC collectors within the land already allocated for their energy supply. Nevertheless, the practical feasibility of this approach remains to be demonstrated, as factors such as air flow and mixing become paramount in the design of large-scale DAC facilities.

Among the evaluated scenarios, those involving nuclear (e.g., DAC+NuP) and natural gas (e.g., DAC+CCGT) energy exhibit the lowest land requirements. In these scenarios, approximately 700–2,300 km^2 of land is required for the removal of 1 $GtpaCO_2$ using DAC. The cost-optimal locations for these DAC facilities often possess the added advantage of being in proximity to potential geological CO_2 storage sites and existing electricity generation and transmission infrastructure. This observation is supported by the fact that the majority of existing and under-construction nuclear power plant sites globally are situated within 100 km of potential CO_2 storage sites, as shown in Figure 3.19 [210]. Moreover, the nuclear and natural gas scenarios that do not involve electricity co-production—i.e., NGTech and certain regions within the AllTech scenario—demonstrate even lower land requirements due to their inherently smaller system scales.

In contrast, all iRE scenarios entail considerably greater land requirements. For DAC systems integrated with iRE and energy storage, the land requirements are linked to the availability of solar and wind resources. As illustrated in Figure 3.20, regions with high solar irradiation exhibit the lowest land requirements. Specifically, regions where CSP is deployed demonstrate lower land requirements in the range of 20–74 km^2 per $MtpaCO_2$. To provide context, this translates to 20,000–74,000 km^2 per $GtpaCO_2$, an area roughly equivalent to 2–6 times the land area of Qatar. Among all the energy system scenarios evaluated, those reliant on wind turbines exhibit the most extensive land requirements. Lastly, the REw/S+FH scenario, which relies on the availability of free/waste heat, achieves significantly lower land requirements compared to the REw/S scenarios.

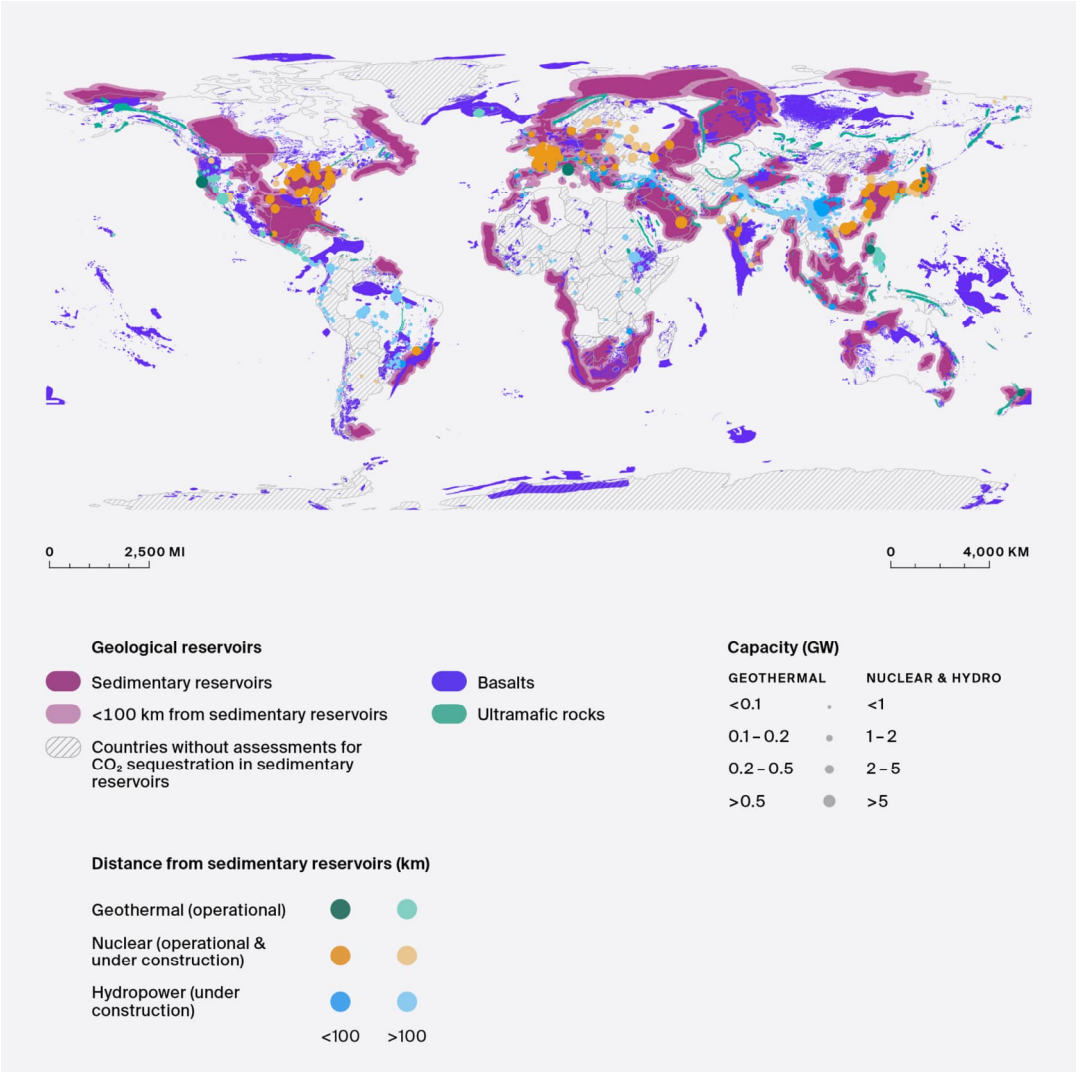


Figure 3.19: Mapping of potential CO_2 storage sites with current and under-construction nuclear power plants. Adapted from Pilorgé et al. [210] under Creative Commons CC-BY 4.0 license.

The deployment of DAC systems coupled with solar PV and wind energy will pose challenges in regions where land availability is constrained. In such regions, alternative energy options with improved land efficiency, such as nuclear or natural gas, would be necessary for large-scale DAC. While solar and wind energy inherently demand substantial land areas, there might be opportunities to enhance land efficiency in regions where land can be utilised for multiple purposes, such as agriculture, in conjunction with iRE generation.

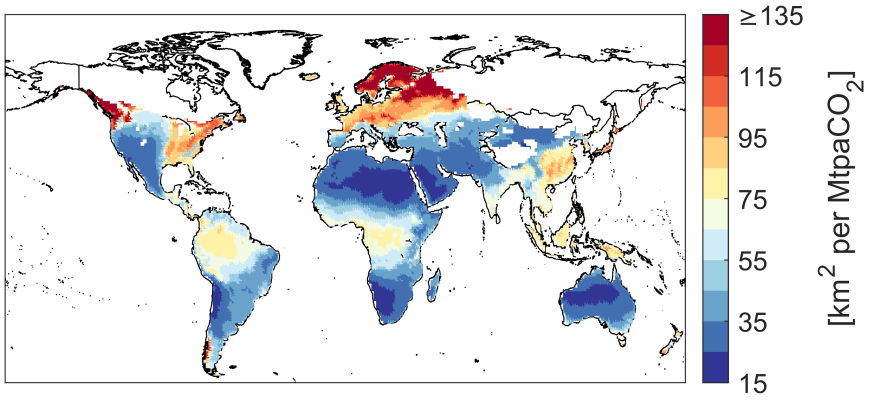


Figure 3.20: Land requirement for coupling DAC to renewable energy and storage system. Adapted from [134].

3.5.5.4 Water footprint

Water consumption can be a critical selection factor for the energy supply used for DAC, particularly in regions facing water scarcity. While solid sorbent DAC processes can generate approximately 0.5–3.5 tH_2O per tCO_2 captured, depending on regional temperature and humidity (Figure 2.15, certain energy production options can exhibit high water consumption. Consequently, the overall water footprint was determined by considering both the water production by DAC and the water consumption by the energy supply. Table 3.7 summarises the water footprint for each energy system scenario. Notably, the majority of scenarios result in a net production of water, with the exception of some nuclear and natural gas cases.

In the AllTech scenario, where nuclear energy is mainly utilised, water is produced in all regions as the DAC system functions as a condenser for the nuclear plant. For the DAC+NuP scenario, water is produced only in humid regions, although at low quantities of 3.3 tH_2O per tCO_2 captured, as some water is consumed for power plant condenser cooling. In dry regions, additional water from external sources is required for condenser cooling, with the maximum requirement reaching up to 2.7 tH_2O per tCO_2. It is important to acknowledge that water consumption is highly dependent on the specific cooling technology employed [211, 212]. With cooling options that have a minimum water consumption value, water production can be achieved in all regions at a rate of 0.1–3.4 tH_2O per tCO_2.

Among the evaluated scenarios, those involving NG technologies (NGTech and DAC+CCGT) exhibit the highest water consumption. The DAC+CCGT scenario has an estimated net consumption of 2.2–2.7 tH_2O per tCO_2 captured. This is attributed to

the combined water consumption of the power plant and the CCS unit. In comparison, the NGTech scenario demonstrates lower water consumption due to the smaller scale of the power plant and CCS process.

All REw/S system scenarios, with the exception of some CSP cases, achieve a net production of water within the range of 0.4–3.4 tH_2O per tCO_2 captured. Furthermore, REw/S+FH system scenarios exhibit lower water consumption, primarily due to their relatively smaller system scales. This is because wind turbines and solar PV panels require minimal water consumption for operation. In the REw/S scenario, for cases involving CSP, the DAC plant functions as a condenser, thereby reducing the water consumption necessary for condenser cooling. In contrast, CSP cases within the REw/S+FH scenario can consume more water, as CSP is utilised for electricity generation using condensing STs.

To put the DAC water production potential in arid regions into perspective, if a 1 $GtpaCO_2$ DAC capacity utilising CSP systems is deployed in Saudi Arabia and is able to produce water at a rate of 1 tH_2O per tCO_2 captured, around 1 billion m^2 of water can be produced annually. This equates to approximately 28% of Saudi Arabia's municipal water demand in 2023 [213, 214], which could meet the water needs of around 9 million people. This calculation only accounts for municipal water demand and assumes a water consumption of 300 litres per person per day, which is the average municipal water demand in the Gulf Cooperation Council (GCC) countries [215].

3.6 Conclusions and future work

This chapter presents a geospatial assessment of different energy supply options for solid sorbent adsorption-based direct air capture (DAC), taking into consideration regional technology performance. Initially, the coupling of DAC to regional electricity grids was analysed, revealing that current grids are not well-suited for large-scale DAC deployment. Consequently, it is concluded that cost-effective and energy-efficient DAC implementation requires the development of new, dedicated energy infrastructure specifically designed to accommodate the energy demands of DAC.

This approach aligns with the current trajectory observed in the low-carbon electrolytic hydrogen production sector within the US and EU, where the addition of dedicated energy infrastructure is being mandated for electrolytic hydrogen to be

classified as low-carbon or green [216, 217]. In the US, this development is being incentivised through substantial measures such as the 45V production tax credit, which offers up to $3 per kg of low-carbon hydrogen produced [218]. These requirements are intended to ensure that the additional low-carbon energy demand from hydrogen production does not inadvertently lead to increased emissions from the grid. This principle of minimising consequential emissions is equally critical in the context of DAC.

Additionally, DAC's integration with new energy infrastructure specifically tailored to support its operations can yield significant improvements in energy efficiency and cost reductions. Illustrative examples include coupling DAC with thermal power plants such as nuclear and natural gas-fired combined cycle gas turbines with carbon capture and storage.

Various nations and private sector entities have recently made significant financial commitments towards the development of large-scale DAC capacity. In the US, the government is investing $1.2 billion to establish two commercial-scale DAC projects, Project Cypress and the South Texas DAC Hub, each with a planned CO_2 removal capacity of up to 1 Mtpa [219]. This investment forms part of a larger $3.5 billion government funding initiative aimed at developing four regional DAC hubs, each with a minimum capacity of 1 MtpaCO_2 [220]. Additionally, the 45Q tax credit offers $180 per t$CO_2$ permanently stored as tax credits for DAC projects [221]. Other notable commercial large-scale DAC projects announced in the US include the Stratos Project, a 0.5 MtpaCO_2 DAC facility with a projected cost of $1.3 billion, which has been attracting investments from the private sector [222, 223].

In the UK, the net-zero strategy encompasses investments of up to approximately $25 billion in the early development of carbon capture and storage (CCS), including DAC and other conventional applications for CCS—e.g., in industry or power generation [224]. Meanwhile, in the Middle East, the UAE's state-owned oil company, ADNOC, is planning to invest $23 billion in decarbonisation projects and technologies, with DAC being a key focus area. ADNOC has also announced a preliminary engineering study for a 1 MtpaCO_2 DAC facility in the UAE [225, 226].

This widespread financial commitment highlights the growing interest in developing large-scale DAC capacity. However, it is crucial to recognise that these substantial public investments and funding are likely to primarily benefit initial DAC projects, often referred to as "anchor projects." These projects are expected to play a pivotal role

in demonstrating the feasibility of DAC technology at a large scale and in bolstering confidence in DAC as a viable carbon dioxide removal (CDR) technology among both private and public sector stakeholders.

3.6.1 Overall performance of different energy supply options for direct air capture

Figure 3.21 presents a comparison chart for the different analysed energy supply options for DAC based on the evaluated performance indicators.

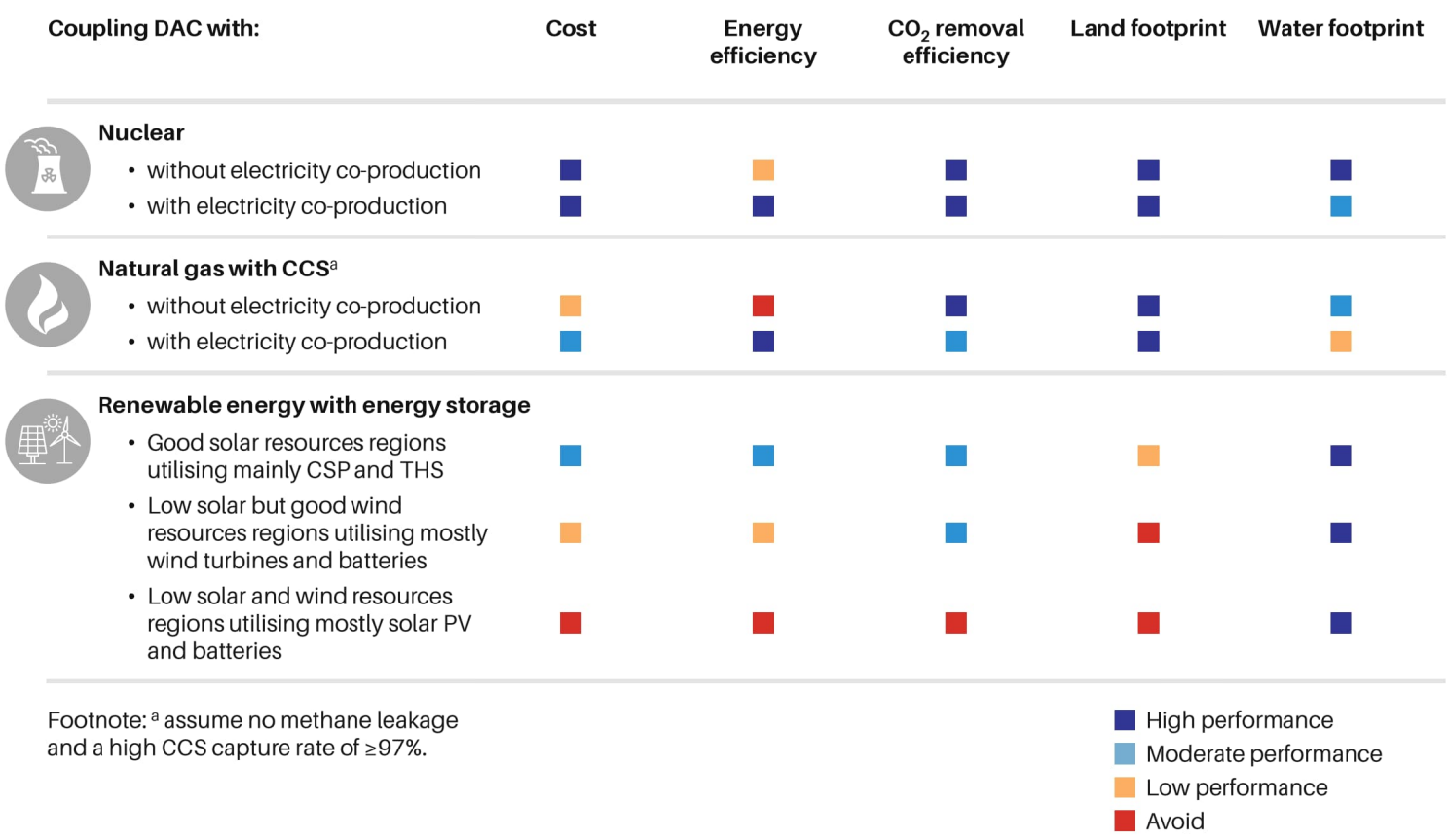


Figure 3.21: Comparison of the different DAC energy supply options. Adapted from [134].

3.6.1.1 Direct air capture with nuclear energy

The coupling of DAC with nuclear power plants where electricity is co-produced, such as in the DAC+NuP scenario, presents the most cost-effective DAC solution across all regions under the low weighted average capital cost (WACC) assumption, achieving a gross levelised cost of direct air capture ($LCOD_{gross}$) ranging from \$246–\$503 per tCO_2. These systems exhibit better energy efficiency compared to DAC coupled with nuclear systems without electricity co-production, as utilisation of high-temperature heat for DAC energy requirements is avoided. Furthermore, these systems can attain very high CO_2 removal efficiencies with a minimal land footprint. Lastly, these systems also have the capability to co-produce water in humid regions, while necessitating water input in dry regions primarily to enhance electricity production.

However, the deployment opportunities for DAC coupled with nuclear energy systems are limited to regions that permit the deployment of nuclear energy and have a demand for co-produced electricity. For instance, certain countries, such as Australia, prohibit the use of nuclear energy, while others are actively phasing out existing nuclear plants due to perceived safety concerns, as exemplified by Germany. Conversely, there exists potential for accelerated deployment of DAC coupled with nuclear energy systems at existing or under-construction nuclear power plant sites, as these regions may have the potential for future nuclear capacity expansion. This potential is attributed to existing valid permits for radioactive activities, greater experience with nuclear power development and the presence of established grid connections.

Moreover, as illustrated in Figure 3.19, the majority of existing and under-construction nuclear power plants are located within 100 km of potential CO_2 storage sites, thus presenting promising locations for DAC deployment [210]. Potential regions for coupling DAC with nuclear energy include the US (e.g., Texas), Europe (e.g., France), the Middle East (e.g., UAE) and Asia (e.g., India and China).

3.6.1.2 Direct air capture with natural gas

The coupling DAC with natural gas-fired combined cycle gas turbines with carbon capture and storage (CCGTw/CCS) power plants, where electricity is co-produced, such as in the DAC+CCGT scenario, demonstrate promising performance under conditions of low methane leakage and a high CCS capture rate—e.g., $\geq$95%. In such scenarios, an $LCOD_{gross}$ ranging from \$314–\$557 per tCO_2 can be attained,

with costs sensitive to natural gas prices.

On the other hand, coupling DAC to natural gas technologies, where electricity is not co-produced, such as in the NGTech scenario, is less efficient from an energy perspective. Nonetheless, this option offers slightly improved CO_2 removal efficiency alongside a reduced land requirement and water footprint, primarily due to its smaller system size compared to DAC+CCGT scenario.

Overall, DAC+CCGT systems possess the potential for both high CO_2 removal efficiency and a low land footprint, with the added economic advantage of generating revenue from the sale of co-produced electricity. However, the deployment of effective DAC+CCGT systems will be limited to regions capable of ensuring a reliable and cost-competitive supply of natural gas with minimal methane leakage, such as in Norway, coupled with the ability to effectively utilise the co-produced electricity.

3.6.1.3 Direct air capture with intermittent renewable energy

The coupling of DAC with intermittent renewable energy (iRE) and energy storage systems depends on the availability of iRE resources within a given region. This can be broken down as follows:

Regions with good solar resources

The most cost-effective DAC systems can be achieved in regions with good solar irradiation when coupling DAC with iRE. Specifically, in certain parts of Asia, Australia, Europe, the US and the Middle East, an $LCOD_{gross}$ as low as \$319–\$352 per tCO_2 can be achieved. These systems leverage concentrated solar power (CSP) with thermal energy storage systems, where DAC can operate at a high capacity factor, reducing levelised costs. Notably, CSP DAC systems have the potential to outperform DAC+CCGT systems, even in the presence of low natural gas prices, provided they are incentivised with a lower WACC. While these systems can achieve high CO_2 removal efficiency, project-specific life cycle assessments are essential due to the considerable uncertainty associated with emission factors. These systems have the ability to co-produce small amounts of water, although the land footprint remains relatively high. Nonetheless, these systems can be strategically deployed in arid and remote areas, preferably near CO_2 storage locations, thus mitigating competition for land utilised for food production, agriculture and other activities.

Regions with low solar but good wind resources

In regions characterised by low solar resources but favourable wind conditions, the most cost-effective DAC systems rely on wind turbines. However, these wind turbine-based DAC systems tend to exhibit lower efficiency compared to CSP DAC systems and necessitate a larger land footprint. This raises concerns about their overall deployment potential in regions with constraints on land availability, where alternative system configurations offering cheaper removal costs and significantly reduced land requirements, such as nuclear or natural gas options, might be more suitable. It is worth noting that the land footprint of wind turbine DAC systems can be substantially reduced if the low-temperature heat requirements of DAC are met by sources that do not require extensive land areas, such as geothermal energy or waste heat. However, the availability of such sources is limited.

Regions with low solar and wind resources

In regions characterised by scarce solar and wind resources, coupling DAC to iRE sources shows low economic viability. The optimised system configuration for such regions would require a comparatively large deployment of solar PV and battery storage capacities, coupled with heat pumps and/or electric boilers to facilitate the conversion of generated electricity into low-temperature heat required for DAC operation. The low levels of solar irradiation inherently constrain operational capacity factors of solar PV in these regions. Furthermore, the CO_2 removal efficiency of these systems can be significantly compromised, and in certain instances, net CO_2—equivalent—removal may not be attainable over the project's lifespan. This low performance is attributed to the relatively high greenhouse gas emissions associated with the supply chain for the production of solar PV components.

3.6.2 Direct air capture cost reduction potential

The conducted sensitivity analysis showed that attaining an $LCOD_{gross}$ of $\leq$\$200 per tCO_2 would require the synergy of several factors:

- Substantial reductions in collector costs—higher than 50%—or an equivalent increase in process productivity.
- Access to low-cost energy sources, for example, electricity prices below \$50 per MWh_{el} and heat prices below $\leq$\$20 per MWh_{th}.
- The availability of low interest rates.

Realising this combination of techno-economic advancements is likely to prove highly challenging. Moreover, reaching the target cost of \$100 per tCO_2, as set by the US Department of Energy for carbon dioxide removal, may be unattainable for DAC without major—and potentially unrealistic—technological breakthroughs.

3.6.3 Limitations and future work

This case study, while comprehensive, possesses certain limitations that warrant further exploration in future investigations. Notably, the present evaluation was confined to adsorption-based DAC technology, specifically employing an amine-functionalised sorbent. This limitation was imposed by the scarcity of information and data pertaining to the performance of diverse DAC sorbents and processes, such as amine scrubbing utilising amino acid salt solutions and moisture swing adsorption.

It is anticipated that as knowledge regarding DAC processes expands and novel sorbents and processes emerge, a better understanding of the regional variations in performance for alternative DAC technologies will be achieved. This enhanced understanding could facilitate the development of DAC systems that are more precisely tailored to specific regions, taking into account the unique performance characteristics of different DAC processes and the availability of various energy supply options.

Future research could expand upon the current work by incorporating the modelling of process transients and optimising operational cycles and process control strategies under dynamic ambient conditions throughout the day and across different seasons.

Additionally, the framework developed in this study can be further expanded to include low-carbon hydrogen production to be coupled with DAC for low-carbon chemical production, such as green methanol or electrofuels.

CHAPTER 4

POLICY ASSESSMENT: IMPLICATION OF HOURLY TIME-MATCHING REQUIREMENT IN HYDROGEN PRODUCTION

4.1 Abstract

This chapter utilises the geospatial modelling framework developed in the previous chapter to explore the implications of policy implementation on electrolytic hydrogen production. Specifically, it analyses the enforcement of an hourly time-matching requirement for grid-connected electrolytic hydrogen production from intermittent renewable energy sources. The framework is used to model grid-connected electrolytic hydrogen production systems by newly built intermittent renewable energy with energy storage capacities under the hourly time-matching constraint, capturing the challenges and costs associated with aligning hydrogen production with fluctuating renewable availability. To account for variability, 20 years of weather data are employed, reflecting inter-annual and intra-annual variations in solar and wind resources and their impact on system design and operational costs when supplying highly reliable baseload hydrogen demand.

Findings indicate that enforcing strict 100% hourly time-matching requirement can significantly increase the levelised cost of hydrogen by \$3.8–\$5.3 per kgH_2, corresponding to a 54–96% increase compared to systems that are powered directly by grid electricity. This cost increase is caused by the additional required capacities in energy generation, electrolysers, and energy storage to mitigate renewable energy

intermittency and ensure agreement with hourly time-matching constraints. The inter-annual variability of renewable energy further increases these costs by requiring additional system redundancies to maintain a consistent hydrogen supply across different years. The study also examines the environmental return on investment of imposing an hourly time-matching requirement. Results show that the CO_2 avoidance cost of enforcing 100% hourly matching can exceed the costs of alternative CO_2 mitigation strategies such as direct air capture. Additionally, as electrical grids continue to decarbonise, the lifetime carbon intensity of 100% grid-powered electrolytic hydrogen decreases, making the strict hourly time-matching less cost-effective as CO_2 avoidance strategy. For instance, in regions with near-term net-zero grid targets, immediate producing hydrogen using only grid electricity can achieve a lifetime carbon intensity comparable to or lower than that of blue hydrogen.

The analysis concludes that while a strict hourly time-matching requirement ensures minimal CO_2 emissions from electrolytic hydrogen, the associated increase in production costs might not justify the environmental return. A modest relaxation of the time-matching requirement can offer a practicable route for scaling up low-carbon hydrogen production, optimising both costs and emission reductions. Priorities should focus on accelerating grid decarbonisation and identifying the most impactful low-carbon hydrogen applications. The results provide critical insights for policymakers and stakeholders in designing cost-effective strategies for scaling up electrolytic hydrogen production and emphasise the importance of a whole-systems perspective in evaluating energy transition pathways.

4.2 Introduction

This chapter utilises the geospatial modelling framework developed in Chapter 3 to explore the implications of policy implementation on electrolytic hydrogen production. Specifically, it analyses the enforcement of the hourly time-matching requirement for electrolytic hydrogen production from intermittent renewable energy (iRE). The analysis addresses both the challenges and the costs associated with matching hydrogen production with fluctuating iRE availability. Understanding these implications is essential for creating smart policies that not only support the transition to net-zero energy systems but also maximise environmental benefits while minimising costs, thereby ensuring an affordable energy transition.

Moreover, the analysis—utilising the developed framework—examines how inter-

annual and intra-annual variations in solar and wind availability, based on 20 years of data, impact system design and costs when highly reliable hydrogen production is required. This aspect highlights the substantial challenges, complexities and costs involved in maintaining consistent hydrogen production from 100% iRE.

The chapter is organised as follows. Section 4.3 presents an overview of the current and future perspectives on the hydrogen economy, a summary of hydrogen production technologies and a review of policies and research on the hourly time-matching requirement. Section 4.4 describes the modified geospatial modelling framework incorporating hydrogen production and different policy scenarios. Section 4.5 discusses the results—highlighting how variations in wind and solar energy availability can influence the system design and costs—and analyses the economic implications of enforcing an hourly time-matching requirement compared with alternative strategies. Finally, Section 4.6 concludes with a summary of the chapter's key findings, discusses the limitations of the current study and outlines potential avenues for future research and policy implications.

4.3 Background

4.3.1 Why low-carbon hydrogen?

Hydrogen plays a significant role in the current global economy, with a global demand of 95 million tonnes per annum of hydrogen (MtpaH_2) in 2022 [227]. Currently, hydrogen production is mainly reliant on fossil fuels, resulting in associated CO_2 emissions of around 900 MtpaCO_2 [227]. The primary applications of hydrogen are in oil refining and various industrial processes.

In oil refining, which accounts for 43% of current usage, hydrogen is used in hydrotreating and hydrocracking processes to remove sulphur impurities and upgrade heavy crude oils [227]. Industrial demand for hydrogen accounts for 56% of current hydrogen usage. Within this industrial sector, 60% is used to produce ammonia via the Haber-Bosch process, which is essential for manufacturing nitrogen-based fertilisers, 30% is used to produce methanol which is used as a feedstock for the petrochemical industry and as a fuel additive, and 10% is used as reducing agent for iron production [227]. The remaining 1% of hydrogen demand is attributed to applications in metal processing, glassmaking and electronics [227].

Due to its versatility as an energy carrier and feedstock, low-carbon hydrogen

is expected to play a role in future global decarbonisation efforts [228]. Projections indicate that low-carbon hydrogen demand could increase to around 500–700 Mtpa by 2050 [227, 229–231]. This significant growth is driven by the potential applications of low-carbon hydrogen in various sectors where hydrogen is not conventionally used, such as in road transport, industrial heating, reductant, sustainable fuels production, energy generation and storage [232, 233].

In transportation, hydrogen fuel cell vehicles offer zero tailpipe emissions and present a viable option for decarbonising the transport sector, particularly for heavy-duty and long-haul applications where battery-electric vehicles face limitations [234–236]. Hydrogen can also be utilised in buses, trains and potentially in maritime and aviation sectors, contributing to broader transport decarbonisation.

In industrial processes, hydrogen can displace natural gas for high-temperature industrial heating, reducing carbon emissions from heat generation [237, 238]. Additionally, sectors such as steel production could adopt hydrogen as a reducing agent to replace carbon-intensive coking coal in direct reduced iron processes, significantly lowering CO_2 emissions [239, 240]. Moreover, hydrogen serves as a building block for synthesising e-fuels and chemicals, aiding in decarbonising aviation, maritime transport and chemical sectors [199, 241, 242].

Hydrogen can further contribute to power generation and storage. It can be combusted in gas turbines for electricity generation, providing a dispatchable and flexible power source that complements iRE [243]. Additionally, hydrogen can enable large-scale energy storage, balancing supply and demand over longer periods and facilitating grid stability [244].

The anticipated expansion in hydrogen applications highlights its potential role in achieving global decarbonisation targets. Nonetheless, the availability of low-carbon and affordable hydrogen production pathways will be essential for hydrogen adoption in different sectors and to realise environmental benefits.

4.3.2 Hydrogen production

The majority of hydrogen production today relies on unabated fossil fuels, predominantly from natural gas (NG)—mainly through steam methane reforming (SMR)—and coal gasification, accounting for 62% and 21% of total production, respectively [227]. The remaining is mainly produced as a by-product in oil refineries and the petrochem-

ical industry, such as from the naphtha reforming process, accounting for 16% of global production [227]. Low-carbon hydrogen production, which is produced through fossil fuels with carbon capture and storage (CCS) and water electrolysis, accounts for less than 1% of global production [227].

4.3.2.1 Steam methane reforming

In SMR, natural gas—primarily CH_4—reacts with steam at high temperatures of around 800–1,000 ℃ and pressure of around 15–20 bar in the presence of a catalyst to produce syngas—H_2, CO and CO_2 [245]. The process involves two main steps:

Steam Reforming

$$CH_4 + H_2O \leftrightarrows CO + 3H_2 \tag{4.1}$$

$$CH_4 + 2H_2O \leftrightarrows CO_2 + 4H_2 \tag{4.2}$$

Water-Gas Shift

$$CO + H_2O \leftrightarrows CO_2 + H_2 \tag{4.3}$$

The typical dry-gas composition after the steam reforming step (Equations 4.1 and 4.2) is around 74% H_2, 15% CO, 8% CO_2 and 3% CH_4. The hydrogen content increases to up to 77%–78% after the water-gas shift step (Equation 4.3 with remaining dry-gas composition: 20% CO_2 and 2–3% CO [246]. After the water-gas shift step, pressure swing adsorption (PSA) technology is typically employed to purify the hydrogen gas from syngas and unreacted CH_4. The SMR process can achieve NG-to-H_2 efficiency of 76% based on the lower heating value (LHV)—not including H_2 compression—and emits 9–13 $kgCO_{2,eq}$ per kgH_2 produced [247–249].

SMR can be coupled with point-of-source CCS, using mature technologies such as amine-based CCS, where the NG-to-H_2 efficiency drops to around 67% [248]. However, this can reduce produced hydrogen carbon intensity (CI) to 1.5–7.3 $kgCO_{2,eq}$ per kgH_2 produced at 90% capture rate and depending on methane leakage [250, 251]. Currently, less than 1 Mtpa of hydrogen is produced globally employing point-of-source CCS [227].

4.3.2.2 Coal gasification

Hydrogen production through coal gasification is mainly used in regions with abundant coal resources, such as China. In this process, coal reacts with oxygen and steam under high temperatures and pressures to form syngas following reactions in Equations 4.4 and 4.5.

Partial oxidation

$$C + \frac{1}{2}O_2 \leftrightarrows CO \tag{4.4}$$

Gasification

$$C + H_2O \leftrightarrows CO + H_2 \tag{4.5}$$

The process has an efficiency of around 55%, which is less than SMR [252]. Hydrogen produced through coal gasification has CI in the range of 22–26 $kgCO_{2,eq}$ per kgH_2, where more than 80% corresponding emissions from the production facility and the remaining correspond to coal mining and supply chain [227]. When CCS is applied to the process, produced hydrogen CI can be reduced to 2.6–6.3 $kgCO_{2,eq}$ per kgH_2 [227].

4.3.2.3 Water electrolysis

Electrolytic hydrogen production, also known as green hydrogen, when powered by renewable energy, offers a low-carbon alternative to fossil-based methods. Electrolysis involves splitting water into hydrogen and oxygen using electricity in an electrolyser. The overall reaction is shown in Equation 4.6.

$$2H_2O_{(l)} \rightarrow H_{2(g)} + O_{2(g)} \tag{4.6}$$

Currently, less than 100 $ktpaH_2$ is produced globally [227]. The limited adoption is primarily due to the higher costs compared to fossil-based methods, largely driven by electricity consumption and capital costs of electrolysers [253]. Electrolytic hydrogen CI is highly dependent on the CI of the electricity used [254]. The main electrolysis technologies used in hydrogen production include alkaline, proton exchange membrane (PEM) and solid oxide electrolysis cell (SOEC) electrolysers.

Alkaline electrolysers are commercially mature (Technology Readiness Level (TRL) 9), with efficiencies—based on LHV—ranging from 58%–77% and capital expenditure (CapEx) in the range of \$500–\$1,400 per kW_{el} [253, 255]. They use a liquid alkaline electrolyte, typically KOH, and non-noble metal electrodes, such as nickel, and operate at low temperatures in the range of 50–80 ℃, pressure of 1–30 bar and low current density of 0.25–0.45 A per cm^2 [256, 257]. These electrolysers are appropriate for continuous hydrogen production where the electricity supply is stable, but can have moderate load flexibility with slower response times [256].

PEM electrolysers are less commercially mature compared to alkaline electrolysers (TRL 8), with efficiencies—based on LHV—ranging from 54%–72% and CapEx in the range of \$1,100–\$1,800 per kW_{el} [253, 255]. They use a solid polymer electrolyte membrane and noble metal catalysts, such as platinum at the cathode and iridium oxide at the anode, and operate at low temperatures and pressure, similar to alkaline electrolysers but with relatively higher current densities of 1–2 A per cm^2 [256, 257]. They exhibit rapid response times, making them ideal for dynamic operation; However, this comes at higher capital costs due to expensive catalysts and membranes [256].

SOEC electrolysers are the least mature among the presented technologies (TRL 5), with efficiencies—based on LHV—ranging from 74%–81% and CapEx in the range of \$2,800–\$5,600 per kW_{el} [253, 255]. They use a solid ceramic oxide electrolyte, commonly yttria-stabilised zirconia, and electrodes compatible with high temperatures [258]. They operate at high temperatures 700–900 ℃, low pressure 1–15 bar and current density of 0.3–1 A per cm^2 [256, 257]. The higher operational temperature allows for increased efficiency; however, this makes the process less flexible and unsuitable for intermittent operation. Additionally, the high-temperature operation results in higher costs due to the need for materials that can withstand elevated temperatures [256].

4.3.3 Low-carbon hydrogen in net-zero strategies

Recognising the potential of low-carbon hydrogen—particularly electrolytic 'green' hydrogen produced using iRE—numerous nations have incorporated it into their strategies for achieving net-zero emissions. To date, more than 40 governments have established hydrogen strategies accompanied by corresponding subsidy programmes [227].

These programmes typically involve substantial financial commitments to low-

carbon hydrogen production, utilising incentives such as production tax credits (PTC) and investment grants to stimulate the development and expansion of production facilities. In contrast, subsidies aimed at consumption are less prominent, though they do exist [227].

For example, the EU's hydrogen strategy under the REPowerEU plan aims to produce 10 Mtpa of green hydrogen domestically and import an additional 10 Mtpa by 2030. These targets are supported by plans to deploy 40 GW of hydrogen electrolysers [259]. The EU has allocated significant funding to support these targets, including over $7 billion (€6.5 billion) from the Innovation Fund for large-scale low-carbon technologies, including electrolytic hydrogen, and $11.6 billion (€10.6 billion) from Important Projects of Common European Interest (IPCEI), including Hy2Tech and Hy2Use, for the production, storage, transport and utilisation of green hydrogen in industrial applications [260–262].

In the UK, the government has committed to establishing 10 GW of low-carbon hydrogen production capacity by 2030, with 6 GW expected to come from green hydrogen. Government support exceeding $27 billion (£21 billion) has been announced to enable these targets [263, 264].

In the US, targets have been set to produce 10 Mtpa of low-carbon hydrogen by 2030, increasing to 50 Mtpa by 2050. Significant incentives support these targets, such as the Section 45V PTC, under which up to $3 per kgH_2 is provided, subject to the produced hydrogen meeting increasingly stringent CI qualifying criteria [217, 218]. However, only two states—Colorado and Illinois—have announced end-use tax credits of up to $1 per kgH_2 [265, 266]. Additional federal support includes up to $7 billion for establishing regional low-carbon hydrogen hubs and a $1 billion budget allocated for end-use subsidies [267, 268].

In Asia, India has announced a strategy to develop a production capacity of at least 5 Mtpa of green hydrogen by 2030. This initiative is supported by government incentives of $2.1 billion (INR 175 billion), aimed at promoting local electrolyser manufacturing and green hydrogen production [269, 270]. Similarly, members of the Gulf Cooperation Council (GCC)—including Saudi Arabia, the UAE and Oman—have set plans to independently produce at least 1 Mtpa of low-carbon hydrogen by 2030, with Saudi Arabia allocating a government grant of $2.75 billion to support the NEOM green hydrogen project [271–273].

While these strategic initiatives primarily focus on increasing low-carbon hydrogen production in anticipation of growing demand, establishing such production capacities may not effectively reduce CO_2 emissions without identifying and developing cost-effective and scalable applications for hydrogen.

4.3.4 Policies and considerations around electrolytic low-carbon hydrogen production

The production of electrolytic low-carbon hydrogen using iRE can be achieved through two primary configurations: off-grid systems and grid-connected systems.

4.3.4.1 Off-grid systems

Off-grid systems are entirely independent of the regional electrical grids, sourcing electricity exclusively from a dedicated iRE system. This can offer inherently low CI hydrogen since the electricity is generated from renewable sources without grid electricity input, resulting in hydrogen that often qualifies as "green hydrogen". Additionally, the direct coupling of renewable energy sources simplifies the verification process for renewable energy use, facilitating compliance with certification schemes [19, 274].

However, off-grid systems face the challenge of the intermittency and variability of iRE sources. This can lead to fluctuating hydrogen production rates unless energy storage systems are integrated. Additionally, backup generation might also be required to meet electrolysers' electricity demand during periods of low iRE availability. These reasons can increase hydrogen production costs significantly [19, 274].

4.3.4.2 Grid-connected systems

Grid-connected systems source electricity from the electrical grid, which may include a mix of renewable and non-renewable energy sources. Electrolysers in this configuration can operate continuously or flexibly, depending on electricity pricing and grid signals [243]. Advantages of grid-connected systems include enhanced utilisation rates due to access to grid electricity, allowing for higher electrolyser utilisation and improving economic viability. Grid-connected systems can also be scaled more easily, leveraging existing grid infrastructure.

Challenges associated with grid-connected systems involve variability in the CI of the hydrogen produced, as it depends on the grid's energy mix, which may include

fossil fuel-generated electricity, potentially increasing emissions. Additionally, demonstrating the renewable content of grid electricity used for hydrogen production may require complex tracking and certification mechanisms. This complexity raises the question of how to effectively classify hydrogen produced in such systems as low-carbon, leading to the development of three key qualifying requirements: additionality (or incremental generation), spatial-matching and temporal-matching [217, 275].

4.3.4.3 Qualifying Requirements for grid-connected low-carbon hydrogen

Additionality (or incremental generation)

Additionality refers to the concept that renewable electricity used for hydrogen production should be sourced from new renewable energy capacity that is additional to what would have been deployed without the electrolyser's demand. This requirement aims to prevent the diversion of existing renewable energy from other uses, which could lead to no net reduction in emissions [217, 275].

Spatial matching

Spatial matching requires that the renewable energy used for hydrogen production is generated within the same geographic area or grid region as the electrolyser. This criterion aims to ensure that the renewable electricity is physically deliverable to the electrolyser, considering grid constraints and transmission losses. Additionally, Spatial matching influences the location of electrolysers, encouraging placement near renewable energy sources or in regions with high renewable resources. This approach can facilitate the localisation of hydrogen production, thereby supporting regional economies, mitigating social impacts—such as reducing the land area required for long-distance energy transmission—and ensuring compliance with locally mandated standards [217, 275].

Time matching

Time matching mandates that the consumption of renewable electricity for hydrogen production occurs simultaneously or within a specified time window relative to its generation. This requirement ensures that hydrogen production aligns with periods of renewable energy generation, reinforcing the use of actual renewable generation rather than relying on grid electricity. Some policies advocate for hourly matching, where hydrogen production must correspond to renewable generation on an hourly basis. Other regulations may allow for daily or monthly matching to provide more

operational flexibility while still promoting renewable integration. At present, the US mandates yearly time-matching, whereas the EU enforces stricter monthly time-matching requirements. However, it appears that both regions will require hourly time-matching in the future, with the US proposing its implementation from 2028 and the EU mandating it from 2030 [217, 275, 276].

4.3.5 Current understanding of the hourly time-matching requirement and its implication in reducing CO_2 emissions

There are different views regarding the strictness required for time-matching requirements needed to qualify grid-connected hydrogen production as low-carbon. For instance, Ricks et al. [277] found that annual time-matching can result in hydrogen CI above that of unabated fossil fuel-based hydrogen—grey hydrogen—and that 100% hourly time-matching is needed, while Zeyen et al. [278] showed that annual time-matching, when coupled with a flexible operation of electrolysers and hydrogen storage, can still achieve emission reductions. Giovanniello et al. [279] build upon these findings, arguing that the effect of hourly time-matching requirement on emissions reductions depends on the specific modelling of additionality, which may vary between competing and non-competing frameworks.

Despite these debates, a consensus is emerging, as highlighted by the conclusions of Zeyen et al. [278] and Giovanniello et al. [279], suggesting that a phased approach to time-matching requirements could balance emission reductions. In the initial phases of scaling up electrolytic hydrogen production, more relaxed time-matching criteria, such as yearly time-matching, could be sufficient in limiting emissions without hindering scale-up efforts. This is because the demand for low-carbon electricity for hydrogen production will remain marginal compared to the total additional low-carbon electricity in the grid. As the low-carbon electricity demand increases, stricter time-matching requirements, such as hourly, can be introduced to mitigate emissions effectively. Ultimately, as the electricity grid becomes increasingly decarbonised, the relevance of time-matching criteria may diminish, negating its impact. Specifically, Mac Dowell et al. [251] showed that until the electricity grid's CI is reduced to below 30–70 $kgCO_{2,eq}$ per MWh_{el}, utilising low-carbon power to decarbonise the grid provides better CO_2 avoidance than utilising low-carbon power for electrolytic hydrogen production.

In this chapter, the implication of mandating a strict 100% hourly time-matching

on iRE is explored in terms of costs and environmental benefits, showing that a strict 100% hourly time-matching requirement could inadvertently inflate the required additional installed capacity for both energy generation and storage technologies, diverting crucial capital resources from other emissions-reduction investments and unnecessarily increasing the cost of electrolytic low-carbon hydrogen and associated emission reduction.

4.4 Methodology

The main objective of the modelling in this analysis is to evaluate the techno-economic and environmental implications of enforcing an hourly time-matching requirement on grid-connected electrolytic hydrogen production supplying baseload hydrogen demand. To address this objective, the geospatial modelling framework presented in Chapter 3 is used to model grid-connected electrolytic hydrogen production using newly built intermittent renewable energy (iRE) with an energy storage (iRE+ES) system with an enforced hourly time-matching requirement. Additional equations required to model hydrogen production based on the hourly time-matching requirements are presented in Section 4.4.1 , while the performance indicators used to evaluate different cases are presented in Section 4.4.2.

The spatial and temporal representations from Chapter 3 are also utilised here. However, 20 years of NASA's MERRA-2 data are employed in this analysis to capture how inter-annual and intra-annual variations in solar and wind availability from year to year can impact system design and costs when highly reliable—baseload—hydrogen production is required.

4.4.1 Grid-connected electrolytic hydrogen production modelling

Following the Resource-Task Network (RTN) framework, Figure 4.1 shows the key technologies and resources included in the hydrogen production model. Electricity can be generated iRE through wind turbines, solar photovoltaic (PV), or concentrated solar power (CSP) through steam turbines. Additionally, electricity can be imported or exported from regional electrical grids. This electricity can be used in electrolysers to produce hydrogen at 20 bar, which is then compressed to 40 bar—suitable for low-pressure hydrogen distribution networks. Hydrogen is assumed to be supplied at a constant flow rate to end users. Energy storage technologies—including thermal heat storage (THS), battery and hydrogen storage—are incorporated to balance

renewable energy intermittency.

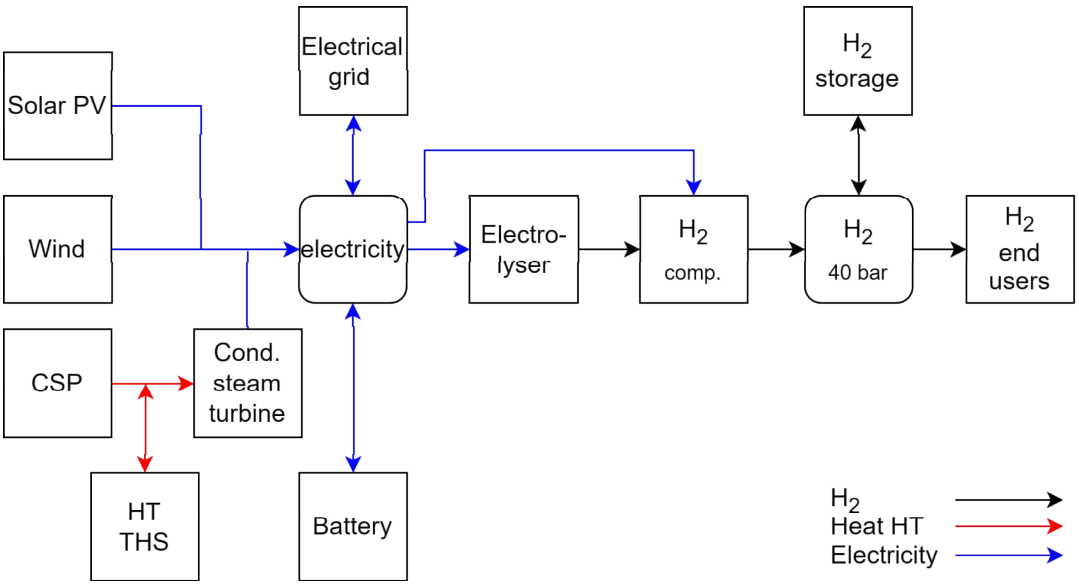


Figure 4.1: Hydrogen production system representation using RTN framework. The model components include tasks—technologies—shown as boxes with sharp corners, and resources, shown as boxes with rounded corners. The coloured lines and arrows correspond to different material and energy type and their flow direction. Abbreviations: compressor (comp.), condensing (cond.), concentrated solar power (CSP), high temperature (HT), thermal heat storage (THS). Adapted from [280].

4.4.2 Mathematical formulation

4.4.2.1 Model constraints

Chapter 3 (Section 3.4.4) presented model constraints for technologies' install capacity, iRE generation and energy storage. This section presents additional model constraints required to model hydrogen production and grid connection.

Hydrogen mass balance

The hourly hydrogen mass balance is defined by Equation 4.7, which balances the hourly produced hydrogen from the electrolysers ($gen_{\text{AWS},H_2,h}$)—based on alkaline technology—and hourly hydrogen charged ($char_{H_2\_\text{tank},H_2,h}$) and discharged ($dish_{H_2\_\text{tank},H_2,h}$) from hydrogen storage with the hourly hydrogen exported from the system ($export_{H_2,h}$), which is based on a baseload hourly demand profile.

$$\left(gen_{\text{AWS},H_2,h}\right) + \left(dish_{H_2\_\text{tank},H_2,h} - char_{H_2\_\text{tank},H_2,h}\right) = export_{H_2,h}, \quad \forall h \tag{4.7}$$

Hydrogen electrolyser

The hourly hydrogen production from the electrolysers in terms of LHV ($gen^{\text{LHV}}_{\text{AWS,H}_2,h}$) is shown in Equation 4.8, which is a function of hourly electricity produced by electrolyser ($cons_{\text{AWS,el},h}$) and the electrolyser efficiency (η_{AWS}) which is assumed to be 61% based on LHV [238, 281]. Equation 4.9 is used to convert the hourly hydrogen production from LHV to mass terms using hydrogen LHV (LHV_{H_2}), which is 33.33 kWh per kgH_2.

$$cons_{\text{AWS,el},h} \times \eta_{\text{AWS}} = gen^{\text{LHV}}_{\text{AWS,H}_2,h}, \quad \forall h \tag{4.8}$$

$$gen^{\text{LHV}}_{\text{AWS,H}_2,h} = gen_{\text{AWS,H}_2,h} \times \text{LHV}_{\text{H}_2}, \quad \forall h \tag{4.9}$$

The electrolyser is assumed to produce hydrogen at temperature ($T^{\text{in}}_{\text{H}_2\text{\_comp}}$) of 60 ℃ and pressure ($P^{\text{in}}_{\text{H}_2\text{\_comp}}$) of 20 bar, which is then compressed to the compressor outlet pressure ($P^{\text{out}}_{\text{H}_2\text{\_comp}}$) of 40 bar. The hourly compressor electricity requirement ($cons_{\text{H}_2\text{\_comp,el},h}$) is calculated using Equation 4.10, assuming ideal gas behaviour.

$$cons_{\text{H}_2\text{\_comp,el},h} = \frac{1}{\eta_{\text{H}_2\text{\_comp}}} \left(\frac{gen_{\text{AWS,H}_2,h}}{\text{MW}_{\text{H}_2}} \right) RT^{\text{in}}_{\text{H}_2\text{\_comp}} \left(\frac{P^{\text{in}}_{\text{H}_2\text{\_comp}}}{P^{\text{out}}_{\text{H}_2\text{\_comp}}} \right), \quad \forall h \tag{4.10}$$

where $\eta_{\text{H}_2\text{\_comp}}$ and MW_{H_2} are hydrogen compressor efficiency—assumed to be 70%—and hydrogen molecular weight.

Electrical grid connection

To account for the electrical grid connection, hourly imported ($import_{\text{grid,El},h}$) and exported ($export_{\text{grid,El},h}$) electricity from the grid are incorporated in the energy balance as shown in Equation 4.11.

$$\begin{aligned} &\sum_{t \in Tns} \left(gen_{t,\text{El},h} - cons_{t,\text{El},h} \right) \\ &+ \left(dish_{\text{batt,El},h} - char_{\text{batt,El},h} \right) \\ &+ \left(import_{\text{grid,El},h} - export_{\text{grid,El},h} \right) \\ &- curt_{\text{El},h} = 0\,, \quad \forall h \end{aligned} \tag{4.11}$$

When modelling 100% hourly time-matching requirement, hourly imported and exported electricity is fixed to zero.

Additionally, constraints, shown in Equations 4.12–4.15, are enforced to allow either electricity export or import from the grid at any given hour.

$$GB_{\text{El},h} = GB_{\text{El},h-1} - export_{\text{grid,El},h} + import_{\text{grid,El},h}, \quad \forall h \tag{4.12}$$

$$import_{\text{grid,El},h} \leq \times y^{\text{import}}_{\text{grid},h}, \quad \forall h \tag{4.13}$$

$$export_{\text{grid,El},h} \leq \times y^{\text{export}}_{\text{grid},h}, \quad \forall h \tag{4.14}$$

$$y^{\text{import}}_{\text{grid},h} + y^{\text{export}}_{\text{grid},h} = 1, \quad \forall h \tag{4.15}$$

where $GB_{\text{El},h}$ is a variable that tracks hourly grid balance, and $y^{\text{import}}_{\text{grid},h}$ and $y^{\text{export}}_{\text{grid},h}$ are binary decision variables that are activated—with a value of 1—if electricity is being imported or exported, respectively, from the grid.

4.4.2.2 Objective function

Similar to the model used in Chapter 3, the objective function is to minimise the total annualised cost of the system (TAC) as shown in Equations 4.16 and 4.17. This includes annualised capital expenditures ($CapEx$), fixed and variable operating expenses ($OpEx$), and cost of imported electricity where $price_{El}$ is electricity price.

$$\begin{aligned} \textbf{min} \quad TAC = & \sum_{t} (CapEx_t \times AF_t + OpEx^{\text{fix}}_t) \times instCap_t \\ & + \sum_{t \in Tns, et, h} OpEx^{\text{var}}_{t,et} \times gen_{t,et,h} \\ & + \sum_{t \in Ts, et, h} OpEx^{\text{var}}_{t,et} \times disch_{t,et,h} \\ & + \sum_{h} import_{\text{grid,El},h} \times price_{\text{El}} \end{aligned} \tag{4.16}$$

$$AF_t = \frac{WACC \times (1 - WACC)^{LT_t}}{(1 + WACC)^{LT_t} - 1} \tag{4.17}$$

where $WACC$ and LT are the weighted average cost of capital and technology lifetime, respectively.

Regional electricity prices are based on the most recent (2019-2022) data available from the International Energy Agency (IEA) database [282] for the industrial sector.

For missing data from the IEA database, the World Bank database for the year 2019 is used [191]. Regional weighted average capital cost (WACC) based on the mid WACC assumption is used in this analysis, which is shown in Appendix B.3.

4.4.2.3 Solution strategy and solver

The mixed-integer linear programming (MILP) model was implemented in Pyomo V6.4.2 and solved using CPLEX V22.1.0 using one full-year hourly resolution data. Thus, each spatial node produced 20 different results representing the considered 20 years of data (2003–2022).

4.4.3 Performance indicators

4.4.3.1 Levelised cost of hydrogen

The levelised cost of hydrogen ($LCOH_2$) is calculated using Equation 4.18 using TAC and the total yearly hydrogen exported from the system ($\sum_h export_{H_2,h}$).

$$LCOH_2 = \frac{TAC}{\sum_h export_{H_2,h}} \tag{4.18}$$

4.4.3.2 Hydrogen carbon intensity

In cases where grid electricity from the grid is used for hydrogen production, the hydrogen CI (CI_{H_2}) is calculated using Equation 4.19.

$$CI_{H_2} = \frac{CI_{grid} \times \sum_h import_{grid,El,h}}{\sum_h export_{H_2,h}} \tag{4.19}$$

where CI_{grid} is the grid CI.

In this analysis, the CIs for hydrogen produced from SMR are estimated based 90% capture rate and methane leakage in the range 0.5%–5.8% based on previous works [250, 251, 283], which results in blue (SMR with CCS) hydrogen CI of 1.5–7.3 $kgCO_{2,eq}$ per kgH_2 and grey (SMR) hydrogen CI of 9.4–14.7 $kgCO_{2,eq}$ per kgH_2.

Table 4.1: Long-haul heavy goods vehicles (HGVs) assumptions.

	Value	Unit	Source
Diesel truck			
Retail price	154,000[a]	$	[284]
Lifetime	1,200,000	km	[284]
Fuel price	0.9–1.4	$ per L	[284, 285]
Fuel consumption	30.7	L per 100 km	[284]
Fuel CI	2.7	$kgCO_{2,eq}$ per L	[286]
Hydrogen truck			
Retail price	314,000[a]	$	[284]
Lifetime	1,200,000	km	[284]
Fuel consumption	8.3	kgH_2 per 100 km	[284]

[a]2025 prices.

4.4.3.3 Levelised cost of driving

When evaluating different alternatives for heavy goods vehicles (HGVs), the levelised cost of driving (LCODriving) in $ per km is calculated using Equation 4.20.

$$\text{LCODriving} = \frac{TRP}{TLF} + FP \times FC \tag{4.20}$$

where TRP is the truck retail price in $, TLF is the truck's lifetime in km, FP is the fuel price and FC is the fuel consumption. The assumption used for collecting LCODriving is shown in Table 1.

4.4.3.4 CO_2 avoidance cost

When comparing the financial effectiveness of CO_2 mitigation between different alternatives, CO_2 avoidance cost in $ per tCO_2 can be calculated using Equation 4.21.

$$CO_2 \text{ avoidance cost} = \frac{\Delta\text{cost}}{\text{avoided } CO_2} \tag{4.21}$$

where Δcost is the investment needed to avoid some amount of CO_2 (avoided CO_2). For example, Δcost can be different the $LCOH_2$ from different hydrogen production pathways, while the avoided CO_2 can be the different hydrogen CI between the different pathways.

4.5 Results and discussion

4.5.1 The techno-economics of hourly time-matching

Two scenarios are considered: (a) 100% grid-powered hydrogen production, where electrolysers are connected directly to the grid and operating at a 100% capacity factor to supply a constant hydrogen output, and (b) hourly time-matching, where iRE electricity generation and consumption are matched on an hourly basis with the electrolysers' electricity consumption. For grid-powered hydrogen production, regional electricity prices are used to calculate the $LCOH_2$. For hourly time-matched hydrogen production, the system configuration and operation are optimised using hourly weather data to achieve the lowest $LCOH_2$. Figure 4.2 and Figure 4.3 show and compare the results of the two scenarios.

The implications of time-matching requirements, particularly hourly time-matching, have been extensively debated within the energy policy literature. The debate's core is mainly focused on the ability of time-matching requirements to reduce emissions and its impact on the $LCOH_2$. Between the two implications, there is consensus that hourly time-matching can increase $LCOH_2$ [277–279]. This is consistent with our observations illustrated in Figure 4.2. Hourly time-matching increases the $LCOH_2$ unless regional electricity prices are above around \$200 per MWh_{el}, as in some European countries (e.g., the UK, Spain, and the Netherlands), Australia, and Japan.

For instance, in the US, the $LCOH_2$ for grid hydrogen is \$5.6 per kgH_2 compared to hourly time-matched hydrogen of \$9.4 per kgH_2—representing the mean of the 25th percentile. This corresponds to an increase in $LCOH_2$ by \$3.8 per kgH_2, or 68%. Similarly, the $LCOH_2$ for grid hydrogen is \$9.7, \$7.1 and \$7.1 per kgH_2 in France, UAE and India, respectively, compared to hourly time-matched hydrogen of \$10.1, \$10.3 and \$12.6 per kgH_2—representing the mean of the 25th percentile. This corresponds to an increase in $LCOH_2$ by \$0.4 (4%), \$3.2 (45%) and \$5.5 (77%) per kgH_2, respectively. Overall, the $LCOH_2$ of grid hydrogen is in the range of \$5.5–\$7.0 per kgH_2 for regions with electricity prices in the range of \$80–\$100 per MWh_{el}, while the global 25th percentile mean for hourly time-matched hydrogen is \$10.8 per kgH_2, which corresponds to an increase in $LCOH_2$ by \$3.8–\$5.3 per kgH_2 (54%–96%).

This increase in $LCOH_2$ for hourly time-matched hydrogen production is mainly attributed to the need for additional energy generation, electrolyser and energy storage capacities. The additional energy generation capacity is needed to generate

renewable energy during periods of low availability and to account for inter-annual variation in the average availability of renewable energy. This results in generating excess renewable energy over the year, requiring energy curtailment and resulting in lower utilisation of energy generation assets. This is illustrated in Figure 4.3A.

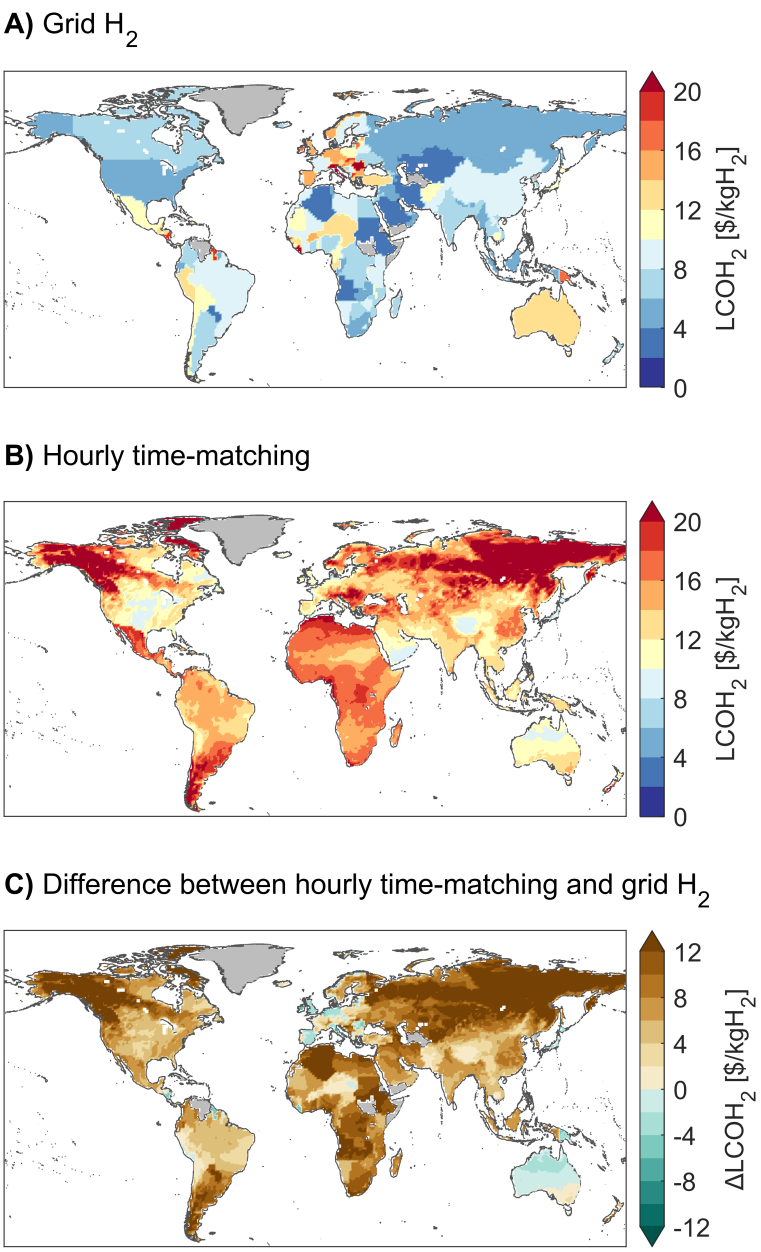


Figure 4.2: Regional levelised cost of hydrogen ($LCOH_2$) for electrolytic hydrogen production. **A)** $LCOH_2$ for 100% grid-powered hydrogen production. **B)** $LCOH_2$ for hourly time-matched hydrogen production utilising intermittent renewable energy (iRE) with an energy storage (iRE+ES) system. This analysis uses 20 years (2003–2022) of weather data, where each planning year, represented by hourly data, is used to generate a unique solution. The presented $LCOH_2$ corresponds to the planning year having the maximum $LCOH_2$. This was done to ensure that the selected system design could deliver a reliable supply of hydrogen even in the year with the lowest renewable energy availability. **C)** The difference (Δ) in $LCOH_2$ between the two scenarios. Adapted from [280].

The additional electrolyser capacity is needed to allow operational flexibility. Excess hydrogen is produced and stored during times of high renewable energy availability to compensate for times of low renewable energy availability. This comes at the expense of reduced electrolyser utilisation, as illustrated by Figure 4.3B. Finally, the additional energy storage capacity is needed to balance intra-annual variation in renewable energy supply, as illustrated by Figure 4.3C.

Additionally, inter-annual iRE variations impact not only the $LCOH_2$ but also the least-cost system design in terms of the choice of technologies and their required installed capacities. This is illustrated in Figure 4.4, which shows the deviations in technology choices and their installed capacities when optimising the system using different years of iRE availability data. For example, using data from one year may result in no CSP deployment, whereas using data from another year can lead to a large deployment of CSP for the same region [19, 287]. Thus, a system optimised with data from a single year or aggregated data from multiple years will be highly unlikely to achieve 100% hourly time-matching in subsequent years [288]. This, in turn, will require redundancy in the installed capacities of electrolysers, energy generation and energy storage technologies to mitigate this uncertainty and ensure 100% hourly time-matching and continuous supply of hydrogen.

On the other hand, while utilising grid electricity might decrease hydrogen production costs by allowing continuous electrolyser operation without the need for additional renewable energy generation and storage capacities, it can result in higher emissions, especially in regions with high grid CI.

Overall, to meet 100% hourly time-matching of iRE, it is necessary to install beyond nameplate capacity in electrolysers, energy generation and energy storage technologies, which, in return, increases the $LCOH_2$ [19, 287, 288]. Aside from increased costs, it can ensure low-carbon hydrogen production. However, the increase in materials requirements will also impose increased non-carbon environmental burdens [251, 254]. This observation is consistent with those of The Royal Society report on large-scale electricity storage [274].

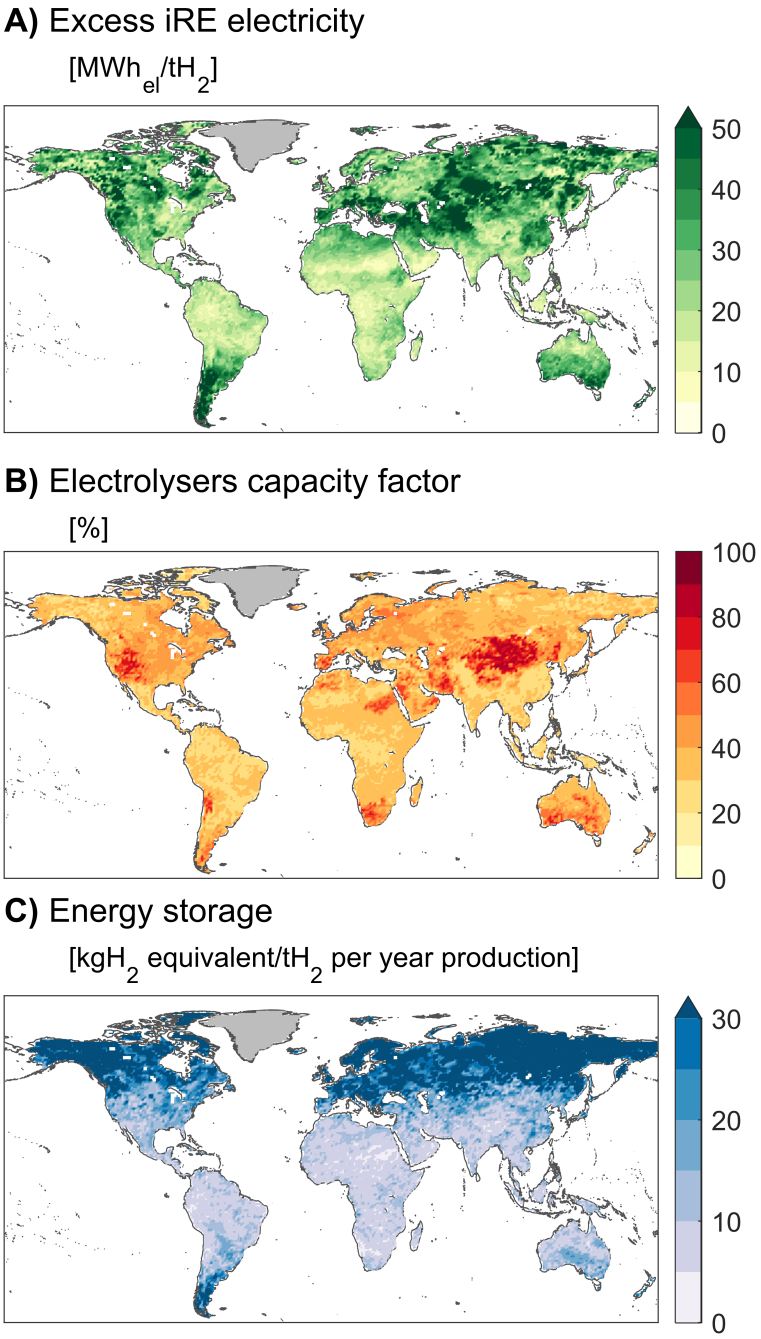


Figure 4.3: The performance hourly time-matched hydrogen production system. The presented values correspond to the system shown in Figure 4.2. **A)** shows excess iRE electricity that is not utilised in hydrogen production. **B)** shows the electrolysers' capacity factor. **C)** shows the installed capacities for energy storage technologies. The capacities of all energy storage technologies, including batteries, thermal heat storage, and hydrogen tanks, are expressed in hydrogen-equivalent terms, assuming an electrolyser efficiency of 61%. Adapted from [280].

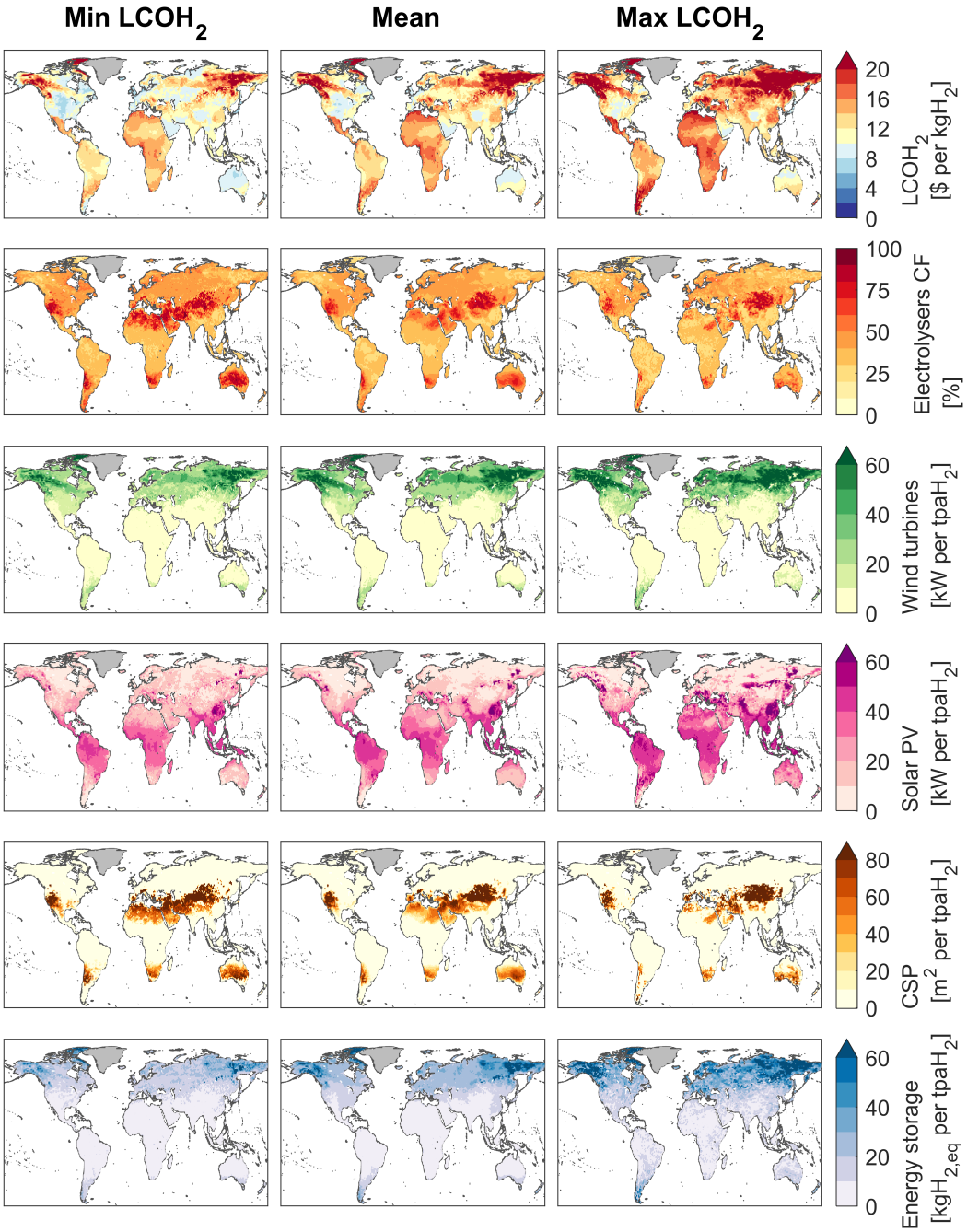


Figure 4.4: Overview of the different solutions for hourly time-matched hydrogen production systems. Min and max $LCOH_2$ show the minimum and maximum $LCOH_2$ optimised system configurations among the 20 different solutions, each representing a full year of hourly weather data (2003-2022). The mean shows the mean of the 20 different solutions. The capacity energy storage technologies are expressed in terms of hydrogen equivalent, assuming an electrolyser efficiency of 61%. Energy storage technologies that are considered include batteries, thermal heat storage and hydrogen tanks. Adapted from [280].

4.5.2 CO_2 avoidance cost of hourly time-matching

In the previous section, it was demonstrated that the requirement of perfect hourly matching can significantly increase the cost of electrolytic hydrogen production. In return, it can ensure that the produced hydrogen is low carbon. This section analyses the environmental return of this increase in $LCOH_2$.

Figure 4.5 illustrates the effects of relaxing iRE's 100% hourly time-matching requirement on $LCOH_2$ by co-supplying electricity from the grid, considering various grid-electricity prices for an iRE+ES system located in Texas, US. A 100% hourly time-matching requirement is equivalent to an iRE electricity ratio of 100%, while relaxing the time-matching requirement is presented here as the ability to utilise some grid electricity in hydrogen production, where the remaining utilised iRE electricity is hourly matched.

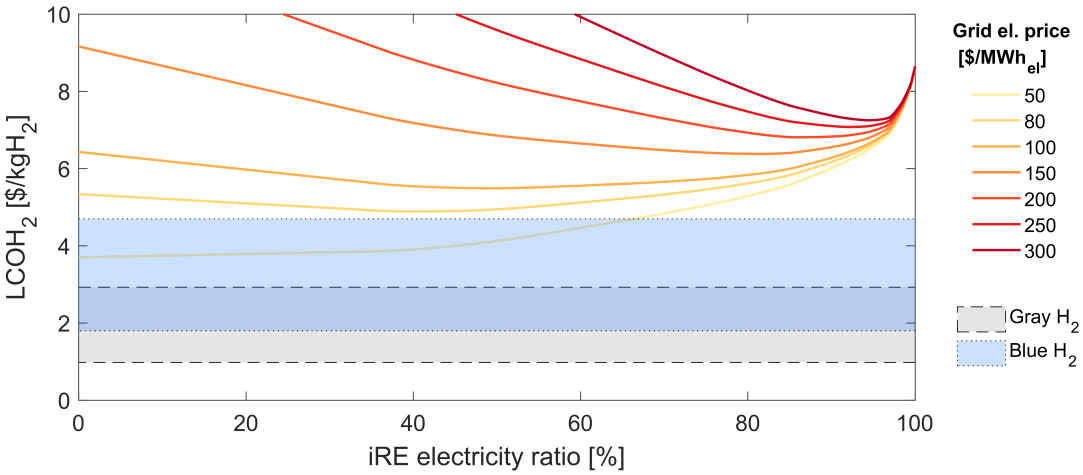


Figure 4.5: Levelised cost of hydrogen ($LCOH_2$) when the hourly time-matching requirement is relaxed. Values represent a system that is placed in Texas, US and utilising an iRE+ES system. Here, hourly time-matching is enforced. Additionally, the system is constrained to consume a fixed annual iRE electricity ratio—remaining from the grid—of the total electricity consumed for hydrogen production (x-axis). Different line colours represent different grid electricity (el.) prices. Grey and blue hydrogen price range adopted from BloombergNEF [289]. Adapted from [280].

Across all scenarios examined, imposing a 100% hourly time-matching requirement leads to an increase in $LCOH_2$ relative to a more lenient time-matching requirement, where some amount of grid electricity is allowed to be utilised.

For example, the cost of electrolytic hydrogen can be competitive with that of blue hydrogen—without the need for tax incentives—when some fraction of grid electricity is used to complement the availability of renewable energy, where $LCOH_2$ around \$4.9 per kgH_2 can be achieved at \$80 per MWh_{el}—around the mean electricity price in the US for the industrial sector [282]. This is comparable with the upper bound of blue hydrogen cost of \$4.7 per kgH_2. However, enforcing 100% hourly time-matching will increase the $LCOH_2$ by 76% to \$8.6 per kgH_2.

The previous example does not account for the CI of hydrogen produced by utilising grid electricity. However, when considering the CI of hydrogen, Figure 4.6 shows how much grid electricity, as a function of the grid CI, can be used to produce hydrogen at a given CI. Grid CI fluctuates with time and is influenced by the amount of renewable availability. In grid-connected systems, it is expected that the utilisation of grid electricity will be preferred during periods with low renewable availability, which corresponds to the highest grid CI periods. The box plots summarise the hourly grid CI for the shown regions in 2023 [290].

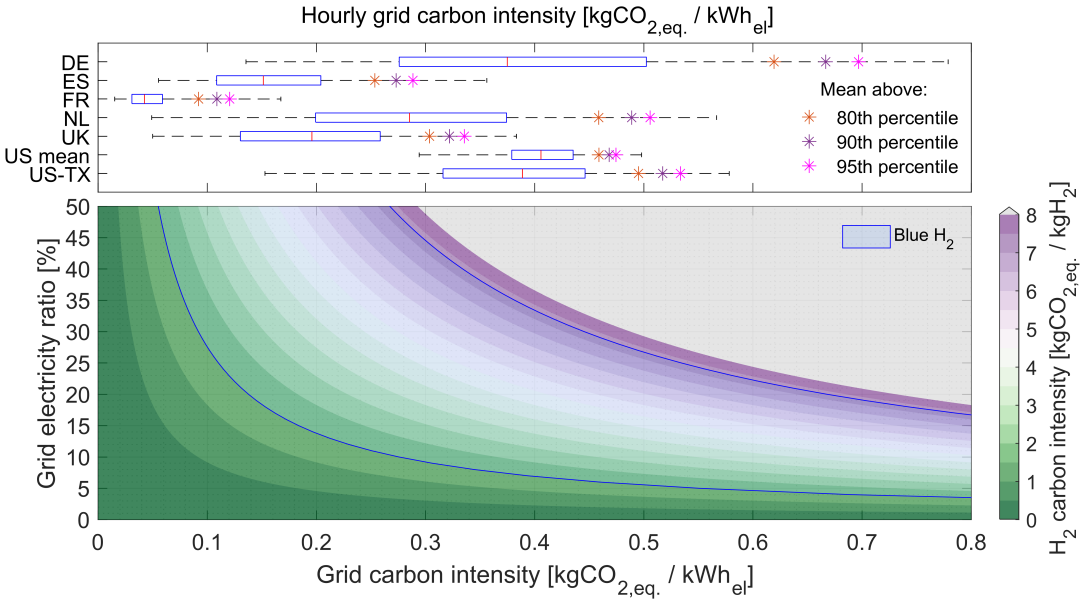


Figure 4.6: Hydrogen carbon intensity when the hourly time-matching requirement is relaxed as a function of consumed grid electricity and its carbon intensity. The box plots show the hourly region grid Cis which are based on the 2023 data [290]. This projection demonstrates that as the electricity grid is decarbonised, one can use progressively more grid power to produce low-carbon hydrogen. Adapted from [280].

Considering the Texas electrical grid as an example, around 14% of grid electricity at a CI of 0.52 $kgCO_{2,eq}$ per kWh_{el}—representing the Texas grid mean hourly CI above the 90th percentile—can be used in hydrogen production. This results in produced hydrogen with a CI of 4.0 $kgCO_{2,eq}$ per kgH_2 (Figure 6) and an $LCOH_2$ of $6 per kgH_2(Figure 5), considering the 2022 mean electricity price in Texas of $100 per MWh_{el} [291]. Similarly, a hydrogen CI of 1.5 $kgCO_{2,eq}$ per kgH_2 can be achieved using 5% of grid electricity with a CI of 0.53 $kgCO_{2,eq}$ per kWh_{el}—representing the Texas grid mean hourly CI above 95th percentile—at an $LCOH_2$ of $6.7 per kgH_2. These levels of CI are comparable to blue hydrogen—which ranges from 1.50–7.30 $kgCO_{2,eq}$ per kgH_2—and are thus equivalent from an environmental outcome perspective.

For these cases, the CO_2 avoidance cost of imposing 100% hourly time-matching requirements can calculated—using Equation 4.21 and assuming that hydrogen has no CI when if produced from 100% iRE—which is shown in Figure 4.7 as a function of difference in $LCOH_2$ ($\Delta LCOH_2$) and avoided CO_2 emissions.

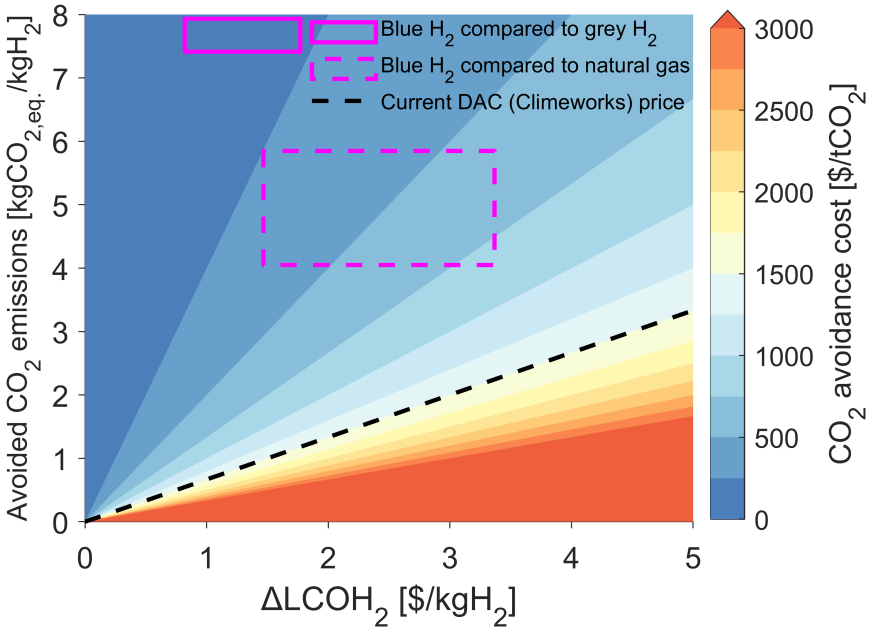


Figure 4.7: CO_2 avoidance cost of imposing 100% hourly time-matching requirement. The CO_2 avoidance cost is calculated using Equation 4.21 where the avoided CO_2 emissions correspond to the reduction in hydrogen CI by imposing a time-matching requirement, and $\Delta LCOH_2$ is the increase in the cost of hydrogen caused by imposing the time-matching requirement. Adapted from [280].

Using the previous Texas examples, when using 14% of grid electricity, the produced hydrogen will have a CI of 4.0 $kgCO_{2,eq}$ per kgH_2 and an $LCOH_2$ of \$6 per kgH_2. This corresponds to a $\Delta LCOH_2$ of \$2.6 per kgH_2 and a CO_2 avoidance cost of \$650 per tCO_2 (Figure 4.7) for imposing the 100% hourly time-matching requirement, assuming that 100% hourly time-matched hydrogen has no carbon footprint. Similarly, if hydrogen is produced at a CI 1.5 $kgCO_{2,eq}$ per kgH_2 by using 5% of grid electricity, the $\Delta LCOH_2$ is \$1.9 per kgH_2, and the CO_2 avoidance cost for imposing the 100% hourly time-matching requirement is \$1267 per tCO_2 (Figure 4.7). This increasing CO_2 avoidance cost trend continues as we target lower hydrogen CI and stricter hourly time-matching requirements, which is illustrated in Figure 4.8.

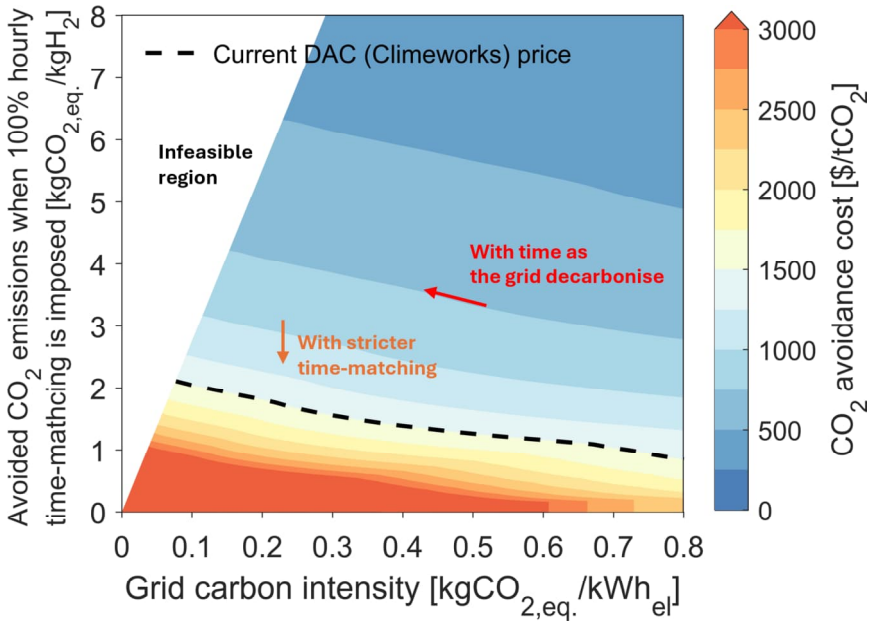


Figure 4.8: CO_2 avoidance cost, for a system that is placed in Texas, US, of imposing a 100% hourly time-matching requirement for grid-connected hydrogen production as a function of grid carbon intensity and avoided CO_2. Here, $\Delta LCOH_2$ and utilised grid electricity are calculated based on the values from Figures 4.5 and 4.6 at an electricity price of \$100 per MWh_{el}, which is the 2022 mean electricity price in Texas [65]. This plot shows that as the grid decarbonises, the CO_2 avoidance cost increases, which is caused by the increase in $\Delta LCOH_2$ since more grid electricity can be utilised, allowing for lower $LCOH_2$ (Figure 4.5) to produce hydrogen at the same CI. Additionally, it shows that CO_2 avoidance cost increases as a stricter time-matching requirement is imposed, which is represented by decreasing the avoided CO_2 from imposing 100% hourly time-matching, when considering a fixed grid electricity CI. Adapted from [280].

Figure 4.8 shows that even if grid electricity with a CI close to 0.6 $kgCO_{2,eq}$ per kWh_{el}—corresponding to around the maximum hourly grid CI in Texas—is used to relax the hourly time-matching requirement, imposing a strict 100% requirement, when the produced hydrogen has a CI of $\leq$1.2 $kgCO_{2,eq}$ per kgH_2, will lead to a CO_2 avoidance cost of $\geq$\$1500 per tCO_2. This is a considerably high CO_2 avoidance cost given the current price for direct air capture and storage (DAC), such as the \$1500 per tCO_2 removed charged by Climeworks [292].

Furthermore, as the Texas grid continues to decarbonise, the feasibility of producing hydrogen at cheaper $LCOH_2$ and lower CI increases due to the potential for using a higher ratio of grid electricity, as illustrated by Figure 4.5 and Figure 4.6. This will widen the gap in $LCOH_2$ between producing low-carbon hydrogen using some grid electricity and adhering to the strict 100% hourly time-matching requirement ($\Delta LCOH_2$), which will, in turn, increase the CO_2 avoidance cost, as depicted in Figure 4.8. Overall, Figure 4.8 shows that adhering to the strict 100% hourly time-matching requirement becomes progressively more costly as electricity grids become cleaner.

4.5.3 The levelised lifecycle emissions of grid-connected hydrogen

Since we showed that hourly matching of renewable energy increases the cost of carbon avoided significantly beyond current carbon prices, this section explores whether, taking a long-term view, only grid electricity will be sufficient to provide low-carbon electrolytic hydrogen by following a thought experiment: What is the lifetime average CI of grid-connected electrolytic hydrogen if you connect an electrolyser to the power grid in a country or region that is already well on the way to decarbonisation?

As things stand today, whilst electricity grids have a non-zero CI, they are broadly tending towards a net zero CI over time, with, for example, the UK aiming at a net zero electricity system by 2035 and India, at the other extreme, aiming at net zero by 2070. Thus, in certain jurisdictions, grid-connected electrolysers will be using zero-carbon electricity for most of their operating lifetime.

We evaluate the thought experiment in Figure 4.9. Here, we assume a 100% grid-powered electrolyser operating for 25 years whilst the grid follows a linear decarbonisation trajectory. This decarbonisation trajectory mimics an emissions trading system (ETS) with a linear reduction factor. Similar ETSs are already implemented in some regions, including the UK, EU, and some US states, such as Washington, California and Eastern US, through the Regional Greenhouse Gas Initiative (RGGI)

[293–298]. Four distinct projects are evaluated for each regional grid, with start dates in 2025, 2030, 2035 and 2040.

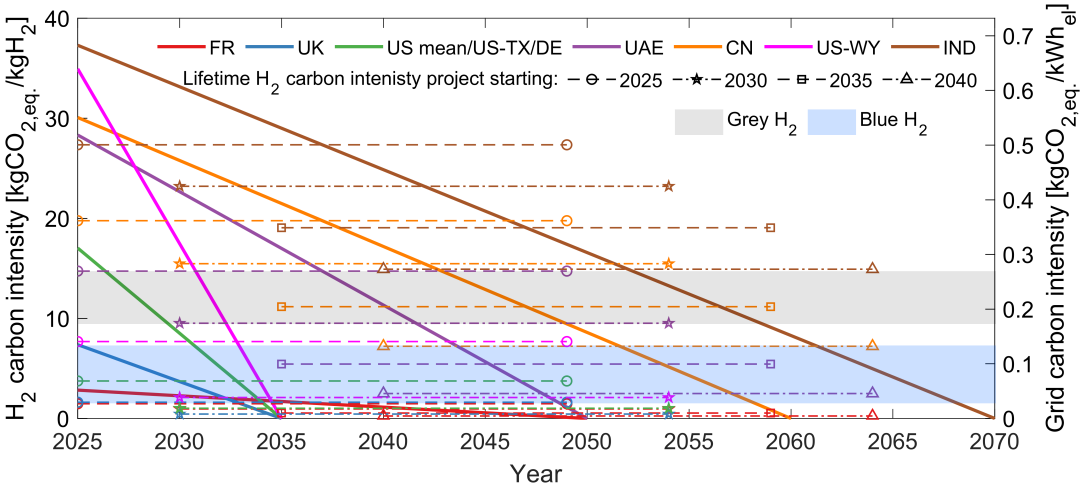


Figure 4.9: Projected hydrogen CI for selected regions for 100% grid-powered hydrogen production. The lifetime hydrogen CI is calculated based on a project lifetime of 25 years, assuming a linear decarbonisation trajectory. Adapted from [280].

As can be observed from Figure 4.9, both the grid CI at the start date and decarbonisation trajectory, with the rate of decarbonisation observed to be of primary importance and the initial CI of the grid observed to be a second-order issue. In many cases, grid-connected electrolysis will produce electrolytic hydrogen with an average lifetime CI approximately less than or equivalent to that of blue hydrogen.

For example, in regions with net-zero electrical grid target by 2035 and forecasted 2025 grid CI between 0.13–0.61 $kgCO_{2,eq}$ per kWh_{el}, such as the US and Germany, using only grid electricity can already achieve a lifetime average hydrogen CI comparable to blue hydrogen, with the UK having lifetime hydrogen CI (1.6 $kgCO_{2,eq}$ per kWh_{el}) equal to the lower range of blue hydrogen. However, considering the UK's gas supply CI [251], lifetime grid hydrogen CI is lower than blue hydrogen (estimated at 1.8 kg $kgCO_{2,eq}$ per kWh_{el}). Similarly, regions with a forecasted 2025 grid CI <0.13 $kgCO_{2,eq}$ per kWh_{el} can achieve a lifetime average hydrogen CI lower than that of blue hydrogen for projects starting in 2025.

Thus, as the grid decarbonises, the lifetime CI of grid electrolytic hydrogen similarly decreases. For example, even today, connecting the "mean US grid" to an electrolyser will produce hydrogen, which is very similar to the mid-range CI for blue hydrogen. In the UK or France, it is already lower CI on a lifetime average than blue hydrogen.

On the other hand, India's 2070 net-zero target means that the lifetime grid hydrogen CI will remain worse than grey hydrogen for projects starting as late as 2040. Only projects starting after 2050–2060 are projected to achieve a hydrogen CI comparable to blue hydrogen, as can be illustrated in Figure 4.10 with 10–20 years to a net-zero electrical grid. Given this trajectory, the current governmental spending on its ambitious strategy to produce at least 5 Mtpa of green hydrogen by 2030 may not yield the best return on investment regarding environmental benefits. Instead, redirecting efforts and resources towards decarbonising the grid could provide a more significant environmental impact and a better strategic focus for achieving cost-effective net-zero energy transition.

Importantly, and as illustrated in Figure 4.10, when the project starts will matter. Given that, in some cases, it can take as long as a decade for a project to go from a conceptual study to actual production, this is important. It is not inconceivable that a project conceived in 2025 will not start producing hydrogen until maybe 2030 or 2035. In this period from concept to reality, much of the rest of the world will change. For example, as electrolyser efficiency improves and grids progressively decarbonise, the CI of the associated hydrogen will also reduce. This demonstrates that focusing on achieving grid decarbonisation targets can ensure long-term low-carbon electrolytic hydrogen production. This should be considered when designing these projects.

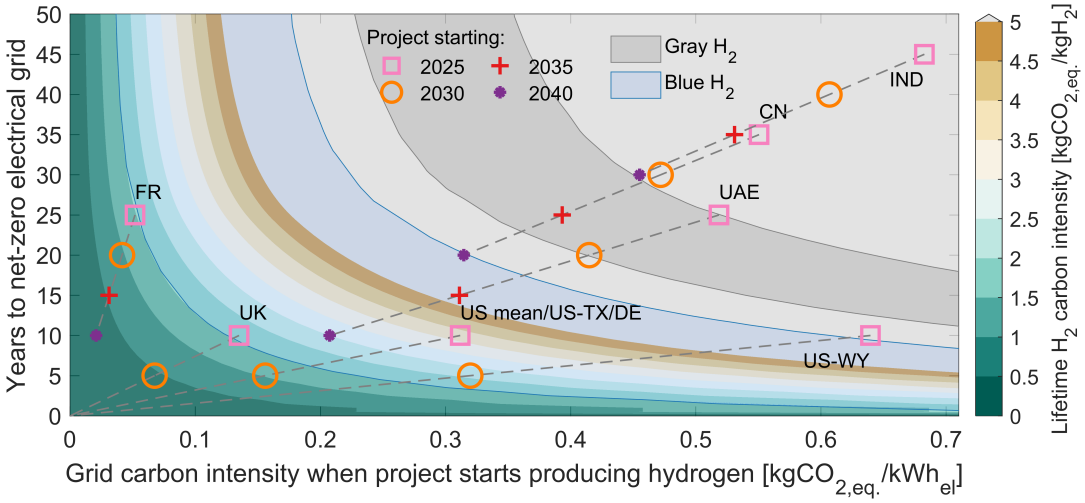


Figure 4.10: Projected 100% grid-powered hydrogen CI as a function of grid carbon intensity when the project starts producing hydrogen and years remaining for the net-zero electrical grid. Adapted from [280].

Similar to other applications that require electrification—such as electric vehicles (EVs), heat pumps, or industrial heating—electrolytic hydrogen production stands to benefit from the ongoing decarbonisation of electrical grids. As the grid becomes cleaner, the carbon footprint of these electrified applications naturally decreases over time. Therefore, integrating electrolytic hydrogen production into broader electrification strategies aligns with the overall goal of reducing emissions across all sectors. This highlights the importance of prioritising grid decarbonisation efforts to maximise the long-term environmental advantages of electrification initiatives across various sectors, including hydrogen production, and, in turn, begs the question of why "hourly matching" for hydrogen but not the other electrification pathways.

4.5.4 The environmental value of electrolytic hydrogen in prospective applications

The value of hydrogen's environmental benefits, however it is produced, depends strongly on how it will be utilised. Is this hydrogen displacing grey hydrogen in an existing industrial facility, methane in the context of high-temperature heat provision, or diesel for mobility? This section explores this question by comparing the CO_2 avoidance cost when grid-powered hydrogen is used in different applications to displace its alternatives.

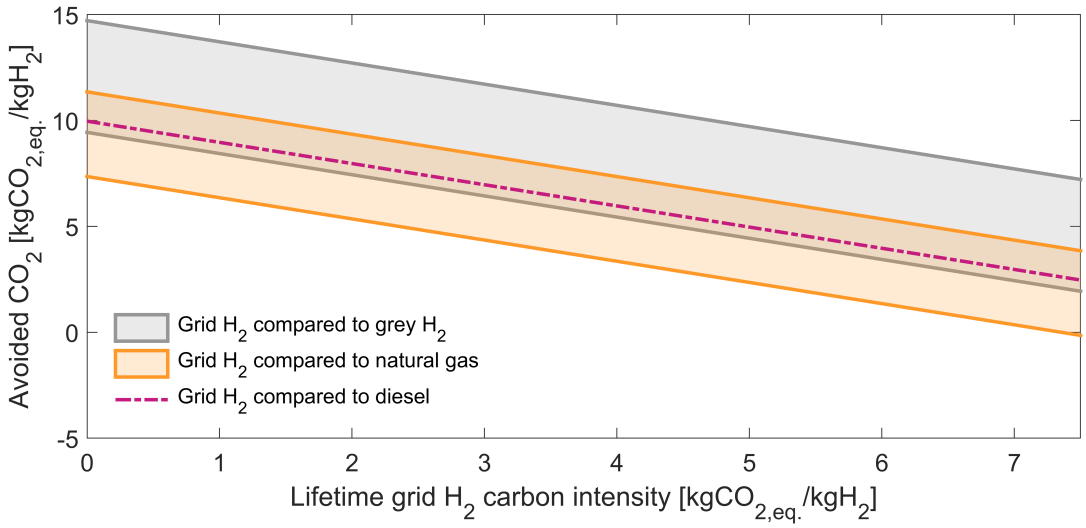


Figure 4.11: Avoided CO_2 as a function of lifetime grid hydrogen CI relative to counterfactual. This plot shows that as the lifetime grid hydrogen CI becomes lower, it can be utilised in more applications with higher CO_2 avoidance. Assumption used: methane leakage (0.5%–5.8%) [250, 251]. Adapted from [280].

The avoided CO_2 for the 100% grid-powered hydrogen when compared to natural gas, grey and blue hydrogen, and diesel—in long-haul heavy goods vehicles (HGVs)—as a function of its lifetime CI is shown in Figure 4.11. Figures 4.12–4.14 show the CO_2 avoidance costs for these cases, where the results are consistent with some recent literature [299].

4.5.4.1 Displacing grey hydrogen

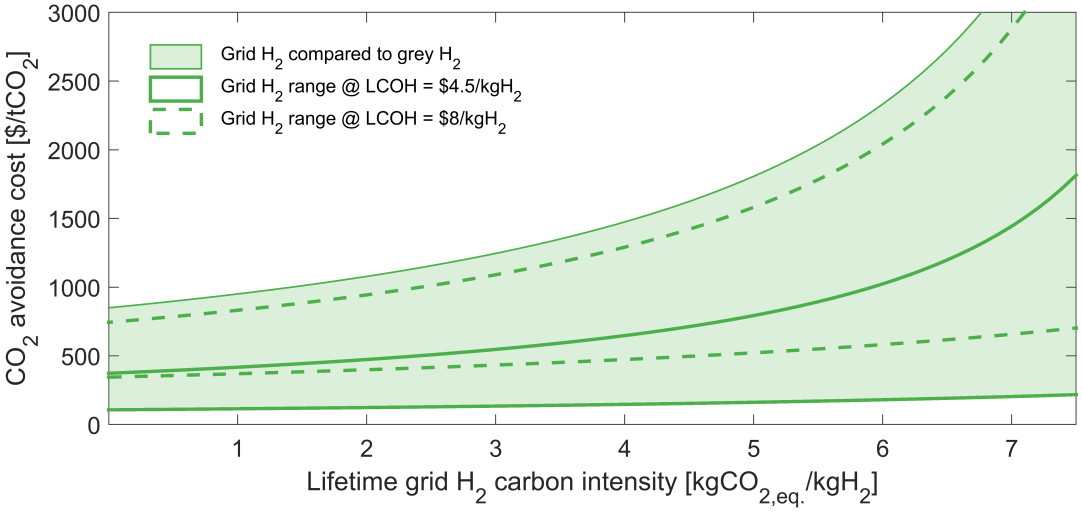


Figure 4.12: CO_2 avoidance cost when 100% grid-powered hydrogen displaces grey hydrogen as a function of its lifetime carbon intensity. Assumption used: methane leakage (0.5%–5.8%) [250, 251], grey hydrogen price ($1–$2.9 per kgH_2) and grid hydrogen price ($4.5–$9 per kgH_2) [289]. Adapted from [280].

Figure 4.11 shows that grid hydrogen can lead to avoided emissions when displacing grey hydrogen (grey-shaded area in Figure 4.11) even at a considerably high CI of 7.5 $kgCO_{2,eq}$ per kgH_2. In Figure 4.13, the green-shaded areas represent the CO_2 avoidance cost when grid hydrogen is used to displace grey hydrogen. Within these shaded regions, two subregions are also bounded using solid and dashed lines, representing the range when $LCOH_2$ are $4.5 per kgH_2 and $8 per kgH_2, respectively. For those regions, the higher range of the CO_2 avoidance cost corresponds to grid hydrogen displacing grey hydrogen with low prices and low associated emissions (i.e., methane leakage).

If we assume that 100% grid-powered hydrogen can be produced for $4.5 per kgH_2, whereas imposing a 100% hourly time-matching requirement increases the $LCOH_2$ to $8 per kgH_2 ($\Delta LCOH_2$ of $3.5 per kgH_2), the range of costs for CO_2

avoided for grid hydrogen (solid green lines) is always lower than that of 100% hourly time-matching (dashed green lines at hydrogen CI of zero) when the lifetime grid hydrogen CI is $\leq$4.7 $kgCO_{2,eq}$ per kgH_2.

For example, at a grid hydrogen CI of 1.6 $kgCO_{2,eq}$ per kgH_2, which is achievable in the UK for projects starting in 2025, the CO_2 avoidance cost is \$120–\$449 per tCO_2, while the CO_2 avoidance cost of hydrogen at zero CI and an $LCOH_2$ of \$8 per kgH_2—corresponding to hydrogen produced when imposing a 100% hourly time-matching requirement—is \$345–\$744 per tCO_2. Thus, switching from grey hydrogen to 100% grid-powered hydrogen is a more cost-effective way to avoid CO_2 emissions than imposing a 100% hourly time-matching requirement in this case.

Furthermore, waiting for a fully decarbonised grid to produce 100% grid-powered hydrogen (\$107–\$373 per tCO_2) does not significantly reduce the CO_2 avoidance cost range when hydrogen grid CI is relatively low, as in the case of UK projects starting in 2025—the CO_2 avoidance cost range only reduces by \$13–\$76 per tCO_2.

4.5.4.2 Displacing natural gas

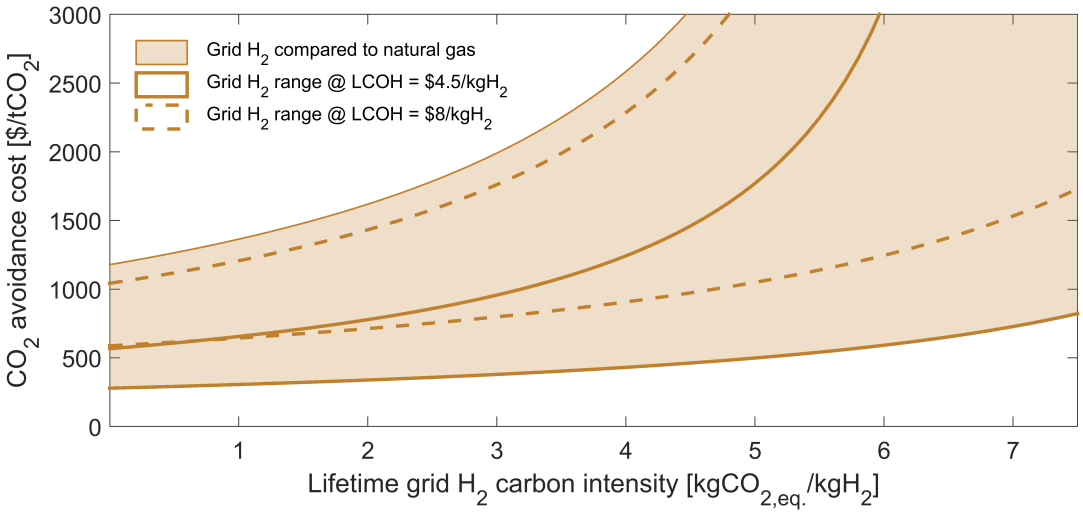


Figure 4.13: CO_2 avoidance cost when 100% grid-powered hydrogen displaces natural gas as a function of its lifetime carbon intensity. Assumption used: methane leakage (0.5%–5.8%) [250, 251], natural gas price (\$10–\$40 per MWh_{LHV}) and grid hydrogen price (\$4.5–\$9 per kgH_2) [289]. Adapted from [280].

Hydrogen can substitute natural gas used for heating. The general observations are similar to the previous case, where Figure 4.11 shows that grid hydrogen can

have lower CO_2 emissions compared to natural gas (orange-shaded area in Figure 4.11) even at a considerably high CI of 7.5 $kgCO_{2,eq}$ per kgH_2. However, the CO_2 avoidance costs are much higher, as shown in the brown-shaded areas in Figure 4.13. Additionally, the intercept where the 100% hourly time-matching requirement is preferred over grid hydrogen occurs at a lower lifetime grid hydrogen CI.

For instance, the CO_2 avoidance cost when imposing a 100% hourly time-matching requirement—$587–$1,042 per tCO_2 (brown dashed lines at hydrogen CI of zero in Figure 13)—is comparable to the CO_2 avoidance of grid hydrogen with a lifetime CI of 3.3 $kgCO_{2,eq}$ per kgH_2—of $393–$1,028 per tCO_2 (orange solid lines). Thus, substituting natural gas with 100% grid-powered hydrogen when grid CI is $\geq$3.3 $kgCO_{2,eq}$ per kgH_2 is not a cost-effective strategy in this case.

4.5.4.3 Displacing diesel in heavy goods vehicles

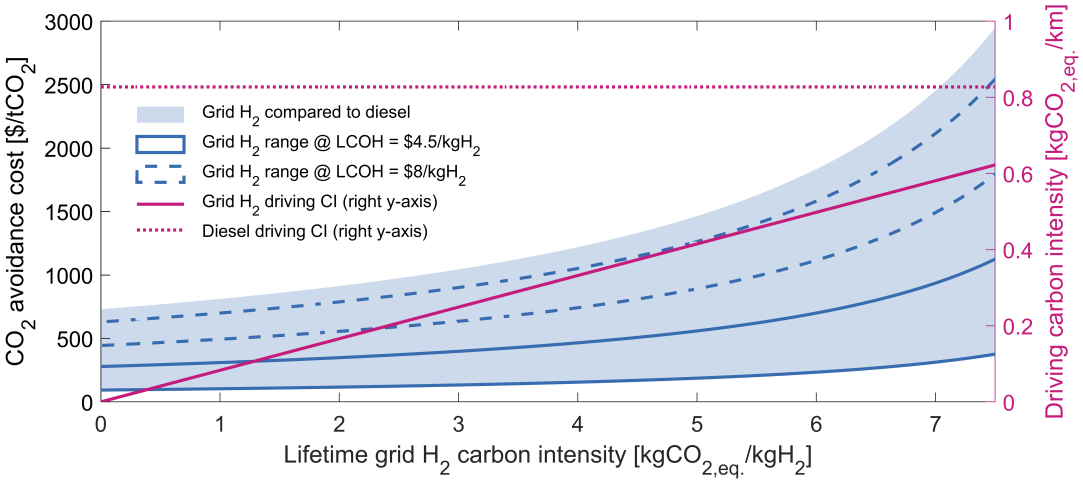


Figure 4.14: CO_2 avoidance cost when 100% grid-powered hydrogen displaces diesel—in long-haul heavy goods vehicles (HGVs)—as a function of its lifetime carbon intensity. Assumption used: grid hydrogen price ($4.5–$9 per kgH_2) [289]. Adapted from [280].

Hydrogen is often proposed as a replacement for diesel in long-haul HGVs. In this context, Figure 4.11 shows that grid hydrogen with a CI of up to 7.5 $kgCO_2$ eq per kgH_2 can result in lower CO_2 emissions than diesel with CO_2 avoidance of at least 2.5 $kgCO_{2,eq}$ per kgH_2 (purple dash-dotted line in Figure 4.11). For this case, the CO_2 avoidance cost is shown in Figure 4.14 (blue-shaded areas). For example, the CO_2 avoidance cost for grid hydrogen with CI of 3.0 $kgCO_{2,eq}$ per kgH_2 is in the range of

$133–$399 per tCO_2 (blue solid lines). As grids further decarbonise, the economics become more favourable.

Similar to the previous cases, waiting for full grid decarbonisation might not offer a significant decrease in CO_2 avoidance costs ($93–$279 per tCO_2) when hydrogen grid CI is in the lower range, e.g., $\leq$3.0 $kgCO_{2,eq}$ per kgH_2. However, the CO_2 avoidance cost for hydrogen with the 100% hourly time-matching requirement ($454–$630 per tCO_2—blue dashed lines at hydrogen CI of 0) is substantially higher.

It is important to note here that these costs only consider hydrogen production and do not include costs associated with hydrogen transport, distribution and fuelling stations.

4.6 Conclusions and future work

4.6.1 Conclusions

While strict 100% hourly time-matching requirement may ensure minimal CO_2 emissions from electrolytic hydrogen, the associated increase in levelised cost of hydrogen leads to CO_2 avoidance costs that are higher than those of even relatively costly alternatives, such as direct air capture.

This raises significant questions about the overall cost-effectiveness of such strict time-matching requirements. The policy priority should be to eliminate barriers to success and ensure that regulatory frameworks facilitate rather than hinder the deployment. In this context, even marginally relaxing the time-matching requirements could offer a more pragmatic approach to scaling up low-carbon electrolytic hydrogen production, effectively balancing cost and emission reduction efforts.

Additionally, immediate production of electrolytic hydrogen using grid electricity in jurisdictions with near-to-medium-term decarbonisation targets could achieve a lifetime carbon intensity that is comparable to or even lower than blue hydrogen and substantially less than diesel. Thus, priority should be given to rapid grid decarbonisation and identifying the most impactful hydrogen applications, i.e., where the avoided CO_2 is greatest, and the associated cost is minimised.

The case of electrolytic hydrogen production should be considered similar to other applications relying on electrification—such as electric vehicles, heat pumps, or electric heating for industrial applications. As the grid becomes cleaner, these

applications' carbon footprints will naturally reduce over time. Integrating electrolytic hydrogen production into broader electrification strategies aligns with the overarching goal of reducing emissions across all sectors. This also highlights the importance of prioritising and ensuring rapid grid decarbonisation.

Policy support should be carefully targeted to deploy hydrogen, or any other emissions mitigation tool, where it can avoid the most CO_2 for the least cost. Where we have existing use of grey hydrogen, this is a relatively easy decision; replacing high carbon intensity hydrogen with low carbon intensity hydrogen is so obvious a choice as to be no choice at all. However, this analysis indicates that great care should be taken in choosing to use hydrogen to displace natural gas, with the rationality of this choice being a function of the current state of natural gas infrastructure and the relevant reference costs of natural gas.

Moreover, no analysis of one element of the energy transition can be complete in isolation; a whole-systems perspective is indispensable to ensure all potential outcomes are rigorously and dispassionately evaluated against appropriate counterfactuals. This requires a whole-systems perspective to ensure comprehensive evaluation against appropriate counterfactuals, considering each region's specific resource endowments and infrastructure capabilities.

For example, this analysis demonstrates that displacing diesel fuels with hydrogen in heavy goods vehicles appears to be cost-effective in certain scenarios. However, this should be coupled with analysing system-wide impacts, including the feasibility of hydrogen trucks, hydrogen distribution and refuelling infrastructure and the viability of alternatives like electrification. Thus, through the lens of this analysis, employing hydrogen to replace diesel in heavy goods vehicles warrants a deeper, more comprehensive examination from a holistic systems perspective across different regions, paying special attention to local resource capabilities.

4.6.2 Limitations and future work

This analysis focuses primarily on hydrogen's carbon intensity and cost. Broader life cycle impacts—such as water consumption, land use, and other environmental externalities—are not considered. Moreover, our discussion of costs mainly reflects production costs and does not fully account for hydrogen transport, storage and end-use infrastructure costs.

We adopt a region-agnostic approach for much of the analysis and use representative or average data for electricity prices, grid carbon intensities and technology costs. Local variations in energy markets, infrastructure constraints, policy support and industrial demands may lead to different outcomes than those presented here.

Our analysis provides high-level comparisons of hydrogen counterfactuals. However, actual feasibility in terms of infrastructure, technical performance and consumer acceptance may pose significant challenges and have not been comprehensively evaluated here.

CHAPTER 5

CONCLUSIONS AND FUTURE WORK

The transition to a net-zero emissions future will require the deployment of a diverse range of low-carbon technologies and strategies to mitigate greenhouse gas emissions and remove CO_2 from the atmosphere. This study has developed a modelling framework that can geospatially evaluate the techno-economic and environmental performance of chemical processes and energy systems, potentially forming part of a future net-zero energy system and chemical industry. The versatility of this framework was demonstrated in its application to direct air capture and electrolytic hydrogen production, showcasing its potential to incorporate a broad spectrum of chemical processes and energy systems technologies. Moreover, the framework's ability to capture detailed process modelling, system-level interactions between different technologies and policy constraints with regional data, such as ambient conditions, energy resources and economic factors, can allow for comprehensive regional analysis, thereby offering valuable insights into the optimal deployment locations of low-carbon technologies and systems.

This concluding chapter synthesises the key findings from the preceding chapters, highlighting their significance and contributions. It also discusses the limitations of the current work and outlines avenues for future research to further enhance the understanding and deployment of low-carbon technologies.

5.1 Key findings and contributions

5.1.1 Chapter 2: Technology assessment of direct air capture

In Chapter 2, a computationally efficient geospatial modelling framework was developed to evaluate technologies whose performance is influenced by regional variations. This framework can assist decision-makers in identifying optimal deployment locations by rapidly assessing technology performance across various regions. The framework was demonstrated through a case study on direct air capture (DAC) utilising solid sorbent adsorption-based technology.

A detailed process-level modelling of the adsorption-based DAC process was developed, incorporating 1D and 2D adsorption models. The information from this model was used to develop simplified DAC performance maps based on temperature and relative humidity, which was used in the geospatial modelling framework. The case study examined the influence of ambient temperature and relative humidity on the performance of a DAC process employing amine-functionalised solid sorbents. Additionally, five years of high-resolution hourly spatial weather data from NASA's MERRA-2 dataset was utilised to capture inter- and intra-annual variations in ambient conditions in different regions.

5.1.1.1 Chapter key findings

Temperature and relative humidity effects

Ambient conditions significantly affect DAC process performance, including capture rate, CO_2 capture rate, process productivity and energy requirements. For the studied sorbent, relative humidity was shown to have a more noticeable effect on process performance—in terms of productivity and energy requirements—with performance heightening at mild relative humidity in the range of 20%–60%. Temperature was shown to have a secondary effect on the process performance in the range of 1–30 ℃. However, as temperature increases above this level, its effect becomes more noticeable, with performance becoming progressively worse.

Process configurations

Two process cycle configurations were analysed—vacuum-pressure temperature swing adsorption (VTSA) and steam-assisted vacuum-pressure temperature swing adsorption (SA-VTSA). The SA-VTSA cycle demonstrated improved process produc-

tivity and generally lower energy requirements across various ambient conditions compared to the VTSA cycle.

Optimal regions for direct air capture deployment

For the studied sorbent operating SA-VTSA cycle, colder and drier regions—with temperatures above the operational limit of -15℃—are most favourable for DAC performance. These regions exhibit higher process productivity and lower energy requirements. This affects the levelised cost of direct air capture (LCOD), which varies based on regional climate conditions, as well as regional weighted average capital cost. At an electricity price of \$50 per MWh_{el}, the estimated LCOD—for 76% of the global land area excluding extremely cold regions—ranges between \$320–\$540 per tCO_2.

Environmental considerations

The DAC process was found to co-produce water, with production rates ranging from 0.4–3.5 tH_2O per tCO_2 captured, with humid regions having higher water co-production. Required land for DAC deployment is relatively small when only accounting for the DAC plants. However, the land requirements for the energy supply to power DAC operations can be substantial, especially if relying on intermittent renewable energy sources like solar photovoltaic (PV). For instance, solar PV-powered DAC at 10 Giga tonnes per annum of CO_2-scale could require 200,000–350,000 km^2, equivalent to 40%–70% of Spain's land area.

Implications for direct air capture deployment

Identifying regions with optimal ambient conditions and favourable economic factors can enhance performance and reduce the costs of DAC deployment. Decision-makers can use these insights to prioritise regions where DAC deployment would be most cost-effective and environmentally beneficial. However, from a holistic perspective, successful DAC deployment requires considering not only the climatic suitability but also the availability of low-carbon energy sources, proximity to secure CO_2 storage sites and the economic landscape.

Study limitations and future work

The study acknowledged several limitations. First, there is a lack of accurate isotherm models and kinetic data for various DAC sorbents, particularly at different ambient conditions and very low temperatures. This limits the ability to fully assess and compare the performance of different sorbents globally. Additionally, the study focused

on a specific DAC technology utilising amine-functionalized solid sorbent, mainly due to the limitation of data availability. Future work could utilise the developed framework to assess other DAC technologies and sorbents, allowing the mapping out of favourable DAC technologies and sorbents based on regional variation. Finally, the regional variation in energy costs was not addressed in this study. Since energy consumption is a significant component of DAC costs, incorporating regional energy prices would provide a more comprehensive assessment of LCOD across different regions.

5.1.1.2 Chapter overall contribution

Chapter 2 contributes to the field by providing an efficient framework for evaluating the regional performance of DAC technologies, as well as presenting how to conduct such an evaluation. The findings emphasise the critical role of ambient conditions and regional economic factors in determining the techno-economic feasibility of DAC deployment. This work lays the groundwork for more detailed system-level and policy assessments in subsequent chapters, ultimately aiding in the strategic planning and optimisation of DAC deployments.

5.1.2 Chapter 3: System assessment of direct air capture and its energy supply options

In Chapter 3, the geospatial modelling framework developed in Chapter 2 was extended to include system-level assessments by employing a process systems engineering approach—Resource-Task Network (RTN) representation—to model the complex interactions between resources (e.g., energy, materials) and tasks (technologies). This approach facilitates the design and optimisation of systems integrating multiple technologies with region-dependent performance. The framework was applied to assess the techno-economic and environmental performance of coupling DAC with various energy supply options, including intermittent renewable energy sources, nuclear energy and natural gas. This extension enables a holistic evaluation of DAC systems, capturing the synergies between different system elements and considering regional variations and constraints.

5.1.2.1 Chapter key findings

Feasibility of coupling direct air capture to using existing electrical grids

The study showed that current electricity grids are generally unsuitable for large-scale DAC deployment. Many grids have high carbon intensity, and coupling DAC with such grids can result in net CO_2 emissions over the project's lifetime. This is because the emissions associated with the electricity consumed by DAC can outweigh the CO_2 captured from the atmosphere, leading to an ineffective carbon removal process.

Performance of direct air capture with different low-carbon energy sources

To ensure net CO_2 removal and cost-effectiveness, the study found that DAC requires coupling with dedicated low-carbon energy sources that are designed to provide DAC with low-cost thermal heat. The most energy-efficient and cost-effective options identified were:

- **Nuclear power plants:** Coupling DAC with nuclear power plants was shown to offer the lowest gross levelised cost of direct air capture ($LCOD_{gross}$), ranging from \$246–\$503 per tCO_2. The integration allows for the co-production of electricity, enhancing overall energy efficiency.
- **Natural gas-fired combined cycle gas turbines with carbon capture and storage power plants:** DAC coupled with combined cycle gas turbines with carbon capture and storage power plants showed an $LCOD_{gross}$ of \$314–\$557 per tCO_2, assuming a natural gas price of \$50 per MWh. However, the viability of this coupling is sensitive to natural gas prices and, more importantly, methane leakage rates.
- **Intermittent renewable energy with energy storage:** Regions with high solar irradiation can achieve $LCOD_{gross}$ starting at \$319 per CO_2 when utilising concentrated solar power with thermal energy storage. In contrast, regions with low solar and wind resources are less suitable due to higher costs and land requirements.

Environmental considerations

The study showed that CO_2 removal efficiency varies across different energy supply options, with nuclear, concentrated solar power, and wind turbine-based systems achieving the highest efficiencies. Moreover, land requirements were the lowest when DAC was coupled with nuclear or natural gas technologies. In contrast, those relying on intermittent renewable energy sources require significantly more land, which may

limit deployment in regions with constrained land availability. Finally, the study showed that the DAC system can co-produce water, which might benefit arid regions. However, some energy supply options, such as concentrated solar power, may have higher water consumption due to system cooling requirements.

Implications for direct air capture deployment

Optimal deployment involves regions where the climate is optimal for the selected DAC technology, low-carbon energy sources are available, and CO_2 storage sites are nearby. Existing nuclear power plant sites are promising for DAC powered by nuclear energy deployment due to their existing licenses and permits and proximity to storage sites—in many cases. Moreover, regions with abundant natural gas reserves, where natural gas can be extracted and utilised with minimal leakage, can offer other promising deployment sites for DAC powered with combined cycle gas turbines with carbon capture and storage power plants. Lastly, arid regions with good solar irradiation and proximity to CO_2 storage sites offer promising potential for effective DAC with intermittent renewable energy deployment when concentrated solar power with thermal energy storage is utilised.

Study limitations and future work

Despite the comprehensive nature of this study, several limitations warrant further investigation. The evaluation was confined to adsorption-based DAC technology using an amine-functionalised sorbent, primarily due to limited data on the performance of diverse DAC sorbents and processes, such as amine scrubbing utilising amino acid salt solutions and moisture swing adsorption. As knowledge about DAC processes expands and novel sorbents and processes emerge, a better understanding of regional performance variations for alternative DAC technologies will be achieved, facilitating the development of systems more precisely tailored to specific regions and energy supply options. Future research could also incorporate the modelling of process transients and optimise operational cycles and control strategies under dynamic ambient conditions throughout the day and across seasons. Additionally, the framework developed in this study could be expanded to include low-carbon hydrogen production coupled with DAC to assess low-carbon fuel and chemical production, such as electrofuels and green methanol.

5.1.2.2 Chapter overall contribution

Chapter 3 enhances the geospatial modelling framework by incorporating system-level assessments, providing a holistic evaluation of DAC systems integrated with various energy supply options. The findings emphasise that coupling DAC with appropriate low-carbon energy sources is crucial for achieving cost-effective and environmentally sustainable CO_2 removal. This work highlights the importance of strategic planning, considering not only the DAC technology but also the energy infrastructure, economic factors and environmental impacts. The extended framework and insights from this chapter can aid in the strategic planning and optimisation of DAC deployments globally, offering valuable guidance to policymakers, investors and researchers.

5.1.3 Chapter 4: Policy assessment of hourly time-matching requirement in electrolytic hydrogen production

In Chapter 4, the geospatial modelling framework developed in the previous chapters was utilised to explore the implications of policy implementation on electrolytic hydrogen production. Specifically, the study analysed the enforcement of an hourly time-matching requirement for grid-connected electrolytic hydrogen production from intermittent renewable energy sources. The framework was used to model grid-connected electrolytic hydrogen production systems utilising newly built intermittent renewable energy and energy storage capacities under the hourly time-matching constraint. This approach captured the challenges and costs associated with synchronising hydrogen production with fluctuating intermittent renewable energy availability. 20 years of NASA's MERRA-2 weather data were employed, reflecting inter-annual and intra-annual variations in solar and wind resources and their impact on system design and costs when supplying highly reliable baseload hydrogen demand.

5.1.3.1 Chapter key findings

Impact of an hourly time-matching requirement on levelised cost of hydrogen

The study found that enforcing strict 100% hourly time-matching requirement significantly increases the levelised cost of hydrogen ($LCOH_2$) by \$3.8.–\$5.3 per kgH_2—corresponds to a 54%–96% increase—compared to systems that are powered directly by grid electricity. This cost increase arises from the need for additional capacities in energy generation, electrolysers and energy storage to mitigate renewable energy

intermittency. Additionally, the inter-annual variability of intermittent renewable energy can further increase costs by requiring additional system redundancies to maintain a consistent hydrogen supply across different years and handle worst-case scenarios. This leads to further increases in costs and material requirements, with lower utilisation rates of assets due to overcapacity and energy curtailment during periods of excess renewable generation.

Environmental return for an hourly time-matching requirement

The analysis showed that while strict hourly time-matching ensures minimal CO_2 emissions from electrolytic hydrogen, the associated increase in hydrogen production cost may not justify the environmental return. A modest relaxation of these time-matching requirements can offer a more practical route for scaling up low-carbon hydrogen production, optimising both costs and emission reductions. Furthermore, in regions with near-to-medium-term net-zero electrical grid targets, immediate electrolytic hydrogen production utilising 100% grid electricity would have a lifetime carbon intensity comparable to or even below blue hydrogen. Thus, priorities should focus on accelerating grid decarbonisation and identifying the most impactful low-carbon hydrogen applications where the avoided CO_2 is greatest, and the associated cost is minimised.

Study limitations and future work

The modelling was based on mean carbon intensity and linear decarbonisation trajectories for regional electrical grids. Incorporating more detailed regional grid decarbonisation models to capture hourly carbon intensity profiles could provide a more accurate assessment. Additionally, expanding the scope to include various hydrogen applications and evaluating their specific emission reduction potentials and economic feasibility using a national energy system model can capture the impact of hydrogen end-use applications and enhance the comprehensiveness of the analysis. Moreover, future research could explore application- and region-specific uses of hydrogen, such as assessing the regional feasibility of hydrogen distribution infrastructure and the viability of alternatives like electrification in long-haul heavy goods vehicles.

5.1.3.2 Chapter overall contribution

Chapter 4 contributes to the field by providing a critical assessment of the techno-economic and environmental implications of enforcing an hourly time-matching re-

quirement for grid-connected electrolytic hydrogen production. The findings highlight the complexities and unintended consequences of implementing stringent policy mandates, emphasising that the associated increase in hydrogen production costs may lead to CO_2 avoidance costs higher than those of alternative mitigation strategies. This work stresses the importance of a balanced policy framework that considers both economic viability and environmental impact. The study offers valuable insights into designing a cost-effective strategy for scaling up electrolytic hydrogen production. It emphasises the need to prioritise rapid grid decarbonisation and to deploy hydrogen where it can avoid the most CO_2 emissions for the least cost, ultimately facilitating a more cost-effective and efficient energy transition.

5.2 Future Work

In addition to highlighting future work and limitations in each chapter, this section summarises these and provides suggestions for potential areas for future work.

Extension of the modelling framework to other technologies and applications

The current modelling framework primarily focused on a specific DAC technology utilising amine-functionalised solid sorbents and on electrolytic hydrogen production using alkaline electrolysers. Future research can extend the framework to incorporate other DAC technologies and sorbents, such as liquid sorbents and moisture swing adsorption. This expansion would enable a more comprehensive assessment of various DAC technologies, allowing for the identification of the most suitable technologies for different regions based on ambient conditions and resource availability. Additionally, additional technologies and processes can be incorporated to assess the utilisation of CO_2 captured from DAC and hydrogen produced from intermittent renewable energy sources to produce electrofuels and chemicals.

Inclusion of CO_2 storage and utilisation mapping

This work did not account for CO_2 storage or utilisation sites in the DAC assessment. Future work can map and integrate CO_2 storage capacities, transportation networks and potential utilisation sites to provide a comprehensive mapping for potential DAC deployment sites. Similarly, in the hydrogen analysis, identifying and incorporating hydrogen utilisation sites, demand centres and infrastructure availability would enhance the assessment of hydrogen supply chains. Mapping low-carbon energy sources, such as nuclear facilities and low-leakage natural gas resources, would also support

more informed decision-making regarding the siting and scaling of DAC and hydrogen production facilities.

Model scalability and computational efficiency

As the modelling framework expands to include more technologies and applications, computational demands increase. Developing solution strategies or model reformulation methods to solve larger problems efficiently will be essential. Employing time series clustering approaches to reduce the number of similar models solves and geospatial clustering to minimise the spatial set without compromising accuracy can improve computational efficiency [300–304]. These enhancements would enable the application of the modelling framework to larger and more complex systems.

Advanced process modelling using machine learning

The simplified DAC model used in the geospatial analysis in this study was assumed to have a single operating condition with set performance parameters. Optimally, DAC process productivity and energy requirements can be operationally adjusted based on energy prices and weather conditions. Future research could employ advanced modelling techniques, such as machine learning, to capture the non-linear relationships between process performance and varying ambient conditions. Machine learning models—such as artificial neural networks (ANNs)—can handle large datasets and non-linear relationships, enabling the development of more accurate and flexible performance maps without excessive computational burdens, which can also be reduced to be used in linear programming formulation [305–307]. For instance, the Python OMLT package can facilitate the integration of ANNs into Pyomo [308].

Multi-year planning and handling of weather variability

The current modelling approach assumes representative weather profiles based on historical data. However, changing weather patterns due to climate change introduce uncertainties in renewable energy availability and process performance over time. Future work can involve multi-year planning that accounts for varying weather profiles and climate projections. Developing strategies to address inter-annual variability and extreme weather events would enhance the robustness of technology deployment plans [309, 310]. This could involve stochastic modelling techniques or scenario analyses that consider a range of possible future climates.

Incorporation of future cost projections and learning curves

The modelling framework currently utilises static cost assumptions for technologies and processes. Future research can incorporate dynamic cost projections and learning curves to reflect technological advancements. Integrating cost reduction trajectories for key technologies, such as DAC components, electrolysers and energy storage systems, would enable more accurate forecasting of long-term economic feasibility [311–313]. This approach would assist in strategic planning and investment decisions by identifying when and where technologies become cost-competitive.

Integration of prospective life cycle assessment

While this work focused on the techno-economic assessment and included some environmental metrics, such as CO_2 emission, water consumption and land requirement, incorporating more comprehensive life cycle assessment (LCA) methodologies would provide a more holistic evaluation of environmental impacts, including resource depletion, human health and ecosystem effects. Additionally, prospective LCA can account for future changes in technology and supply chains, reducing the risk of overestimating environmental impacts based on current data [314, 315]. Integrating LCA into the modelling framework would enable the identification of potential trade-offs and co-benefits associated with different low-carbon technologies and inform more sustainable technology choices.

Assessment of regional socio-economic impacts

Expanding the modelling framework to consider broader regional variables and impacts would provide valuable insights for policymakers. This includes assessing job creation potentials, supply chain considerations and regional economic development associated with deploying low-carbon technologies. Analysing the socio-economic benefits and challenges can help in designing policies that maximise positive outcomes for communities, support fair transitions and address potential inequalities.

REFERENCES

[1] Lee, H., Calvin, K., Dasgupta, D., Krinner, G., Mukherji, A., Thorne, P., Trisos, C., Romero, J., Aldunce, P., and Barrett, K. (2023). Climate change 2023: synthesis report. Contribution of working groups I, II and III to the sixth assessment report of the intergovernmental panel on climate change.

[2] Masson-Delmotte, V., Zhai, P., Pörtner, H.-O., Roberts, D., Skea, J., Shukla, P. R., Pirani, A., Moufouma-Okia, W., Péan, C., and Pidcock, R. (2018). Global Warming of 1.5℃. An IPCC Special Report on the impacts of global warming of 1.5℃ above pre-industrial levels and related global greenhouse gas emission pathways, in the context of strengthening the global response to the threat of climate change, sustainable development, and efforts to eradicate poverty, 1(5).

[3] United Nations. (2015). Chapter XXVII Environment, 7. d Paris Agreement. Available at: `https://treaties.un.org/doc/Treaties/2016/02/20160215%2006-03%20PM/Ch_XXVII-7-d.pdf`.

[4] Geels, F. W., Sovacool, B. K., Schwanen, T., and Sorrell, S. (2017). The Socio-Technical Dynamics of Low-Carbon Transitions. Joule, 1(3):463–479. 10.1016/j.joule.2017.09.018.

[5] Rogelj, J., Popp, A., Calvin, K. V., Luderer, G., Emmerling, J., Gernaat, D., Fujimori, S., Strefler, J., Hasegawa, T., Marangoni, G., Krey, V., Kriegler, E., Riahi, K., van Vuuren, D. P., Doelman, J., Drouet, L., Edmonds, J., Fricko, O., Harmsen, M., Havlík, P., Humpenöder, F., Stehfest, E., and Tavoni, M. (2018). Scenarios towards limiting global mean temperature increase below 1.5 ℃. Nature Climate Change, 8(4):325–332. 10.1038/s41558-018-0091-3.

[6] International Energy Agency (IEA). (2023). Greenhouse Gas Emissions from Energy Data Explorer. Available at: `https://www.iea.org/data-and-stati`

stics/data-tools/greenhouse-gas-emissions-from-energy-data-explorer.

[7] Ritchie, H. (2020). Sector by sector: where do global greenhouse gas emissions come from? Available at: https://ourworldindata.org/ghg-emissions-by-sector.

[8] Ritchie, H. and Rosado, P. (2024). Energy Mix. Available at: https://ourworldindata.org/energy-mix.

[9] Davis, S. J., Lewis, N. S., Shaner, M., Aggarwal, S., Arent, D., Azevedo, I. L., Benson, S. M., Bradley, T., Brouwer, J., Chiang, Y.-M., Clack, C. T. M., Cohen, A., Doig, S., Edmonds, J., Fennell, P., Field, C. B., Hannegan, B., Hodge, B.-M., Hoffert, M. I., Ingersoll, E., Jaramillo, P., Lackner, K. S., Mach, K. J., Mastrandrea, M., Ogden, J., Peterson, P. F., Sanchez, D. L., Sperling, D., Stagner, J., Trancik, J. E., Yang, C.-J., and Caldeira, K. (2018). Net-zero emissions energy systems. Science, 360(6396). 10.1126/science.aas9793.

[10] National Academies of Sciences, Engineering, and Medicine. (2019). Negative Emissions Technologies and Reliable Sequestration: A Research Agenda. The National Academies Press, Washington, DC.

[11] Royal Society and Royal Academy of Engineering. (2018). Greenhouse gas removal. Royal Society London.

[12] Smith, S., Geden, O., Nemet, G., Gidden, M., Lamb, W., Powis, C., Bellamy, R., Callaghan, M., Cowie, A., and Cox, E. (2023). The State of Carbon Dioxide Removal. 10.17605/OSF.IO/W3B4Z.

[13] Mac Dowell, N., Reiner, D. M., and Haszeldine, R. S. (2022). Comparing approaches for carbon dioxide removal. Joule, 6(10):2233–2239. 10.1016/j.joule.2022.09.005.

[14] Chiquier, S., Patrizio, P., Bui, M., Sunny, N., and Mac Dowell, N. (2022). A comparative analysis of the efficiency, timing, and permanence of CO_2 removal pathways. Energy & Environmental Science, 15(10):4389–4403. 10.1039/D2EE01021F.

[15] Hanna, R., Abdulla, A., Xu, Y., and Victor, D. G. (2021). Emergency deployment of direct air capture as a response to the climate crisis. Nature Communications, 12(1):368. 10.1038/s41467-020-20437-0.

[16] Vogt, E. T. C. and Weckhuysen, B. M. (2024). The refinery of the future. Nature, 629(8011):295–306. 10.1038/s41586-024-07322-2.

[17] International Energy Agency (IEA). (2023). World Energy Outlook 2023. Available at: https://www.iea.org/reports/world-energy-outlook-2023.

[18] Küng, L., Aeschlimann, S., Charalambous, C., McIlwaine, F., Young, J., Shannon, N., Strassel, K., Maesano, C. N., Kahsar, R., Pike, D., van der Spek, M., and Garcia, S. (2023). A roadmap for achieving scalable, safe, and low-cost direct air carbon capture and storage. Energy & Environmental Science, 16(10):4280–4304. 10.1039/D3EE01008B.

[19] Freire Ordóñez, D., Ganzer, C., Halfdanarson, T., González Garay, A., Patrizio, P., Bardow, A., Guillén-Gosálbez, G., Shah, N., and Mac Dowell, N. (2023). Quantifying global costs of reliable green hydrogen. Energy Advances, 2(12):2042–2054. 10.1039/D3YA00318C.

[20] Ameli, N., Dessens, O., Winning, M., Cronin, J., Chenet, H., Drummond, P., Calzadilla, A., Anandarajah, G., and Grubb, M. (2021). Higher cost of finance exacerbates a climate investment trap in developing economies. Nature Communications, 12(1):4046. 10.1038/s41467-021-24305-3.

[21] Global Wind Atlas. 3.0, a free, web-based application developed, owned and operated by the Technical University of Denmark (DTU). Available at: https://globalwindatlas.info.

[22] Global Solar Atlas. 2.0, a free, web-based application is developed and operated by the company Solargis sro on behalf of the World Bank Group, utilizing Solargis data, with funding provided by the Energy Sector Management Assistance Program (ESMAP). Available at: https://globalsolaratlas.

[23] Smith, P., Davis, S. J., Creutzig, F., Fuss, S., Minx, J., Gabrielle, B., Kato, E., Jackson, R. B., Cowie, A., Kriegler, E., van Vuuren, D. P., Rogelj, J., Ciais, P., Milne, J., Canadell, J. G., McCollum, D., Peters, G., Andrew, R., Krey, V., Shrestha, G., Friedlingstein, P., Gasser, T., Grübler, A., Heidug, W. K., Jonas, M., Jones, C. D., Kraxner, F., Littleton, E., Lowe, J., Moreira, J. R., Nakicenovic, N., Obersteiner, M., Patwardhan, A., Rogner, M., Rubin, E., Sharifi, A., Torvanger, A., Yamagata, Y., Edmonds, J., and Yongsung, C. (2016).

Biophysical and economic limits to negative CO_2 emissions. Nature Climate Change, 6(1):42–50. 10.1038/nclimate2870.

[24] Smith, S. M., Geden, O., Gidden, M. J., Lamb, W. F., Nemet, G. F., Minx, J. C., Buck, H., Burkevii, J., Cox, E., Edwards, M. R., Fuss, S., Injy Johnstone, , Müller-Hansen, F., Pongratz, J., Benedict S. Probst, , Roe, S., Schenuit, F., Schulte, I., and Vaughan, N. E. (2024). The State of Carbon Dioxide Removal 2024 - 2nd Edition. 10.17605/OSF.IO/F85QJ.

[25] The State of Carbon Dioxide Removal Data Portal. Available at: `https://portal.stateofcdr.org/explorer`.

[26] Gunnarsson, I., Aradóttir, E. S., Oelkers, E. H., Clark, D. E., Arnarson, M. , Sigfússon, B., Snæbjörnsdóttir, S. , Matter, J. M., Stute, M., Júlíusson, B. M., and Gíslason, S. R. (2018). The rapid and cost-effective capture and subsurface mineral storage of carbon and sulfur at the CarbFix2 site. International Journal of Greenhouse Gas Control, 79:117–126. 10.1016/j.ijggc.2018.08.014.

[27] Matter, J. M., Stute, M., Snæbjörnsdottir, S. , Oelkers, E. H., Gislason, S. R., Aradottir, E. S., Sigfusson, B., Gunnarsson, I., Sigurdardottir, H., Gunnlaugsson, E., Axelsson, G., Alfredsson, H. A., Wolff-Boenisch, D., Mesfin, K., Taya, D. F. d. l. R., Hall, J., Dideriksen, K., and Broecker, W. S. (2016). Rapid carbon mineralization for permanent disposal of anthropogenic carbon dioxide emissions. Science, 352(6291):1312–1314. 10.1126/science.aad8132.

[28] Scott, V., Haszeldine, R. S., Tett, S. F. B., and Oschlies, A. (2015). Fossil fuels in a trillion tonne world. Nature Climate Change, 5(5):419–423. 10.1038/nclimate2578.

[29] Fajardy, M., Patrizio, P., Daggash, H. A., and Mac Dowell, N. (2019). Negative Emissions: Priorities for Research and Policy Design. Frontiers in Climate, 1(6). 10.3389/fclim.2019.00006.

[30] Fasihi, M., Efimova, O., and Breyer, C. (2019). Techno-economic assessment of CO_2 direct air capture plants. Journal of Cleaner Production, 224:957–980. 10.1016/j.jclepro.2019.03.086.

[31] Herzog, H. (2022). Direct Air Capture. Greenhouse Gas Removal Technologies. The Royal Society of Chemistry.

[32] Zeman, F. S. and Lackner, K. S. (2004). Capturing carbon dioxide directly from the atmosphere. World Res. Rev., 16(2):157–172.

[33] Bouaboula, H., Chaouki, J., Belmabkhout, Y., and Zaabout, A. (2024). Comparative review of Direct air capture technologies: From technical, commercial, economic, and environmental aspects. Chemical Engineering Journal, 484:149411. https://doi.org/10.1016/j.cej.2024.149411.

[34] Erans, M., Sanz-Pérez, E. S., Hanak, D. P., Clulow, Z., Reiner, D. M., and Mutch, G. A. (2022). Direct air capture: process technology, techno-economic and socio-political challenges. Energy & Environmental Science. 10.1039/D1EE03523A.

[35] Boot-Handford, M. E., Abanades, J. C., Anthony, E. J., Blunt, M. J., Brandani, S., Mac Dowell, N., Fernández, J. R., Ferrari, M.-C., Gross, R., Hallett, J. P., Haszeldine, R. S., Heptonstall, P., Lyngfelt, A., Makuch, Z., Mangano, E., Porter, R. T. J., Pourkashanian, M., Rochelle, G. T., Shah, N., Yao, J. G., and Fennell, P. S. (2014). Carbon capture and storage update. Energy & Environmental Science, 7(1):130–189. 10.1039/C3EE42350F.

[36] Bui, M., Adjiman, C. S., Bardow, A., Anthony, E. J., Boston, A., Brown, S., Fennell, P. S., Fuss, S., Galindo, A., Hackett, L. A., Hallett, J. P., Herzog, H. J., Jackson, G., Kemper, J., Krevor, S., Maitland, G. C., Matuszewski, M., Metcalfe, I. S., Petit, C., Puxty, G., Reimer, J., Reiner, D. M., Rubin, E. S., Scott, S. A., Shah, N., Smit, B., Trusler, J. P. M., Webley, P., Wilcox, J., and Mac Dowell, N. (2018). Carbon capture and storage (CCS): the way forward. Energy & Environmental Science, 11(5):1062–1176. 10.1039/C7EE02342A.

[37] McQueen, N., Gomes, K. V., McCormick, C., Blumanthal, K., Pisciotta, M., and Wilcox, J. (2021). A review of direct air capture (DAC): scaling up commercial technologies and innovating for the future. Progress in Energy, 3(3):032001. 10.1088/2516-1083/abf1ce.

[38] Low, M.-Y., Barton, L. V., Pini, R., and Petit, C. (2023). Analytical review of the current state of knowledge of adsorption materials and processes for direct air capture. Chemical Engineering Research and Design, 189:745–767. 10.1016/j.cherd.2022.11.040.

[39] Azarabadi, H. and Lackner, K. S. (2019). A sorbent-focused techno-economic analysis of direct air capture. Applied Energy, 250:959–975. 10.1016/j.apenergy.2019.04.012.

[40] Climeworks. (2024). Climeworks switches on world's largest direct air capture plant. Available at: https://climeworks.com/press-release/climeworks-switches-on-worlds-largest-direct-air-capture-plant-mammoth.

[41] Keith, D. W., Holmes, G., St. Angelo, D., and Heidel, K. (2018). A Process for Capturing CO_2 from the Atmosphere. Joule, 2(8):1573–1594. 10.1016/j.joule.2018.05.006.

[42] Deutz, S. and Bardow, A. (2021). Life-cycle assessment of an industrial direct air capture process based on temperature–vacuum swing adsorption. Nature Energy, 6(2):203–213. 10.1038/s41560-020-00771-9.

[43] Madhu, K., Pauliuk, S., Dhathri, S., and Creutzig, F. (2021). Understanding environmental trade-offs and resource demand of direct air capture technologies through comparative life-cycle assessment. Nature Energy, 6(11):1035–1044. 10.1038/s41560-021-00922-6.

[44] Terlouw, T., Treyer, K., Bauer, C., and Mazzotti, M. (2021). Life Cycle Assessment of Direct Air Carbon Capture and Storage with Low-Carbon Energy Sources. Environmental Science & Technology. 10.1021/acs.est.1c03263.

[45] Holmes, G., Nold, K., Walsh, T., Heidel, K., Henderson, M. A., Ritchie, J., Klavins, P., Singh, A., and Keith, D. W. (2013). Outdoor Prototype Results for Direct Atmospheric Capture of Carbon Dioxide. Energy Procedia, 37:6079–6095. https://doi.org/10.1016/j.egypro.2013.06.537.

[46] Sabatino, F., Grimm, A., Gallucci, F., van Sint Annaland, M., Kramer, G. J., and Gazzani, M. (2021). A comparative energy and costs assessment and optimization for direct air capture technologies. Joule. 10.1016/j.joule.2021.05.023.

[47] Storegga. Phase 1 Final Report: Project Dreamcatcher. Available at: https://assets.publishing.service.gov.uk/media/62a054bf8fa8f5038ccc1a7b/pale-blue-dot-project-dreamcatcher.pdf.

[48] Barzagli, F., Giorgi, C., Mani, F., and Peruzzini, M. (2020). Screening Study of Different Amine-Based Solutions as Sorbents for Direct CO_2 Capture from Air.

ACS Sustainable Chemistry & Engineering, 8(37):14013–14021. 10.1021/acssuschemeng.0c03800.

[49] Rochelle, G. T. (2009). Amine Scrubbing for CO_2 Capture. Science, 325(5948):1652–1654. 10.1126/science.1176731.

[50] Kiani, A., Jiang, K., and Feron, P. (2020). Techno-Economic Assessment for CO_2 Capture From Air Using a Conventional Liquid-Based Absorption Process. Frontiers in Energy Research, 8. 10.3389/fenrg.2020.00092.

[51] Kiani, A., Feron, P., Conway, W., Pourkhesalian, A., Bennett, R. D., Grillmeier, D., Neoh, C. R., and Puxty, G. Direct Air Capture of CO_2 using Amine-based Capture Technology. The 16th Greenhouse Gas Control Technologies Conference (GHGT-16). Lyon, France, 23–27 October 2022.

[52] Brethomé, F. M., Williams, N. J., Seipp, C. A., Kidder, M. K., and Custelcean, R. (2018). Direct air capture of CO_2 via aqueous-phase absorption and crystalline-phase release using concentrated solar power. Nature Energy, 3(7):553–559. 10.1038/s41560-018-0150-z.

[53] Custelcean, R., Williams, N. J., Garrabrant, K. A., Agullo, P., Brethomé, F. M., Martin, H. J., and Kidder, M. K. (2019). Direct Air Capture of CO_2 with Aqueous Amino Acids and Solid Bis-iminoguanidines (BIGs). Industrial & Engineering Chemistry Research, 58(51):23338–23346. 10.1021/acs.iecr.9b04800.

[54] Rolls-Royce and CSIRO. (2021). Project ENCORE - Direct Air Capture Final Report. Available at: `https://assets.publishing.service.gov.uk/media/6281f3428fa8f5562179576b/rolls-royce-encore-project.pdf`.

[55] Sanz-Pérez, E. S., Murdock, C. R., Didas, S. A., and Jones, C. W. (2016). Direct Capture of CO_2 from Ambient Air. Chemical Reviews, 116(19):11840–11876. 10.1021/acs.chemrev.6b00173.

[56] Panda, D., Kulkarni, V., and Singh, S. K. (2023). Evaluation of amine-based solid adsorbents for direct air capture: a critical review. Reaction Chemistry & Engineering, 8(1):10–40. 10.1039/D2RE00211F.

[57] Wurzbacher, J. A., Gebald, C., Piatkowski, N., and Steinfeld, A. (2012). Concurrent Separation of CO_2 and H_2O from Air by a Temperature-Vacuum Swing Adsorption/Desorption Cycle. Environmental Science & Technology, 46(16):9191–9198. 10.1021/es301953k.

[58] Liu, J., Wei, Y., and Zhao, Y. (2019). Trace Carbon Dioxide Capture by Metal–Organic Frameworks. ACS Sustainable Chemistry & Engineering, 7(1):82–93. 10.1021/acssuschemeng.8b05590.

[59] Shi, X., Xiao, H., Azarabadi, H., Song, J., Wu, X., Chen, X., and Lackner, K. S. (2020). Sorbents for the Direct Capture of CO_2 from Ambient Air. Angewandte Chemie International Edition, 59(18):6984–7006. 10.1002/anie.201906756.

[60] Sun, J., Zhao, M., Huang, L., Zhang, T., and Wang, Q. (2023). Recent progress on direct air capture of carbon dioxide. Current Opinion in Green and Sustainable Chemistry, page 100752. 10.1016/j.cogsc.2023.100752.

[61] Zhu, X., Xie, W., Wu, J., Miao, Y., Xiang, C., Chen, C., Ge, B., Gan, Z., Yang, F., Zhang, M., O'Hare, D., Li, J., Ge, T., and Wang, R. (2022). Recent advances in direct air capture by adsorption. Chemical Society Reviews, 51(15):6574–6651. 10.1039/D1CS00970B.

[62] Guo, M., Wu, H., Lv, L., Meng, H., Yun, J., Jin, J., and Mi, J. (2021). A Highly Efficient and Stable Composite of Polyacrylate and Metal–Organic Framework Prepared by Interface Engineering for Direct Air Capture. ACS Applied Materials & Interfaces, 13(18):21775–21785. 10.1021/acsami.1c03661.

[63] Bhatt, P. M., Belmabkhout, Y., Cadiau, A., Adil, K., Shekhah, O., Shkurenko, A., Barbour, L. J., and Eddaoudi, M. (2016). A Fine-Tuned Fluorinated MOF Addresses the Needs for Trace CO_2 Removal and Air Capture Using Physisorption. Journal of the American Chemical Society, 138(29):9301–9307. 10.1021/jacs.6b05345.

[64] Thakkar, H., Eastman, S., Hajari, A., Rownaghi, A. A., Knox, J. C., and Rezaei, F. (2016). 3D-Printed Zeolite Monoliths for CO_2 Removal from Enclosed Environments. ACS Applied Materials & Interfaces, 8(41):27753–27761. 10.1021/acsami.6b09647.

[65] Gebald, C., Meier, W., Repond, N., Rüesch, T., and Wurzbacher, J. A. (2017). Direct air capture device. US Patent Number: 20170106330A1.

[66] Gebald, C., Piatkowski, N., Rüesch, T., and Wurzbacher, J. A. (2014). Low-pressure drop structure of particle adsorbent bed for adsorption gas separation process. WIPO Patent Number: 2014170184A1.

[67] Gebald, C., Repond, N., and Wurzbacher, J. A. (2019). Steam assisted vacuum desorption process for carbon dioxide capture. US Patent Number: 10279306B2.

[68] Stampi-Bombelli, V., van der Spek, M., and Mazzotti, M. (2020). Analysis of direct capture of CO_2 from ambient air via steam-assisted temperature–vacuum swing adsorption. Adsorption, 26(7):1183–1197. 10.1007/s10450-020-00249-w.

[69] Heydari-Gorji, A., Belmabkhout, Y., and Sayari, A. (2011). Degradation of amine-supported CO_2 adsorbents in the presence of oxygen-containing gases. Microporous and Mesoporous Materials, 145(1-3):146–149. 10.1016/j.micromeso.2011.05.010.

[70] Lee, W. H., Zhang, X., Banerjee, S., Jones, C. W., Realff, M. J., and Lively, R. P. (2023). Sorbent-coated carbon fibers for direct air capture using electrically driven temperature swing adsorption. Joule, 7(6):1241–1259. 10.1016/j.joule.2023.05.016.

[71] Schellevis, M., Jacobs, T., and Brilman, W. (2020). CO_2 Capture From Air in a Radial Flow Contactor: Batch or Continuous Operation? Frontiers in Chemical Engineering, 2. 10.3389/fceng.2020.596555.

[72] Yu, Q. and Brilman, W. (2020). A Radial Flow Contactor for Ambient Air CO_2 Capture. Applied Sciences, 10(3):1080. 10.3390/app10031080.

[73] Zhang, W., Liu, H., Sun, C., Drage, T. C., and Snape, C. E. (2014). Capturing CO_2 from ambient air using a polyethyleneimine–silica adsorbent in fluidized beds. Chemical Engineering Science, 116:306–316. 10.1016/j.ces.2014.05.018.

[74] Abanades, J. C., Criado, Y. A., and White, H. I. (2023). Direct capture of carbon dioxide from the atmosphere using bricks of calcium hydroxide. Cell Reports Physical Science, 4(4):101339. 10.1016/j.xcrp.2023.101339.

[75] Erans, M., Nabavi, S. A., and Manović, V. (2020). Carbonation of lime-based materials under ambient conditions for direct air capture. Journal of Cleaner Production, 242:118330. 10.1016/j.jclepro.2019.118330.

[76] McQueen, N., Kelemen, P., Dipple, G., Renforth, P., and Wilcox, J. (2020). Ambient weathering of magnesium oxide for CO_2 removal from air. Nature Communications, 11(1):3299. 10.1038/s41467-020-16510-3.

[77] Graham, E. J., Sheha, M., Mallapragada, D. S., Herzog, H. J., Gençer, E., Cross, P., Custer, J. P., Goff, A., and Cormier, I. (2024). Optimization of a combined power plant CO_2 capture and direct air capture concept for flexible power plant operation. Energy & Environmental Science. 10.1039/D4EE00309H.

[78] Sheha, M., Graham, E. J., Gençer, E., Mallapragada, D., Herzog, H., Cross, P., Custer, J., Goff, A., and Cormier, I. (2024). Techno-economic analysis of a combined power plant CO_2 capture and direct air capture concept for flexible power plant operation. Computers & Chemical Engineering, 180:108472. 10.1016/j.compchemeng.2023.108472.

[79] McQueen, N. and Drennan, D. (2024). The use of warehouse automation technology for scalable and low-cost direct air capture. Frontiers in Climate, 6. 10.3389/fclim.2024.1415642.

[80] McQueen, N., Ghoussoub, M., Mills, J., and Scholten, M. (2022). A scalable direct air capture process based on accelerated weathering of calcium hydroxide. Heirloom Carbon Technologies.

[81] Lackner, K. S. (2009). Capture of carbon dioxide from ambient air. The European Physical Journal Special Topics, 176(1):93–106. 10.1140/epjst/e2009-01150-3.

[82] Wang, T., Lackner, K. S., and Wright, A. B. (2013). Moisture-swing sorption for carbon dioxide capture from ambient air: a thermodynamic analysis. Physical Chemistry Chemical Physics, 15(2):504–514. 10.1039/C2CP43124F.

[83] Rahimi, M., Khurram, A., Hatton, T. A., and Gallant, B. (2022). Electrochemical carbon capture processes for mitigation of CO_2 emissions. Chemical Society Reviews, 51(20):8676–8695. 10.1039/D2CS00443G.

[84] Massen-Hane, M., Diederichsen, K. M., and Hatton, T. A. (2024). Engineering redox-active electrochemically mediated carbon dioxide capture systems. Nature Chemical Engineering, 1(1):35–44. 10.1038/s44286-023-00003-3.

[85] Ozkan, M., Shiner, A., Kongi, N., Hatton, T. A., Oldham, S., and Sanders, E. (2024). Electrochemical direct air capture and direct ocean capture: The next frontier in carbon removal. Chem, 10(1):3–6. https://doi.org/10.1016/j.chempr.2023.12.015.

[86] Sabatino, F., Mehta, M., Grimm, A., Gazzani, M., Gallucci, F., Kramer, G. J., and van Sint Annaland, M. (2020). Evaluation of a Direct Air Capture Process Combining Wet Scrubbing and Bipolar Membrane Electrodialysis. Industrial & Engineering Chemistry Research, 59(15):7007–7020. 10.1021/acs.iecr.9b05641.

[87] Shu, Q., Legrand, L., Kuntke, P., Tedesco, M., and Hamelers, H. V. M. (2020). Electrochemical Regeneration of Spent Alkaline Absorbent from Direct Air Capture. Environmental Science & Technology, 54(14):8990–8998. 10.1021/acs.est.0c01977.

[88] Sabatino, F., Gazzani, M., Gallucci, F., and van Sint Annaland, M. (2022). Modeling, Optimization, and Techno-Economic Analysis of Bipolar Membrane Electrodialysis for Direct Air Capture Processes. Industrial & Engineering Chemistry Research, 61(34):12668–12679. 10.1021/acs.iecr.2c00889.

[89] Bui, J. C., Lucas, , Lees, E. W., Liu, A. K., Atwater, H. A., Xiang, C., Bell, A. T., and Weber, A. Z. (2023). Analysis of bipolar membranes for electrochemical CO_2 capture from air and oceanwater. Energy & Environmental Science, 16(11):5076–5095. 10.1039/D3EE01606D.

[90] Jin, S., Wu, M., Gordon, R. G., Aziz, M. J., and Kwabi, D. G. (2020). pH swing cycle for CO_2 capture electrochemically driven through proton-coupled electron transfer. Energy & Environmental Science, 13(10):3706–3722. 10.1039/D0EE01834A.

[91] Seo, H. and Hatton, T. A. (2023). Electrochemical direct air capture of CO_2 using neutral red as reversible redox-active material. Nature Communications, 14(1):313. 10.1038/s41467-023-35866-w.

[92] Seo, H., Rahimi, M., and Hatton, T. A. (2022). Electrochemical Carbon Dioxide Capture and Release with a Redox-Active Amine. Journal of the American Chemical Society, 144(5):2164–2170. 10.1021/jacs.1c10656. doi: 10.1021/jacs.1c10656.

[93] Xie, H., Wu, Y., Liu, T., Wang, F., Chen, B., and Liang, B. (2020). Low-energy-consumption electrochemical CO_2 capture driven by biomimetic phenazine derivatives redox medium. Applied Energy, 259:114119. 10.1016/j.apenergy.2019.114119.

[94] Gobaille-Shaw, G., Ghosh, S., and Chadwick, N. (2022). Method of capturing a target species from a gas. Patent Number: WO2022195299A1.

[95] Diederichsen, K. M., Liu, Y., Ozbek, N., Seo, H., and Hatton, T. A. (2022). Toward solvent-free continuous-flow electrochemically mediated carbon capture with high-concentration liquid quinone chemistry. Joule, 6(1):221–239. 10.1016/j.joule.2021.12.001.

[96] Hemmatifar, A., Kang, J. S., Ozbek, N., Tan, K.-J., and Hatton, T. A. (2022). Electrochemically Mediated Direct CO_2 Capture by a Stackable Bipolar Cell. ChemSusChem, 15(6):e202102533. 10.1002/cssc.202102533.

[97] Liu, Y., Ye, H.-Z., Diederichsen, K. M., Van Voorhis, T., and Hatton, T. A. (2020). Electrochemically mediated carbon dioxide separation with quinone chemistry in salt-concentrated aqueous media. Nature Communications, 11(1):2278. 10.1038/s41467-020-16150-7.

[98] Voskian, S. and Hatton, T. A. (2019). Faradaic electro-swing reactive adsorption for CO_2 capture. Energy & Environmental Science, 12(12):3530–3547. 10.1039/C9EE02412C.

[99] Li, Q., Batchelor-McAuley, C., Lawrence, N. S., Hartshorne, R. S., and Compton, R. G. (2011). Semiquinone Intermediates in the Two-Electron Reduction of Quinones in Aqueous Media and their Exceptionally High Reactivity towards Oxygen Reduction. ChemPhysChem, 12(7):1255–1257. 10.1002/cphc.201100174.

[100] An, K., Farooqui, A., and McCoy, S. T. (2022). The impact of climate on solvent-based direct air capture systems. Applied Energy, 325:119895. 10.1016/j.apenergy.2022.119895.

[101] Gebald, C., Wurzbacher, J. A., Borgschulte, A., Zimmermann, T., and Steinfeld, A. (2014). Single-Component and Binary CO_2 and H_2O Adsorption of Amine-Functionalized Cellulose. Environmental Science & Technology, 48(4):2497–2504. 10.1021/es404430g.

[102] Young, J., García-Díez, E., Garcia, S., and van der Spek, M. (2021). The impact of binary water–CO_2 isotherm models on the optimal performance of sorbent-based direct air capture processes. Energy & Environmental Science. 10.1039/D1EE01272J.

[103] Ward, A., Papathanasiou, M. M., and Pini, R. (2024). The impact of design and operational parameters on the optimal performance of direct air capture units using solid sorbents. Adsorption. 10.1007/s10450-024-00526-y.

[104] Wiegner, J. F., Grimm, A., Weimann, L., and Gazzani, M. (2022). Optimal Design and Operation of Solid Sorbent Direct Air Capture Processes at Varying Ambient Conditions. Industrial & Engineering Chemistry Research, 61(34):12649–12667. 10.1021/acs.iecr.2c00681.

[105] Leonzio, G., Fennell, P., and Shah, N. (2022). Modelling and Analysis of Direct Air Capture Systems in Different Locations. Chemical Engineering Transactions, 96:1–6.

[106] Schellevis, H. M., van Schagen, T. N., and Brilman, D. W. F. (2021). Process optimization of a fixed bed reactor system for direct air capture. International Journal of Greenhouse Gas Control, 110:103431. 10.1016/j.ijggc.2021.103431.

[107] Schellevis, H. M., de la Combé, J. D., and Brilman, D. W. F. (2024). Optimizing direct air capture under varying weather conditions. Energy Advances, 3(7):1678–1687. 10.1039/D4YA00200H.

[108] Bos, M. J., Kreuger, T., Kersten, S. R. A., and Brilman, D. W. F. (2019). Study on transport phenomena and intrinsic kinetics for CO_2 adsorption in solid amine sorbent. Chemical Engineering Journal, 377:120374. 10.1016/j.cej.2018.11.072.

[109] Liu, H., Lin, H., Dai, S., and Jiang, D.-e. (2024). Minimal Kinetic Model of Direct Air Capture of CO_2 by Supported Amine Sorbents in Dry and Humid Conditions. Industrial & Engineering Chemistry Research, 63(13):5871–5879. 10.1021/acs.iecr.3c04535.

[110] Low, M.-Y. A., Danaci, D., Sturman, C., and Petit, C. (2025). Quantification of temperature-dependent CO_2 adsorption kinetics in Lewatit VP OC 1065, Purolite A110, and TIFSIX-3-Ni for direct air capture. Chemical Engineering Research and Design, 215:443–452. 10.1016/j.cherd.2025.01.048.

[111] Brooks, B.-G. J., Geissler, C. H., An, K., McCoy, S. T., Middleton, R. S., and Ogland-Hand, J. D. (2024). The performance of solvent-based direct air capture across geospatial and temporal climate regimes. Frontiers in Climate, 6. 10.3389/fclim.2024.1394728.

[112] Terlouw, T., Pokras, D., Becattini, V., and Mazzotti, M. (2024). Assessment of Potential and Techno-Economic Performance of Solid Sorbent Direct Air Capture with CO_2 Storage in Europe. Environmental Science & Technology. 10.1021/acs.est.3c10041.

[113] Sachio, S., Ward, A., Pini, R., and Papathanasiou, M. M. (2024). Operability-economics trade-offs in adsorption-based CO_2 capture processes. Communications Engineering, 3(1):94. 10.1038/s44172-024-00244-x.

[114] Sendi, M., Bui, M., Mac Dowell, N., and Fennell, P. (2022). Geospatial analysis of regional climate impacts to accelerate cost-efficient direct air capture deployment. One Earth, 5(10):1153–1164. 10.1016/j.oneear.2022.09.003.

[115] Sendi, M., Bui, M., Mac Dowell, N., and Fennell, P. Regional techno-economic analysis of different solid sorbent-based direct air capture configurations. The 16th Greenhouse Gas Control Technologies Conference (GHGT-16). Lyon, France, 23–27 October 2022.

[116] Sinha, A., Darunte, L. A., Jones, C. W., Realff, M. J., and Kawajiri, Y. (2017). Systems Design and Economic Analysis of Direct Air Capture of CO_2 through Temperature Vacuum Swing Adsorption Using MIL-101(Cr)-PEI-800 and mmen-Mg2(dobpdc) MOF Adsorbents. Industrial & Engineering Chemistry Research, 56(3):750–764. 10.1021/acs.iecr.6b03887.

[117] Wijesiri, R. P., Knowles, G. P., Yeasmin, H., Hoadley, A. F. A., and Chaffee, A. L. (2019). Technoeconomic Evaluation of a Process Capturing CO_2 Directly from Air. Processes, 7(8):503. 10.3390/pr7080503.

[118] Zhu, X., Ge, T., Yang, F., and Wang, R. (2021). Design of steam-assisted temperature vacuum-swing adsorption processes for efficient CO_2 capture from ambient air. Renewable and Sustainable Energy Reviews, 137:110651. 10.1016/j.rser.2020.110651.

[119] Leonzio, G., Fennell, P. S., and Shah, N. (2022). A Comparative Study of Different Sorbents in the Context of Direct Air Capture (DAC): Evaluation of

Key Performance Indicators and Comparisons. Applied Sciences, 12(5):2618. 10.3390/app12052618.

[120] Haghpanah, R., Majumder, A., Nilam, R., Rajendran, A., Farooq, S., Karimi, I. A., and Amanullah, M. (2013). Multiobjective Optimization of a Four-Step Adsorption Process for Postcombustion CO_2Capture Via Finite Volume Simulation. Industrial & Engineering Chemistry Research, 52(11):4249–4265. 10.1021/ie302658y.

[121] Casas, N., Schell, J., Pini, R., and Mazzotti, M. (2012). Fixed bed adsorption of CO_2/H2 mixtures on activated carbon: experiments and modeling. Adsorption, 18(2):143–161. 10.1007/s10450-012-9389-z.

[122] Javeed, S., Qamar, S., Seidel-Morgenstern, A., and Warnecke, G. (2011). Efficient and accurate numerical simulation of nonlinear chromatographic processes. Computers & Chemical Engineering, 35(11):2294–2305. 10.1016/j.compchemeng.2010.10.002.

[123] Webley, P. A. and He, J. (2000). Fast solution-adaptive finite volume method for PSA/VSA cycle simulation; 1 single step simulation. Computers & Chemical Engineering, 23(11):1701–1712. https://doi.org/10.1016/S0098-1354(99)00320-8.

[124] Hasan, M. F., Baliban, R. C., Elia, J. A., and Floudas, C. A. (2012). Modeling, simulation, and optimization of postcombustion CO_2 capture for variable feed concentration and flow rate. 2. Pressure swing adsorption and vacuum swing adsorption processes. Industrial & engineering chemistry research, 51(48):15665–15682. 10.1021/ie301572n.

[125] Wurzbacher, J. A., Gebald, C., Brunner, S., and Steinfeld, A. (2016). Heat and mass transfer of temperature–vacuum swing desorption for CO_2 capture from air. Chemical Engineering Journal, 283:1329–1338. 10.1016/j.cej.2015.08.035.

[126] Wurzbacher, J. A. Development of a temperature-vacuum swing process for CO_2 capture from ambient air. Thesis, (2015).

[127] LeVeque, R. J. (2002). Finite volume methods for hyperbolic problems, volume 31. Cambridge University Press.

[128] Vogtenhuber, H., Pernsteiner, D., and Hofmann, R. (2019). Experimental and Numerical Investigations on Heat Transfer of Bare Tubes in a Bubbling Fluidized

Bed with Respect to Better Heat Integration in Temperature Swing Adsorption Systems. Energies, 12(14):2646. 10.3390/en12142646.

[129] Johnson Controls. (2019). High Pressure Rotary Screw Compressors Specifications. Available at: https://docs.johnsoncontrols.com/industrialrefrigeration/api/khub/documents/qOJN~RMGQli9hh1XWleuvQ/content.

[130] White, C. W. and Weiland, N. T. (2018). Evaluation of Property Methods for Modeling Direct-Supercritical CO_2 Power Cycles. Journal of Engineering for Gas Turbines and Power, 140(1):011701. 10.1115/1.4037665.

[131] Esen, H., Inalli, M., Esen, M., and Pihtili, K. (2007). Energy and exergy analysis of a ground-coupled heat pump system with two horizontal ground heat exchangers. Building and Environment, 42(10):3606–3615. 10.1016/j.buildenv.2006.10.014.

[132] Ozgener, O. and Hepbasli, A. (2005). Experimental performance analysis of a solar assisted ground-source heat pump greenhouse heating system. Energy and Buildings, 37(1):101–110. 10.1016/j.enbuild.2004.06.003.

[133] Gelaro, R., McCarty, W., Suárez, M. J., Todling, R., Molod, A., Takacs, L., Randles, C. A., Darmenov, A., Bosilovich, M. G., Reichle, R., Wargan, K., Coy, L., Cullather, R., Draper, C., Akella, S., Buchard, V., Conaty, A., da Silva, A. M., Gu, W., Kim, G.-K., Koster, R., Lucchesi, R., Merkova, D., Nielsen, J. E., Partyka, G., Pawson, S., Putman, W., Rienecker, M., Schubert, S. D., Sienkiewicz, M., and Zhao, B. (2017). The Modern-Era Retrospective Analysis for Research and Applications, Version 2 (MERRA-2). Journal of Climate, 30(14):5419–5454. 10.1175/jcli-d-16-0758.1.

[134] Sendi, M., Bui, M., Mac Dowell, N., and Fennell, P. (2024). Geospatial techno-economic and environmental assessment of different energy options for solid sorbent direct air capture. Cell Reports Sustainability, 1:100151. 10.1016/j.crsus.2024.100151.

[135] Rim, G., Kong, F., Song, M., Rosu, C., Priyadarshini, P., Lively, R. P., and Jones, C. W. (2022). Sub-Ambient Temperature Direct Air Capture of CO_2 using Amine-Impregnated MIL-101(Cr) Enables Ambient Temperature CO_2 Recovery. JACS Au, 2(2):380–393. 10.1021/jacsau.1c00414.

[136] Song, M., Rim, G., Kong, F., Priyadarshini, P., Rosu, C., Lively, R. P., and Jones, C. W. (2022). Cold-Temperature Capture of Carbon Dioxide with Water Coproduction from Air Using Commercial Zeolites. Industrial & Engineering Chemistry Research, 61(36):13624–13634. 10.1021/acs.iecr.2c02041.

[137] Climwroks. Climeworks Plant. Available at: https://www.venturelab.swiss/demandit/files/M_BB941CC4DCEF687AD98/dms/File/CLIMEWORKS_productsheet_P_mail.pdf.

[138] Olympios, A., Mersch, M., Sapin, P., Pantaleo, A., and Markides, C. (2021). Library of price and performance data of domestic and commercial technologies for low-carbon energy systems. Zenodo. 10.5281/zenodo.5758943.

[139] Towler, G. and Sinnott, R. (2021). Chemical engineering design: principles, practice and economics of plant and process design. Butterworth-Heinemann.

[140] Fuss, S., Lamb, W. F., Callaghan, M. W., Hilaire, J., Creutzig, F., Amann, T., Beringer, T., de Oliveira Garcia, W., Hartmann, J., Khanna, T., Luderer, G., Nemet, G. F., Rogelj, J., Smith, P., Vicente, J. L. V., Wilcox, J., del Mar Zamora Dominguez, M., and Minx, J. C. (2018). Negative emissions—Part 2: Costs, potentials and side effects. Environmental Research Letters, 13(6):063002. 10.1088/1748-9326/aabf9f.

[141] Viebahn, P., Scholz, A., and Zelt, O. (2019). The Potential Role of Direct Air Capture in the German Energy Research Program—Results of a Multi-Dimensional Analysis. Energies, 12(18):3443. 10.3390/en12183443.

[142] Cheng, V. K. M. and Hammond, G. P. (2017). Life-cycle energy densities and land-take requirements of various power generators: A UK perspective. Journal of the Energy Institute, 90(2):201–213. 10.1016/j.joei.2016.02.003.

[143] Ong, S., Campbell, C., Denholm, P., Margolis, R., and Heath, G. Land-use requirements for solar power plants in the United States. (2013). Report, National Renewable Energy Lab (NREL), Golden, CO (United States).

[144] U.S. Energy Information Administration (EIA). (2022). Net electricity consumption worldwide in select years from 1980 to 2021 (in terawatt-hours). Statista. Available at: https://www.statista.com/statistics/280704/world-power-consumption/.

[145] International Energy Agency (IEA). (2019). Global Energy & CO_2 Status Report 2019. Available at: https://www.iea.org/reports/global-energy-co2-status-report-2019/emissions.

[146] Bertoni, L., Roussanaly, S., Riboldi, L., Anantharaman, R., and Gazzani, M. (2024). Integrating direct air capture with small modular nuclear reactors: understanding performance, cost, and potential. Journal of Physics: Energy, 6(2):025004. 10.1088/2515-7655/ad2374.

[147] Cheng, P., Thierry, D. M., Hendrix, H., Dombrowski, K. D., Sachde, D. J., Realff, M. J., and Scott, J. K. (2023). Modeling and optimization of carbon-negative NGCC plant enabled by modular direct air capture. Applied Energy, 341:121076. 10.1016/j.apenergy.2023.121076.

[148] Fahr, S., Powell, J., Favero, A., Giarrusso, A. J., Lively, R. P., and Realff, M. J. (2022). Assessing the physical potential capacity of direct air capture with integrated supply of low-carbon energy sources. Greenhouse Gases: Science and Technology, 12(1):170–188. 10.1002/ghg.2136.

[149] Favero, A., Realff, M., Lucas, M., Giarrusso, A., and Lang, K. (2023). Geo-Spatial Economic Assessment of the Potential Development of Bioenergy Combined with Direct Air Carbon Capture (BEDAC) in the USA. Environmental Science & Technology, 57(51):21681–21690. 10.1021/acs.est.3c06975.

[150] McQueen, N., Psarras, P., Pilorgé, H., Liguori, S., He, J., Yuan, M., Woodall, C. M., Kian, K., Pierpoint, L., Jurewicz, J., Lucas, J. M., Jacobson, R., Deich, N., and Wilcox, J. (2020). Cost Analysis of Direct Air Capture and Sequestration Coupled to Low-Carbon Thermal Energy in the United States. Environmental Science & Technology, 54(12):7542–7551. 10.1021/acs.est.0c00476.

[151] Singh, U. and Colosi, L. M. (2022). Capture or curtail: The potential and performance of direct air capture powered through excess renewable electricity. Energy Conversion and Management: X, 15:100230. 10.1016/j.ecmx.2022.100230.

[152] Slesinski, D. and Litzelman, S. (2021). How Low-Carbon Heat Requirements for Direct Air Capture of CO_2 Can Enable the Expansion of Firm Low-Carbon Electricity Generation Resources. Frontiers in Climate, 3(101). 10.3389/fclim.2021.728719.

[153] Young, J., McQueen, N., Charalambous, C., Foteinis, S., Hawrot, O., Ojeda, M., Pilorgé, H., Andresen, J., Psarras, P., Renforth, P., Garcia, S., and van der Spek, M. (2023). The cost of direct air capture and storage can be reduced via strategic deployment but is unlikely to fall below stated cost targets. One Earth, 6(7):899–917. 10.1016/j.oneear.2023.06.004.

[154] Cooney, G. (2022). Best practices for life cycle assessment (LCA) of direct air capture with storage (DACS). U.S. Department of Energy.

[155] de Jonge, M. M. J., Daemen, J., Loriaux, J. M., Steinmann, Z. J. N., and Huijbregts, M. A. J. (2019). Life cycle carbon efficiency of Direct Air Capture systems with strong hydroxide sorbents. International Journal of Greenhouse Gas Control, 80:25–31. 10.1016/j.ijggc.2018.11.011.

[156] Leonzio, G., Mwabonje, O., Fennell, P. S., and Shah, N. (2022). Environmental performance of different sorbents used for direct air capture. Sustainable Production and Consumption, 32:101–111. 10.1016/j.spc.2022.04.004.

[157] Qiu, Y., Lamers, P., Daioglou, V., McQueen, N., de Boer, H.-S., Harmsen, M., Wilcox, J., Bardow, A., and Suh, S. (2022). Environmental trade-offs of direct air capture technologies in climate change mitigation toward 2100. Nature Communications, 13(1):3635. 10.1038/s41467-022-31146-1.

[158] Terlouw, T., Bauer, C., Rosa, L., and Mazzotti, M. (2021). Life cycle assessment of carbon dioxide removal technologies: a critical review. Energy & Environmental Science, 14(4):1701–1721. 10.1039/D0EE03757E.

[159] Wang, J., Li, S., Deng, S., Zeng, X., Li, K., Liu, J., Yan, J., and Lei, L. (2023). Energetic and Life Cycle Assessment of Direct Air Capture: A Review. Sustainable Production and Consumption, 36:1–16. 10.1016/j.spc.2022.12.017.

[160] Breyer, C., Fasihi, M., and Aghahosseini, A. (2020). Carbon dioxide direct air capture for effective climate change mitigation based on renewable electricity: a new type of energy system sector coupling. Mitigation and Adaptation Strategies for Global Change, 25(1):43–65. 10.1007/s11027-019-9847-y.

[161] Breyer, C., Fasihi, M., Bajamundi, C., and Creutzig, F. (2019). Direct Air Capture of CO_2: A Key Technology for Ambitious Climate Change Mitigation. Joule, 3(9):2053–2057. 10.1016/j.joule.2019.08.010.

[162] Pett-Ridge, J., Kuebbing, S., Mayer, A. C., Hovorka, S., Pilorgé, H., Baker, S. E., Pang, S. H., Scown, C. D., Mayfield, K. K., and Wong, A. A. Roads to removal: options for carbon dioxide removal in the United States. (2023). Report, Lawrence Livermore National Laboratory (LLNL), Livermore, CA (United States).

[163] Pantelides, C. C. Unified frameworks for optimal process planning and scheduling. Proceedings on the second conference on foundations of computer aided operations, pages 253–274.

[164] Kondili, E., Pantelides, C. C., and Sargent, R. W. H. (1993). A general algorithm for short-term scheduling of batch operations—I. MILP formulation. Computers & Chemical Engineering, 17(2):211–227. 10.1016/0098-1354(93)80015-F.

[165] Shah, N., Pantelides, C. C., and Sargent, R. W. H. (1993). A general algorithm for short-term scheduling of batch operations—II. Computational issues. Computers & Chemical Engineering, 17(2):229–244. 10.1016/0098-1354(93)80016-G.

[166] Huld, T., Šúri, M., and Dunlop, E. D. (2008). Geographical variation of the conversion efficiency of crystalline silicon photovoltaic modules in Europe. Progress in Photovoltaics: Research and Applications, 16(7):595–607. 10.1002/pip.846.

[167] Staffell, I. and Green, R. (2014). How does wind farm performance decline with age? Renewable Energy, 66:775–786. 10.1016/j.renene.2013.10.041.

[168] Manwell, J. F., McGowan, J. G., and Rogers, A. L. (2010). Wind energy explained: theory, design and application. John Wiley & Sons.

[169] Ghirardi, E., Brumana, G., Franchini, G., and Perdichizzi, A. (2021). The optimal share of PV and CSP for highly renewable power systems in the GCC region. Renewable Energy, 179:1990–2003. 10.1016/j.renene.2021.08.005.

[170] Wagner, M. J., Newman, A. M., Hamilton, W. T., and Braun, R. J. (2017). Optimized dispatch in a first-principles concentrating solar power production model. Applied Energy, 203:959–971. 10.1016/j.apenergy.2017.06.072.

[171] Stein, J. S., Holmgren, W. F., Forbess, J., and Hansen, C. W. PVLIB: Open source photovoltaic performance modeling functions for Matlab and Python.

2016 ieee 43rd photovoltaic specialists conference (pvsc), pages 3425–3430. IEEE.

[172] Wagner, M. J. (2008). Simulation and predictive performance modeling of utility-scale central receiver system power plants. Available at: https://www.researchgate.net/profile/Michael-Wagner-47/publication/44205074_Simulation_and_predictive_performance_modeling_of_utility-scale_central_receiver_system_power_plants/links/5c9be3ec299bf111694bc4ae/Simulation-and-predictive-performance-modeling-of-utility-scale-central-receiver-system-power-plants.pdf.

[173] Pioro, I. (2022). Handbook of generation IV nuclear reactors: A guidebook. Woodhead Publishing.

[174] Tanuma, T. (2022). Advances in steam turbines for modern power plants. Woodhead Publishing.

[175] Friedmann, S. J., Fan, Z., and Tang, K. (2019). Low-carbon heat solutions for heavy industry: sources, options, and costs today. Columbia University Center on Global Energy Policy.

[176] Society, R. (2020). Nuclear Cogeneration: Civil Nuclear Energy in a Low-Carbon Future. Policy Briefing. The Royal Society London, UK.

[177] Hasan, N., Rai, J. N., and Arora, B. B. (2014). Optimization of CCGT power plant and performance analysis using MATLAB/Simulink with actual operational data. SpringerPlus, 3(1):275. 10.1186/2193-1801-3-275.

[178] Bui, M., Gunawan, I., Verheyen, V., Feron, P., Meuleman, E., and Adeloju, S. (2014). Dynamic modelling and optimisation of flexible operation in post-combustion CO_2 capture plants—A review. Computers & Chemical Engineering, 61:245–265. 10.1016/j.compchemeng.2013.11.015.

[179] Vakkilainen, E. K. (2016). Steam generation from biomass: construction and design of large boilers. Butterworth-Heinemann.

[180] Bui, M., Sunny, N., and Mac Dowell, N. (2023). The prospects of flexible natural gas-fired CCGT within a green taxonomy. iScience, 26(8). 10.1016/j.isci.2023.107382. doi: 10.1016/j.isci.2023.107382.

[181] Danaci, D., Bui, M., Petit, C., and Mac Dowell, N. (2021). En Route to Zero Emissions for Power and Industry with Amine-Based Post-combustion Capture. Environmental Science & Technology, 55(15):10619–10632. 10.1021/acs.est.0c07261.

[182] Department for Energy Security and Net Zero (DESNZ). (2023). Greenhouse gas reporting: conversion factors 2023. Available at: https://www.gov.uk/government/publications/greenhouse-gas-reporting-conversion-factors-2023.

[183] Popa, A., Edwards, R., and Aandi, I. (2011). Carbon capture considerations for combined cycle gas turbine. Energy Procedia, 4:2315–2323. 10.1016/j.egypro.2011.02.122.

[184] Zeman, F. (2007). Energy and Material Balance of CO_2 Capture from Ambient Air. Environmental Science & Technology, 41(21):7558–7563. 10.1021/es070874m.

[185] Department for Business Energy & Industrial Strategy (UK). (2021). Greenhouse gas reporting: conversion factors 2021.

[186] Forster, P., Storelvmo, T., Armour, K., Collins, W., Dufresne, J.-L., Frame, D., Lunt, D., Mauritsen, T., Palmer, M., Watanabe, M., Wild, M., and Zhang, H. Chapter 7: The Earth's Energy Budget, Climate Feedbacks, and Climate Sensitivity. Climate Change 2021: The Physical Science Basis. Contribution of Working Group I to the Sixth Assessment Report of the Intergovernmental Panel on Climate Change.

[187] MIT Energy Initiative. (2022). The Future of Energy Storage.

[188] Hossein, S., Sioshansi, M., and Sioshansi, D. (2011). Capacity Value of Concentrating Solar Power Plants. National Renewable Energy Laboratory, Colorado.

[189] Our World in Data. Carbon intensity of electricity. Available at: `https://ourworldindata.org/grapher/carbon-intensity-electricity`.

[190] U.S. Energy Information Administration (EIA). Available at: `www.eia.gov`.

[191] World Bank Group. The official site of GovData360. Available at: `https://govdata360.worldbank.org/`.

[192] Climate Change Committee. (2020). The Sixth Carbon Budget Greenhouse gas removals. Available at: https://www.theccc.org.uk/publication/sixth-carbon-budget/.

[193] National Infrastructure Commission. (2021). Engineered Greenhouse Gas Removals. Available at: https://nic.org.uk/app/uploads/NIC-July-2021-Engineered-Greenhouse-Gas-Removals-UPDATED.pdf (Accessed: 9 April 2022). Available at: https://nic.org.uk/app/uploads/NIC-July-2021-Engineered-Greenhouse-Gas-Removals-UPDATED.pdf.

[194] Wohland, J., Witthaut, D., and Schleussner, C.-F. (2018). Negative Emission Potential of Direct Air Capture Powered by Renewable Excess Electricity in Europe. Earth's Future, 6(10):1380–1384. 10.1029/2018EF000954.

[195] House, K. Z., Baclig, A. C., Ranjan, M., van Nierop, E. A., Wilcox, J., and Herzog, H. J. (2011). Economic and energetic analysis of capturing CO_2 from ambient air. Proceedings of the National Academy of Sciences, 108(51):20428–20433. 10.1073/pnas.1012253108.

[196] International Renewable Energy Agency (IRENA). Hydrogen. Available at: https://www.irena.org/Energy-Transition/Technology/Hydrogen#:~:text=Hydrogen%20is%20produced%20on%20a,of%20a%20mix%20of%20gases.

[197] Almushaikah, A. S. and Almasri, R. A. (2021). Evaluating the potential energy savings of residential buildings and utilizing solar energy in the middle region of Saudi Arabia–Case study. Energy Exploration & Exploitation, 39(5):1457–1490. 10.1177/0144598720975144.

[198] Demirbas, A., Hashem, A. A., and Bakhsh, A. A. (2017). The cost analysis of electric power generation in Saudi Arabia. Energy Sources, Part B: Economics, Planning, and Policy, 12(6):591–596. 10.1080/15567249.2016.1248874.

[199] Gonzalez-Garay, A., Heuberger-Austin, C., Fu, X., Klokkenburg, M., Zhang, D., van der Made, A., and Shah, N. (2022). Unravelling the potential of sustainable aviation fuels to decarbonise the aviation sector. Energy & Environmental Science, 15(8):3291–3309. 10.1039/D1EE03437E.

[200] Kalogirou, S. A. (2005). Seawater desalination using renewable energy sources. Progress in Energy and Combustion Science, 31(3):242–281. 10.1016/j.pecs.2005.03.001.

[201] Barnhart, C. J., Dale, M., Brandt, A. R., and Benson, S. M. (2013). The energetic implications of curtailing versus storing solar- and wind-generated electricity. Energy & Environmental Science, 6(10):2804–2810. 10.1039/C3EE41973H.

[202] Niaz, H., Shams, M. H., Liu, J. J., and You, F. (2022). Mining bitcoins with carbon capture and renewable energy for carbon neutrality across states in the USA. Energy & Environmental Science, 15(9):3551–3570. 10.1039/D1EE03804D.

[203] Moogal, F. (2019). Climeworks Starts Paid Carbon Dioxide Removal. CleanTechnica. Available at: https://cleantechnica.com/2019/06/17/climeworks-starts-paid-carbon-dioxide-removal/.

[204] U.S. DOE Office of Fossil Energy and Carbon Management. Carbon Negative Shot. Available at: https://www.energy.gov/fecm/carbon-negative-shot.

[205] Valentine, J., Zoelle, A., Homsy, S., Mantripragada, H., Woods, M., Roy, N., Kilstofte, A., Sturdivan, M., Steutermann, M., and Fout, T. Direct air capture case studies: sorbent system. (2022). Report, National Energy Technology Laboratory (NETL),.

[206] Trading Economics. (2024). Aluminum. Available at: https://tradingeconomics.com/commodity/aluminum.

[207] Trading Economics. (2024). HRC Steel. Available at: https://tradingeconomics.com/commodity/hrc-steel.

[208] Young, J., McIlwaine, F., Smit, B., Garcia, S., and van der Spek, M. (2023). Process-informed adsorbent design guidelines for direct air capture. Chemical Engineering Journal, 456:141035. 10.1016/j.cej.2022.141035.

[209] International Energy Agency (IEA). (2022). Oil and gas methane emissions and methane intensity of production in selected countries. Available at: https://www.iea.org/data-and-statistics/charts/oil-and-gas-methane-emissions-and-methane-intensity-of-production-in-selected-countries-2022.

[210] Pilorgé, H., Kolosz, B., Wu, G. C., Freeman, J., and Wilcox, J. (2021). Global mapping of CDR opportunities. Available at: https://cdrprimer.org/read.

[211] Brandl, P., Soltani, S. M., Fennell, P. S., and Dowell, N. M. (2017). Evaluation of cooling requirements of post-combustion CO_2 capture applied to coal-fired power plants. Chemical Engineering Research and Design, 122:1–10. 10.1016/j.cherd.2017.04.001.

[212] Byers, E. A., Hall, J. W., and Amezaga, J. M. (2014). Electricity generation and cooling water use: UK pathways to 2050. Global Environmental Change, 25:16–30. 10.1016/j.gloenvcha.2014.01.005.

[213] Ministry of Environment, Water and Agriculture of Saudi Arabia. (2023). Statistical Year Book 2023. Available at: https://www.mewa.gov.sa/ar/InformationCenter/Researchs/Reports/Pages/default.aspx.

[214] US-Saudi Business Council. (2022). Saudi Arabia's Water Sector. Available at: https://ussaudi.org/wp-content/uploads/2022/02/Water-2022-Economic-Brief.pdf.

[215] Gulf Cooperation Council (GCC) Statistical Center. (2024). Water Statistics in GCC Countries 2022. Available at: https://gccstat.org/en/statistic/publications/water-statistics-bulletin-in-gcc-countries.

[216] EU Commission. (2023). Delegated regulation on Union methodology for RFNBOs. Available at: https://energy.ec.europa.eu/delegated-regulation-union-methodology-rfnbos_en.

[217] US Department of Energy (DOE). (2023). Assessing Lifecycle Greenhouse Gas Emissions Associated with Electricity Use for the Section 45V Clean Hydrogen Production Tax Credit. Available at: https://www.energy.gov/sites/default/files/2023-12/Assessing_Lifecycle_Greenhouse_Gas_Emissions_Associated_with_Electricity_Use_for_the_Section_45V_Clean_Hydrogen_Production_Tax_Credit.pdf.

[218] US Department of Energy (DOE). (2023). U.S. National Clean Hydrogen Strategy and Roadmap. Available at: https://www.hydrogen.energy.gov/library/roadmaps-vision/clean-hydrogen-strategy-roadmap.

[219] US Department of Energy. (2023). Biden-Harris Administration Announces Up To $1.2 Billion For Nation's First Direct Air Capture Demonstrations in Texas and Louisiana. Available at: https://www.energy.gov/articles/biden-har

ris-administration-announces-12-billion-nations-first-direct-air-capture.

[220] US Department of Energy. (2023). Regional direct air capture hubs. Available at: https://www.energy.gov/oced/DACHubs.

[221] International Energy Agency (IEA). (2023). Section 45Q Credit for Carbon Oxide Sequestration. Available at: https://www.iea.org/policies/4986-section-45q-credit-for-carbon-oxide-sequestration.

[222] Occidental Petroleum. (2023). Occidental Enters into Agreement to Acquire Direct Air Capture Technology Innovator Carbon Engineering. Available at: https://www.oxy.com/news/news-releases/occidental-enters-into-agreement-to-acquire-direct-air-capture-technology-innovator-carbon-engineering/.

[223] Valle, S. (2023). BlackRock to invest $550 mln in Occidental's carbon capture project. Reuters. Available at: https://www.reuters.com/sustainability/climate-energy/blackrock-invest-550-mln-occidentals-carbon-capture-project-2023-11-07/.

[224] HM Treasury. (2023). Spring Budget 2023. Available at: https://www.gov.uk/government/publications/spring-budget-2023/spring-budget-2023-html.

[225] Abu Dhabi National Oil Company (ADNOC). (2023). ADNOC and Occidental to Advance Direct Air Capture Project in the UAE. Available at: https://www.adnoc.ae/en/news-and-media/press-releases/2023/adnoc-and-occidental-to-advance-direct-air-capture-project-in-the-uae.

[226] Reuters. (2024). UAE's ADNOC boosts lower-carbon budget to $23 billion. Available at: https://www.reuters.com/sustainability/climate-energy/uaes-adnoc-boosts-lower-carbon-budget-23-billion-2024-01-22/.

[227] International Energy Agency (IEA). (2023). Global Hydrogen Review 2023. Available at: https://www.iea.org/reports/global-hydrogen-review-2023.

[228] Abdin, Z., Zafaranloo, A., Rafiee, A., Mérida, W., Lipiński, W., and Khalilpour, K. R. (2020). Hydrogen as an energy vector. Renewable and Sustainable Energy Reviews, 120:109620. 10.1016/j.rser.2019.109620.

[229] Hydrogen Council. (2021). Hydrogen for net zero-a critical cost-competitive energy vector. Available at: https://hydrogencouncil.com/en/hydrogen-for-net-zero/.

[230] International Energy Agency (IEA). (2021). Net Zero by 2050. Available at: https://www.iea.org/reports/net-zero-by-2050.

[231] International Renewable Energy Agency (IRENA). Global Hydrogen Trade to Meet the 1.5℃ Climate Goal: Green Hydrogen Cost and Potential. Available at: https://www.irena.org/Publications/2022/May/Global-hydrogen-trade-Cost.

[232] Dunn, S. (2002). Hydrogen futures: toward a sustainable energy system. International Journal of Hydrogen Energy, 27(3):235–264. 10.1016/S0360-3199(01)00131-8.

[233] Staffell, I., Scamman, D., Velazquez Abad, A., Balcombe, P., Dodds, P. E., Ekins, P., Shah, N., and Ward, K. R. (2019). The role of hydrogen and fuel cells in the global energy system. Energy & Environmental Science, 12(2):463–491. 10.1039/C8EE01157E.

[234] Gonzalez-Garay, A., Bui, M., Freire Ordóñez, D., High, M., Oxley, A., Moustafa, N., Sáenz Cavazos, P. A., Patrizio, P., Sunny, N., Mac Dowell, N., and Shah, N. (2022). Hydrogen Production and Its Applications to Mobility. Annual Review of Chemical and Biomolecular Engineering, 13(Volume 13, 2022):501–528. 10.1146/annurev-chembioeng-092220-010254.

[235] Wallington, T. J., Woody, M., Lewis, G. M., Keoleian, G. A., Adler, E. J., Martins, J. R. R. A., and Collette, M. D. (2024). Green hydrogen pathways, energy efficiencies, and intensities for ground, air, and marine transportation. Joule, 8(8):2190–2207. 10.1016/j.joule.2024.07.012.

[236] Wang, Z., Acha, S., Bird, M., Sunny, N., Stettler, M. E. J., Wu, B., and Shah, N. (2024). A total cost of ownership analysis of zero emission powertrain solutions for the heavy goods vehicle sector. Journal of Cleaner Production, 434:139910. 10.1016/j.jclepro.2023.139910.

[237] Sunny, N., Bernardi, A., Danaci, D., Bui, M., Gonzalez-Garay, A., and Chachuat, B. (2022). A Pathway Towards Net-Zero Emissions in Oil Refineries. Frontiers in Chemical Engineering, 4. 10.3389/fceng.2022.804163.

[238] Sunny, N., Mac Dowell, N., and Shah, N. (2020). What is needed to deliver carbon-neutral heat using hydrogen and CCS? Energy & Environmental Science, 13(11):4204–4224. 10.1039/D0EE02016H.

[239] Bahzad, H., Katayama, K., Boot-Handford, M. E., Mac Dowell, N., Shah, N., and Fennell, P. S. (2019). Iron-based chemical-looping technology for decarbonising iron and steel production. International Journal of Greenhouse Gas Control, 91:102766. 10.1016/j.ijggc.2019.06.017.

[240] Fan, Z. and Friedmann, S. J. (2021). Low-carbon production of iron and steel: Technology options, economic assessment, and policy. Joule, 5(4):829–862. 10.1016/j.joule.2021.02.018.

[241] Freire Ordóñez, D., Halfdanarson, T., Ganzer, C., Shah, N., Dowell, N. M., and Guillén-Gosálbez, G. (2022). Evaluation of the potential use of e-fuels in the European aviation sector: a comprehensive economic and environmental assessment including externalities. Sustainable Energy & Fuels, 6(20):4749–4764. 10.1039/D2SE00757F.

[242] Gabrielli, P., Rosa, L., Gazzani, M., Meys, R., Bardow, A., Mazzotti, M., and Sansavini, G. (2023). Net-zero emissions chemical industry in a world of limited resources. One Earth, 6(6):682–704. 10.1016/j.oneear.2023.05.006.

[243] Glenk, G. and Reichelstein, S. (2019). Economics of converting renewable power to hydrogen. Nature Energy, 4(3):216–222. 10.1038/s41560-019-0326-1.

[244] Pellow, M. A., Emmott, C. J. M., Barnhart, C. J., and Benson, S. M. (2015). Hydrogen or batteries for grid storage? A net energy analysis. Energy & Environmental Science, 8(7):1938–1952. 10.1039/C4EE04041D.

[245] Sikiru, S., Oladosu, T. L., Amosa, T. I., Olutoki, J. O., Ansari, M. N. M., Abioye, K. J., Rehman, Z. U., and Soleimani, H. (2024). Hydrogen-powered horizons: Transformative technologies in clean energy generation, distribution, and storage for sustainable innovation. International Journal of Hydrogen Energy, 56:1152–1182. 10.1016/j.ijhydene.2023.12.186.

[246] Bartholomew, C. H. and Farrauto, R. J. (2011). Fundamentals of industrial catalytic processes. John Wiley & Sons.

[247] Bhandari, R., Trudewind, C. A., and Zapp, P. (2014). Life cycle assessment of hydrogen production via electrolysis – a review. Journal of Cleaner Production, 85:151–163. 10.1016/j.jclepro.2013.07.048.

[248] National Academy of Engineering. (2004). The hydrogen economy: opportunities, costs, barriers, and R&D needs. Washington, DC: The National Academies Press. 10.17226/10922.

[249] Spath, P. L. and Mann, M. K. (2001). Life cycle assessment of hydrogen production via natural gas steam reforming. National Renewable Energy Lab (NREL), Golden, CO (United States). Available at: `https://www.nrel.gov/docs/fy01osti/27637.pdf`.

[250] Balcombe, P., Anderson, K., Speirs, J., Brandon, N., and Hawkes, A. (2015). Methane and CO_2 emissions from the natural gas supply chain: an evidence assessment. Sustainable Gas Institute, Imperial College London.

[251] Mac Dowell, N., Sunny, N., Brandon, N., Herzog, H., Ku, A. Y., Maas, W., Ramirez, A., Reiner, D. M., Sant, G. N., and Shah, N. (2021). The hydrogen economy: A pragmatic path forward. Joule, 5(10):2524–2529. 10.1016/j.joule.2021.09.014.

[252] Mueller-Langer, F., Tzimas, E., Kaltschmitt, M., and Peteves, S. (2007). Techno-economic assessment of hydrogen production processes for the hydrogen economy for the short and medium term. International Journal of Hydrogen Energy, 32(16):3797–3810. 10.1016/j.ijhydene.2007.05.027.

[253] Clarke, L., Wei, Y.-M., de la Vega Navarro, A., Garg, A., Hahmann, A. N., Khennas, S., Azevedo, I. M., Löschel, A., Singh, A. K., and Steg, L. (2022). Energy Systems. In IPCC, 2022: Climate Change 2022: Mitigation of Climate Change. Working Group III Contribution to the IPCC Sixth Assessment Report. pages 613–746. 10.1017/9781009157926.008.

[254] Al-Qahtani, A., Parkinson, B., Hellgardt, K., Shah, N., and Guillen-Gosalbez, G. (2021). Uncovering the true cost of hydrogen production routes using life cycle monetisation. Applied Energy, 281:115958. 10.1016/j.apenergy.2020.115958.

[255] Varela, C., Mostafa, M., and Zondervan, E. (2021). Modeling alkaline water electrolysis for power-to-x applications: A scheduling approach. International Journal of Hydrogen Energy, 46(14):9303–9313. 10.1016/j.ijhydene.2020.12.111.

[256] Buttler, A. and Spliethoff, H. (2018). Current status of water electrolysis for energy storage, grid balancing and sector coupling via power-to-gas and power-to-liquids: A review. Renewable and Sustainable Energy Reviews, 82:2440–2454. 10.1016/j.rser.2017.09.003.

[257] International Energy Agency (IEA). (2019). The Future of Hydrogen. Available at: https://www.iea.org/reports/the-future-of-hydrogen.

[258] Holladay, J. D., Hu, J., King, D. L., and Wang, Y. (2009). An overview of hydrogen production technologies. Catalysis Today, 139(4):244–260. 10.1016/j.cattod.2008.08.039.

[259] European Commission. (2022). REPowerEU: A plan to rapidly reduce dependence on Russian fossil fuels and fast forward the green transition. Available at: https://ec.europa.eu/commission/presscorner/detail/en/IP_22_3131.

[260] European Commission. Innovation Fund: Large-scale calls. Available at: https://climate.ec.europa.eu/eu-action/eu-funding-climate-action/innovation-fund/calls-proposals/large-scale-calls_en.

[261] European Commission. (2022). State Aid: Commission approves up to €5.2 billion of public support by thirteen Member States for the second Important Project of Common European Interest in the hydrogen value chain. Available at: https://ec.europa.eu/commission/presscorner/detail/en/ip_22_5676.

[262] European Commission. (2022). State Aid: Commission approves up to €5.4 billion of public support by fifteen Member States for an Important Project of Common European Interest in the hydrogen technology value chain. Available at: https://ec.europa.eu/commission/presscorner/detail/en/ip_22_4544.

[263] UK Department for Energy Security and Net Zero. (2023). Major boost for hydrogen as UK unlocks new investment and jobs. Available at: https://www.gov.uk/government/news/major-boost-for-hydrogen-as-uk-unlocks-new-investment-and-jobs#:~:text=Hydrogen%20presents%20a%20massive%20economic,at%20once%20anywhere%20in%20Europe.

[264] UK Government. (2024). Boost for UK hydrogen as government backs world-leading industry. Available at: https://www.gov.uk/government/news/boost-for-uk-hydrogen-as-government-backs-world-leading-industry.

[265] Hydrogen Insight. (2023). World first | Colorado approves clean hydrogen tax credit of up to $1/kg for usage in hard-to-abate sectors. Available at: https://www.hydrogeninsight.com/policy/world-first-colorado-approves-clean-hydrogen-tax-credit-of-up-to-1-kg-for-usage-in-hard-to-abate-sectors/2-1-1448364.

[266] Illinois General Assembly. (2023). Bill Status of HB5818: REVENUE-HYDROGEN FUEL CREDIT. Available at: https://www.ilga.gov/legislation/BillStatus.asp?DocNum=5818&GAID=16&DocTypeID=HB&SessionID=110&GA=102.

[267] US Department of Energy (DOE). Regional Clean Hydrogen Hubs. Available at: https://www.energy.gov/oced/regional-clean-hydrogen-hubs-0.

[268] US Department of Energy (DOE). (2023). Biden-Harris Administration to Jumpstart Clean Hydrogen Economy with New Initiative to Provide Market Certainty And Unlock Private Investment. Available at: https://www.energy.gov/articles/biden-harris-administration-jumpstart-clean-hydrogen-economy-new-initiative-provide-market.

[269] India Ministry of New and Renewable Energy. (2023). National Green Hydrogen Mission. Available at: https://mnre.gov.in/national-green-hydrogen-mission/.

[270] National Portal of India. (2022). National Green Hydrogen Mission. Available at: https://www.india.gov.in/spotlight/national-green-hydrogen-mission.

[271] Chibani, A. (2023). Hydrogen as a fuel of the future: Moving the GCC's climate mitigation agenda forward. Middle East Institute. Available at: https://www.mei.edu/publications/hydrogen-fuel-future-moving-gccs-climate-mitigation-agenda-forward.

[272] Saudi Exchange. (2023). ACWA Power Announces the signing of agreements for the project financing of the NEOM Green Hydrogen Company ("NGHC"). Available at: https://tinyurl.com/2a424r7n.

[273] The United Arab Emirates' Government portal. (2024). National Hydrogen Strategy. Available at: https://u.ae/en/about-the-uae/strategies-initi

atives-and-awards/strategies-plans-and-visions/environment-and-energy/national-hydrogen-strategy.

[274] The Royal Society. (2023). Large-scale electricity storage. Available at: https://royalsociety.org/news-resources/projects/low-carbon-energy-programme/large-scale-electricity-storage/.

[275] Erbach, G. and Svensson, S. (2023). EU rules for renewable hydrogen. Available at: https://www.europarl.europa.eu/RegData/etudes/BRIE/2023/747085/EPRS_BRI(2023)747085_EN.pdf.

[276] Internal Revenue Service (IRS), Treasury. (2023). Section 45V Credit for Production of Clean Hydrogen; Section 48(a)(15) Election To Treat Clean Hydrogen Production Facilities as Energy Property. Available at: https://www.federalregister.gov/documents/2023/12/26/2023-28359/section-45v-credit-for-production-of-clean-hydrogen-section-48a15-election-to-treat-clean-hydrogen.

[277] Ricks, W., Xu, Q., and Jenkins, J. D. (2023). Minimizing emissions from grid-based hydrogen production in the United States. Environmental Research Letters, 18(1):014025. 10.1088/1748-9326/acacb5.

[278] Zeyen, E., Riepin, I., and Brown, T. (2024). Temporal regulation of renewable supply for electrolytic hydrogen. Environmental Research Letters, 19:024034. 10.1088/1748-9326/ad2239.

[279] Giovanniello, M. A., Cybulsky, A. N., Schittekatte, T., and Mallapragada, D. S. (2024). The influence of additionality and time-matching requirements on the emissions from grid-connected hydrogen production. Nature Energy. 10.1038/s41560-023-01435-0.

[280] Sendi, M., Mersch, M., and Mac Dowell, N. (2025). Electrolytic hydrogen production; how green must green be? iScience. 10.1016/j.isci.2025.111955.

[281] Schmidt, O., Gambhir, A., Staffell, I., Hawkes, A., Nelson, J., and Few, S. (2017). Future cost and performance of water electrolysis: An expert elicitation study. International Journal of Hydrogen Energy, 42(52):30470–30492. 10.1016/j.ijhydene.2017.10.045.

[282] International Energy Agency (IEA). (2024). Energy Prices. Available at: https://www.iea.org/data-and-statistics/data-product/energy-prices.

[283] Collodi, G., Azzaro, G., Ferrari, N., and Santos, S. (2017). Techno-economic Evaluation of Deploying CCS in SMR Based Merchant H2 Production with NG as Feedstock and Fuel. Energy Procedia, 114:2690–2712. 10.1016/j.egypro.2017.03.1533.

[284] Basma, H., Zhou, Y., and Rodríguez, F. (2022). Fuel-cell hydrogen long-haul trucks in Europe: A total cost of ownership analysis. International Council on Clean Transportation: Washington, DC, USA.

[285] U.S. Energy Information Administration (EIA). (2024). Gasoline and Diesel Fuel Update. Available at: https://www.eia.gov/petroleum/gasdiesel/.

[286] US Energy Information Administration (EIA). (2023). Carbon Dioxide Emissions Coefficients. Available at: https://www.eia.gov/environment/emissions/co2_vol_mass.php.

[287] Antonini, E. G. A., Virgüez, E., Ashfaq, S., Duan, L., Ruggles, T. H., and Caldeira, K. (2024). Identification of reliable locations for wind power generation through a global analysis of wind droughts. Communications Earth & Environment, 5(1):103. 10.1038/s43247-024-01260-7.

[288] Ruggles, T. H., Virgüez, E., Reich, N., Dowling, J., Bloomfield, H., Antonini, E. G. A., Davis, S. J., Lewis, N. S., and Caldeira, K. (2024). Planning reliable wind- and solar-based electricity systems. Advances in Applied Energy, 15:100185. 10.1016/j.adapen.2024.100185.

[289] Schelling, K. (2023). Green Hydrogen to Undercut Gray Sibling by End of Decade. BloombergNEF. Available at: https://about.bnef.com/blog/green-hydrogen-to-undercut-gray-sibling-by-end-of-decade/.

[290] Electricity Maps. Data Portal. Available at: https://www.electricitymaps.com/data-portal.

[291] US Energy Information Administration (EIA). (2023). Texas Electricity Profile 2022. Available at: https://www.eia.gov/electricity/state/Texas/.

[292] Climeworks. Available at: https://climeworks.com/.

[293] Climate Change Committee. (2020). The sixth carbon budget: the UK's path to net zero. Available at: https://www.theccc.org.uk/wp-content/uploads/2020/12/The-Sixth-Carbon-Budget-The-UKs-path-to-Net-Zero.pdf.

[294] Department of Ecology, State of Washington. Washington's Cap-and-Invest Program. Available at: https://ecology.wa.gov/air-climate/climate-commitment-act/cap-and-invest.

[295] European Commission. EU ETS emissions cap. Available at: https://climate.ec.europa.eu/eu-action/eu-emissions-trading-system-eu-ets/eu-ets-emissions-cap_en.

[296] The Legislative Analyst's Office, State of California. (2023). California's Cap-and-Trade Program: Frequently Asked Questions. Available at: https://lao.ca.gov/Publications/Report/4811.

[297] The Regional Greenhouse Gas Initiative (RGGI). (2024). Elements of RGGI. Available at: https://www.rggi.org/program-overview-and-design/elements.

[298] World Bank Group. (2024). State and Trends of Carbon Pricing 2024. Available at: http://hdl.handle.net/10986/41544.

[299] Shafiee, R. T. and Schrag, D. P. (2024). Carbon abatement costs of green hydrogen across end-use sectors. Joule. 10.1016/j.joule.2024.09.003.

[300] Bistline, J. E. T. (2021). The importance of temporal resolution in modeling deep decarbonization of the electric power sector. Environmental Research Letters, 16(8):084005. 10.1088/1748-9326/ac10df.

[301] Hoffmann, M., Kotzur, L., Stolten, D., and Robinius, M. (2020). A Review on Time Series Aggregation Methods for Energy System Models. Energies, 13(3):641. 10.3390/en13030641.

[302] Kannengießer, T., Hoffmann, M., Kotzur, L., Stenzel, P., Schuetz, F., Peters, K., Nykamp, S., Stolten, D., and Robinius, M. (2019). Reducing Computational Load for Mixed Integer Linear Programming: An Example for a District and an Island Energy System. Energies, 12(14):2825. 10.3390/en12142825.

[303] Kotzur, L., Markewitz, P., Robinius, M., and Stolten, D. (2018). Impact of different time series aggregation methods on optimal energy system design. Renewable Energy, 117:474–487. 10.1016/j.renene.2017.10.017.

[304] Kotzur, L., Markewitz, P., Robinius, M., and Stolten, D. (2018). Time series aggregation for energy system design: Modeling seasonal storage. Applied Energy, 213:123–135. 10.1016/j.apenergy.2018.01.023.

[305] Fahmi, I. and Cremaschi, S. (2012). Process synthesis of biodiesel production plant using artificial neural networks as the surrogate models. Computers & Chemical Engineering, 46:105–123. 10.1016/j.compchemeng.2012.06.006.

[306] Henao, C. A. and Maravelias, C. T. (2011). Surrogate-based superstructure optimization framework. AIChE Journal, 57(5):1216–1232. https://doi.org/10.1002/aic.12341.

[307] Klimek, A., Ganzer, C., and Sundmacher, K. (2024). Enhancing superstructure optimization via embedded neural networks in optimal process design for sustainable aviation fuel (SAF) production. Available at: `https://www.aidic.it/escape34-pse24/programma/186Klimek.docx`.

[308] Ceccon, F., Jalving, J., Haddad, J., Thebelt, A., Tsay, C., Laird, C. D., and Misener, R. (2022). OMLT: Optimization & machine learning toolkit. Journal of Machine Learning Research, 23(349):1–8.

[309] Al-falahi, M. D. A., Jayasinghe, S. D. G., and Enshaei, H. (2017). A review on recent size optimization methodologies for standalone solar and wind hybrid renewable energy system. Energy Conversion and Management, 143:252–274. 10.1016/j.enconman.2017.04.019.

[310] Gupta, R. A., Kumar, R., and Bansal, A. K. (2015). BBO-based small autonomous hybrid power system optimization incorporating wind speed and solar radiation forecasting. Renewable and Sustainable Energy Reviews, 41:1366–1375. 10.1016/j.rser.2014.09.017.

[311] Heuberger, C. F., Rubin, E. S., Staffell, I., Shah, N., and Mac Dowell, N. (2017). Power capacity expansion planning considering endogenous technology cost learning. Applied Energy, 204:831–845. 10.1016/j.apenergy.2017.07.075.

[312] Malhotra, A. and Schmidt, T. S. (2020). Accelerating Low-Carbon Innovation. Joule, 4(11):2259–2267. 10.1016/j.joule.2020.09.004.

[313] Sievert, K., Schmidt, T. S., and Steffen, B. (2024). Considering technology characteristics to project future costs of direct air capture. Joule, 8(4):979–999. 10.1016/j.joule.2024.02.005.

[314] Charalambous, M. A., Sacchi, R., Tulus, V., and Guillén-Gosálbez, G. (2024). Integrating emerging technologies deployed at scale within prospective life cycle assessments. Sustainable Production and Consumption, 50:499–510. 10.1016/j.spc.2024.08.016.

[315] Weidner, T., Tulus, V., and Guillén-Gosálbez, G. (2023). Environmental sustainability assessment of large-scale hydrogen production using prospective life cycle analysis. International Journal of Hydrogen Energy, 48(22):8310–8327. 10.1016/j.ijhydene.2022.11.044.

[316] International Renewable Energy Agency (IRENA). (2021). Renewable Power Generation Costs in 2020. IRENA Abu Dhabi, UAE.

[317] Pratama, Y. W. and Mac Dowell, N. (2022). Carbon capture and storage investment: Fiddling while the planet burns. One Earth, 5(4):434–442. 10.1016/j.oneear.2022.03.008.

[318] U.S. Energy Information Administration (EIA). (2022). Cost and performance characteristics of new generating technologies, annual energy outlook 2022. US Energy Information Administration, Department of Energy Washington, DC, USA.

[319] Matche. (2014). Available at: `https://www.matche.com/`.

[320] Department for Energy Security and Net Zero and Department for Business, Energy Industrial Strategy (BEIS), UK. (2016). BEIS Electricity Generation Costs (November 2016). Available at: `https://www.rggi.org/program-overview-and-design/elements`.

[321] Grosse, R., Christopher, B., Wöll, S., Geyer, R., and Robbi, S. (2017). Long term (2050) projections of techno-economic performance of large-scale heating and cooling in the EU.

[322] Barbosa, L. d. S. N. S., Bogdanov, D., Vainikka, P., and Breyer, C. (2017). Hydro, wind and solar power as a base for a 100% renewable energy supply for South and Central America. PloS one, 12(3):e0173820.

[323] International Energy Agency (IEA). (2023). Electrolysers. Available at: https://www.iea.org/energy-system/low-emission-fuels/electrolysers.

[324] Couper, J. R., Penney, W. R., Fair, J. R., and Walas, S. M. (2005). Chemical process equipment: selection and design. Gulf professional publishing.

[325] Cooper, M. Car Weights From 2012-2023 (& Why You Should Know Yours). Available at: https://cars.lovetoknow.com/List_of_Car_Weights.

[326] Brandl, P., Bui, M., Hallett, J. P., and Mac Dowell, N. (2021). Beyond 90 International Journal of Greenhouse Gas Control, 105:103239. 10.1016/j.ijggc.2020.103239.

[327] Bruckner, T., Bashmakov, I. A., Mulugetta, Y., Chum, H., De la Vega Navarro, A., Edmonds, J., Faaij, A., Fungtammasan, B., Garg, A., Hertwich, E., Honnery, D., Infield, D., Kainuma, M., Khennas, S., Kim, S., Nimir, K., Riahi, K., Strachan, N., Wiser, R., and Zhang, X. (2014). Energy systems. In: Climate Change 2014: Mitigation of Climate Change. Contribution of Working Group III to the Fifth Assessment Report of the Intergovernmental Panel on Climate Change.

[328] Pehl, M., Arvesen, A., Humpenöder, F., Popp, A., Hertwich, E. G., and Luderer, G. (2017). Understanding future emissions from low-carbon power systems by integration of life-cycle assessment and integrated energy modelling. Nature Energy, 2(12):939–945. 10.1038/s41560-017-0032-9.

[329] Stevens, L., Anderson, B., Cowan, C., Colton, K., and Johnson, D. (2017). The footprint of energy: land use of US electricity production. STRATA: Logan, UT, USA.

[330] Baumann, M., Peters, J. F., Weil, M., and Grunwald, A. (2017). CO_2 Footprint and Life-Cycle Costs of Electrochemical Energy Storage for Stationary Grid Applications. Energy Technology, 5(7):1071–1083. 10.1002/ente.201600622.

[331] Thaker, S., Oni, A. O., Gemechu, E., and Kumar, A. (2019). Evaluating energy and greenhouse gas emission footprints of thermal energy storage systems for

concentrated solar power applications. Journal of Energy Storage, 26:100992. 10.1016/j.est.2019.100992.

[332] Meldrum, J., Nettles-Anderson, S., Heath, G., and Macknick, J. (2013). Life cycle water use for electricity generation: a review and harmonization of literature estimates. Environmental Research Letters, 8(1):015031. 10.1088/1748-9326/8/1/015031.

[333] Xu, C., Wang, Z., Li, X., and Sun, F. (2011). Energy and exergy analysis of solar power tower plants. Applied Thermal Engineering, 31(17):3904–3913. 10.1016/j.applthermaleng.2011.07.038.

[334] El Marazgioui, S. and El Fadar, A. (2022). Impact of cooling tower technology on performance and cost-effectiveness of CSP plants. Energy Conversion and Management, 258:115448. 10.1016/j.enconman.2022.115448.

[335] Awan, A. B., Zubair, M., and Chandra Mouli, K. V. V. (2020). Design, optimization and performance comparison of solar tower and photovoltaic power plants. Energy, 199:117450. 10.1016/j.energy.2020.117450.

[336] Francisco, B.-R., César, A.-C., and Sebastián, R.-M. *Methodologies Used in the Extrapolation of Wind Speed Data at Different Heights and Its Impact in the Wind Energy Resource Assessment in a Region*, page Ch. 4. IntechOpen, Rijeka, (2011).

[337] Gualtieri, G. and Secci, S. (2011). Wind shear coefficients, roughness length and energy yield over coastal locations in Southern Italy. Renewable Energy, 36(3):1081–1094. 10.1016/j.renene.2010.09.001.

APPENDIX A

DIRECT AIR CAPTURE PROCESS MODEL

A.1 Process performance maps

The following are the model fittings of the simplified models for SA-VTSA DAC performance used.

Low-temperature heat requirements

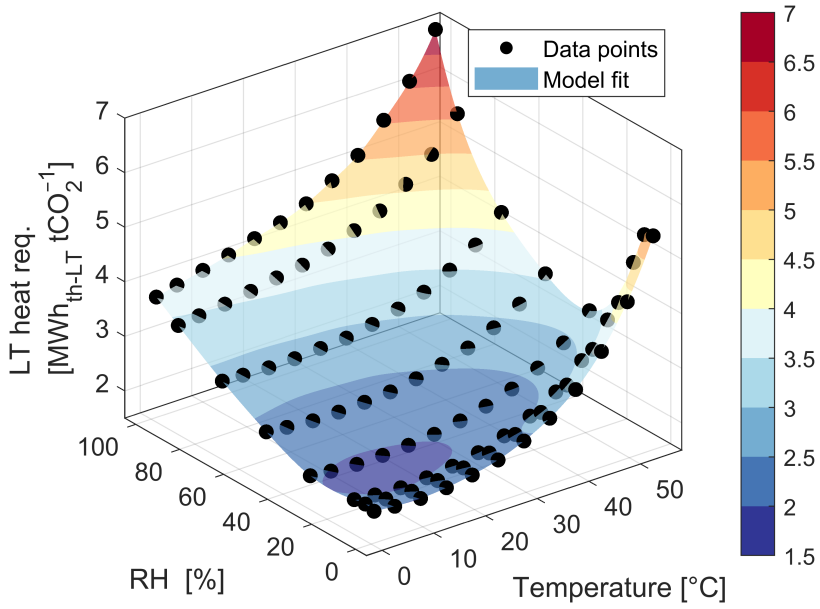


Figure A.1: SA-VTSA DAC process low-temperature heat requirements simplified 3D model. Adapted from [134].

Total electricity requirements

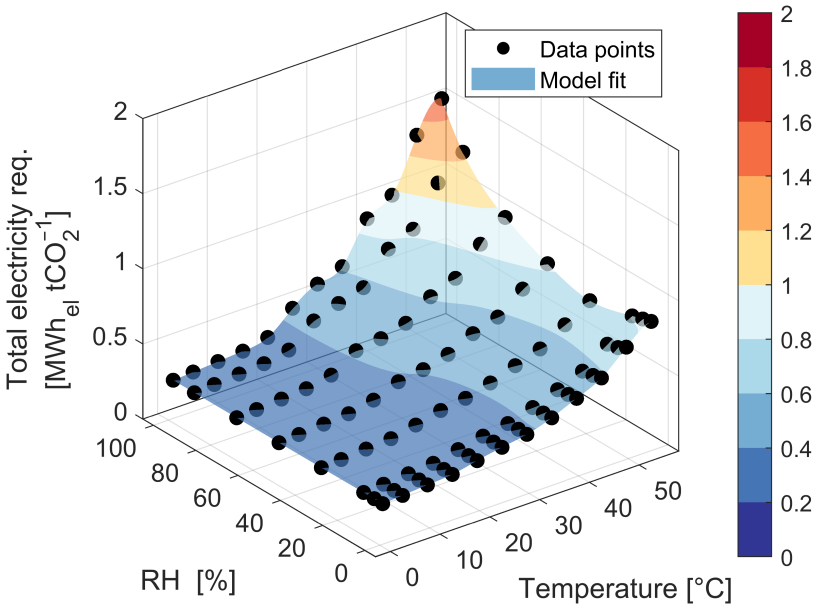


Figure A.2: SA-VTSA DAC process total electricity requirements simplified 3D model. Adapted from [134].

Compressors and vacuum pumps electricity requirements

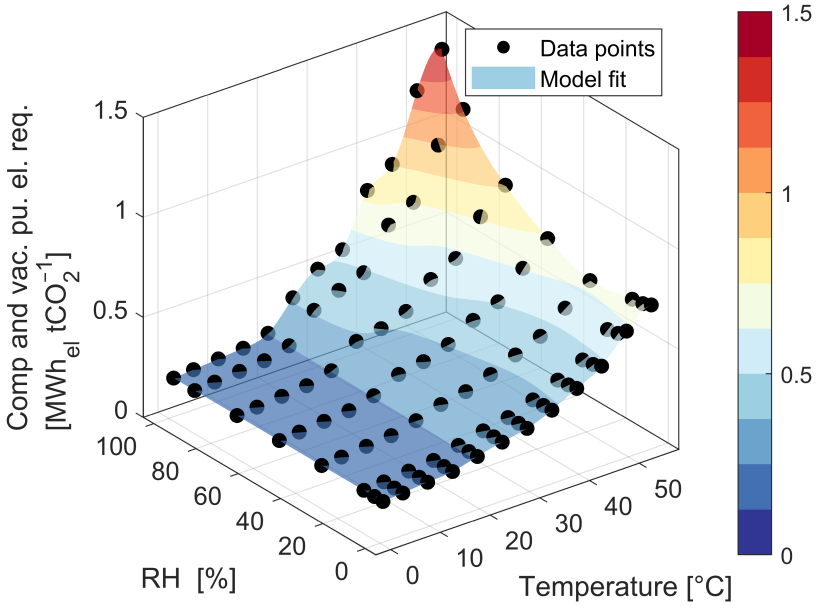


Figure A.3: SA-VTSA DAC process compressors and vacuum pumps electricity requirements simplified 3D model. Adapted from [134].

Required air volume

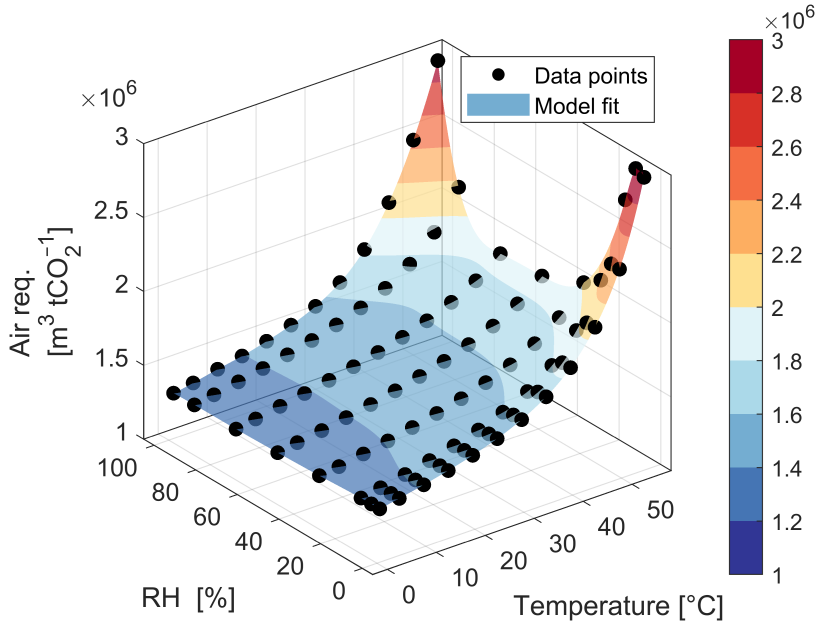


Figure A.4: SA-VTSA DAC process required air volume simplified 3D model. Adapted from [134].

Water production

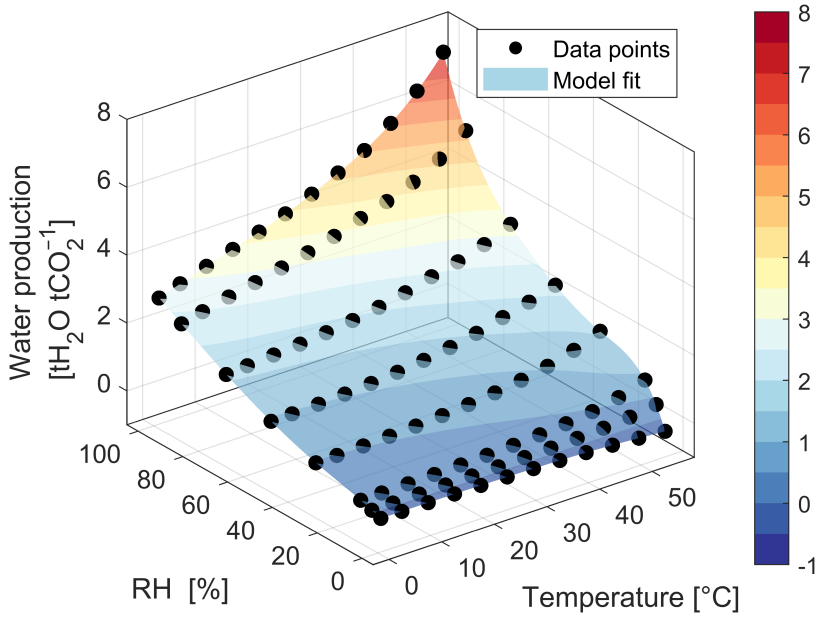


Figure A.5: SA-VTSA DAC process water production simplified 3D model. Adapted from [134].

A.2 Process sensitivity analysis

To investigate how process design parameters influence DAC performance, a sensitivity analysis was performed, varying two cycle step parameters simultaneously under nine different ambient conditions. The results are visualised as Pareto fronts in Figure A.6–A.10. and are summarised in Table 2.8.

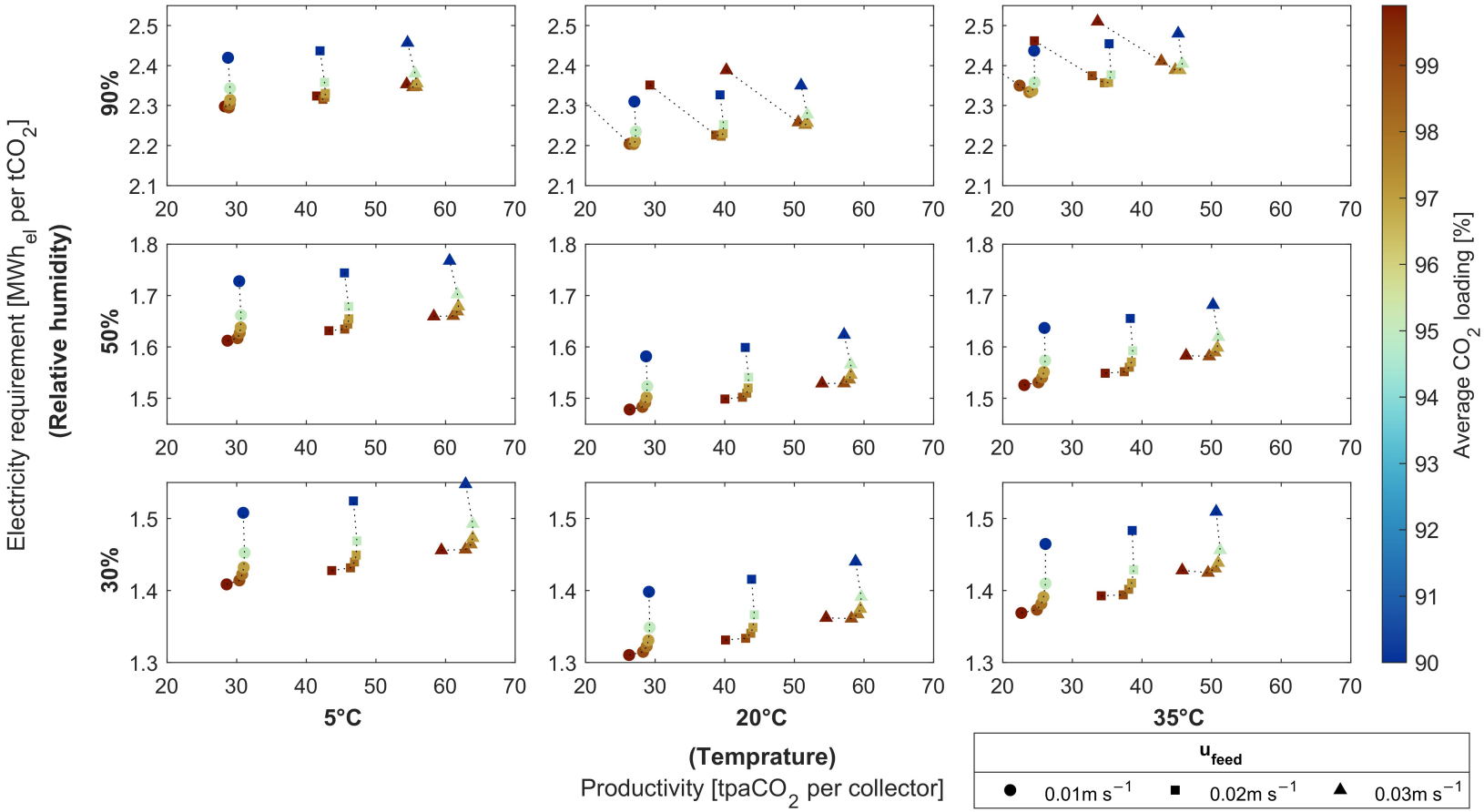


Figure A.6: SA-VTSA adsorption step sensitivity analysis. The sensitivity to two key variables is demonstrated: the symbol colours show different average bed loadings at the end of the adsorption step, defined as the ratio between the achieved CO_2 loading and the equilibrium CO_2 loading (CO_2 loading %), and the symbol shape corresponds to different Feed velocities (u_{feed}). Please note that the y-axis has a different scale for different relative humidity. Adapted from [115].

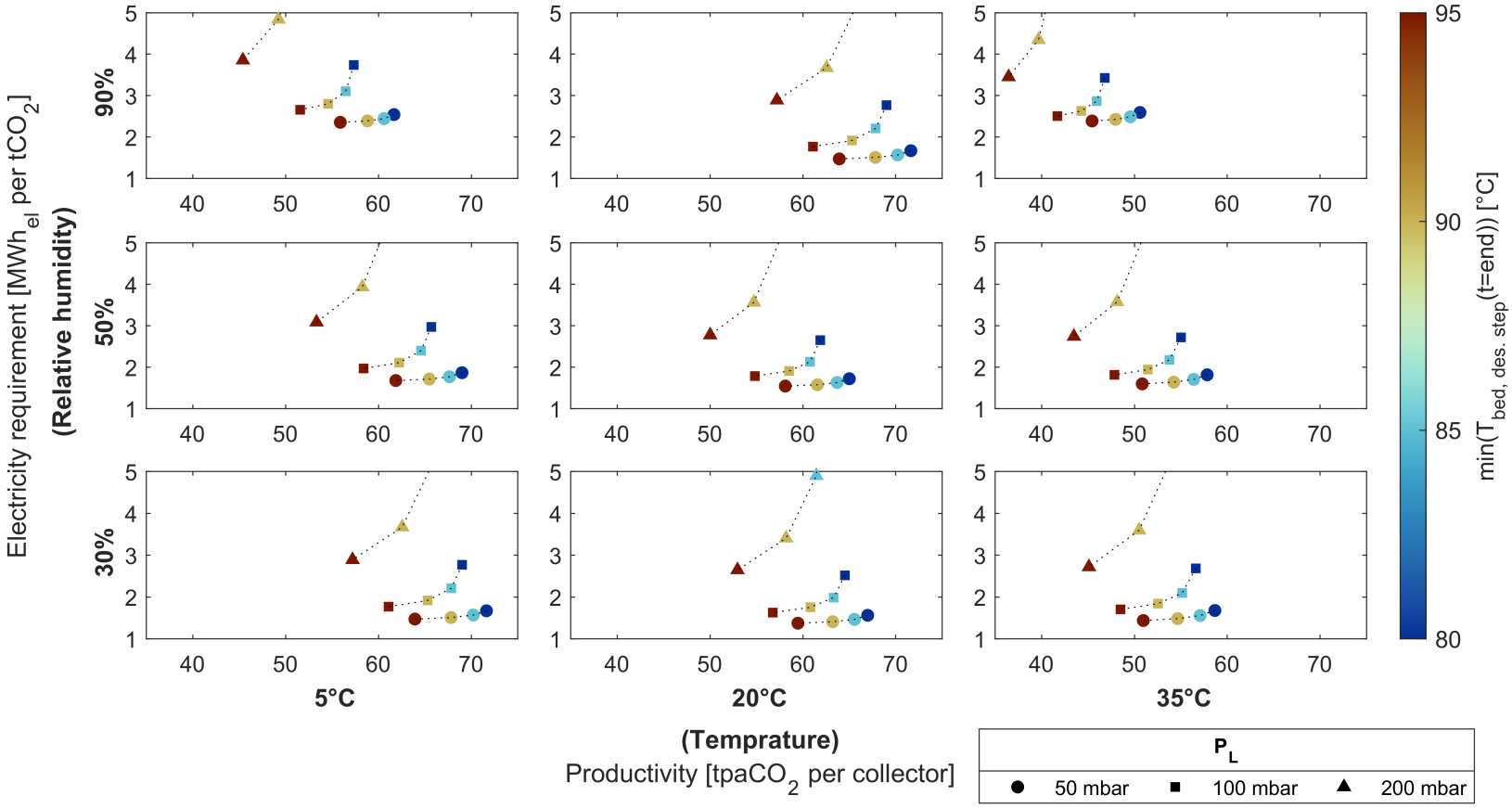


Figure A.7: SA-VTSA bed heating step sensitivity analysis. The sensitivity to two key variables is demonstrated: the symbol colours show different lowest temperatures in the sorbent bed at the end of the bed heating step ($\min(T_{bed,des\,step}(t = end))$), and the symbol shape corresponds to different vacuum pressures during desorption (P_L). Adapted from [115].

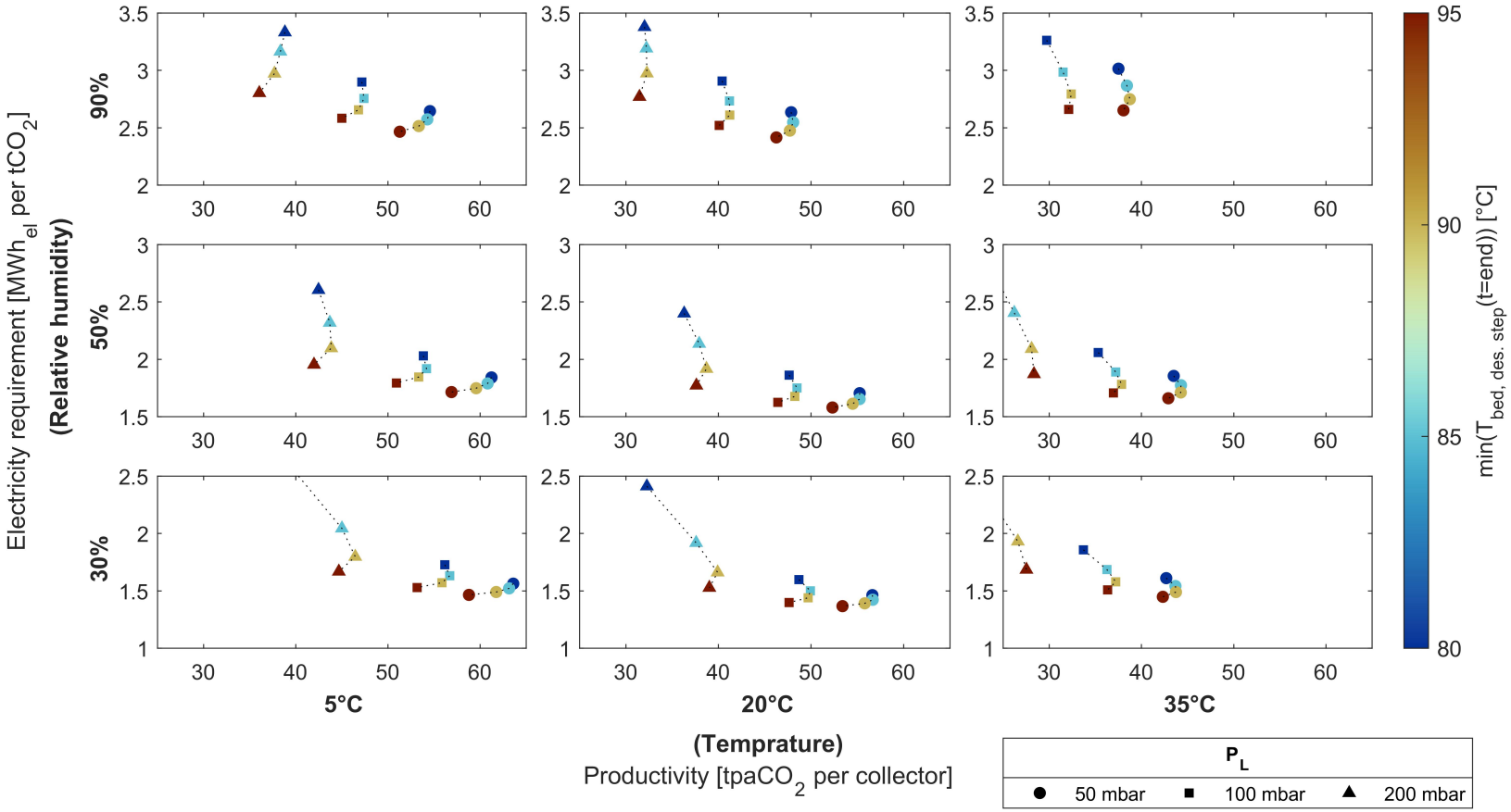


Figure A.8: VTSA bed heating step sensitivity analysis. The sensitivity to two key variables is demonstrated: the symbol colours show different lowest temperatures in the sorbent bed at the end of the bed heating step ($\min(T_{bed,des\,step}(t = end))$), and the symbol shape corresponds to different vacuum pressures during desorption (P_L). Please note that the y-axis has a different scale for different relative humidity. Adapted from [115].

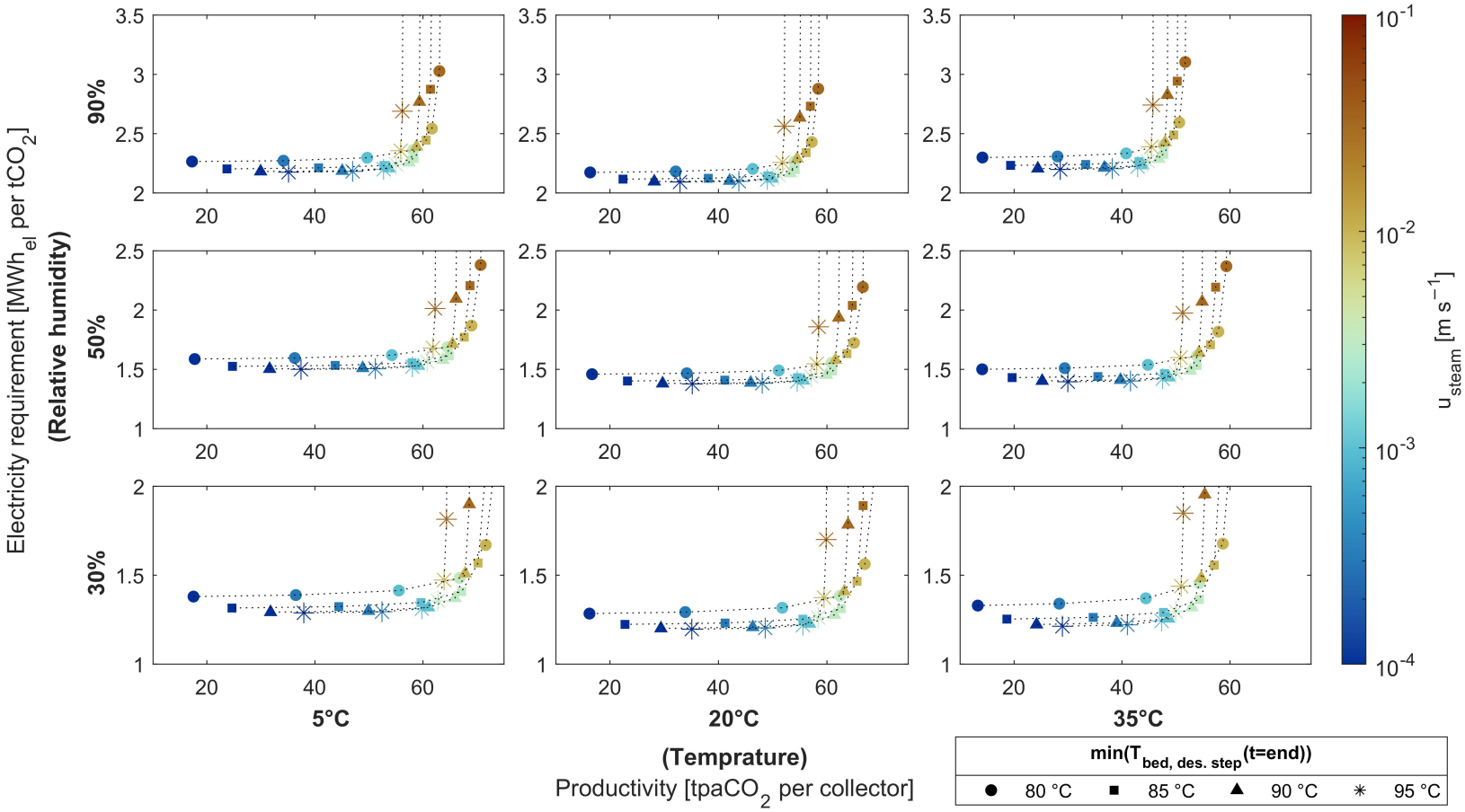


Figure A.9: SA-VTSA bed desorption (bed heating and steam purging steps) sensitivity analysis. The sensitivity to two key variables is demonstrated: the symbol colours show different steam velocities (u_{steam}), and the symbol shape corresponds to different lowest temperatures in the sorbent bed at the end of the bed heating step ($\min(T_{bed,des\ step}(t = end))$). Please note that the y-axis has a different scale for different relative humidity. Adapted from [115].

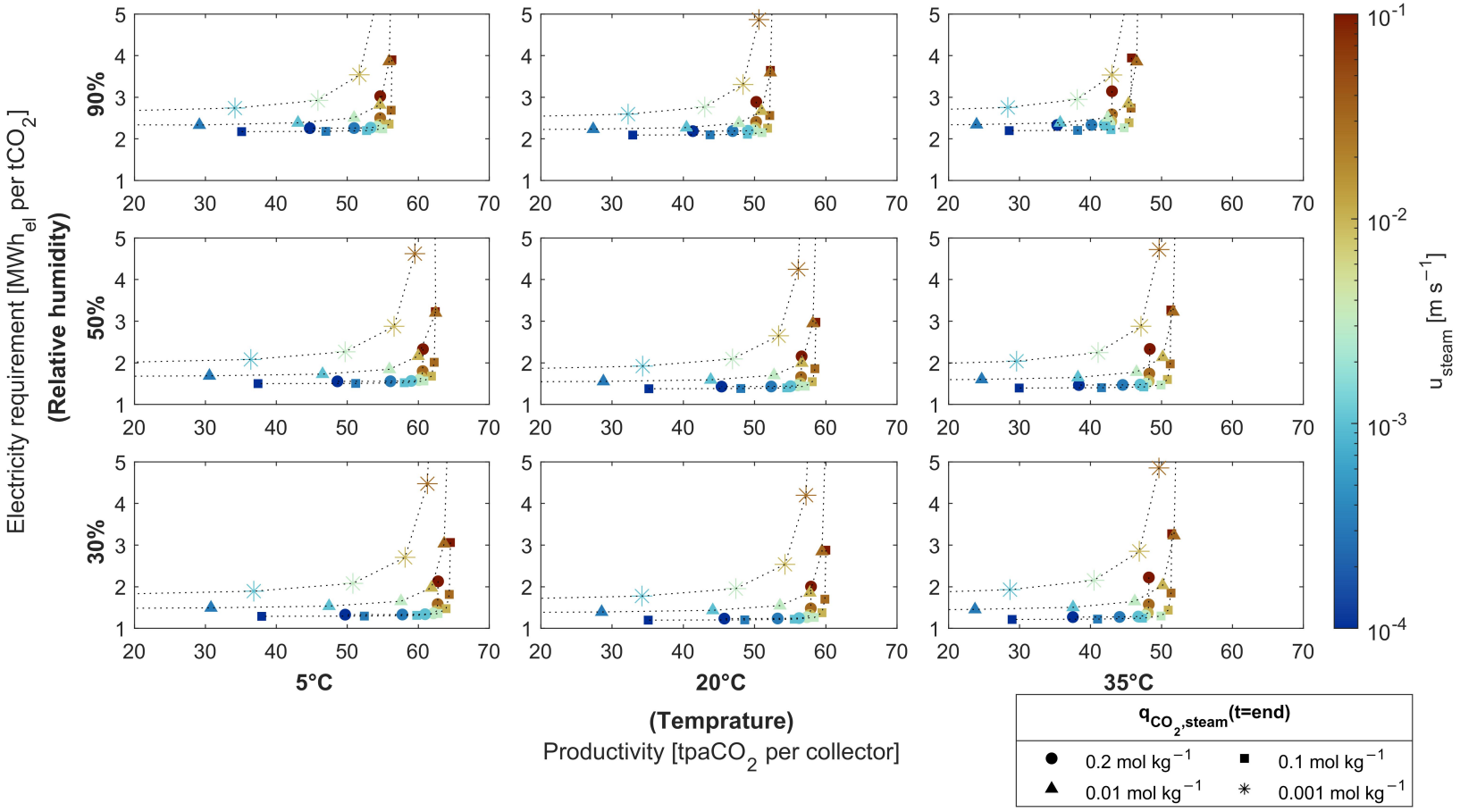


Figure A.10: SA-VTSA steam purging step sensitivity analysis. The sensitivity to two key variables is demonstrated: the symbol colours show different steam velocities (u_{steam}), and the symbol shape corresponds to different average bed CO_2 loading at the end of the steam purging step ($q_{CO_2,steam}(t = end)$). Adapted from [115].

APPENDIX B

TECHNO-ECONOMIC ASSUMPTIONS

B.1 Energy generation, storage and conversion technologies

Table B.1: Cost assumptions for energy generation, storage and conversion. Adapted from [134].

	Unit	Value	Source
Solar PV			
CapEx	$/kW$_p$	883	[316]
OpEX$_{fix}$	$/(kW$_p$.a)	3% of CAPEX	
Lifetime	year	30	[317]
Wind			
CapEx	$/kW$_p$	1349	[316]
OpEX$_{fix}$	$/(kW$_p$.a)	3% of CAPEX	
Lifetime	year	30	[317]
CSP			
CapEx	$/m^2	332	[169, 316]$^{\alpha}$
OpEX$_{fix}$	$/(m^2.a)	3% of CAPEX	
Lifetime	year	35	[169]
Gas turbine			
CapEx	$/kW$_{el}$	785	[318]
OpEX$_{fix}$	$/(kW$_{el}$.a)	7.33	[318]
OpEX$_{var}$	$/kWh$_{el}$	0.00471	[318]
Lifetime	year	40	[317]

Fired boiler			
CapEx	$/kW$_{th}$	346	[139, 319][b]
OpEX$_{fix}$	$/(kW$_{th}$.a)	16	[139, 319][b]
Lifetime	year	20	
Nuclear			
CapEx	$/kW$_{el}$	6695	[318][c]
OpEX$_{fix}$	$/(kW$_{el}$.a)	127.35	[318][c]
OpEX$_{var}$	$/kWh$_{el}$	0.00248	[318][c]
Fuel	$/(kWh$_{th}$)	0.0026	[320][c,d]
Lifetime	year	60	[320]
Battery (Li-ion)			
CapEx	$/kWh$_{el}$	277	[187]
OpEX$_{fix}$	$/(kWh$_{el}$.a)	6.8	[187]
Lifetime	year	15	[317]
Battery inverter			
CapEx	$/kW$_{el}$	257	[187]
OpEX$_{fix}$	$/(kW$_{el}$.a)	1.4	[187]
Lifetime	year	15	[317]
Thermal heat storage[e]			
CapEx	$/kWh$_{th}$	22	[169]
OpEX$_{fix}$	$/(kWh$_{th}$.a)	3% of CAPEX	
Lifetime	year	35	
Heat pump			
CapEx	$/kW$_{el}$	1446	[139][f]
OpEX$_{fix}$	$/(kW$_{el}$.a)	65	[139]
Lifetime	year	25	[321]
Steam turbine			
CapEx	$/kW$_{el}$	720	[322][g]
OpEX$_{fix}$	$/(kW$_{el}$.a)	14.4	[322][g]
Lifetime	year	30	[322][g]
Electric boiler			
CapEx	$/kW$_{el}$	144	[321][g]
OpEX$_{fix}$	$/(kW$_{el}$.a)	0.6	[321][g]
OpEX$_{var}$	$/(kWh$_{el}$)	0.00024	[321][g]
Lifetime	year	20	[321]

Electrolyser (alkaline)			
CapEx	\$/kW$_{el}$	800	[253, 255, 323]
OpEX$_{fix}$	\$/(kW$_{el}$.a)	3% of CAPEX	
Lifetime	year	10	
Hydrogen tank			
CapEx	\$/kgH$_2$	727	[19]
OpEX$_{fix}$	\$/(kgH$_2$.a)	3% of CAPEX	
Lifetime	year	20	[19]
Gas compressor			
CapEx	\$/kW$_{el}$	1446	[139][f]
OpEX$_{fix}$	\$/(kW$_{el}$.a)	65	[139]
Lifetime	year	25	[321]

[a] From Ghirardi et al. [169], the heliostat field cost 140 USD/m^2. From the IRENA report [316], the ratio of the tower and receiver to the solar field (i.e., heliostat field) is 0.714. From this ratio, the tower and receiver costs can be estimated to be 100 USD/m^2. Also, from the IRENA report [316], indirect EPC and owner's cost have a ratio of 0.316 from the total cost of the CSP plant. Thus, the indirect EPC and owner's cost can be estimated from the calculated heliostat field, tower and receiver costs which correspond to 76 USD/m^2. Lastly, the site improvement cost is estimated to be 16 USD/m^2 [169]. By adding all the costs, the CSP CAPEX is found to be 332 USD/m$^2_{heliostat}$.

[b] Purchase cost from [319]. CapEX and OpeEX were estimated using the method from Towler and Sinnott [139] and a CE index of 596.2 (2020).

[c] Currently, the majority of commercial nuclear reactors are light water reactors (LWRs). These reactors typically produce high-pressure steam with a pressure of around 70 bar and a maximum temperature of around 330 ℃ [174]. This results in a thermal-to-electricity efficiency of 30%–33%. However, this work defines high-temperature heat as high-pressure steam at 560 ℃ and 100 bar, which LWRs are unsuitable for generating. However, This steam grade can be generated using advanced nuclear reactors (Generation IV) such as high-temperature gas reactors. These advanced reactor designs can generate heat at much higher temperatures where a thermal-to-electricity efficiency of 45% could be achieved [175, 176]. However, information regarding the cost of these reactors' design is still limited; thus, the cost assumptions of LWRs are used. However, the available estimated cost of the heat generated from advanced nuclear reactors is \$31.5–\$49.5 per MWh$_{th}$

using thermal to electricity efficiency of 45% [175]. Based on these assumptions for LWRs and an interest rate of 7%, the heating cost is $33.1 per MWh_{th}, which is aligned with the available information on nuclear-advanced reactors.

[d] 1.35 USD/£.

[e] For HT and LT THS.

[f] Based on compressor cost and Lang Factor = 3.

[g] 1.2 USD/€.

B.2 Direct air capture and point-of-source carbon capture and storage

Direct air capture

Table B.2: DAC process economic assumptions. Adapted from [114].

	Purchased cost[a]		**Life-time Years**	**Source**
CO_2 collector	20,000	$ per collector	25	[b]
Fan	0.89[c]	$ per (m^3/h)	25	[324]
Vacuum pump, compressor and heat pumps[d]	312,547	$ per MW_{el}	25	[324]
Sorbent	2,000	$ per ton sorbent	4	[101]

[a] All costs are adjusted to 2020 using CE index = 596.2.

[b] The CO2 collector cost can be estimated based on the similarity of the materials used to manufacture it compared to cars [44, 66], including steel, aluminium, plastics, insulation, etc. Similar to a car, the CO2 collector is modular; therefore, it can be manufactured using similar process methods used for car manufacturing. Moreover, a material assessment of the CO2 collector can estimate the amount of materials needed for each collector. Each collector has 6 square-shaped steel walls, two of which are movable, with each side having dimensions of around 1.45 m. Assuming a wall thickness of 0.01 m, the total steel weight needed is 990 kg at a density of 7850 kg per m^3. Each collector has 88 frames. Each frame

consists of 21.3 m of aluminium tubes with a diameter of 0.01 m and a thickness of 0.001 m. Thus, each collector contains 242 kg of aluminium tubes at a density of 2710 kg per m^3. Aluminium mesh is used to improve the bed thermal conductivity where each frame contains 1.9 kg of aluminium mesh based on the ratio used in Climeworks patent [66], resulting in an additional 166.5 kg of aluminium per collector. Additional aluminium and plastic are used for C-profiles, wedge spacers and sealing strips at a ratio of 0.53 kg per frame or 46.5 kg per collector. Based on this calculation, the material needed for one collector is around 1446 kg per collector, including steel, aluminium and plastic. This can be compared to a mid-sized car's average weight of around 1500 kg [325].

[c] CapEx.

[d] Heat pumps are estimated based on the main process equipment—compressors—cost, then adjusted to account for the total installed cost, including auxiliary equipment, using a Lang Factor of 3.

Carbon capture and storage

The non-energy associated cost for CCS was estimated from [181, 326], where $15 per tCO_2 was assumed. CCS LT heat and electricity requirements are provided directly from the system.

B.3 Regional weighted average capital cost

The 3 regional WACC assumptions used in this work are shown below. The low WACC assumption is based on Ameli et al. [20] low-carbon investment assumptions for different regions. Mid WACC is two times low WACC, and high WACC is three times the low WACC.

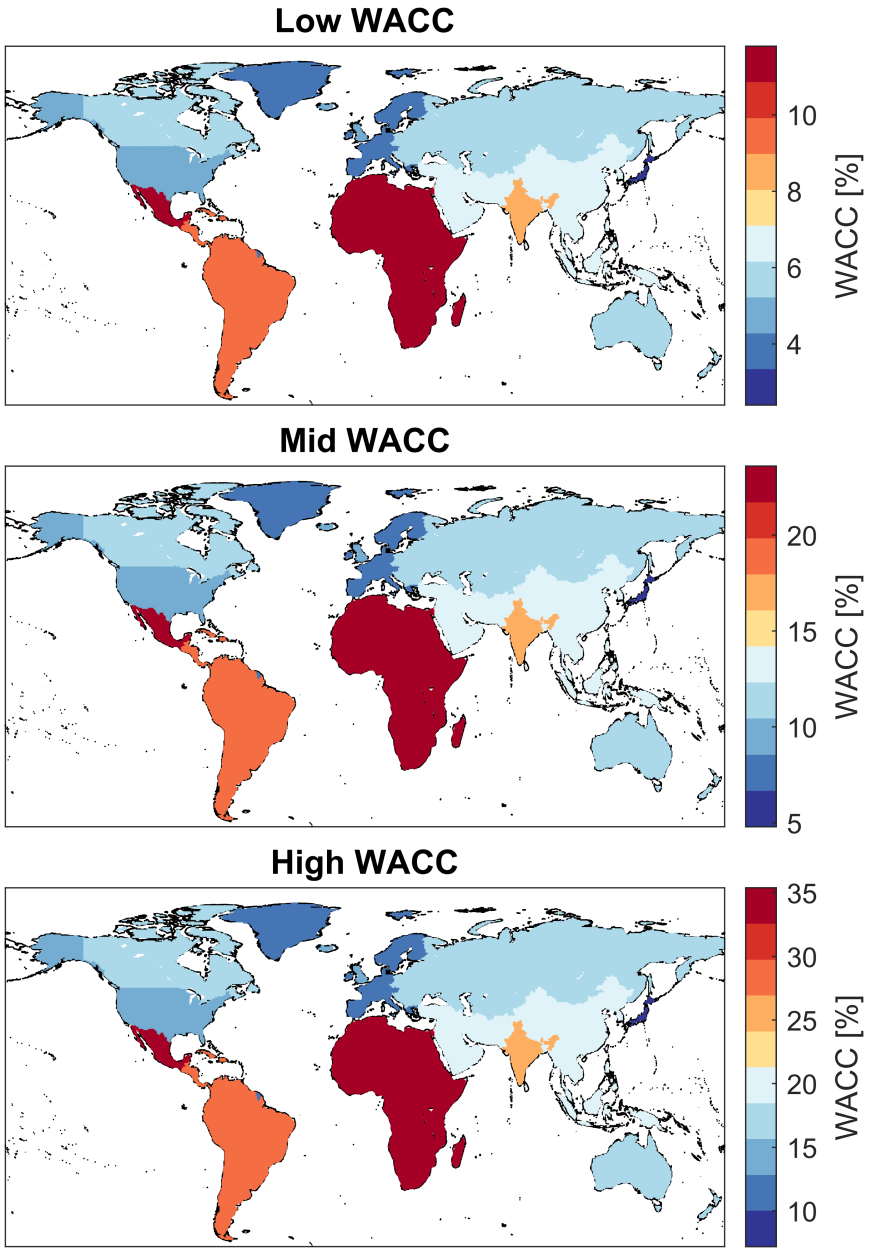


Figure B.1: Regional WACC assumptions.

APPENDIX C

ENVIRONMENTAL ASSUMPTIONS

C.1 Lifecycle greenhouse gas emissions

Table C.1: Lifecycle greenhouse gas emissions from infrastructure and supply chain assumptions. Adapted from [134].

Technology	Unit	Baseline	Min	Max	Source
Nuclear	$gCO_{2,eq}$ per kWh_{th}	4.6	1.4	41.8	[327, 328]
GT w/CCS	$gCO_{2,eq}$ per kWh_{el}	14.1	11.0	18.8	[327, 328]
Wind	$kgCO_{2,eq}$ per kW_{el} per year	31.0	19.7	158.0	[327, 328]
Solar PV	$kgCO_{2,eq}$ per kW_{el} per year	108.5	41.7	406.8	[327, 328]
CSP	$kgCO_{2,eq}$ per $m^2_{heliostat}$ per year	15.5	5.7	40.6	[327–329]
Battery	$gCO_{2,eq}$ per $kWh_{el,discharge}$	300	60	640	[330]
THS	$gCO_{2,eq}$ per $kWh_{th,discharge}$	17.9	5.0	46.9	[331]

C.2 Land requirement

Table C.2: Land requirement assumptions. Adapted from [134].

Technology	Unit	Baseline	Source
Nuclear	m^2 per kW_{th}	1.39	[329]
GT	m^2 per kW_{el}	2.23	[329]
Solar PV	m^2 per kW_{el}	33.59	[143, 329]
Wind	m^2 per kW_{el}	78.20	[329]
CSP	m^2 per $m^2_{heliostat}$	12.00	[143]

C.3 Water requirement

Table C.3: Water requirement. Adapted from [134].

Technology	Unit	Baseline	Min	Max	Source
Condensing ST	tH_2O per MWh_{el}	2.18	0.38	3.37	[332]
GT	tH_2O per MWh_{el}	0.19	0.19	1.29	[332]
CCS	tH_2O per MWh_{NG} (LHV)	0.20	0.20	0.20	[332]
Wind	tH_2O per year per MW_{el}	5	0	21	[329, 332]
Solar PV	tH_2O per year per MW_{el}	51	9	222	[329, 332]
CSP	tH_2O per year per $m^2_{heliostat}$	5.7E-2	5.7E-2	5.7E-2	[329, 332]

APPENDIX D

SOLAR AND WIND RESOURCES VALIDATION

D.1 Solar resources

D.1.1 Global horizontal irradiation and solar photovoltaic potential

Figure D.1 shows the global horizontal irradiance (GHI) data used in this work integrated over a full year (2020) obtained from NASA MERRA-2 [133], and Figure D.2 show the yearly GHI obtained from Global Solar Atlas that has been calculated for at least 10 years for most locations. It can be seen that the two data sets are in agreement. Similarly, Figure D.3 shows the solar photovoltaic (PV) potential data used in this work, which was calculated using the simplified model from Huld et al. [166] and input data, including temperature and GHI from NASA MERRA-2 [133]. This solar PV potential data set can be compared with the ones obtained from Global Solar Atlas shown in Figure D.4, where it can be seen that the two data sets are aligned.

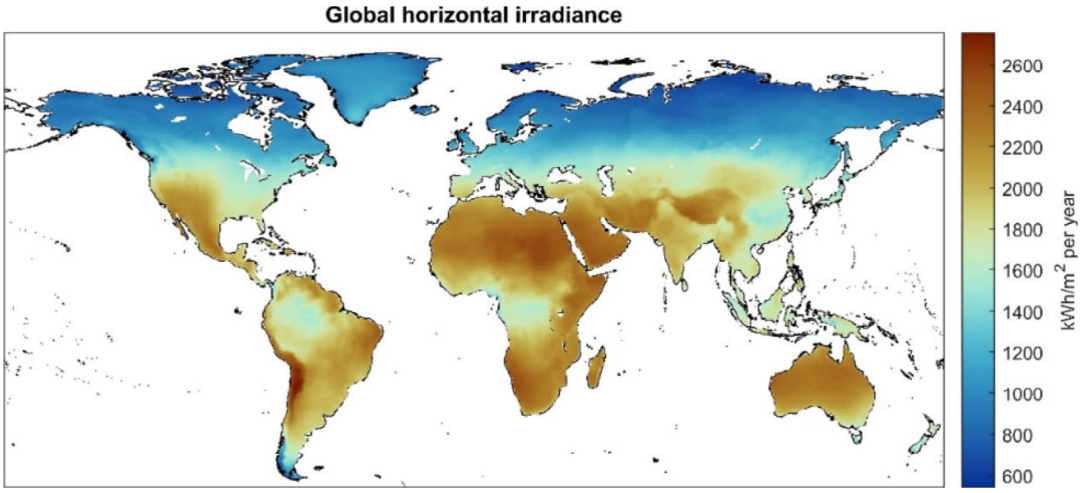


Figure D.1: Yearly global horizontal irradiance data for 2020. The data is based on NASA MERRA-2 data [133]. Adapted from [134].

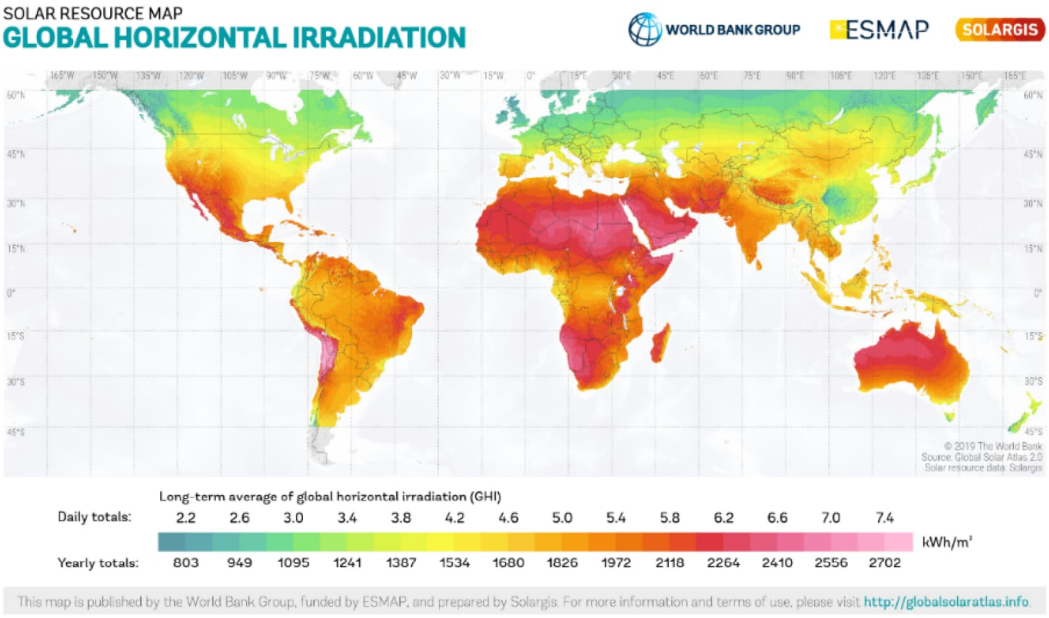


Figure D.2: Yearly global horizontal irradiance obtained from the Global Solar Atlas 2.0. Global Solar Atlas 2.0 is a free, web-based application developed and operated by the company Solargis s.r.o. on behalf of the World Bank Group, utilising Solargis data, with funding provided by the Energy Sector Management Assistance Program (ESMAP). For additional information: https://globalsolaratlas.info. Reproduced under Creative Commons CC-BY 4.0 license.

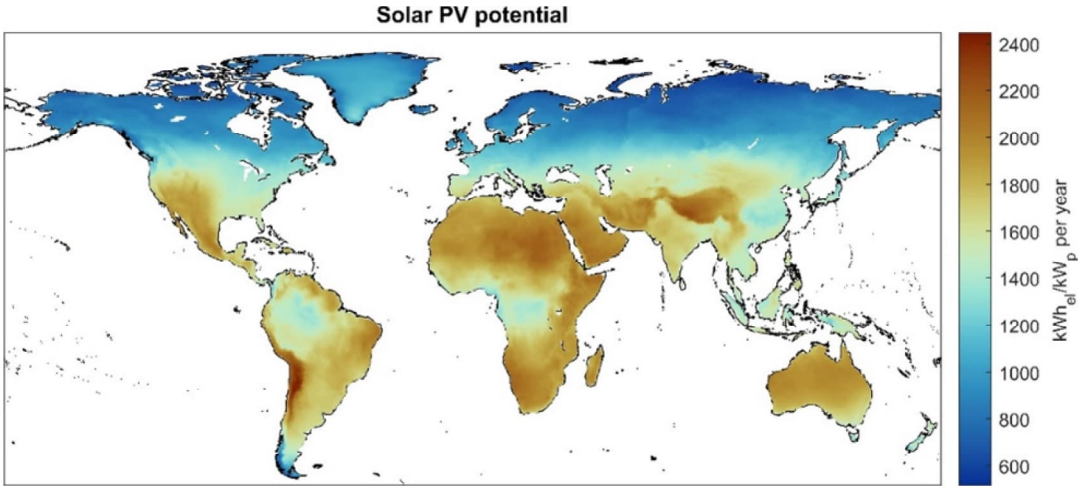


Figure D.3: Yearly solar photovoltaic potential for 2020. The data is calculated based on the method of Huld et al. [166] and input data from NASA MERRA-2 [133]. Adapted from [134].

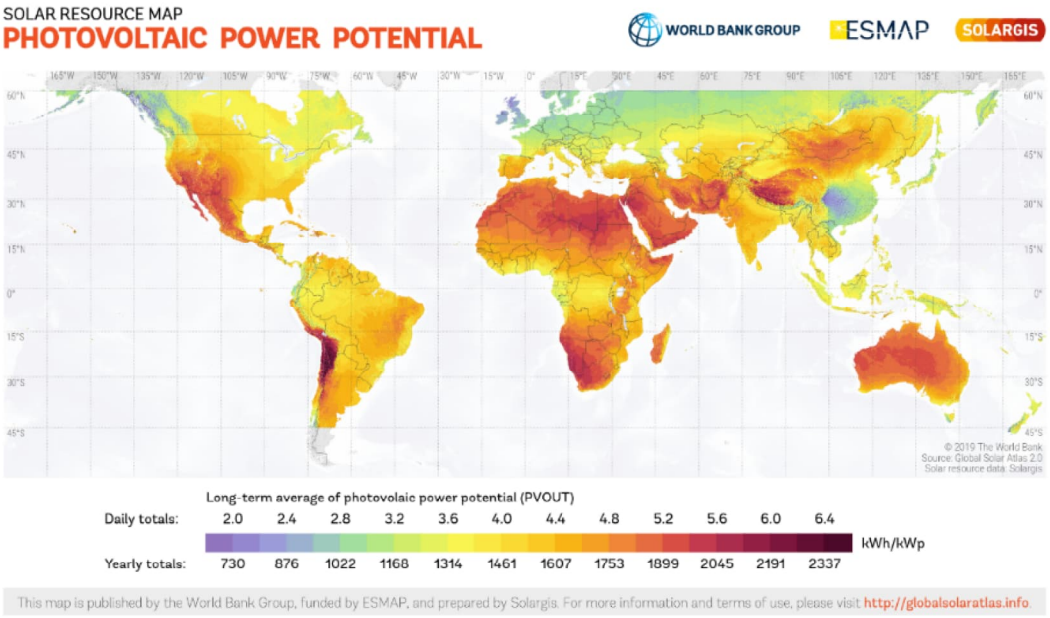


Figure D.4: Yearly solar photovoltaic potential obtained from the Global Solar Atlas 2.0. Global Solar Atlas 2.0 is a free, web-based application developed and operated by the company Solargis s.r.o. on behalf of the World Bank Group, utilising Solargis data, with funding provided by the Energy Sector Management Assistance Program (ESMAP). For additional information: https://globalsolaratlas.info. Reproduced under Creative Commons CC-BY 4.0 license.

D.1.2 Direct normal irradiation and concentrated solar power potential

The concentrated solar power (CSP) potential in this work is calculated based on the model developed in previous works [169, 170], where direct normal irradiation (DNI) is the required input of the model. Since NASA MERRA-2 [133] does not provide information regarding DNI directly, the Direct Insolation Simulation Code (DISC) model provided available from the PVLIB toolbox for MATLAB [171] was used to estimate hourly DNI using NASA MERRA-2 [133] data as model input. The calculated hourly DNI is integrated over a year (2020) and is shown in Figure D.5. This yearly DNI can be compared to the annual DNI obtained from Global Solar Atlas, as shown in Figure D.6, where both sets show a good agreement. To validate CSP potential, we calculate the CSP efficiency of converting DNI using the heliostat field area to thermal energy, which is shown in Figure D.7, which is in the range 50%–57%. Thus, an efficiency of converting DNI to electricity of 19–22% can be obtained when a thermal-to-electric efficiency of 0.38 is used. This calculated DNI to electricity efficiency can be compared with the data available in the literature, such as 19%-26% (DNI = 200–400 W/m^2) [333], 9%–20% [334], and 17%–19% [335].

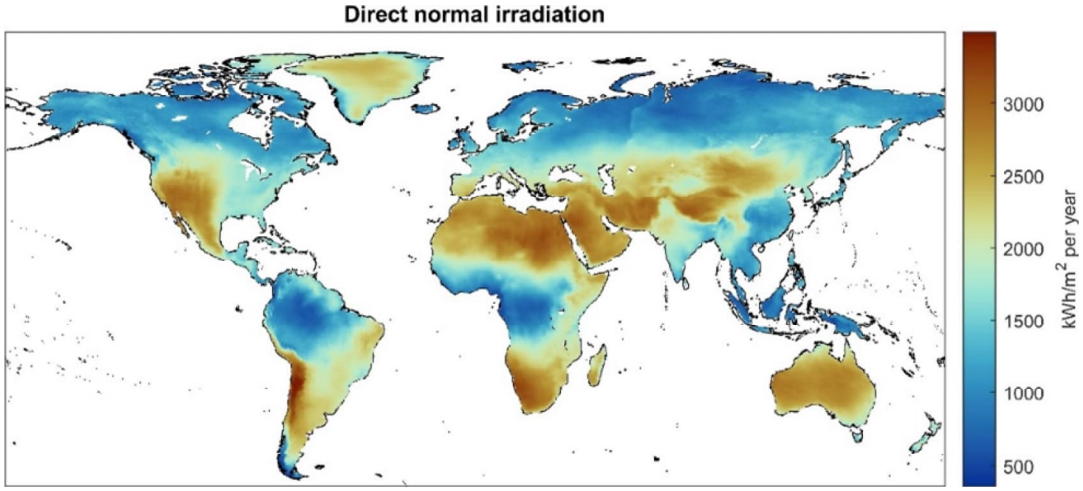


Figure D.5: Yearly direct normal irradiance for 2020. The data is calculated using the Direct Insolation Simulation Code (DISC) model [171] and data from NASA MERRA-2 [133]. Adapted from [134].

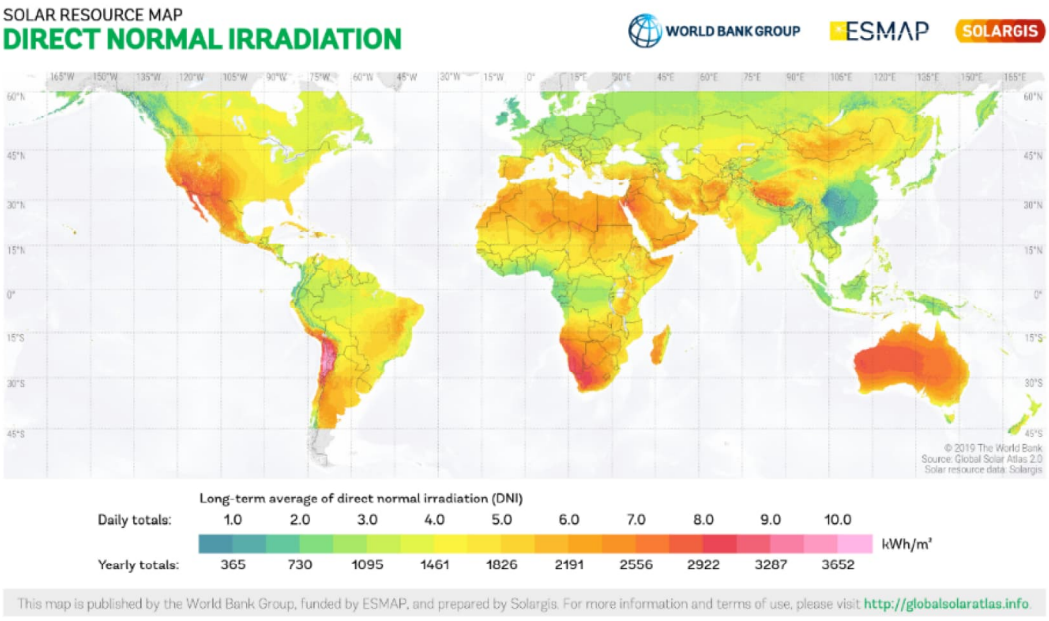


Figure D.6: Yearly direct normal irradiance obtained from the Global Solar Atlas 2.0. Global Solar Atlas 2.0 is a free, web-based application developed and operated by the company Solargis s.r.o. on behalf of the World Bank Group, utilising Solargis data, with funding provided by the Energy Sector Management Assistance Program (ESMAP). For additional information: https://globalsolaratlas.info. Reproduced under Creative Commons CC-BY 4.0 license.

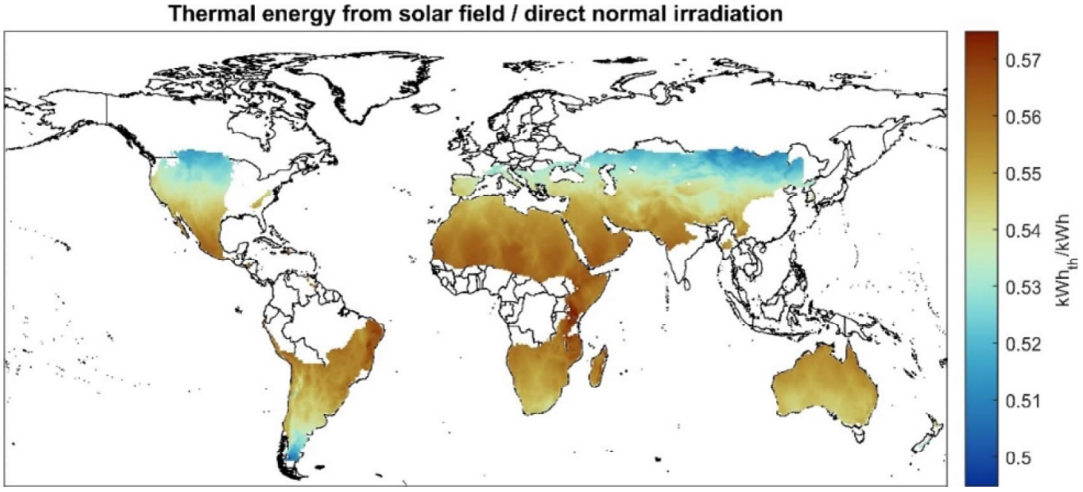


Figure D.7: Normalised concentrated solar power potential for 2020. The values are based on direct normal irradiation calculated using the method from previous works [169, 170] using input data from NASA MERRA-2 [133]. Regions with yearly DNI below 1800 kWh/m^2 (around 205 W/m^2) and high latitudes are excluded. Adapted from [134].

D.2 Wind speed

D.8 shows the average wind speed calculated at the height of 100m using data obtained from NASA MERRA-2 [133] and the method detailed in the method section. D.9 shows similar data for average wind speed obtained from Global Wind Atlas, which was sampled in the period between 1998–2017. General trends from both data sets are aligned as estimating there is large uncertainty with estimating wind speed at different hights [336, 337].

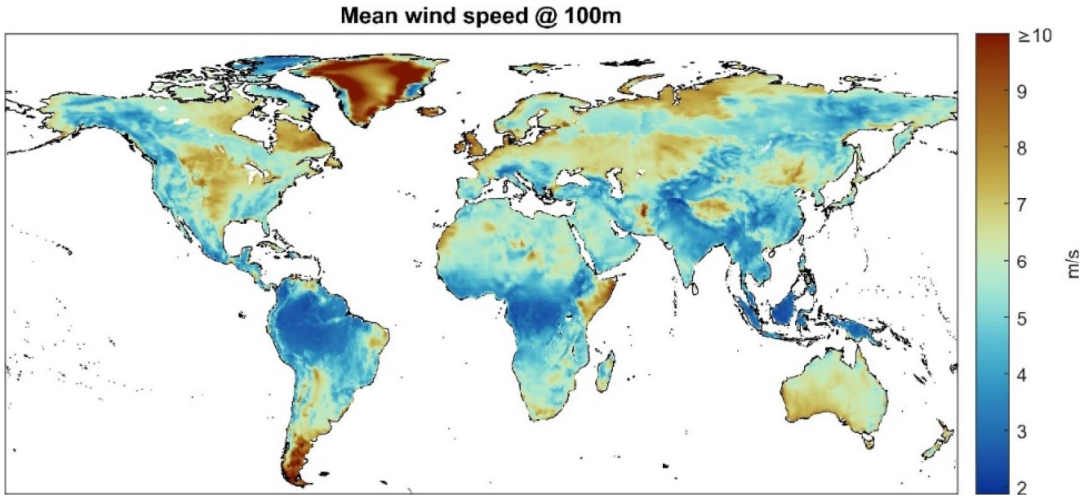


Figure D.8: Average wind speed calculated at 100m for 2020. The data is calculated using the method detailed in Section 3.4.4 and input data from NASA MERRA-2 [133]. Adapted from [134].

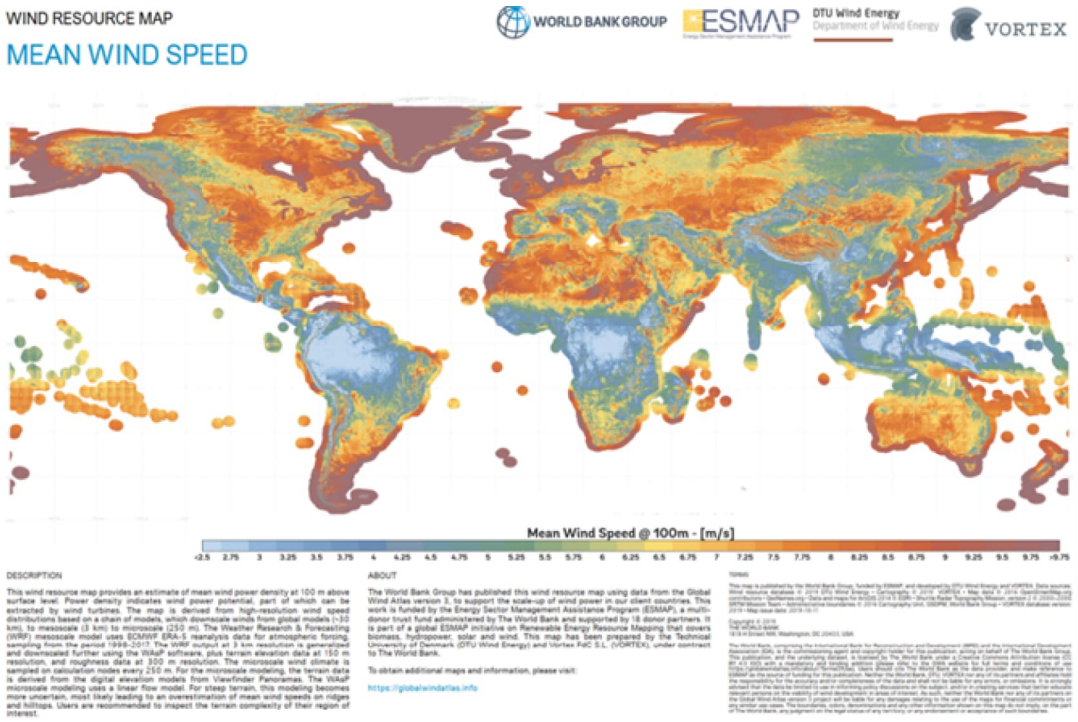


Figure D.9: Average wind speed calculated at 100m obtained from Global Wind Atlas 3.0. Global Wind Atlas 3.0 is a free, web-based application developed, owned and operated by the Technical University of Denmark (DTU). The Global Wind Atlas 3.0 is released in partnership with the World Bank Group, utilising data provided by Vortex, using funding provided by the Energy Sector Management Assistance Program (ESMAP). For additional information: https://globalwindatlas.info. Reproduced under Creative Commons CC-BY 4.0 license.